Studies Of Fluctuations And Transport In Active Matter Systems

THESIS SUBMITTED FOR THE DEGREE OF

Doctor of Philosophy (Science)

IN PHYSICS (THEORETICAL)

BY

TANMOY CHAKRABORTY

DEPARTMENT OF PHYSICS
University of Calcutta
2024

To my beloved parents for their unconditional love and support.

Acknowledgements

I am indebted to Prof. Punyabrata Pradhan, my doctoral supervisor, for introducing me to the fascinating realm of active matter. His patience, mentorship, and encouragement to delve deeply into the subject have been invaluable throughout this extensive journey. I have always admired his simplistic and intuitive approach to explaining complex physics problems, and I aspire to bring this feature forward into my future research endeavors. I express my gratitude to my two thesis committee members, Prof. Sakuntala Chatterjee and Prof. Gautam Gangopadhyay, for their assessment, suggestions, and engaging discussions during our annual evaluation sessions.

I acknowledge the Council of Scientific and Industrial Research (CSIR), India [Grant No. 09/575(0124) /2019-EMRI], for the financial assistance throughout my Ph.D. tenure. Furthermore, I extend my appreciation to the Thematic Unit of Excellence on Computational Materials Science and the Cray Supercomputing Facility at the Technical Research Centre (TRC), S. N. Bose National Centre for Basic Sciences, funded by the Department of Science and Technology (DST), India, for providing computational resources.

I am grateful to the S. N. Bose National Centre for Basic Sciences (SNBNCBS) for not only providing a calm and tranquil environment but also for allowing me to meet some wonderful people with whom I hope to stay in touch forever. I consider myself fortunate to be a member of the research group, which includes incredibly talented yet unique individuals: Arghya Da, Sayani Di, Subhadip Da, Dhiraj Da, and Anirban Da as seniors, my colleague Deepsikha and Animesh, as the junior. They have consistently been the person I go to for advice on both academic and personal matters. Indeed, many thanks to them. Let me now introduce those people who have made my Ph.D. journey so enjoyable and fulfilling. My heartfelt gratitude to the members of the "2nd-floor bay": Premashis, Prasun, Krishnendu (Kaka), Krishnendu (Sinha), and Dibyendu, with whom I have spent a significant amount of time on campus. Premashis's willingness to take on new challenges and never-give-up mentality is truly inspiring. Prasun's confidence and ability to simplify complicated situations are captivating. Kaka, as a unique character in the community, exudes an aura of enlightenment even in the most difficult situations. I appreciate the simplicity and helpfulness of the tech savvies, Krishnendu (Sinha) and Dibyendu; they have always been my go-to person for any

technical queries. Besides them, I must mention the appearance of innocent and punctual Biswajit (Panda), charming Debayan, carefree Susmita (Changdar), melodious Shobhan, and well-composed Nur, who have made my doctoral journey quite pleasurable. Thank you for all of the moments that I will cherish forever. Additionally, outside of academics, I participated in a variety of sports activities, including cricket, badminton, and football (part-time), which allowed me to socialize with my lovable juniors such as Anirban (Paul), Samir, Manodip, Rik, Sayan, Anutosh, Avijit, Bivas, Shuvam, Shivam, Sabuj, Jayarshi, Ram Krishna, Samrat, Pratap, Soumen, Anirban (Roy Chowdhury), Ardhendu, and Arnab, among others. Thank you for the healthy competition, especially during SNB tournaments, which were quite entertaining throughout. Thanks to the other juniors, Chandradip, Ramesh, Ritwick, Sayari, Sutanu, Pallavi, Shreyan, and Anusri, with whom I have interacted on multiple occasions.

I extend my sincere gratitude to the wonderful friends I made before beginning my Ph.D., and our friendship endures to this day. Thanks to my school friends, Sobhoraj, Pikoraj, Biswajit, Souvik, Pinaki, Utsa, Dipankar, Kushal, Sayan, Bhaskar, Bandhan, Rahul (Roy), Rahul (Sarkar), Rajat, and Amit, for staying connected. During the challenging days of the COVID lockdown, amidst the prevailing negativity, these individuals were my sole source of entertainment. I thank Madhurima for turning out to be a good friend and well-wisher since my bachelor days. Since meeting Vipul and Vishal in 2016, our bond has grown significantly, reflecting the mutual trust and respect we share. I deeply appreciate their constant availability, and our group video calls never fail to bring me joy.

Finally, it is time to acknowledge those individuals without whom the world would be incomplete for me. I can never express enough gratitude for how Maa and Baba have molded me with their unconditional love and sacrifices throughout. Without their support and belief in me, I would not have been able to pursue Physics. I consider myself extremely blessed to have them as my parents. I am fortunate to always have Tanugatri (Tora) by my side. I am extremely grateful to her for being the frustration absorber, for her love and emotional support, and, for routinely sending "Google Scholar alert" emails, helping me stay updated with regular articles. A simple thank you would be insufficient to acknowledge it. I am extremely thankful to Didun, Dadu, Baro Mama, Choto Mama, Baro Mami, and Choto Mami for all their love and affection, which immensely helped me stay in my bachelor days. That specific period in my life was highly impactful, and it is the reason I am writing this thesis today. So, a heartfelt thank you to all of them. I am also grateful to senior members Dida, Baro Pisi, Mejo Pisi, Choto Pisi, Arun Kaku, Khokon Kaku, Nano Kaku, Liton Kaku, and fellow members from my generation, Pikai, Bunu, and Guddu, who have constantly supported me with true affection, undoubtedly contributing to where I am today.

Abstract

By using a microscopic theoretical framework, we investigate time-dependent properties of interacting self-propelled particles (SPPs), such as hardcore run-and-tumble particles (RTPs), and their analytically tractable variants. These minimal models, governed by persistence and interaction, give rise to complex many-body correlations and exhibit rich collective dynamical behavior, including phase transitions, which we characterize in this thesis.

We find that, in RTPs with a single conservation law, the large-scale relaxation and fluctuation properties can be characterized by two density- and activity-dependent transport coefficients: the collective- or bulk-diffusion coefficient and mobility. Indeed, we determine these transport coefficients for hardcore RTPs for arbitrary density and tumbling rate. Interestingly, in the limit of strong persistence and low density, we observe a scaling regime for the transport coefficients, where the scaling variable encapsulates the nontrivial interplay between persistence and interaction—the hallmark of the RTPs.

We show that the bulk-diffusion coefficient of athermal RTPs does not possess the motility-induced phase-separation or MIPS-like diffusive instability in any finite dimension; rather, it decays as a power-law in a wide range of density with a parameter-dependent exponent. Consequently, the early-time relaxation of an initial density perturbation is governed by a highly nonlinear diffusion equation, which we show to exhibit superdiffusive scaling. The system, however, eventually reaches the normal diffusive limit.

We use a closure scheme to study the dynamic correlations of currents in one-dimensional hardcore (athermal) RTPs. In moderate time regimes, the bond-current fluctuation grows subdiffusively before exhibiting diffusive growth at large times, with prefactors determined by the bulk-diffusion coefficients and the mobility. Indeed, the suitably scaled current fluctuation follows a universal scaling law on large spatiotemporal scales. Additionally, at low tumbling rates, the spatial correlation of instantaneous currents, akin to velocity correlations, displays a long-ranged correlation, with the correlation length diverging as the inverse square root of the tumbling rate.

We derive hydrodynamics of a prototypical one-dimensional model with variable-range hopping, which mimics passive diffusion and ballistic motion of thermal SPPs. We calculate two density-dependent transport coefficients—the bulk-diffusion coefficient and the mobil-

ity—the ratio of which, despite the violation of detailed balance, is connected to particle-number fluctuation by an Einstein relation. In the limit of infinite-range hopping, the model exhibits a "superfluid"-like transition, characterized by a divergence in the mobility, thus exhibiting giant number fluctuations (GNF) at the transition point.

Overall, our microscopic dynamical framework, which is characterized by the bulk-diffusion coefficient and mobility, elucidates time-dependent properties of a broad class of interacting active matter.

Publications

Papers to be included in this thesis

1. "Hydrodynamics, superfluidity, and giant number fluctuations in a model of self-propelled particles", **Tanmoy Chakraborty**, Subhadip Chakraborti, Arghya Das, and Punyabrata Pradhan, Phys. Rev. E **101**, 052611 (2020).

2. "Transport and fluctuations in mass aggregation processes: Mobility-driven clustering", Subhadip Chakraborti, **Tanmoy Chakraborty**, Arghya Das, Rahul Dandekar, and Punyabrata Pradhan, Phys. Rev. E **103**, 042133 (2021).

3. "Time-dependent properties of run-and-tumble particles: Density relaxation", **Tanmoy Chakraborty** and Punyabrata Pradhan, Phys. Rev. E **109**, 024124 (2024).

4. "Time-dependent properties of run-and-tumble particles. II. Current fluctuations", **Tanmoy Chakraborty** and Punyabrata Pradhan, Phys. Rev. E **109**, 044135 (2024).

5. "Dynamic fluctuations in finite- and infinite-ranged lattice gases and mobility-driven phase separation", **Tanmoy Chakraborty** and Punyabrata Pradhan (manuscript under preparation).

Contents

List of Figures

1

Introduction

Consider a system comprising of N number of (classical) interacting particles. To characterize the system from a dynamical perspective, one would typically use the framework of classical mechanics and derive the equations of motion, employing either Newton's laws of motion or the Lagrange (or Hamiltonian) formalism. The above method could work well for a small number of particles. However, with increasing particle number N, it requires an enormous amount of information to keep track of each particle trajectory, and solving the dynamical equations becomes quite difficult. Interestingly, in such cases, to characterize the dynamic properties, it is possible to construct an analytic description using the techniques of probability theory; this framework is known as statistical mechanics, serving as a link between microscopic dynamics and (coarse-grained) macroscopic observables, which can be measured in typical experiments.

For equilibrium systems, statistical mechanics have become an essential tool to connect the microscopic properties with the macroscopic or thermodynamic variables. The first approach in this direction was made back in the late eighteenth century when Maxwell derived the velocity distribution of ideal gas molecules in Ref. [1, 2]. Following these works, Boltzmann and Gibbs generalized those concepts to generic equilibrium systems (having short-ranged interaction) and provided a prescription for the probability distribution of a microscopic configuration $\mathcal{C}$ in terms of the associated total energy function $E(\mathcal{C})$, which depends on the microstate C. The distribution is the celebrated Boltzmann-Gibbs distribution [3, 4], which

is given by

$$P(\mathcal{C}) = \frac{1}{Z(T)} \exp\left[-\frac{E(\mathcal{C})}{k_B T}\right], \tag{1.1}$$

where k_B is the Boltzmann constant, T is the temperature, and $Z(T)$ is the temperature-dependent normalization factor, called the partition function. It is important to note that Eq. (1.1) is *universal*, i.e., as long as the system has constituents (molecules or atoms) having short-ranged interactions and is in equilibrium, thermodynamic laws governing the systems are independent of the microscopic details. Certainly, the Boltzmann-Gibbs theory is a remarkable achievement in the context of equilibrium systems and allows for developing a unifying framework of equilibrium statistical mechanics.

Despite its numerous achievements, equilibrium statistical mechanics has limited applicability when it comes to describing real-world systems, which are predominantly nonequilibrium in nature. The limitation arises because these systems lack time-reversal symmetry and their microscopic probability weights are no longer described by the Boltzmann-Gibbs distribution; perhaps not surprisingly, systems out of equilibrium are considerably more complex compared to equilibrium ones. Examples of such out-of-equilibrium systems include biological systems, chemical reactions, and energy or matter flows influenced by bulk or boundary drives. As mentioned above, the probability measures $P(\mathcal{C})$ for a microstate $\mathcal{C}$ in a nonequilibrium system deviate significantly from the equilibrium counterpart as given in Eq. (1.1); in fact, it strongly depends on the microscopic details of the model system and apriori unknown. Indeed, there is no generic statistical mechanics framework known for nonequilibrium systems, and one would then focus on microscopic model-dependent analysis [5–7]. With this in mind, in this thesis, we employ a microscopic model-based ("bottom-up") approach to characterize the large-scale statistical properties of a special type of nonequilibrium system, called active matter, as discussed below.

1.1 Active matter

Active matter (AM) refers to a collection of self-propelled particles (SPPs), each of which being capable of performing directed or persistent motion. AM are ubiquitous, spanning over various living elements across length scales ranging from macroscopically observed bird flocks [8], insect swarms [9], and fish schools [10] to microscopically found bacterial colonies [11–15], as well as artificially made photoactivated colloids [16]. Unlike typical Brownian motion in thermal equilibrium, which is governed by the balance of thermal agitation and viscous drag in the medium (via the fluctuation-dissipation relation), persistent propulsion in SPP occurs at the expense of internal or stored energy in the surrounding medium. This

continual energy dissipation drives the system out of equilibrium at the microscopic level, and eventually, the system attains a nonequilibrium steady state (NESS).

Notably, the collection of SPPs in the presence of interaction exhibits a variety of fascinating collective behaviors and, as a result, nontrivial steady-state features. Broadly, SPPs interact through two fundamental mechanisms: (a) *alignment interaction* and (b) *excluded-volume interaction*. In systems with *alignment interactions*, particles tend to orient their velocity vectors toward the average direction of their neighboring particles. However, this perfect alignment is distorted by thermal fluctuations. Eventually, under conditions of sufficient particle density and low thermal noise strength, a collective alignment emerges, leading to coordinated motion or flocking among the particles. This minimal setup is the well-known Vicsek model [17] which assumes SPPs to be point-like objects propelling at a constant speed. Notably, this simplistic model, along with the variants [18, 19], have been successful in explaining the formation of flocking behavior observed in various biological systems [8–10]. On the contrary, the *excluded-volume interaction* involves particles possessing specific shapes that exhibit repulsive forces over short distances. In this situation, persistently moving repulsive particles tend to self-trap and form large clusters. In fact, for particles with isotropic shapes, this mechanism of jamming has been reported to result in motility-induced phase separation (MIPS) [20, 21], see [22] for reviews. Notably, in an interesting scenario for SPPs with shape anisotropy, this excluded volume interaction could lead to an effective alignment, as found in Refs. [23, 24]. The shape-induced macroscopic alignment was also observed experimentally in Ref. [25] with *Myxococcus xanthus*, an elongated bacteria with a rod-shaped structure. Apart from the above-mentioned collective features, the nontrivial interplay between interaction and persistence in SPPs has also been shown to give rise to anomalous scaling of density fluctuation in the system. According to the central limit theorem, the number fluctuation ΔN over a region of volume V scales with the average number of particles $\langle N \rangle$, i.e., $\Delta N \sim \langle N \rangle$. However, this is not the case for SPPs, where ΔN shows non-linear scaling with $\langle N \rangle$, i.e., $\Delta N \sim \langle N \rangle^{\alpha}$, where $\alpha \neq 1$. For $\alpha > 1$, number fluctuation increases and eventually diverges in the thermodynamic limit, leading to *giant* number fluctuations (GNF) in the system. GNF has been found in SPPs through experiments on active granular rods [26], rod-shaped bacteria like *Myxococcus xanthus* [25] and *Bacillus subtilis* [27], and various other theoretical studies [21, 28, 29]. Apart from the atypical increase in number fluctuations, recent experiments on microorganisms having circular motility [30] have noted a substantial suppression of number fluctuations, denoted by $\alpha < 1$. This decrease in number fluctuation effectively vanishes density fluctuations in the system at the thermodynamic limit, leading to hyperuniformity in active systems [31, 32].

In this thesis, we concentrate on isotropic self-propelled particles (SPPs) that interact

via excluded-volume interactions and aim to characterize their large-scale fluctuations and transport behaviors. To elucidate the intriguing properties of such systems, significant effort has been devoted to developing minimal model systems that account for the interaction and persistence of constituent particles. To this end, three models have been extensively studied in the literature: run-and-tumble particles (RTPs), active Brownian particles (ABPs), and active Ornstein-Uhlenbeck particles (AOUPs), which we will discuss in the subsequent section.

1.1.1 Run-and-tumble particles (RTPs)

Consider a bacterium such as Escherichia coli (E. coli), which moves by rotating its flagella. Tracking the trajectories of individual E. coli via microscopy, Berg and Brown in Ref. [33], later Berg and Anderson in Ref. [34] observed that the coherent counterclockwise rotation drives the E. coli to *run* in a straight line up to a typical time of ~ 1 sec, whereas disassembled clockwise rotation causes the bacterium to *tumble* for a much shorter duration of ~ 0.1 sec in a random direction. This observation motivated researchers to come up with a minimal model system that mimics the motion of E. coli. To this end, Schnitzer [35] first proposed a continuum model that incorporates the run-and-tumble dynamics to explain the chemotaxis of a single E. coli. In this model, each particle propels with speed v_R along a randomly chosen direction $\hat{u}$. The particle also changes the propulsion direction $\hat{u}$, i.e., tumbles along any randomly chosen direction instantaneously with rate γ. The time evolution of the position $\vec{r}(t)$ in the overdamped limit can be expressed as,

$$\frac{d\vec{r}}{dt} = v_R\hat{u} + \sqrt{2D_T}\vec{\eta}(t), \tag{1.2}$$

where D_T is the translational or thermal diffusivity, which was set to zero in [35]. Note that $\vec{\eta}(t)$ is the Gaussian white noise with zero mean and unit variance. Later, this noninteracting description of RTP was generalized to the many-particle systems in one dimension by Tailleur and Cates in Ref. [20]. In this case, the time evolution of the position of a particle (say ith) follows the overdamped Langevin's equation written below,

$$\frac{d\vec{r_i}}{dt} = v_R\hat{u}_i - \mu\vec{\nabla}_i\sum_{j\neq i}U(|\vec{r}_i - \vec{r}_j|) + \sqrt{2D_T}\vec{\eta}(t), \tag{1.3}$$

where μ is the translational mobility and the interaction potential $U(|\vec{r}_i - \vec{r}_j|)$ is repulsive and short-ranged. The above continuum description of many-body RTPs has also been extended to the lattice model with hardcore interactions in Refs. [36–38]. In a lattice geometry with d dimensions, the orientation of particles $\hat{u}$ is confined to $2d$ possible directions, conse-

quently constraining particle movement along those $2d$ directions. For hardcore interactions, the run-and-tumble dynamics on the lattice can be expressed as follows: a particle (say ith) stochastically hops with rate v_R to the nearest neighboring site along $\hat{u}_i$ provided the destination site is vacant. Additionally, particles randomly change their orientation stochastically with rate γ. Notably, when two hard-core RTPs collide, they block each other's movements. This bound state is only broken when one of the two particles tumbles, as determined by the tumbling rate γ. When γ is small, this duration is significantly small (around $1/\gamma$), during which additional particles join the cluster, leading to the formation of larger clusters. As a result, this model promotes particle clustering with strong persistence and high density. Using a mean-field description, Tailleur and Cates showed that this clustering effect observed in RTPs in one dimension can result in instability, indicating phase separation in the system [20]. This phenomenon is essentially known as motility-induced phase separation (MIPS) [see Sec. 1.2]. In Ref. [36], Soto and Golestanian conducted a numerical simulation to study clustering in hardcore RTPs on a lattice in both one and two dimensions. Particle clusters were found to have a characteristic length scale of $1/\sqrt{\gamma}$ in both dimensions. To provide a microscopic description of particle clustering, Slowman, Evans, and Blythe considered the simplest nontrivial scenario of two hardcore RTPs on a lattice in one dimension [37]. To this end, they calculated the steady-state distribution function of the inter-particle separation. Their findings suggest that, despite being repulsive, there is an "effective" attraction between the particles when they are very close together. Recently, Das, Kundu, and Dhar extended the problem in the continuum space in the presence of thermal diffusion in [39]. However, when dealing with multiple particles (more than two), precise analytical methods have primarily been limited to scenarios involving harmonic interactions [40, 41]. In situations involving hardcore repulsion, efforts to develop analytical treatments are currently in progress [42–44].

1.1.2 Active Brownian particles

As discussed, the run-and-tumble particles (RTPs) model represents the movement pattern of bacteria such as E. coli, which consists of an extended ballistic run followed by an abrupt reorientation. In contrast, synthetic active particles [45, 46] often exhibit smoother orientation changes. For these systems, the model of active Brownian particles (ABPs), in which orientation follows Brownian motion, is useful. This model essentially generalizes the Brownian motion to active particles, initially introduced in two dimensions by Fily and Marchetti in [21] and subsequently by Redner, Hagan, and Baskaran in [47]. The model consists of spherical SPPs with diameter σ, propelling at a constant speed v_A, with the direction of propulsion $\hat{u} = (\cos\theta, \sin\theta)$ [where θ is the angle between the propulsion direction and the x

axis] experiencing rotational diffusion with diffusivity D_R. In the case of multiple particles, the configuration of the system is described by the position and propulsion direction, denoted as $\vec{r}_i(t), \theta_i(t)$, for all particles, where $i = 1, 2, \ldots, N$. Under the overdamped condition, their evolutions obey the coupled Langevin equations:

$$\frac{d\vec{r}_i}{dt} = v_A \hat{u}_i - \mu \vec{\nabla}_i \sum_{j \neq i} U(|\vec{r}_i - \vec{r}_j|) + \sqrt{2D_T}\vec{\eta}(t), \tag{1.4}$$

$$\frac{d\theta_i}{dt} = \sqrt{2D_R}\vec{\eta}_i^{(R)}(t), \tag{1.5}$$

where μ and D_T are the translational mobility and diffusivity, respectively, and $\vec{\eta}_i(t)$ and $\vec{\eta}_i^{(R)}(t)$ are the Gaussian white noises with zero mean and unit variance. The interaction potential $U(r)$ is typically considered to be the Weeks-Chandler-Anderson (WCA) potential $U(r) = 4[(\sigma/r)^{12} - (\sigma/r)^6] + 1$ for $r < 2^{1/6}\sigma$ and 0 otherwise [48]. However, alternative potentials were also explored in various other works: Fily et. al. in [21] used the short-ranged repulsive potential $U(r) \propto [2\sigma^2 - (2\sigma - r)^2/2]$ for $r < 2\sigma$ and 0 otherwise; Bialke et. al. considered Gaussian $U(r) \propto e^{-r^2}$, harmonic $U(r) \propto (r-1)^2$, and Yukawa potential $U(r) \propto e^{-r}/r$ in [28, 49], Caporusso et. al. employed Mie potential $U(r) = 4[(\sigma/r)^{64} - (\sigma/r)^{32}] + 1$ for $r < 2^{1/32}\sigma$ and 0 otherwise in [50].

1.1.3 Active Ornstein-Uhlenbeck particles

Both ABP and RTP share the characteristic of having a constant magnitude of self-propulsion across all particles. However, in many biological contexts [51], it is essential to account for intrinsic fluctuations in the self-propulsion speed of individual particles. This consideration leads to the modeling of active Ornstein-Uhlenbeck particles (AOUPs) [52, 53], where the self-propulsion speed follows Ornstein-Uhlenbeck dynamics. The configuration of the system is defined by the set of position and self-propulsion velocities $\{\vec{r}_i(t), \vec{v}_i\}$ for all particles, which in the overdamped limit are governed by the following equations:

$$\frac{d\vec{r}_i}{dt} = \vec{v}_i(t) - \mu \vec{\nabla}_i \sum_{j \neq i} U(|\vec{r}_i - \vec{r}_j|) + \sqrt{2D_T}\vec{\eta}(t), \tag{1.6}$$

$$\frac{d\vec{v}_i}{dt} = -\omega \vec{v}_i(t) + \sqrt{2\Delta}\vec{\xi}_i(t), \tag{1.7}$$

where D_T and Δ are the noise strengths, $1/\omega$ is the persistence time, and $\vec{\eta}(t)$ and $\vec{\xi}_i(t)$ are Gaussian white noise with zero mean and unit variance. Note that, unlike the other two models studied earlier, the self-propulsion speed is not bounded here. One can then define the characteristic speed of AOUPs as $v_{AO} = \sqrt{\omega\Delta}$ [54].

The models mentioned above provide paradigmatic examples of active matter, defined by two key components: inherent persistence and excluded volume interactions. An obvious question arises: are these models interconnected, and is there any emerging universality among them? In this direction, there are a few studies that we will now discuss. In [55], Cates and Tailleur investigated the relationship between RTPs and ABP in d dimensions. They find that when the propulsion speed and tumbling rate of RTPs (i.e., γ) or the rotational diffusion of ABPs (i.e., D_R) remain isotropic (i.e., not dependent on the propulsion directions), both systems exhibit identical time-evolution of density. This equivalence is established using the transformation $\gamma = (d-1)D_R$. Later, Solon, Cates, and Tailleur extended the comparison between RTPs and ABPs in the presence of a trapping potential [56]. Their findings indicate that the equivalence holds within the limits of weak trapping forces. However, in other scenarios, the dynamics become crucially dependent on the reorientation events (discrete for RTPs and continuous for ABPs), and consequently, the equivalence breaks down. Furthermore, Dolai et al. compared the steady-state properties of RTPs, ABPs, and AOUPs in a single-file continuum space in [54]. In these models, the nontrivial interplay of repulsion and persistence causes large clusters to form. In all three models, the clusters were found to be motile, with an exponential distribution of cluster size. Using the transformations $v_R = v_{AO} = v_A/\sqrt{2}$ and $\gamma = \omega/2 = D_R/2$, it is possible to show that the distribution functions for each model follow a *universal* scaling relation. They also find that the static and dynamic density correlations for these models behave identically after undergoing the aforementioned transformations. Notably, the authors found no bulk phase separations in the system. The observations presented thus far indicate the existence of a universal picture, even though the corresponding microscopic dynamics are different.

1.2 Motility-induced phase separation

Motility-induced phase separation (MIPS) refers to the spontaneous segregation of phases in active systems that interact through repulsive forces. This is counterintuitive in terms of equilibrium physics, which states that phase separation happens only when particles interact attractively. Over the last two decades, extensive research has speculated the existence of MIPS for the model systems of RTPs [20], ABPs [21, 28], and AOUPs [53], which are crucial in modeling various living microorganisms as well as synthetic active colloids. In this section, we will briefly explore the theory, implications, and current status of MIPS.

The first key ingredient of MIPS came from the work of Schnitzer back in 1993 [35] which concluded that active particles accumulate where they move slowly. He studied a single RTP in two dimensions with position-dependent self-propulsion speed, i.e., $v_R = v_R(\vec{r})$. The quantity of interest here is the probability of finding the RTP at position $\vec{r}$ with orientation

$\hat{u}$ at time t, i.e., $P[\vec{r}, \hat{u}(\theta), t]$. This can be computed using the master equation corresponding to the Langevin equation described in Eq. (1.2). In the athermal limit, achieved by setting $D_T = 0$, the master equation can be expressed as:

$$\frac{\partial}{\partial t} P[\vec{r}, \hat{u}(\theta), t] = -\nabla . [v_R(\vec{r}) \hat{u} P(\vec{r}, \hat{u}, t)] - \gamma P[\vec{r}, \hat{u}(\theta), t] + \frac{\gamma}{2\pi} \int_0^{2\pi} d\theta' P[\vec{r}, \hat{u}(\theta'), t]. \quad (1.8)$$

For isotropic processes, the steady-state solution of the above equation can be simply shown to be

$$P_{st}(\vec{r}, \hat{u}) \propto \frac{1}{v_R(\vec{r})}. \quad (1.9)$$

The equation above indicates that the RTP is more likely to be located where the velocity is lower, and vice versa. Motivated by this observation, Tailleur and Cates developed a phenomenological theory of MIPS [22], assuming that the presence of crowders alters self-propulsion speed. In other words, the explicit position dependence in the self-propulsion speed is replaced by an implicit dependence through the local density, i.e., $v \equiv v[\rho(\vec{r})]$. This assumption incorporates the effect of interactions among active particles that result via quorum sensing in a variety of biological settings and is sufficient to demonstrate phase separation in the system, as shown by the following linear stability analysis.

Consider that the system is at a uniform density $\rho(\vec{r}) = \rho_0 = k/v(\rho_0)$ (k is a constant), above which we apply a small perturbation $\delta\rho(\vec{r})$. Since the velocity depends on the local density, this perturbation modifies the local self-propulsion velocity $v[\rho_0 + \delta\rho(\vec{r})]$, which would then further perturb the local density

$$\rho_0 + \overline{\delta\rho}(\vec{r}) = \frac{k}{v[\rho_0 + \delta\rho(\vec{r})]} \simeq \rho_0 - \rho_0 \frac{v'(\rho_0)}{v(\rho_0)} \delta\rho(\vec{r}). \quad (1.10)$$

Since the interaction employed among particles is repulsive, it is obvious that $v'(\rho)$ is negative. In that case, the above equation is linearly unstable if $\overline{\delta\rho} > \delta\rho$, which immediately gives us the condition

$$\frac{v'(\rho_0)}{v(\rho_0)} > -\frac{1}{\rho_0}. \quad (1.11)$$

This suggests that if the effective self-propulsion speed decays sufficiently with density, as the bound set in Eq. (1.11), the system becomes linearly unstable, signaling the onset of MIPS [22]. Several approaches to characterizing MIPS have previously been considered, all of which have led to the same limiting condition in Eq. (1.11). Tailleur and Cates developed an effective equilibrium description for interacting RTPs in one dimension [20]. Using mean-field theory, they demonstrated that the free-energy density $f(\rho)$ satisfies the following relation:

$f''(\rho) = 1/\rho + v'(\rho)/v(\rho)$, where $v(\rho)$ represents the effective self-propulsion speed. The onset of phase separation is then identified by the instability in the system where $f''(\rho) < 0$, which directly implies Eq. (1.11). Later, Fily and Marchetti characterized ABPs in two dimensions using a set of coupled nonlinear hydrodynamic equations, obtained from the phenomenological ground, for coarse-grained density $\rho(\vec{r},t) = \sum_i \delta[\vec{r} - \vec{r}_i(t)]$ and polarization $\vec{p}(\vec{r},t) = \sum_i \hat{u}_i(t)\delta[\vec{r} - \vec{r}_i(t)]$ fields [21]:

$$\partial_t \rho = -\vec{\nabla}.\left[v(\rho)\vec{p} - D_0\vec{\nabla}\rho + \vec{f_\rho}\right], \tag{1.12}$$

$$\partial_t \vec{p} = -D_r\vec{p} - \frac{1}{2}\vec{\nabla}(\rho v) + K\vec{\nabla}^2\vec{p} + \vec{f_p}, \tag{1.13}$$

where D_0 and K are the bare diffusion coefficients corresponding to density and polarization fields, respectively, and $\vec{f_\rho}$ and $\vec{f_p}$ are the Gaussian white noises with zero mean and variance Δ_ρ and Δ_p, respectively (which have been calculated explicitly in Ref. [29]). By identifying the fact that $\vec{p}$ decays at a much faster rate D_r, the authors finally have shown that the convection-diffusion equation for density in Eq. (1.12) is effectively governed by a diffusive process at large times, i.e.,

$$\frac{\partial \rho}{\partial t} = \vec{\nabla}.\left[D(\rho, D_r)\vec{\nabla}\rho\right], \tag{1.14}$$

where the collective- or bulk-diffusion coefficient is given by

$$D(\rho, D_r) = D_0 + \frac{v^2(\rho)}{2D_r}\left[1 + \rho\frac{v'(\rho)}{v(\rho)}\right]. \tag{1.15}$$

The stable phase is defined by $D(\rho, D_r) > 0$. However, when $v' > -v/\rho$, the collective diffusivity is strongly suppressed and becomes negative for $v(\rho)|w| > D_r D$, where $2w = v(\rho) + \rho v'(\rho)$, and the system becomes unstable, indicating MIPS. As a result, the instability in effective self-propulsion speed implicitly leads to diffusive instability in the system. This observation has also been verified in a microscopic study by Bialke, Lowen, and Speck in Ref. [28]. In this study, starting from a many-particle Smoluchowski equation and employing a closure scheme, the authors derived the evolution equation for density $\rho(\vec{r},t)$ on the mean-field level. They identified the related collective diffusion coefficient $D(\rho, D_r)$, possessing a similar structure as Eq. (1.15), and characterized the phase separation in the light of diffusive instability in the system. In addition to the continuum systems discussed above, Kourbane-Houssene et al. found MIPS in the lattice gas model in Ref. [57]. The authors investigated a system of "weakly interacting" RTPs on a one-dimensional lattice. RTPs in this model have a finite rate of diffusion (symmetric hopping), whereas run and tumble dynamics have

vanishingly small system-size-dependent rates; thus, in the thermodynamic limit, diffusion dynamics dominate locally, resulting in the derivation of hydrodynamics at the mean-field level. The authors observe that as the onset of MIPS occurs, the density evolution equation becomes unstable for a finite tumbling rate, suggesting diffusive instability within the system.

Although MIPS has achieved success over the years, it remains a topic of ongoing debate. Traditionally, MIPS has been viewed as a competition between self-propulsion and repulsion. However, Levis and Berthier's work in Ref. [58] provided a different perspective. They investigated clustering in repulsive self-propelled hard disks using a kinetic Monte Carlo algorithm and found that thermal fluctuations are required for phase separation. Their work thus implies that phase separation results from a complex interplay of thermal noise, interparticle interactions, and self-propulsion. Recently, the fate of MIPS in RTPs was investigated by Mukherjee et. al. [59] and Ray et. al. in [60]. In the former study, the authors considered a one-dimensional system of hardcore RTPs and showed that the critical density for MIPS is larger than the maximum achievable density, i.e., $\rho_c > \rho_{max} = 1$, implying no phase separation is possible in one dimension. The latter study found that adding motility hindered phase separation in a two-dimensional system of interacting particles. Furthermore, the diffusive instability, serving as the primary criteria for MIPS, has not been rigorously established in any model systems except for those in infinite dimensions [61] and the diffusion-dominated weakly interacting RTPs [57], where the description corresponds to the mean-field explanation. However, conventional SPPs, which are defined on finite dimensions, possess nontrivial many-point correlations, and thus the mean-field framework in Refs. [57, 61] may not be useful. In such an unsettling situation, it is very much required to rigorously probe the collective- or bulk-diffusion coefficient from a microscopic perspective and show whether diffusive instability exists in conventional SPPs.

1.3 Anomalous collective transport in active matter

Aside from MIPS, SPPs have been shown to exhibit fascinating transport characteristics at the collective level. In this section, we will briefly go over the transport mechanism of the collection of interacting SPPs. Indeed, understanding the transport properties of many-body systems is a problem of practical and fundamental interest in statistical physics. From the seminal experiment of Robert Brown [62] on the random motion of micron-sized granules contained in Pollen grains and the theoretical formulation by Einstein [63], Sutherland [64], Smoluchowski [65], and Langevin [66], we know that a collection of particles immersed in a homogeneous medium exhibits normal diffusion, which is characterized by gaussian distribution of particle displacements and linear growth of mean squared displacement (MSD) with time, i.e., MSD $\propto t^{\alpha}$ and $\alpha = 1$. However, transport in many complex systems shows sig-

nificant deviation from the above-mentioned properties of normal diffusion, and such kind of transport is said to be anomalous (see [67], for a quick review). In most cases, the anomaly is in the MSD sense, and the system exhibits either superdiffusion $\alpha > 1$ or subdiffusion $\alpha < 1$. There is another interesting class of anomalous transport observed experimentally in glassy systems [68], cell environments [69–74] which shows linear time dependence of MSD as in normal diffusion; however, the displacement distribution strongly violates the gaussian statistics and in literature, this is referred to as Brownian yet non-gaussian diffusion (BnGD). Such transport is often realized in systems with heterogeneous environments, leading to nonuniform diffusion in different regions and theoretically, this effect is modeled by considering the fluctuating diffusivity of the particle, also called diffusing diffusivity [75–82], which has been quite successful in explaining such phenomena.

Anomalous transport is omnipresent in active matter. There have been several experimental studies on biological systems like bacterial colonies, amoeboid cells and artificially made active Janus particles [12,83–85], signaling superdiffusive and non-Gaussian transport. In [12], swarming bacteria are shown to migrate through Levy walk and exhibit superdiffusion. The relaxation of microswimmers from a localized region was found to undergo ballistic "explosion" at early times [83,84], where the width of the density perturbation grows as $\sim t^{1/z}$ with the dynamical exponent $z = 1$, and eventually crosses over to normal diffusive transport at long times ($z = 2$). In a related numerical study on single file motion of SPPs [54], the space-time scaling of two-point density correlations was found to exhibit superdiffusion with $z = 1.67$. In present times, the origins of such anomalous growth, the resulting exponent, and whether one expects any universality among SPPs remain elusive. Despite advancements in recent studies [25, 37, 57, 86–89], a comprehensive theoretical understanding of the dynamic characteristics of SPPs, particularly considering many-body correlations, is lacking.

Over the last decade, various models of SPPs have been studied in the literature to characterize their dynamic properties. While the majority of them focused on characterizing the MSD of tracer active particles in terms of the self-diffusion coefficient [38, 40, 42, 58, 90–99], a few others studied other relevant quantities, such as effective self-propulsion velocity, mechanical pressure, and chemical potential, among others [29,61,100–103]. However, it is important to note that the characterization of collective transport properties in SPPs is still in progress, with a lack of rigorous theoretical understanding. A relevant quantity for this purpose would be the two-point dynamic density correlation or the Van-Hove function [104]. Recently, the Van-Hove function was numerically studied to exhibit superdiffusion in a single-file setup for RTPs, ABPs, and AOUPs [54]. Notably, the Fourier space representation of the Van-Hove function, also known as the intermediate scattering function (ISF), has received considerable attention in the literature. It comprises *self* and *distinct* components: the self part relates

to the mean square displacement (MSD) of an individual tracer particle, while the distinct part encompasses correlations of displacements among multiple particles. Attempts have been made to analyze the ISF for active matter systems. However, due to computational complexity, most studies have focused on either single or noninteracting active particle systems [96, 97, 105–108]. These investigations consistently demonstrate that the ISF initially displays wave-like behavior in the short term before transitioning to diffusive behavior over longer timescales. Recently, to a further extent, relaxation dynamics in the interacting active particle systems were studied in Refs. [91, 109] by considering the self-part of the ISF, thus characterizing the self-diffusion coefficient, which governs the dynamics of a tracer particle in the system. However, when studying transport at the collective level, one must consider the other density- and activity-dependent diffusion coefficient, the bulk-diffusion coefficient which governs density relaxation according to Eq. (1.14). Importantly, the subtle interplay between persistence and interaction gives rise to nontrivial density dependence in the bulk-diffusion coefficient. As a result, the local structural relaxation becomes density-dependent and the governing equation [i.e., Eq. (1.14)] becomes nonlinear. Notably, such nonlinearity gives rise to dynamical heterogeneity and thus accounts for anomalous transport in the system of interacting SPPs, as explored in Chapter 2.

In the previous two sections, we have emphasized the importance of the rigorous determination of the collective or bulk diffusion coefficient in a system of interacting conventional SPPs. While the presence of a vanishing instability would prove the existence of MIPS, the explicit density dependence of the bulk-diffusion coefficient could provide a novel nonlinear diffusion mechanism to explain the remarkable collective anomalous relaxation of interacting SPPs. It should be noted that the bulk-diffusion coefficient is, in general, different from the self-diffusion coefficient of a tagged or tracer particle [110–112]. However, this distinction, which can be quite striking, particularly in one-dimensional models [113, 114], is somewhat less emphasized in the context of active matter systems [28, 86]. While the former governs the relaxation phenomena, the latter is related to the displacement fluctuation of the tracer particle. Notably, particle displacement generates current in the system, and the fluctuation of total or space-time-integrated in the entire system is related to another important transport coefficient, the collective particle mobility of the system [see Eq. (3.67)]. Therefore, the mobility and the self-diffusion coefficient could be related; however, determining the exact relationship for SPPs is outside the scope of this thesis. Indeed, the characterization of the macroscopic transport coefficients - the bulk-diffusion coefficient, and the collective particle mobility - is of crucial importance to formulate a fluctuating hydrodynamic framework in driven-diffusive systems that we will discuss below.

1.4 Fluctuating hydrodynamics of diffusive systems

There is a well-established statistical mechanics framework for many-particle systems satisfying detailed balance. For example, consider a one-dimensional "diffusive" system in a near-equilibrium scenario; the time evolution of coarse-grained local density $\rho(x,\tau)$ at suitably rescaled space x and time τ is described by the following fluctuating hydrodynamic equation:

$$\frac{\partial \rho(x,\tau)}{\partial \tau} = \frac{\partial}{\partial x}\left[D(\rho)\frac{\partial \rho}{\partial x} + \sqrt{\frac{2\chi(\rho)}{L}}\zeta_x(\tau)\right]. \tag{1.16}$$

In the thermodynamic limit (i.e., for system size $L \to \infty$), density relaxation is governed by the first term alone, with $D(\rho)$ the density-dependent collective- or *bulk-diffusion coefficient* of the system. However, for finite L, one must always incorporate the fluctuations, which is represented here by the Gaussian white noise $\zeta_x(\tau)$ with zero mean and unit variance, and the fluctuation strength is determined by the linear response function, i.e., *mobility* $\chi(\rho)$. This is a direct consequence of the fluctuation-response relation in equilibrium. However, a comprehensive theory incorporating fluctuations and transport for systems that violate detailed balance is still lacking. In this context, several relevant questions arise:

(i) Is there a hydrodynamic description analogous to Eq. (1.16) for many-particle systems violating detailed balance?

(ii) If so, can one derive fluctuating hydrodynamics using a rigorous microscopic approach?

(iii) How are fluctuations and transport related in such systems?

Indeed, addressing the above issues is of crucial importance. Recently, a deeper theoretical understanding of driven diffusive systems has gradually unfolded through the development of macroscopic fluctuation theory (MFT) [115, 116] and an additivity principle [117], which we briefly describe next.

1.4.1 Macroscopic Fluctuation Theory (MFT)

Over the past two decades, a theoretical formulation, called macroscopic fluctuation theory (MFT) introduced by Bertini et al. in Refs. [115, 116] (also, see [118] for review), has been proposed to deal with driven diffusive systems; indeed, the MFT has become quite successful in providing a fluctuating hydrodynamic description for such systems. The main goal of the MFT is to characterize rare fluctuations of coarse-grained density and current and to

calculate the associated large deviation functions. Although the formalism applies to systems operating far from equilibrium, there are certain criteria that the system needs to satisfy:

(a) On the large space-time scale, the coarse-grained local variables, such as density $\rho(x,\tau)$ and current $j(x,\tau)$, satisfies a continuity equation:

$$\partial_\tau \rho(x,\tau) + \partial_x j(x,\tau) = 0, \tag{1.17}$$

where x and τ represent the diffusive scaled space and time.

(b) The system should satisfy a *gradient* property, i.e., the local instantaneous (average) currents corresponding to the time-evolution of conserved quantities should be expressed as a gradient of a local observable [113, 119]. This ensures that the large-time behavior of the system will be diffusive, and the corresponding diffusive current $j^{(D)}[\rho(x,\tau)]$ must follow the Fick's law, i.e.,

$$j^{(D)}(\rho) = -D(\rho)\frac{\partial \rho}{\partial x}. \tag{1.18}$$

(c) The instantaneous current should have a diffusive and fluctuating component. Importantly, the temporal correlation of the fluctuating part must be short-ranged, i.e., much smaller than the hydrodynamic time scales. In other words, we can decompose $j(x,\tau)$ in the following manner:

$$j(x,\tau) = j^{(D)}[\rho(x,\tau)] + j^{(fl)}(x,\tau), \tag{1.19}$$

where $j^{(fl)}(x,\tau)$ is the uncorrelated Gaussian white noise with zero mean. However, to calculate the strength of the noise, Bertini et al. followed a strategy that is described below.

Note that Eq. (1.17), along with the contribution to $j(x,\tau)$ only from the diffusive current $j^{(D)}(x,\tau)$, leads to a deterministic time evolution of $\rho(x,\tau)$, and the corresponding solution would lead to the typical trajectory of ρ and j of the system. In the thermodynamic limit, the probability of observing such a typical trajectory approaches unity. However, the atypical trajectories, according to the large-deviation principle [120], occur with exponentially small probability with system size L. Here, we are interested in such trajectories, essentially generated by the fluctuating component $j^{(fl)}$. We now note that, for stochastic systems with Markov properties, it is in principle possible to bias the system to achieve the otherwise rare

configuration [121–123]. Therefore, the atypical or large deviated trajectories of ρ and j in the original or unbiased system could be generated by a suitably biased system for which they are typical. To this end, Bertini et. al. introduced a biasing force by assuming that the system satisfies a local detailed balance structure, i.e., the transition rates from one configuration to another in this biased system should follow an equilibrium-like detailed balance criterion. For example, consider biasing a small force field $\vec{F} = F\hat{x}$ ($\hat{x}$ is the unit vector along the positive x axis) on a system that possesses stochastic particle transfer on a one-dimensional lattice. The introduction of the biasing force modifies the hopping rates $c_{i\to j}$ from the site i to j in the original (unbiased) to $c^{(F)}_{i\to j}$ in the biased system, as given by,

$$c^{(F)}_{i\to j} = c_{i\to j}\Phi\left(\Delta e_{ij}\right). \tag{1.20}$$

Importantly, the factor $\Phi\left(\Delta e_{ij}\right)$ is a non-negative function of the energy cost $\Delta e_{i,j}$ resulting from the biasing force F for particle hopping from i to j. We can straightforwardly express $\Delta e_{i,j}$ as:

$$\Delta e_{i,j} = \vec{F}.\vec{\delta x}, \tag{1.21}$$

where the displacement vector is defined as $\vec{\delta x} = (j - i)$ (setting the lattice spacing to unity). We now implement the local detailed balance assumption, which suggests $\Phi\left(\Delta e_{ij}\right)$ to have the following form: $\Phi\left(\Delta e_{i,j}\right) = \exp(\Delta e_{i,j}/2)$, which in the limit of the small biasing force F, can be linearized as follows:

$$\begin{aligned}\Phi\left(\Delta e_{i,j}\right) &\simeq 1 + \Delta e_{i,j}\left[\frac{d\Phi}{d\Delta e}\right]_{\Delta e=0} \\ &= 1 + \frac{1}{2}\vec{F}.\vec{\delta x}.\end{aligned} \tag{1.22}$$

Using the above form of $\Phi\left(\Delta e_{i,j}\right)$ in Eq. (1.20) we obtain the modified transition rates. Upon utilizing those modified rates, it can be shown that the "typical" instantaneous current in the biased system has the following drift-diffusion form:

$$j(x,\tau) = j^{(D)}[\rho(x,\tau)] + j^{(d)}[\rho(x,\tau)], \tag{1.23}$$

where the diffusive current $j^{(D)}$ is already defined in Eq. (1.18), and the drift current $j^{(d)}$ is related to the biasing force F through the linear response function, i.e., mobility $\chi(\rho)$ in the following manner:

$$j^{(d)}(\rho) = \chi(\rho)F. \tag{1.24}$$

The physical significance of Eqs. (1.23) and (1.24) can be understood as follows. Note that $j^{(D)} = -D(\rho)\partial_x\rho$ is the typical current in the unbiased or original system, whereas the observed large-deviated current is given by j. Therefore, in order to generate this additional current, the force of biasing should be $F = [j+D(\rho)\partial_x\rho]/\chi(\rho)$. This force, akin to Ohm's law, dissipates energy, proportionate to $\int d\tau \int dx F^2\chi(\rho)$. This realization immediately implies that the joint distributions of the atypical density and current profiles $\{\rho(x,\tau), j(x,\tau)\}$ in a given domain of space $x \in \Lambda$ in the original model should have the following large-deviation structure:

$$\mathcal{P}\left[\{\rho(x,\tau), j(x,\tau)\}; \tau \in [\tau_1,\tau_2]\right] \approx \exp\left[-L\int_{\tau_1}^{\tau_2} d\tau \int_{\Lambda} dx \frac{(j+D(\rho)\partial_x\rho)^2}{4\chi(\rho)}\right]. \tag{1.25}$$

Notably, one can interpret Eq. (1.25) from the perspective of fluctuating hydrodynamics by writing it in the form of a stochastic differential equation satisfied by the coarse-grained density $\rho(x,\tau)$ and current $j(x,\tau)$

$$\partial_\tau\rho(x,\tau) = -\partial_x j(x,\tau), \tag{1.26}$$

$$j(x,\tau) = -D(\rho)\partial_x\rho + \sqrt{\frac{2\chi(\rho)}{L}}\xi(x,\tau), \tag{1.27}$$

where $\xi(x,\tau)$ is the coarse-grained multiplicative uncorrelated Gaussian white noise term and is characterized by $\langle\xi(x,\tau)\rangle = 0$ and $\langle\xi(x,\tau)\xi(x',\tau')\rangle = \delta(x-x')\delta(\tau-\tau')$. The formulation of $j(x,\tau)$ in Eq.(1.27) is identical to our previous decomposition of current in Eq.(1.19), but with the fluctuating component $j^{(fl)}(x,\tau)$ replaced with a multiplicative noise term. This observation allows for direct determination of the two-point correlation of $j^{(fl)}(x,\tau)$, as shown below,

$$\langle j^{(fl)}(x,\tau)j^{(fl)}(x',\tau')\rangle = \frac{2\chi(\rho)}{L}\delta(x-x')\delta(\tau-\tau'). \tag{1.28}$$

Thus, the prescription of MFT suggests that the fluctuating current is delta-correlated in space and time, with the strength determined by the mobility $\chi(\rho)$ of the system. It is now easy to see that the fluctuating hydrodynamics of a nonequilibrium diffusive system essentially boils down to an "effective" equilibrium framework in Eq. (1.16), where the non-equilibrium aspects are captured by the two macroscopic transport coefficients: $D(\rho)$ and $\chi(\rho)$, effectively addressing the first inquiry.

We would now like to find a connection between macroscopic transport coefficients and fluctuations in density and current within the system. To this end, we use the joint probability distribution of trajectories $\mathcal{P}\left[\{\rho(x,\tau), j(x,\tau)\}\right]$, as shown in Eq. (1.25), which would help

determine the density large deviations in the system. For instance, if we want to calculate the probability of observing a density profile $\{\rho(x,\tau)\}$, i.e., $\mathcal{P}\left[\{\rho(x,\tau)\}\right]$, we have to maximize the joint distribution $\mathcal{P}\left[\{\rho(x,\tau'),j(x,\tau')\}\right]$ over infinite history $\tau' \in [-\infty,\tau]$ through the constraint provided by the continuity equation in Eq. (1.17). Finally, the large-deviation probability $\mathcal{P}\left[\{\rho(x,\tau)\}\right]$ can be obtained simply in terms of a local equilibrium-like free energy-density functional $V[\{\rho(x,\tau)\}]$,

$$\mathcal{P}\left[\{\rho(x,\tau)\}\right] \sim \exp[-LV(\{\rho(x,\tau)\})], \tag{1.29}$$

where $V[\rho] = \int_\Lambda dx[f(\rho) - f(\rho_0) - \mu(\rho)(\rho-\rho_0)]$. Here, ρ_0 is the global density of the system; $f(\rho)$ and $\mu(\rho)$ are the nonequilibrium free energy density and chemical potential, respectively, which are mutually related in the following manner [118]:

$$\frac{df}{d\rho} = \mu(\rho). \tag{1.30}$$

Now, it can be shown that the procedure of maximization of the joint distribution leads the free energy functional $V[\rho(x)]$ to satisfy the following Hamilton-Jacobi relation [118],

$$\int_\Lambda dx \left[\left\{ \frac{\partial}{\partial x}\left(\frac{\delta V}{\delta \rho}\right) \right\}^2 \chi(\rho) + \left(\frac{\delta V}{\delta \rho}\right) \frac{\partial}{\partial x}\left(D(\rho)\frac{\partial \rho}{\partial x}\right) \right] = 0. \tag{1.31}$$

Upon utilizing the suitable boundary conditions, one can solve for the functional $V[\rho(x)]$, which in turn leads to the determination of the free energy density $f(\rho)$. On a periodic domain, after some algebraic manipulations, the solution of the above equation connects transport coefficients with the free energy density $f(\rho)$ through the following relation,

$$f''(\rho) = \frac{D(\rho)}{\chi(\rho)}, \tag{1.32}$$

which by using the relation in Eq. (1.30), we arrive at the following identity connecting transport coefficients with the nonequilibrium compressibility,

$$\frac{d\mu}{d\rho} = \frac{D(\rho)}{\chi(\rho)}. \tag{1.33}$$

Finally, using the fluctuation-response relation between the nonequilibrium compressibility and number fluctuation [124–129],

$$\frac{d\mu}{d\rho} = \frac{1}{\sigma^2(\rho)}, \tag{1.34}$$

we connect density fluctuation $\sigma^2(\rho)$ with transport coefficients $D(\rho)$ and $\chi(\rho)$ through an equilibrium-like Einstein Relation (ER),

$$\frac{\chi(\rho)}{D(\rho)} = \sigma^2(\rho), \tag{1.35}$$

where we define $\sigma^2(\rho) = \lim_{1 \ll l_{sub} \ll L} \left(\langle N_{l_{sub}}^2 \rangle - \langle N_{l_{sub}} \rangle^2 \right) / l_{sub}$ as the scaled fluctuation of particle number $N_{l_{sub}}$ in a subsystem of size l_{sub}. According to Eq. (1.35), for gradient systems, the macroscopic transport coefficients $D(\rho)$ and $\chi(\rho)$ jointly determine the system's density fluctuation $\sigma^2(\rho)$. This is a powerful relation, and the extension of ER to nonequilibrium diffusive systems is a significant achievement of MFT. The ER has been derived in the past for several nonequilibrium mass transport processes [121, 130]. In this thesis, we derive the ER for a class of lattice-gas models for active matter in Chapters 4 and 5.

1.4.2 Additivity Principle

In the previous section, we characterized the large deviation of the density profiles and quantified the density fluctuation $\sigma^2(\rho)$ in terms of the macroscopic transport coefficients, bulk-diffusion coefficient $D(\rho)$ and mobility $\chi(\rho)$ using the Einstein Relation. Since driven-diffusive systems are primarily defined by a coarse-grained density $\rho(x, \tau)$ and current $j(x, \tau)$, it is important to explore the fluctuation properties of $j(x, \tau)$ as well. To this end, we describe here the additivity principle, developed by Bodineau and Derrida in Ref. [117], which plays a prominent role in characterizing current fluctuations in nonequilibrium diffusive systems.

Let us consider a one-dimensional diffusive system of length L, connected at two ends with particle reservoirs at density ρ_a and ρ_b, respectively. Without any loss of generality, we assume $\rho_a = \rho_b + \Delta\rho$ and $\Delta\rho > 0$, and in that case, the system shows directional particle flow or current from left to right. We now define the time-integrated current $Q_t = jt$ which measures the number of particles entering the system up to time t. At the steady state, we expect the system to satisfy the Fick's law,

$$\lim_{t \to \infty} \frac{\langle Q_t \rangle}{t} = D(\rho) \frac{\Delta\rho}{L}, \tag{1.36}$$

where $D(\rho)$ is the bulk-diffusion coefficient of the system, defined in Eq. (1.18). In the limit of vanishing density gradient, i.e., $\Delta\rho = 0$, we can also express the fluctuation at the large time in terms of the local mobility variable $\chi(\rho)$, as defined in Eq. (1.24), in the following manner,

$$\lim_{t \to \infty} \frac{\langle Q_t^2 \rangle}{t} = \frac{2\chi(\rho)}{L}. \tag{1.37}$$

We want to calculate the probability of observing Q_t, which in the limit of large observation time t takes the form of the following large-deviation structure:

$$\mathcal{P}_L\left[\frac{Q_t}{t} = j, \rho_a, \rho_b, t\right] \approx \exp[-t\mathcal{C}_L(j, \rho_a, \rho_b)], \tag{1.38}$$

where the large-deviation function $\mathcal{C}_L(j, \rho_a, \rho_b)$ is strictly non-negative and depends on the current j, system size L, and densities ρ_a and ρ_b at the two ends. Our goal is to determine $\mathcal{C}_L(j, \rho_a, \rho_b)$ and express it in terms of the transport coefficients, $D(\rho)$ and $\chi(\rho)$.

Before proceeding further, we partition the entire system into two subsystems, each of size L_1 and L_2 respectively, where $L = L_1 + L_2$. It is important to note that as these subsystems are integral parts of the overall system, the identical current j flows through each subsystem. Additionally, at the junction where the right boundary of the first subsystem meets the left boundary of the second one, they share the same density ρ. We now ask how the current distribution of the overall system $\mathcal{P}_L\left(j, \rho_a, \rho_b, t\right)$ relates to the distribution functions of individual subsystems $\mathcal{P}_{L_1}\left(j, \rho_a, \rho, t\right)$ and $\mathcal{P}_{L_2}\left(j, \rho, \rho_b, t\right)$. To address this question, Bodineau and Derrida in [117] assumed the statistical independence between the subsystems while introducing an additional constraint. They proposed that the joint distribution function could be expressed as the product of individual distributions, subject to a constraint on the junction density ρ to maximize the product. This assumption can be mathematically expressed as

$$\mathcal{P}_L\left(j, \rho_a, \rho_b, t\right) \sim \max_{\rho}\left[\mathcal{P}_{L_1}\left(j, \rho_a, \rho, t\right)\mathcal{P}_{L_2}\left(j, \rho, \rho_b, t\right)\right]. \tag{1.39}$$

Notably, by substituting the large-deviation functions, as expressed in Eq. (1.38), into the above equation, we obtain the following *additive* relation among the large deviation functions,

$$\mathcal{C}_L\left(j, \rho_a, \rho_b\right) \sim \min_{\rho}\left[\mathcal{C}_{L_1}\left(j, \rho_a, \rho\right) + \mathcal{C}_{L_2}\left(j, \rho, \rho_b\right)\right]. \tag{1.40}$$

Suppose we now keep dividing the system into k number of subsystems, each with length δL which is assumed to be larger than the correlation length of the system. In that case, one can generalize Eq. (1.40) in the following manner:

$$\mathcal{C}_L\left(j, \rho_a, \rho_b\right) \sim \min_{\rho_1, \rho_2, \ldots, \rho_{k-1}}\left[\sum_{i=1}^{k}\mathcal{C}_{\delta L}\left(j, \rho_i - \delta\rho_i, \rho_i\right)\right], \tag{1.41}$$

where the minimization is done over the junction densities $\rho_1, \rho_2, \ldots, \rho_{k-1}$. In the limit of

large system size L, the current in the system $j \sim 1/L$ is vanishingly small. Consequently, the gradient in density between these subsystems also becomes quite negligible. In this case, it is reasonable to assume that the local current at ith subsystem would follow Gaussian distribution with mean $-D(\rho_i)\delta\rho_i/\delta L$ and variance $2\chi(\rho_i)/\delta L$. Therefore, following Eq. (1.38), one can write down the corresponding large-deviation function as,

$$\mathcal{C}_{\delta L}\left(j, \rho_i + \delta\rho_i, \rho_i\right) = \frac{\left[j + D(\rho_i)\delta\rho_i/\delta L\right]^2}{4\chi(\rho_i)}\delta L. \tag{1.42}$$

Rescaling the space units $i \to x = i/L$ results in a finite order contribution to the current, i.e. $j \to J = jL \sim \mathcal{O}(1)$. Furthermore, in the limit of the infinitely large number of subsystems $k \gg 1$, the scaled subsystem sizes become vanishingly small: $\delta L \to \delta x = \delta L/L = 1/k$. By applying this scale transformation in Eq. (1.42) and plugging it in Eq. (1.41), we can now take the continuum limit, which is given by

$$L\mathcal{C}_L\left(j, \rho_a, \rho_b\right) = G\left(J, \rho_a, \rho_b\right) \sim \min_{\{\rho(x)\}}\left[\int_0^1 dx \frac{\left[J + D(\rho)d\rho/dx\right]^2}{4\chi(\rho)}\right]. \tag{1.43}$$

The task is now reduced to minimizing the scaled large-deviation function $G\left(J, \rho_a, \rho_b\right)$, and the minimization approach must be done over the entire density profile $\rho(x)$. Solving the equation above produces an optimal profile for sustaining the current J in the system while minimizing the R.H.S of Eq. (1.43). Such an optimal profile can be shown to satisfy the equation [117]:

$$\frac{d\rho}{dx} = \frac{J}{D(\rho)}\sqrt{1 + 4K\chi(\rho)}, \tag{1.44}$$

where the constant K can be evaluated by using the boundary conditions: $\rho(0) = \rho_a$ and $\rho(1) = \rho_b$. Thus, the additivity principle allows for the determination of the optimum density profile in Eq. (1.44) and the current large deviation function $G\left(J, \rho_a, \rho_b\right)$ in Eq. (1.43) in terms of the transport coefficients $D(\rho)$ and $\chi(\rho)$. It has also been tested numerically in the context of heat conduction in Refs. [131, 132]. The theory, first suggested for diffusive systems with open boundary conditions [117], can also be applied to periodic diffusive systems where the steady-state density profile is flat, as studied in Ref. [133]. The authors examined the stability of the flat profiles under a fixed current situation. They reported that above a certain current, the system undergoes a dynamic phase transition, causing the flat profile to become unstable and yielding a time-dependent optimal profile.

In Secs. 1.4.1 and 1.4.2, we have briefly described the macroscopic fluctuation theory (MFT) and the additivity principle which allows for the dynamic characterization of

nonequilibrium diffusive systems. The main ingredients in these analyses are the macroscopic transport coefficients - the bulk-diffusion coefficient and the mobility - which must be evaluated to characterize both density fluctuations and current fluctuation in the system. Notably, there is no rigorous proof of the above assertions for many-particle systems with nontrivial space-time correlations such as system of interacting SPPs. Of course, calculating the density- and activity-dependent transport coefficients $D(\rho, \gamma)$ and $\chi(\rho, \gamma)$ for interacting active systems is a nontrivial task, especially because the system is driven out-of-equilibrium and its nonequilibrium steady-state measure is *a-priori* unknown, as well as the presence of many-body correlations. Recently, an attempt was made in Ref. [134] to characterize the transport coefficients in a directed mass transfer variant of hardcore RTPs on one dimension in the limit of small tumbling rate γ. However, in order to understand how the intricate relationship between persistence and interaction influences transport mechanisms in interacting RTPs, it is crucial to derive the relevant transport coefficients from a microscopic dynamical perspective, for arbitrary density and tumbling rates. Indeed, this constitutes the first main objective of this thesis. Another aim is to analyze current and density fluctuations for interacting RTPs through microscopic dynamical calculations and establish connections with the resulting macroscopic transport coefficients. As a result, our microscopic study could support the prediction of MFT and the additivity principle for complex systems such as interacting RTPs.

1.5 Outline of the thesis

The microscopic approach employed in this thesis aims to bridge the gap between the complex fluctuation and transport properties in systems of interacting RTPs, which is the central focus of this study. To this end, the thesis is outlined as follows:

In Chapter 2, we characterize collective diffusion in hardcore athermal RTPs by calculating the bulk-diffusion coefficient $D(\rho, \gamma)$ at arbitrary dimension, density ρ, and tumbling rate γ. To this end, we perform an efficient Monte Carlo algorithm by studying long-wavelength density relaxations [135] for conventional hardcore RTPs [36]. We also determine $D(\rho, \gamma)$ analytically through the exact calculation of the first moment of the time-integrated current via Fick's law for a long-range variant, called hardcore long-ranged lattice gas (LLG). We then bring forward a scaling theory, in the regime of strong persistence ($\gamma \to 0$) and low density ($\rho \to 0$), that encapsulates the nontrivial interplay between persistence and interaction via a previously unknown scaling relation $D(\rho, \gamma) \simeq D^{(0)}\mathcal{F}(\rho/\gamma)$, which we supplement both from numerical and analytical calculations. We further calculate the explicit density-dependence in $D(\rho, \gamma)$, and by using the framework of nonlinear diffusion, we provide a novel mechanism

of early-time anomalous collective relaxation of RTPs. Surprisingly, unlike the phenomenological claim in Ref. [20], we do not find any diffusive instability in conventional (athermal) RTPs, even at strong persistence and high density, where the bulk-diffusion coefficient decays gradually as $D(\rho, \gamma) \sim 1/\rho^2$.

In Chapter 3, we have characterized the steady-state current fluctuations in two one-dimensional models of hardcore athermal RTPs studied in the previous chapter. Upon introducing a truncation (closure) scheme, we show that in the limit of large system size L, the suitably scaled space-time integrated current fluctuation corresponds to another density- and tumbling rate-dependent macroscopic transport coefficient, collective particle mobility $\chi(\rho, \gamma)$. Notably, to characterize the competing effects of persistence and interaction on current fluctuations, similar to $D(\rho, \gamma)$, we derive a scaling relationship for $\chi(\rho, \gamma)$ as well. Furthermore, our microscopic theory enables calculating the growth of time-integrated bond-current fluctuations $\langle Q^2(T)\rangle$; it grows subdiffusively ($\sim \sqrt{T}$) for moderate time-regime while making a crossover to a diffusive or linear growth with L dependent growth ($\sim T/L$). Interestingly, the prefactors arising in the above growth laws can be solely expressed by the two transport coefficients, $D(\rho, \gamma)$ and $\chi(\rho, \gamma)$, and upon suitable rescaling, we discover the time-integrated bond-current fluctuation exhibits a scaling relation $D\langle Q^2(T)\rangle/(2L\chi) = \mathcal{W}(DT/L^2)$, with the scaling function $\mathcal{W}$ presumably universal, i.e., independent of the dynamical rules of the models and parameter values. We also calculate the equal-time spatial correlation of the instantaneous current (somewhat related to velocity correlation), an exponential function of distance, with the correlation length diverging as the square root of the persistent time.

In Chapter 4, we try to incorporate thermal fluctuations in the system of interacting SPPs. To this end, we first define a prototypical model consisting of hardcore particles, on a one-dimensional periodic lattice, employing symmetric short- and long-ranged hopping, respectively. Possibly in the simplest terms, this model dynamics correspond to the thermal or passive and active or ballistic motion of typical thermal hardcore SPPs. In this model, using the theory of many-body Markov processes, we have derived hydrodynamics governing the (presumably exact) time evolution of the density field from a given initial profile in terms of the bulk-diffusion coefficient and mobility. Indeed, in a few special cases of next-nearest and infinite-range hopping, we analytically obtain the explicit density dependence of the above-mentioned transport coefficients. In the presence of "activity" (essentially the hopping range in our model), we show that the system exhibits intriguing collective features, which we characterize by the anomaly in the transport coefficient. In the most interesting case of infinite range hopping, we show the system undergoes a condensation transition, and

at the transition point, the mobility diverges but the bulk-diffusion coefficient remains finite. Notably, such instability in mobility offers zero resistance to particle flows, thus the system achieves a "superfluid"-like state at the transition point and provides a different perspective of phase transition in active systems from the usual MIPS, which is characterized by the vanishing bulk-diffusion coefficient at the transition point. Notably, for this nonequilibrium system, we show the existence of an equilibrium-like Einstein Relation (ER) in the system, which connects density fluctuations to the ratio of mobility to the bulk diffusion coefficient. Interestingly, similar to MIPS, the system exhibits diverging density fluctuation, although the origin is entirely different in this case.

In Chapter 5, we provide a dynamical origin to the above mobility-driven condensation transition by calculating current fluctuations in the model system considered above. We proceed with the microscopic analysis by using the truncation scheme employed in Chapter 3. We microscopically demonstrate that the condensation transition occurs due to anomalous current fluctuation in the system at the critical phase. Put differently, we observe the system at criticality exhibits enhanced fluctuation of time-integrated bond-current compared to the same in the normal phase. We further show that such an enhancement of fluctuation at the level of each bond together contributes to diverging scaled fluctuation of the total current in the system. Such a current fluctuation-induced phase transition is unique for nonequilibrium systems and distinguishes itself significantly from the phenomenology of equilibrium phase separation, which occurs due to the vanishing bulk-diffusion coefficient and eventually results in critical slowing down in the system. Notably, the phenomenology of MIPS also relies on the same mechanism. Therefore, in this chapter, we try to provide an alternative novel mechanism of phase separation in active systems. Finally, we summarize the thesis in Chapter 6.

2

Collective diffusion of athermal hardcore run-and-tumble particles

2.1 Introduction

Understanding the collective diffusion of systems with many-body correlations is a problem of central interest in statistical mechanics. Typically, this phenomenon is characterized by the density and other parameter-dependent bulk-diffusion coefficient $D(\rho)$, which governs the particle current following Fick's law

$$J_D = -D(\rho)\frac{\partial \rho}{\partial X} \tag{2.1}$$

in response to a density gradient $\partial\rho/\partial X$. Indeed, the determination of $D(\rho)$ is a crucial step in characterizing the framework of fluctuating hydrodynamics in the driven-diffusive systems (as discussed in the introduction) [115,117]. Although there have been considerable achievements in the past regarding the characterization of interacting particle systems [119, 136], precise determination of $D(\rho)$ has posed a challenge for such systems, especially for the conventional models of self-propelled particles (SPPs), which commonly exhibit complex spatiotemporal correlations.

This chapter is based on the paper "Time-dependent properties of run-and-tumble particles: Density relaxation", Tanmoy Chakraborty and Punyabrata Pradhan, Phys. Rev. E **109**, 024124 (2024).

In the past, there have been a few attempts to characterize bulk-diffusion for SPPs using phenomenological theories [20,21]. Such studies predict an instability (vanishing) in the bulk-diffusion coefficient, which in turn leads to the motility-induced phase separation (MIPS) [22] in the system. Later, these hydrodynamic theories were complemented using microscopic descriptions at the mean-field level [28]. In recent times, there has been some advancement in characterizing bulk diffusion within a particular class of run-and-tumble particles (RTPs), where the dynamics are thermal diffusion dominated, while run, and tumble events take place at vanishingly small and system-size dependent rates; consequently, one can characterize such systems exactly within a *mean-field* hydrodynamic framework [57]. Conversely, in the case of conventional SPPs with a finite persistence length, the system exhibits nontrivial many-body spatial correlations, thus the mean-field descriptions presented in Refs. [28, 57] is inapplicable. In such scenarios, a thorough exploration of the bulk diffusion coefficient in conventional SPPs, incorporating the many-body correlations is desirable.

In this chapter, we employ efficient numerical techniques, for conventional hardcore athermal RTPs [36], and microscopic calculations, for an analytic long-ranged variant, to characterize the collective diffusion on a periodic lattice in d dimensions, for arbitrary density ρ and tumbling rate γ, which is the inverse of the persistence time τ_p (related to the persistence length $l_p = v\tau_p$, where v represents the self-propulsion speed). We emphasize that we first consider the limit of large system size L, followed by the limit of large persistence length l_p, ensuring that L significantly exceeds l_p. Our microscopic theory relies on characterizing the average bond current, which, in the long-time limit, has been shown to possess the structure of Fick's law [see Eqs. (2.1) and (2.19)]. This enables the analytical determination of $D(\rho, \gamma)$. In contrast, numerically determining $D(\rho, \gamma)$ involves studying the relaxation of the local density $\rho(\mathbf{X}, t)$, at position $\mathbf{X}$ and time t, from a predefined initial profile $\rho(\mathbf{X}, t = 0) = \rho_{in}(\mathbf{x} = \mathbf{X}/L)$ at large space-time scales. For this purpose, we examine long-wavelength sinusoidal perturbation: $\delta\rho(\mathbf{X}, 0) = \text{const.}\sin(q\mathbf{X})$, where $q = 2\pi/L \to 0$ as $L \to \infty$. Using an efficient Monte Carlo algorithm, we examine relaxation in the weak perturbation regime and numerically compute the relaxation rate, which directly allows for the determination of $D(\rho, \gamma)$ [see Section 2.4.2]. Furthermore, we provide numerical evidence for the diffusive scaling limit governing particle transport, akin to Fick's law as expressed in Eq. (2.1). Specifically, we illustrate that RTPs display long-term diffusive relaxation for any finite γ and an initial profile $\rho_{in}(\mathbf{X}/L)$, as evidenced by the diffusive scaling $\rho(\mathbf{X}, t) \equiv \rho(\mathbf{x} = \mathbf{X}/L, \tau = t/L^2)$ for $L \gg 1$. In this scenario, the dynamic evolution of the coarse-grained density field $\rho(\mathbf{x}, \tau)$ follows the diffusion equation,

$$\partial_\tau \rho(\mathbf{x}, \tau) = \nabla[D(\rho, \gamma)\nabla\rho(\mathbf{x}, \tau)]. \tag{2.2}$$

which, due to the explicit local-density dependence in $D(\rho,\gamma)$, is *nonlinear* at early times and thus exhibits *anomalous* relaxations. We substantiate these assertions by calculating the bulk-diffusion coefficients numerically and analytically in a broad class of RTPs described in Sec. 2.2. It is important to note that, along with the local density ρ, $D(\rho,\gamma)$ depends on the tumbling rate γ, which together determines the nontrivial influences of interaction and persistence on collective transport in hardcore RTPs. Interestingly, we have identified a scaling regime for $D(\rho,\gamma)$: in the limit of low density $\rho \to 0$ and strong persistence $\gamma \to 0$, the subtle interplay between interaction and persistence can be quantified by a single scaling variable $\psi = \rho v/\gamma$ through the scaling relation,

$$D(\rho,\gamma) = D^{(0)}\mathcal{F}(\psi), \tag{2.3}$$

with the prefactor $D^{(0)} = v^2/2d\gamma$ representing the bulk-diffusion coefficient in the noninteracting limit. We further calculate the scaling function $\mathcal{F}(\psi)$ analytically for a variant of RTPs and numerically for the others. Although persistent random walks are long known in the literature [35, 137], the scaling function $\mathcal{F}(\psi)$ as given in Eq. (2.3), to the best of our knowledge, has not yet been reported.

The chapter is structured as follows: We begin by introducing the class of hardcore RTPs under investigation in Sec. 2.2, followed by presenting a scaling theory in Sec. 2.3. We then derive a macroscopic hydrodynamic description in Sec. 2.4 by computing the bulk-diffusion coefficient $D(\rho,\gamma)$, which depends on density and tumbling rate, for hardcore RTPs. In Sec. 2.5.1, we analyze the parameter dependence of $D(\rho,\gamma)$ and establish a scaling law across one and two dimensions. Furthermore, in Sec. 2.5.2, we validate the diffusive hydrodynamic evolution by simulating density relaxation directly. We also study the relaxation of a *delta* initial density perturbation in Sec. 2.5.3, relaxing on an infinite domain, to demonstrate an early-time anomalous (ballistic) transport. Finally, in Sec. 2.6, we summarize our findings and offer concluding remarks.

2.2 Model description

We consider two minimalistic models of interacting RTPs: model I and model II. In both models, there are N hardcore particles situated on a d-dimensional periodic lattice with length L, maintaining a constant global density $\rho = N/L^d$. Model I represents conventional hardcore (athermal) RTPs, introduced in Ref. [36], whereas model II is a "long-range" variant of model I that is amenable to analytic studies. In both models, particles experience *excluded-volume repulsion*, which indicates that each site can maximally accommodate only one particle and inter-particle crossing is prohibited. We introduce the occupancy variable $\eta_{\mathbf{x}}$ at a given site

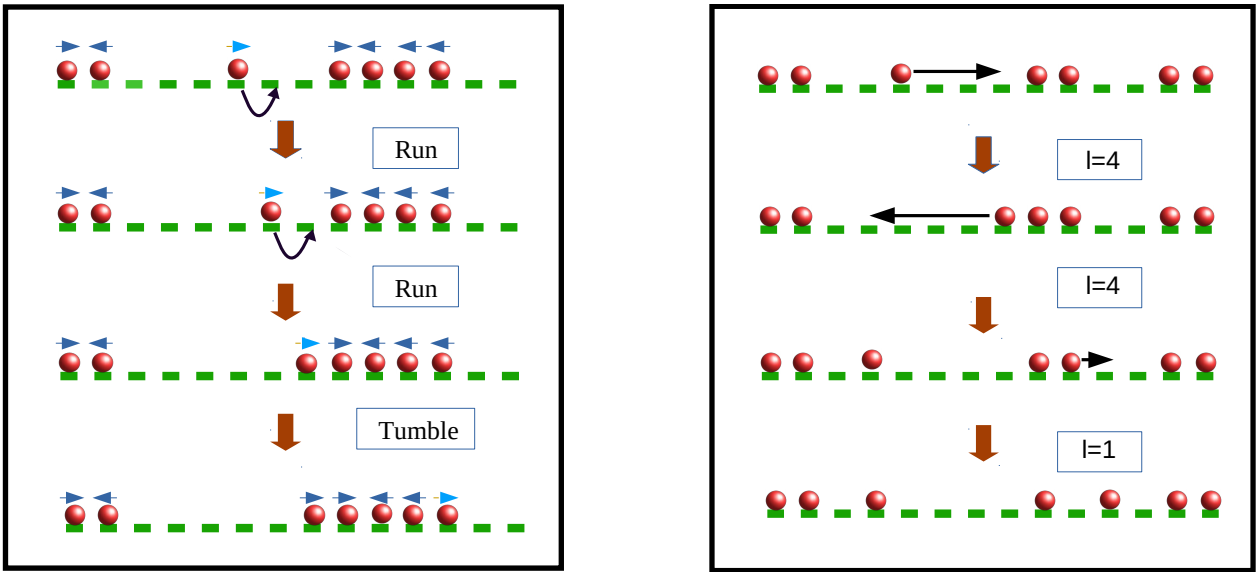

Figure 2.1: In the left panel, we illustrate the dynamics of model I (the conventional RTPs) which involves hardcore RTPs (depicted as red circles) on a one-dimensional periodic lattice. These particles move to adjacent lattice sites along their spin directions, as indicated by the arrows above them. On the right panel, we present the dynamics of hardcore particles (also depicted as red circles) in model II, which is defined here on the one-dimensional periodic lattice. In this model, particles move symmetrically either to the right or left. The length of each movement, denoted as l, is randomly drawn from an exponential distribution $\phi(l) \propto e^{-l/l_p}$, where $l \in [0, 1, 2, \dots]$.

$\mathbf{X}$, where $\eta_{\mathbf{X}} = 1$ or 0 depending on whether the site is occupied or vacant, respectively.

Model I: Standard hardcore RTPs

We look into the paradigmatic model of hardcore RTPs evolving in continuous time. In this model, particles are characterized by a spin variable $\mathbf{s}$ and can be randomly oriented along any of the $2d$ directions. The stochastic dynamical rules for this model are defined below.

A. *Run:* A particle hops to the nearest neighboring site along its spin direction at a rate of v, given that the destination site is unoccupied.

B. *Tumble:* At a rate of γ, which is the inverse of the persistence time τ_p, a particle's spin flips. In this flipping event, a new direction is chosen randomly from among $2d - 1$ other available directions (excluding the initial direction), with each direction having an equal probability of being selected.

According to rules A and B, during two successive tumbling events that occur on a timescale $\tau_p = 1/\gamma$, RTPs move ballistically with constant speed v along the empty stretches in the direction of their spins. In the noninteracting limit, the typical distance traveled by a particle in this duration is known as *persistence length* $l_p = v\tau_p = v/\gamma$. While the model is numerically

accessible, its analytical characterization is challenging due to the additional spin variables. To overcome this challenge, we explore an analytically amenable idealized version of model I, denoted as model II - a long-ranged lattice gas (LLG).

Model II: Hardcore long-ranged lattice gas (LLG)

Unlike model I, particles in this model do not have intrinsic spins and hop uniformly along the available $2d$ directions. The particle dynamics proceed as follows: Each particle attempts to execute symmetric hopping with a unit rate, employing a variable hop length $l \in [0, 1, 2, \dots]$, which is drawn from a distribution $\phi(l)$. The hopping event is successful if the consecutive stretch of vacancies in the hopping direction, referred to as the "gap" g, is at least of length l (i.e., if the gap size $g \geq l$). Otherwise, if the gap size is less than the attempted hop length, the particle, constrained by the hard-core rule, moves across the entire stretch and settles next to the nearest occupied site in that direction. While the hop-length distribution $\phi(l)$ could be arbitrary, we opt for simplicity by selecting a single-parameter family of an exponential distribution,

$$\phi(l) = Be^{-l/l_p}. \tag{2.4}$$

Here, $l_p = v/\gamma$ is the persistence length defined in the model I, and $B = 1 - e^{-1/l_p}$ represents the normalization constant.

It is worth mentioning that the long-range hopping dynamics in model II closely resemble the ballistic "run" observed in conventional RTPs, where the run length follows an exponential distribution with the mean length l_p. Hence, model II is anticipated to reproduce the anomalous collective behavior in model I (standard RTPs) on the persistence time scale τ_p. However, it should be noted that, although eliminating spin variables simplifies the model, due to the long-range dynamics, model II lacks a product-measure steady-state and gives rise to nontrivial spatial correlations, leading to clustering and large density fluctuations [138].

Although these two models have different microscopic dynamics, they are related to each other by a simple rescaling of time and share remarkably similar features [see the space-time trajectory in Fig. 2.3], which we discuss in detail in the following sections.

2.3 Relevant length scales and a scaling theory

Before delving into the calculational details, let us first identify the relevant length scales in the strong persistence regime (i.e., $l_p \gg 1$) in the context of the model I (the arguments can be easily extended to other RTP variants). We do not consider here thermal diffusion as it is irrelevant in the strong-persistence regime. Because of persistence, particles move ballistically with a characteristic speed v ("run") and then randomly change direction ("tumble") at a rate

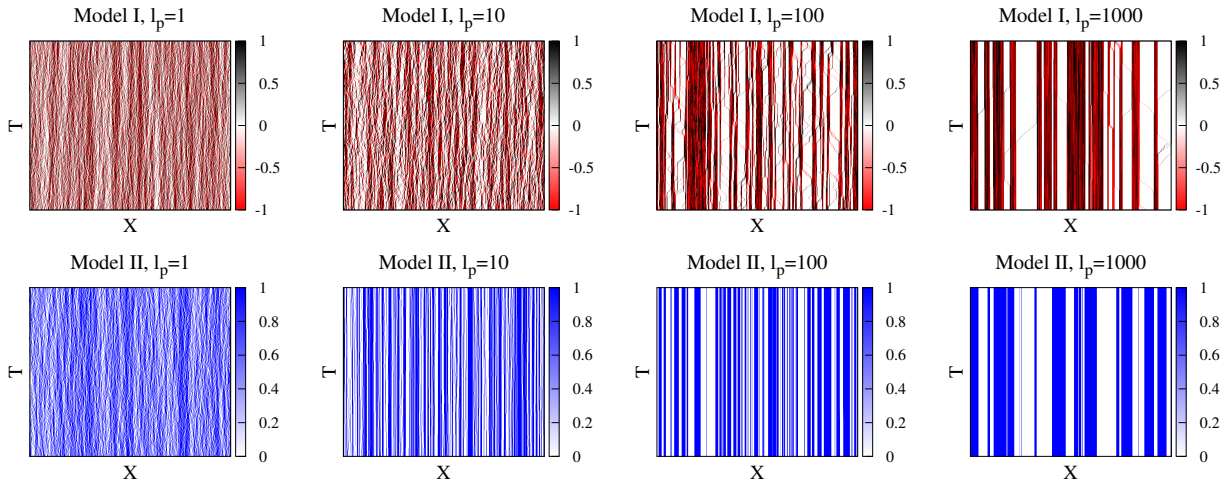

Figure 2.2: The space-time trajectories of run-and-tumble particles in models I (top panel) and II (bottom panel) are plotted in the steady-state at density $\rho = 0.5$ and persistence lengths $l_p = \gamma^{-1} = 1$, 10, 100, and 1000. In model I, black and red colors signify particles with spins $s = 1$ (moving right) and $s = -1$ (moving left), respectively, while white indicates vacancies or empty spaces. Conversely, in model II, blue represents particles, and white denotes vacancies within the system.

$\gamma = 1/\tau_p = v/l_p$, where τ_p and l_p are the persistence time and length, respectively. Clearly, l_p is a microscopic length scale induced by the persistence effect in the system. However, because of excluded-volume, or hardcore, interactions, the persistent motion of individual particles is cut off by the presence of other particles along the direction of motion. Therefore, there is another microscopic length-scale arising due to the interaction - the mean *gap* $\langle g \rangle$ (equivalent to a "mean free path") between two consecutive particles *along* the direction of motion. Notably, in one dimension, $\langle g \rangle$ is a measure of the average distance between neighboring particles (or the inter-particle spacing), however, for higher dimensions, it makes no difference where all the neighboring particles are (as defined by inter-particle spacing), $\langle g \rangle$ is determined by the average position of the next particle along the direction of a moving one. Indeed, the only relevant length scales in the system are l_p and $\langle g \rangle$, which carry the signatures of persistence and interaction, respectively. As a result, from dimensional ground, any physical quantities can be constructed by combining only these two length scales l_p and $\langle g \rangle$. This immediately implies that the bulk-diffusion coefficient can be cast in a form

$$D = D^{(0)} \mathcal{F}\left(\frac{l_p}{\langle g \rangle}\right), \tag{2.5}$$

where $\mathcal{F}(\psi)$ is the scaling function that depends on a single dimensionless scaling variable $\psi = l_p/\langle g \rangle = v/\langle g \rangle \gamma$, and the prefactor $D^{(0)} \sim \gamma l_p^2 = v^2/\gamma$ is proportional to the effective

diffusion coefficient of noninteracting RTPs. Moreover, in the dilute system [i.e., $\rho \to 0$], as the average number of particles in any row (consisting of L sites) is equal to $L/\langle g \rangle$ and using the conservation relation $(L/\langle g \rangle) \times (L^{d-1}/a) = N$, we obtain an exact relation,

$$\langle g \rangle = \frac{1}{\rho a}, \tag{2.6}$$

where $a \sim r_0^{d-1}$ and r_0 are particle cross-section and diameter, respectively. The above relation immediately implies the scaling variable to have the following form: $\psi = \rho a v/\gamma$ (now onwards, we put $r_0 = 1$, $a = 1$ and $v = 1$ on a hypercubic lattice of unit spacing). The asymptotic form of $\mathcal{F}(\psi)$ is determined as follows. In the *noninteracting* limit, as given by $\rho \ll 1$ and $\langle g \rangle \gg l_p$ hence $\psi \ll 1$, we have $D \sim l_p^2/\tau_p \sim 1/\gamma$, implying $\mathcal{F}(\psi) = \text{const.}$ However, in *strongly interacting* limit $l_p \gg \langle g \rangle$, D is proportional to γ as microscopic events occur on a time scale $\tau_p = \gamma^{-1}$, implying $\mathcal{F}(\psi) \sim 1/\psi^2$ as $\psi \to \infty$. This suggests the power-law dependence of D on ρ. The aforementioned arguments, though reasonable, must be validated, which we do next in both models I and II by obtaining their hydrodynamic descriptions.

2.4 Hydrodynamics

Hydrodynamics deals with large-scale spatiotemporal properties of slow variable(s). Since we are interested in systems with total particle number conservation, and in the regime of small but finite γ, there is only one slow variable: particle density $\rho(\mathbf{X}, t) = \langle \eta_{\mathbf{X}}(t) \rangle$. We want to characterize the large space-time scale evolution of $\rho(\mathbf{X}, t)$. Although at short time scales $\mathcal{O}(\tau_p)$, the movement of a typical RTP is expected to be ballistic (assuming low density), over time scales significantly longer than τ_p, the RTP would experience numerous tumblings, effectively resulting in diffusive collective motion. Consequently, large-scale density relaxation should primarily be governed by diffusive processes. Utilizing Eq. (2.1) and the continuity equation, we can then directly express the time evolution of local density as:

$$\frac{\partial \rho(\mathbf{X}, t)}{\partial t} = \frac{\partial}{\partial \mathbf{X}} \cdot \left[D(\rho, \gamma) \frac{\partial \rho(\mathbf{X}, t)}{\partial \mathbf{X}} \right]. \tag{2.7}$$

Note that, due to an explicit density dependence of the bulk-diffusion coefficient, the density relaxation is in fact governed by a *nonlinear* diffusion equation and has interesting consequences. Clearly, Eq. (2.7) is invariant under the scale transformation $\mathbf{X} \to \lambda \mathbf{X}$ and $t \to \lambda^2 t$. Therefore, on large spatio-temporal scales, i.e., typically space $\sim \mathcal{O}(L)$ and time $\sim \mathcal{O}(L^2)$, the time-evolution equation as in Eq. (2.7) is reduced to the following diffusion equation for

the coarse-grained density variable $\rho(\mathbf{x},\tau)$,

$$\frac{\partial\rho(\mathbf{x},\tau)}{\partial\tau} = \nabla.\left[D(\rho,\gamma)\nabla\rho(\mathbf{x},\tau)\right], \tag{2.8}$$

where we transform the density field as $\rho(\mathbf{X},t) \equiv \rho\left(\mathbf{x}=\mathbf{X}/L, \tau=t/L^2\right)$, which is now a function of the coarse-grained space $\mathbf{x}=\mathbf{X}/L$ and time $\tau=t/L^2$ variables. In the subsequent section, we verify the above hydrodynamic description by explicitly calculating the density- and tumbling-rate-dependent bulk-diffusion coefficient $D(\rho,\gamma)$ for both models I and II. To calculate $D(\rho,\gamma)$, we develop a microscopic theory for model II (LLG) and an efficient Monte Carlo algorithm for model I.

2.4.1 Microscopic theory: Model II (LLG)

We describe here the details of our analytical calculation scheme, which is performed in one dimension for simplicity, unless mentioned otherwise; generalization to higher dimensions is straightforward, and the final results are given for any dimension d. We begin with the cumulative, or time-integrated, bond-current $Q_X(t)$, which measures the net particle current across bond $[X, X+1]$ in a time interval t. Notably, the stochastic quantity $Q_X(t)$ is macroscopic and can be measured quite efficiently in simulations. This macroscopic quantity, however, is related to its microscopic counterpart, the instantaneous current $J_X(t)$ in the following way:

$$J_X(t) = \lim_{\Delta t\to 0}\frac{\Delta Q_X}{\Delta t}, \tag{2.9}$$

where $\Delta Q_X(t) = \int_t^{t+\Delta t} J_X(t)dt$ is the time-integrated current in the time interval Δt. In this section, we characterize the behavior of average bond current to calculate the bulk-diffusion coefficient for model II.

It is worth noting that whenever a particle makes a long-range hop of length l and arrives at the destination site, it travels the entire length of vacant sites. As a result, for a rightward (leftward) hop, current across *all* bonds in that empty vacant stretch increases (decreases) by unity. Therefore, in an infinitesimal time interval $[t, t+dt]$, the continuous-time evolution of the time-integrated current $Q_X(t)$ can be written as

$$Q_X(t+dt) = \begin{cases} Q_X(t)+1, & \text{prob.} \quad \mathcal{P}_X^R(t)dt, \\ Q_X(t)-1, & \text{prob.} \quad \mathcal{P}_X^L(t)dt, \\ Q_X(t), & \text{prob.} \quad 1-(\mathcal{P}_X^R+\mathcal{P}_X^L)dt, \end{cases} \tag{2.10}$$

where $\mathcal{P}_X^R dt$ and $\mathcal{P}_X^L dt$ are the probabilities of the corresponding hopping events; the explicit

identification of the stochastic variables $\mathcal{P}_X^R$ and $\mathcal{P}_X^L$ are discussed below. By using the above microscopic update rules, average instantaneous current $\langle J_X(t)\rangle$ can be immediately written as

$$\langle J_X(t)\rangle \;=\; \frac{d\,\langle Q_X(t)\rangle}{dt} = \left\langle \mathcal{P}_X^R(t)\right\rangle - \left\langle \mathcal{P}_X^L(t)\right\rangle . \tag{2.11}$$

We now define the following stochastic variables, which will be required in the subsequent calculations,

$$\mathcal{U}_{X+l}^{(l)} \;\equiv\; \overline{\eta}_{X+1}\overline{\eta}_{X+2}\cdots\overline{\eta}_{X+l}, \tag{2.12}$$

$$\mathcal{V}_{X+l+1}^{(l+2)} \;\equiv\; \eta_X\overline{\eta}_{X+1}\overline{\eta}_{X+2}\cdots\overline{\eta}_{X+l}\eta_{X+l+1}, \tag{2.13}$$

where $\bar{\eta}_X = (1-\eta_X)$, $\mathcal{U}^{(l)}$ is an indicator function of l consecutive sites being vacant and $\mathcal{V}^{(l+2)}$ is that of a vacancy cluster of size l. Notably, in Eq. (2.10), $\mathcal{P}_X^R(t)dt$ corresponds to the probability of a unit increment in $Q_X(t)$ caused by the rightward hopping event. Therefore, to identify the stochastic variable $\mathcal{P}_X^R(t)$, we simply consider rightward hopping and compute the probability term corresponding to the increment in current $Q_X(t)$. Now, depending on hop length l and gap size g, we must consider the two possibilities.

Case I. $l > g$.– In this scenario, a particle traverses the entire empty lane (a cluster of vacancies) of size g in an infinitesimal time dt, increasing current across all g bonds by unity. Therefore, for the above hopping event to cause an increase in $Q_X(t)$, the vacancy cluster must contain the bond $(X, X+1)$ itself. Moreover, one can retain the bond $(X, X+1)$ inside a hole cluster of size g by translating the entire cluster in g different ways, each of which corresponds to a unit increment of $Q_X(t)$. As a result, the probability of increasing current by a unit amount is given by $\mathcal{P}_X^{>,R}dt$, with

$$\begin{aligned}\mathcal{P}_X^{>,R}(g) \;&\equiv\; \frac{1}{2}\sum_{k=1}^{g}\eta_{X+k-g}(t)\overline{\eta}_{X+k-g+1}\cdots\overline{\eta}_{X+k}\eta_{i+k+1},\\ &=\; \frac{1}{2}\sum_{k=1}^{g}\mathcal{V}_{X+k+1}^{(g+2)}.\end{aligned} \tag{2.14}$$

Case II. $l \leq g$.– In this case, the particle hops rightward by l units during time dt, increasing current by unity across all l bonds. As a result, if the bond $(X, X+1)$ is one of these l bonds, $Q_X(t)$ increases by one. Similarly to Case I, the current $Q_X(t)$ increases by

unity in l possible ways, with the corresponding probability given by $\mathcal{P}_X^{\leq,R}(t)dt$, where

$$\begin{aligned}\mathcal{P}_X^{\leq,R}(l) &\equiv \frac{1}{2}\sum_{k=1}^{l}\eta_{X+k-l}\overline{\eta}_{X+k-l+1}\overline{\eta}_{X+k-l+2}\cdots\overline{\eta}_{X+k},\\ &= \frac{1}{2}\sum_{k=1}^{l}\left(\mathcal{U}_{X+k}^{(l)}-\mathcal{U}_{X+k}^{(l+1)}\right).\end{aligned} \tag{2.15}$$

Therefore, by combining cases I and II, the total probability that $Q_X(t)$ increases by unity during time interval dt, can be written as $\mathcal{P}_X^R dt$, where

$$\begin{aligned}\mathcal{P}_X^R &\equiv \sum_{l=1}^{\infty}\phi(l)\left[\mathcal{P}_X^{\leq,R}(l)+\sum_{g=1}^{l-1}\mathcal{P}_X^{>,R}(g)\right],\\ &= \frac{1}{2}\sum_{l=1}^{\infty}\phi(l)\left[\sum_{k=1}^{l}\left(\mathcal{U}_{X+k}^{(l)}-\mathcal{U}_{X+k}^{(l+1)}\right)+\sum_{g=1}^{l-1}\sum_{k=1}^{g}\mathcal{V}_{X+k+1}^{(g+2)}\right].\end{aligned} \tag{2.16}$$

Similarly the total probability of current $Q_X(t)$ decreasing by unity, during time interval dt, due to leftward hopping can be written as $\mathcal{P}_X^L dt$, where

$$\mathcal{P}_X^L \equiv \frac{1}{2}\sum_{l=1}^{\infty}\phi(l)\left[\sum_{k=1}^{l}\left(\mathcal{U}_{X+k-1}^{(l)}-\mathcal{U}_{X+k}^{(l+1)}\right)+\sum_{g=1}^{l-1}\sum_{k=1}^{g}\mathcal{V}_{X+k}^{(g+2)}\right]. \tag{2.17}$$

By substituting $\mathcal{P}_X^R(t)$ and $\mathcal{P}_X^L(t)$ in Eq. (2.11), the average instantaneous current can be immediately obtained as

$$\langle J_X(t)\rangle = \frac{1}{2}\sum_{l=1}^{\infty}\phi(l)\left[\sum_{g=1}^{l-1}\left(\langle\mathcal{V}_{X+g+1}^{(g+2)}\rangle-\langle\mathcal{V}_{X+1}^{(g+2)}\rangle\right)+\left(\langle\mathcal{U}_{X+l}^{(l)}\rangle-\langle\mathcal{U}_X^{(l)}\rangle\right)\right]. \tag{2.18}$$

It is noteworthy that the instantaneous current, denoted as $\langle J_X(t)\rangle$ and defined in Eq. (2.18), can be expressed as a (generalized) gradient of the observables $\langle\mathcal{V}^{(g+2)}\rangle$ and $\langle\mathcal{U}^{(l)}\rangle$. This indicates that the system satisfies the gradient property [113, 119]. Now, in the long-time limit, assuming the system attains a *local equilibrium-like state*, one expects that the "fast" variables $\langle\mathcal{V}_X^{(g+2)}\rangle(t)$ and $\langle\mathcal{U}_X^{(l)}\rangle(t)$ are effectively governed by the slowly varying conserved local density $\rho(X,t)=\langle\eta_X(t)\rangle$. To this end, by substituting $\langle\mathcal{V}_X^{(g+2)}\rangle(t)\equiv\langle\mathcal{V}^{(g+2)}\rangle[\rho(X,t)]$ and $\langle\mathcal{U}_X^{(l)}\rangle(t)\equiv\langle\mathcal{U}^{(l)}\rangle[\rho(X,t)]$, and then by performing gradient expansion in Eq. (2.18), we

obtain

$$\langle J_X(t)\rangle = \frac{1}{2}\sum_{l=1}^{\infty}\phi(l)\frac{\partial}{\partial\rho}\left[\sum_{g=1}^{l-1} g\langle\mathcal{V}^{(g+2)}\rangle + l\langle\mathcal{U}^{(l)}\rangle\right]\frac{\partial\rho}{\partial X}, \tag{2.19}$$

Now, by using the expression of $\langle J_X(t)\rangle$, the time-evolution equation of local-density $\rho(X,t)$ can be written as continuity equation,

$$\frac{\partial\rho}{\partial t} = \langle J_{X-1}(t)\rangle - \langle J_X(t)\rangle \tag{2.20}$$

$$\equiv \frac{\partial}{\partial X}\left[D_{II}(\rho,\gamma)\frac{\partial\rho}{\partial X}\right], \tag{2.21}$$

where $D_{II}(\rho,\gamma)$ is the desired bulk-diffusion coefficient for model II in one dimension, and is given by

$$D_{II}(\rho,\gamma) = -\frac{1}{2}\sum_{l=1}^{\infty}\phi(l)\frac{\partial}{\partial\rho}\left[\sum_{g=1}^{l-1} g\langle\mathcal{V}^{(g+2)}\rangle + l\langle\mathcal{U}^{(l)}\rangle\right]. \tag{2.22}$$

However, in arbitrary (finite) dimensions d, the above expression can be written as

$$D_{II}(\rho,\gamma) = -\frac{1}{2d}\sum_{l=1}^{\infty}\phi(l)\frac{\partial}{\partial\rho}\left[\sum_{g=1}^{l-1} g\langle\mathcal{V}^{(g+2)}\rangle + l\langle\mathcal{U}^{(l)}\rangle\right]. \tag{2.23}$$

Note that, the above equation expresses $D_{II}(\rho,\gamma)$ in terms of the correlation functions $\langle\mathcal{V}^{(g+2)}\rangle$ and $\langle\mathcal{U}^{(l)}\rangle$. With some algebraic manipulations, we can write the correlation functions as a function of gap distribution function $P(g)$ in the following manner:

$$\langle\mathcal{V}^{(g+2)}(\rho,\gamma)\rangle = \rho P(g), \tag{2.24}$$

$$\langle\mathcal{U}^{(l)}(\rho,\gamma)\rangle = \rho\sum_{g=l}^{\infty}(g-l+1)P(g). \tag{2.25}$$

Finally, substituting the above functional dependence of $\langle\mathcal{V}^{(g+2)}(\rho,\gamma)\rangle$ and $\langle\mathcal{U}^{(l)}(\rho,\gamma)\rangle$ in Eq. (2.23), we can explicitly write $D_{II}(\rho,\gamma)$ in terms of $P(g)$,

$$D_{II}(\rho,\gamma) = -\frac{1}{2d}\frac{\partial}{\partial\rho}\left[\rho\sum_{l=1}^{\infty}\phi(l)\left(\sum_{g=1}^{l-1} gP(g) + l\sum_{g=l-1}^{\infty}(g-l+1)P(g)\right)\right]. \tag{2.26}$$

According to Eq. (2.26), determining $D_{II}(\rho,\gamma)$ requires first to find $P(g)$. Although numerical computation of this is straightforward, explicitly calculating $P(g)$ for arbitrary ρ and γ

is generally challenging. However, for large g, $P(g)$ is expected to follow an exponential form, $P(g) \simeq N_* e^{-g/g_*}$, where $N_*(\rho,\gamma)$ and $g_*(\rho,\gamma)$ represent the proportionality constant and typical gap size, respectively. The determination of N_* is based on the normalization condition $\sum_g P(g) = 1$ and Eq. (2.6). Now, using the above form of gap distribution $P(g)$ and replacing $\phi(l)$ from Eq. (2.4) in Eq. (2.26), we obtain the expression of the bulk-diffusion coefficient,

$$D_{II}(\rho,\gamma) = -\frac{B}{2d}\frac{\partial}{\partial\rho}\left[(1-\rho)\left\{\frac{1}{e^{1/l_p}-1} + \frac{1}{(e^{1/\xi}-1)^2}\right\}\right], \tag{2.27}$$

where we determine the following length scale,

$$\xi = \frac{1}{l_p^{-1} + g_*^{-1}}. \tag{2.28}$$

Notably, the above form of $D_{II}(\rho,\gamma)$ is valid for arbitrary ρ and γ. In the subsequent analysis, we consider the following special cases.

Case I: Arbitrary density and small persistence $\gamma \gg 1$

In the regime of small persistence, characterized by $\gamma \gg 1$, density correlations vanish in the thermodynamic limit. Consequently, the steady-state distribution transforms into a product measure, expressed as $P(g) \sim (1-\rho)^g \simeq e^{-g/g_*}$, where $g_* = -1/\log(1-\rho)$. By substituting this g_* into Eq. (2.27) and imposing the conditions $\gamma \gg 1$ and ρ being finite, we derive:

$$D_{II}(\rho,\gamma) \simeq \frac{e^{-\gamma}}{2d} = e^{-\gamma} D_{SSEP}. \tag{2.29}$$

It is important to note that the above expression is independent of density, and through an appropriate time scaling ($t \to t' = te^{\gamma}$), it converges to the bulk-diffusion coefficient $D_{SSEP} = 1/2d$ for the symmetric simple exclusion process (SSEP); see Appendix A.2 for details. The inclusion of the exponential prefactor $e^{-\gamma}$ in the equation is elucidated as follows. In this scenario, the distribution $\phi(l)$ predominantly favors $l = 0$, while all other hop lengths, i.e., $l > 0$, exhibit an exponentially diminishing probability of $1 - \phi(0) = e^{-\gamma}$. Moreover, among these non-zero hop lengths, it is evident that the nearest-neighbor or unit-distance hop with $l = 1$ dominates, and contributions from larger l are negligible in the relaxation process. Consequently, in the limit $\gamma \gg 1$ or, equivalently, $l_p \ll 1$, particles effectively perform SSEP-like dynamics with an exponentially small rate of $e^{-\gamma}$ - the factor that accounts for the prefactor in Eq. (2.29).

Case II: High density $\rho \to 1$ and strong persistence $\gamma \to 0$

In this regime characterized by strong persistence and high density, the persistence length l_p is considerably larger than the mean gap size $\langle g \rangle$. This substantial difference induces nontrivial density correlations and thus makes the analytical determination of g_* difficult. Recently, by incorporating independent interval approximations, the analytical expression for g_* in this regime in one dimension has been calculated to be $g_* = \sqrt{\langle g \rangle / \gamma}$ in Ref. [139], where $\langle g \rangle = 1/\rho - 1$ represents the average gap for any density ρ. By substituting this expression of g_* and the condition $g_* \ll l_p \to \infty$ in Eq. (2.27), we obtain the bulk-diffusion coefficient,

$$D_{II}(\rho, \gamma) \simeq \frac{1}{2\rho^2}; \tag{2.30}$$

see Appendix A.2 for details. It is interesting to note that, in this parameter regime, $D_{II}(\rho, \gamma)$ is independent of γ, and it exhibits a power-law behavior as a function of density ρ.

Case III: Low density $\rho \to 0$ and strong persisitence $\gamma \to 0$

In this scenario, both length scales, l_p and $\langle g \rangle$, are diverging, specifically $l_p \sim \langle g \rangle \to \infty$, and they are in competition with each other. As these are the only relevant length scales, one can readily formulate a dimensionless quantity $\psi = l_p / \langle g \rangle$, which serves as the parameter for characterizing various physical quantities in the system (see Sec 2.3). Consequently, the typical gap size is expected to exhibit a scaling form:

$$g_* \simeq \frac{1}{\rho} \mathcal{G}(\psi), \tag{2.31}$$

with $\psi = \rho v / \gamma = l_p \rho$; these assertions are verified in simulations, see Appendix A.1 for details. The prefactor $1/\rho$ is fixed from the fact that in the limit $\psi \to 0$, the system reduces to a noninteracting one and therefore $\mathcal{G}(0) = 1$. Now, using the above form of g_* in Eq. (2.27) and putting $B = 1/l_p$, we obtain

$$D_{II}(\rho, \gamma) = \frac{e^{1/\xi}}{l_p d (e^{1/\xi} - 1)^3} \frac{1}{\mathcal{G}(\psi)} \left(1 - \psi \frac{\mathcal{G}'(\psi)}{\mathcal{G}(\psi)} \right), \tag{2.32}$$

where ξ is given by

$$\xi = \frac{l_p}{1 + \psi / \mathcal{G}(\psi)}. \tag{2.33}$$

Furthermore, using the fact that $\xi \gg 1$ for large l_p, we perform an asymptotic analysis of Eq. (2.32), leading to $D_{II}(\rho, \gamma)$ which satisfies the following scaling law,

$$D_{II}(\rho, \gamma)/D_{II}^{(0)} \equiv \mathcal{F}_{II}(\psi), \tag{2.34}$$

where $D_{II}^{(0)} = \langle l^2 \rangle / 2d = l_p^2/d$ is the diffusion coefficient calculated using the central limit theorem in the noninteracting limit (i.e., the single-particle case), and $\mathcal{F}_{II}(\psi)$ is the desired scaling function, which is given by

$$\mathcal{F}_{II}(\psi) = \frac{\mathcal{G}^2(\psi)}{(\mathcal{G}(\psi) + \psi)^3} \left(1 - \psi \frac{\mathcal{G}'(\psi)}{\mathcal{G}(\psi)}\right) \tag{2.35}$$

see Appendix A.2 for details.

For the purpose of demonstration, let us consider model II in one dimension. In the limit of large ψ, as shown in [139], the typical gap size in one dimension is expressed as $g_* = \sqrt{\psi}/\rho$. By combining the two limiting behaviors for small and large ψ, we can straightforwardly write $\mathcal{G}(\psi) \simeq (1 + \psi)^{1/2}$ which is then substituted in Eq. (2.35) to explicitly obtain the scaling function,

$$\mathcal{F}_{II}(\psi) = \frac{(2 + \psi)}{2(\psi + \sqrt{1 + \psi})^3}. \tag{2.36}$$

Note that, for $\psi \ll 1$, $\mathcal{F}_{II}(\psi) = 1$ and consequently $D_{II} \simeq l_p^2$, which diverges when the persistence length $l_p \to \infty$; for $\psi \gg 1$, $\mathcal{F}_{II}(\psi) \simeq 1/2\psi^2$ and $D_{II} \simeq 1/2\rho^2$. Interestingly, expanding $\mathcal{F}_{II}(\psi)$ around $\psi = 0$, we obtain

$$\mathcal{F}_{II}(\psi) \simeq 1 - 4\psi - \mathcal{O}(\psi^2). \tag{2.37}$$

Now, putting back all the dimensional factors explicitly in the expression of the bulk-diffusion coefficient in Eq. (2.34), we get

$$D_{II}(\rho, \gamma) \simeq D_{II}^{(0)} \left(1 - \frac{\rho}{\rho_*}\right). \tag{2.38}$$

In the above expression, we identify a characteristic density $\rho_* = 1/4al_p$, where a represents the particle cross-section. Although the expansion is derived in one dimension, the stated form of $D_{II}(\rho, \gamma)$ should remain valid across any dimension, with $\rho_* \sim 1/al_p$. Now, assuming that the aforementioned low-density approximation ($\rho \ll \rho_*$) holds true even in the high-density regime, it would suggest a diffusive instability in the system for $\rho > \rho_*$, leading to a negative bulk diffusion coefficient. However, this scenario does not occur; in the higher density range ($\rho \gg \rho_*$), the bulk diffusion coefficient gradually transitions to a power-law

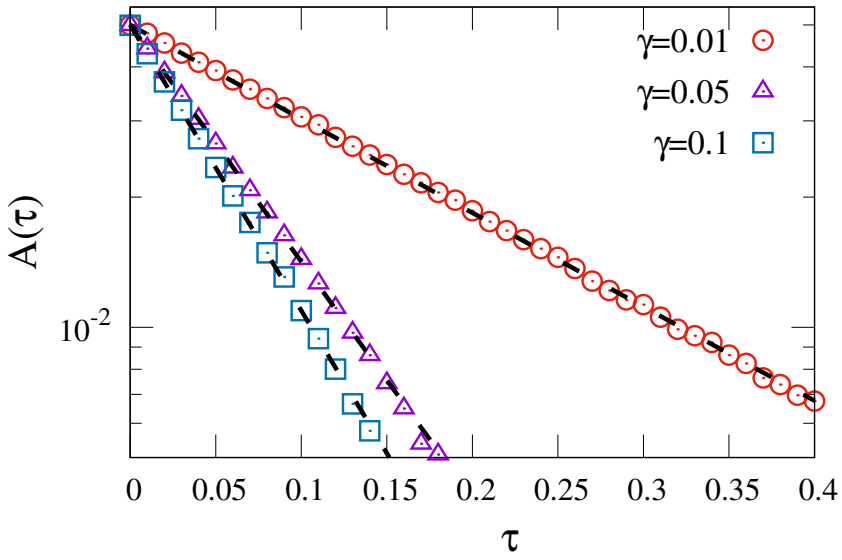

Figure 2.3: We illustrate the perturbation amplitude $A(\tau)$ plotted against the hydrodynamic time τ for various tumbling rates $\gamma = 0.01$ (depicted by red circles), 0.05 (represented by magenta triangles), and 0.1 (shown as blue squares). The dashed black lines indicate the exponential functions best fitted to the data, as in Eq. (2.41), with relaxation rates $\Gamma = 5.03$, 12.82, and 15.24 corresponding to $\gamma = 0.01$, 0.05, and 0.1, respectively. Both panels maintain fixed values of $\rho_0 = 0.5$ and $A(0) = 0.05$.

form, $D_{II} \sim \rho^{-\alpha}$ with $\alpha > 0$, as specified in Eq. (2.44), and it never reaches zero within the range $0 < \rho < 1$.

2.4.2 Numerical scheme for model I

Our scaling argument, outlined in Section 2.3, implies that the scaled bulk-diffusivity $D_I/D_I^{(0)} = \mathcal{F}_I(\rho v/\gamma)$ should be expressed in terms of a scaling function for the model I as well, as we verify in the subsequent analysis. Since the analytic calculation of $D_I(\rho, \gamma)$ for arbitrary densities and tumbling rates is difficult at this stage, we employ an efficient numerical technique detailed below [135]. For simplicity, the numerical method is discussed in the context of a one-dimensional system and it can be immediately generalized to higher dimensions. We study relaxation of a long-wave-length - typically sinusoidal - initial density perturbation $\rho(X, 0) = \rho_{in}(X/L)$ with wave number $2\pi/L$,

$$\rho(X, 0) = \rho_0 + A(0) \sin\left(\frac{2\pi X}{L}\right), \tag{2.39}$$

i.e., $\rho_{in}(x) = \rho_0 + A(0)\sin(2\pi x)$, where $X = xL$ is the lattice position and ρ_0 is the global density, around which the perturbation is applied. For higher dimensions ($d > 1$), the perturbation is applied in a single spatial direction, while maintaining a uniform density

profile in all other directions. Over long time scales $t \sim \mathcal{O}(L^2) \gg 1/\gamma$, the influence of short-time ballistic motion fades away after numerous tumbling events, leading the system to exhibit diffusive behavior. Consequently, on the scales of coarse-grained (macroscopic) space $x = X/L$ and time $\tau = t/L^2$, the evolution of the density profile $\rho(x,\tau)$ is expected to follow the nonlinear diffusion equation as given in Eq. (2.8). Moreover, in the limit of weak perturbation, characterized by $A(0) \ll \rho_0$, we can linearize Eq. (2.8) by taking $D_I[\rho(x,\tau),\gamma] \simeq D_I(\rho_0,\gamma)$ and, the resulting equation takes the following form:

$$\frac{\partial \rho(x,\tau)}{\partial \tau} = D_I(\rho_0,\gamma)\frac{\partial^2 \rho(x,\tau)}{\partial x^2}. \tag{2.40}$$

The diffusive scaling limit described above will be confirmed shortly through direct Monte Carlo simulations of Model I. Now, by using Eq. (2.40), the density perturbation at a later time can be easily computed to have the following expression: $\delta\rho(x,\tau) = \rho(x,\tau) - \rho_0 = A(\tau)\sin(2\pi x)$, where the amplitude is determined by

$$A(\tau) = A(0)e^{-\Gamma\tau}, \tag{2.41}$$

where $\Gamma(\rho_0,\gamma)$ is the density and tumbling rate dependent relaxation rate, which is directly related to the bulk-diffusion coefficient $D_I(\rho_0,\gamma)$ in the following way,

$$\Gamma(\rho_0,\gamma) = 4\pi^2 D_I(\rho_0,\gamma). \tag{2.42}$$

In our simulations, we compute the average excess number of particles, denoted as $\Delta(\tau)$, in the first half of the system. This quantity is directly connected to the amplitude $A(\tau)$, and the relationship is given by $\Delta(\tau) = L^d \int_0^{1/2} \delta\rho(x,\tau)dx = L^d \pi A(\tau)$. Once we obtain $\Delta(\tau)$, and consequently $A(\tau)$, at various τ values, we assess the relaxation rate and determine the bulk diffusion coefficient using the relation provided in Eq. (2.42). To ensure diffusive relaxation, it is crucial to first take the thermodynamic limit, where both the system size L and the number of particles N tend to infinity, while keeping the density fixed at $\rho_0 = N/L$. Subsequently, the tumbling rate γ can be systematically varied, with a particular focus on the regime where γ is small, i.e., $\gamma \ll 1$. To validate Eq. (2.41) in one dimension, we plotted the numerically obtained $A(\tau)$ in Fig. 2.4.2 as a function of τ for various tumbling rates $\gamma = 0.01$, 0.05, and 0.1 at density $\rho_0 = 0.5$ and system size $L = 1000$. We find $A(\tau)$ to be a simple exponential, as predicted by Eq. (2.41). Fitting the simulation data with Eq. (2.41) yields the corresponding relaxation rates Γ, which are then used in Eq. (2.42) to obtain the bulk-diffusion coefficient for the model I for the corresponding values of density and tumbling rate.

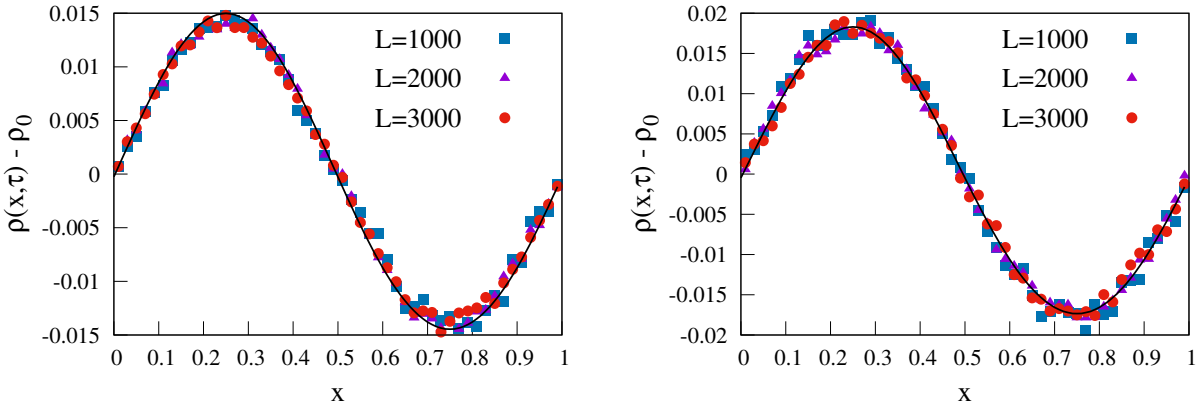

Figure 2.4: We plot the numerically obtained excess density $\delta\rho(x,\tau) = \rho(x,\tau) - \rho_0$ for model I at two different tumbling rates, $\gamma = 0.05$ (left panel) and 0.01 (right panel), against the scaled position $x = X/L$ at hydrodynamic times $\tau = 0.1$ and 0.2, respectively. We initialize the system by employing a sinusoidal initial condition outlined in Eq. (2.39), with $\rho_0 = 0.5$ and $A(0) = 0.05$. The corresponding curves are generated by numerically integrating the hydrodynamic equation, as described in Eq. (2.8), utilizing the determined bulk-diffusion coefficients.

Numerical verification of diffusive scaling

A key assumption in the computation of $D_I(\rho,\gamma)$ relies on the existence of diffusive scaling limits, as outlined in Eq. (2.8). We can immediately verify, through direct Monte Carlo simulations, the existence of such a diffusive scaling limit for model I (standard hardcore RTPs), which also leads to a direct verification of Eq. (2.8). For this purpose, we investigate the relaxation of coarse-grained (hydrodynamic) density field $\rho(x,\tau)$ as a function of scaled position $x = X/L$ for different system sizes L and different microscopic times $t \sim \mathcal{O}(L^2)$ such that the hydrodynamic time $\tau = t/L^2$ remains fixed. The diffusive scaling limit is confirmed when different curves corresponding to distinct L values, at the same τ, converge onto each other. In such a case, the collapsed data should represent the solution of the nonlinear diffusion equation, as specified in Eq. (2.8).

To implement the aforementioned numerical approach, we conduct simulations for model I (for simplicity, data presented for one dimension only) with an initial sinusoidal density profile defined in Eq. (2.39). The background density is set to $\rho_0 = 0.5$, and the perturbation height is $A(0) = 0.05$. In Fig. 2.4.2, we plot the numerically obtained excess density field $\delta\rho(x,\tau) = \rho(x,\tau) - \rho_0$ for tumbling rates $\gamma = 0.05$ (left panel) and 0.01 (right panel), as a function of the scaled position $x = X/L$, for various system sizes $L = 1000$ (blue square), 2000 (magenta triangle), and 3000 (red circle), at hydrodynamic times $\tau = 0.1$ (for $\gamma = 0.05$) and 0.2 (for $\gamma = 0.01$), respectively. Throughout the analysis, we perform averaging over 10^4 realizations. In both panels of the figure, we numerically integrate Eq. (2.8) with the above mentioned sinusoidal initial condition and the already calculated $D_I(\rho,\gamma)$ for the respective

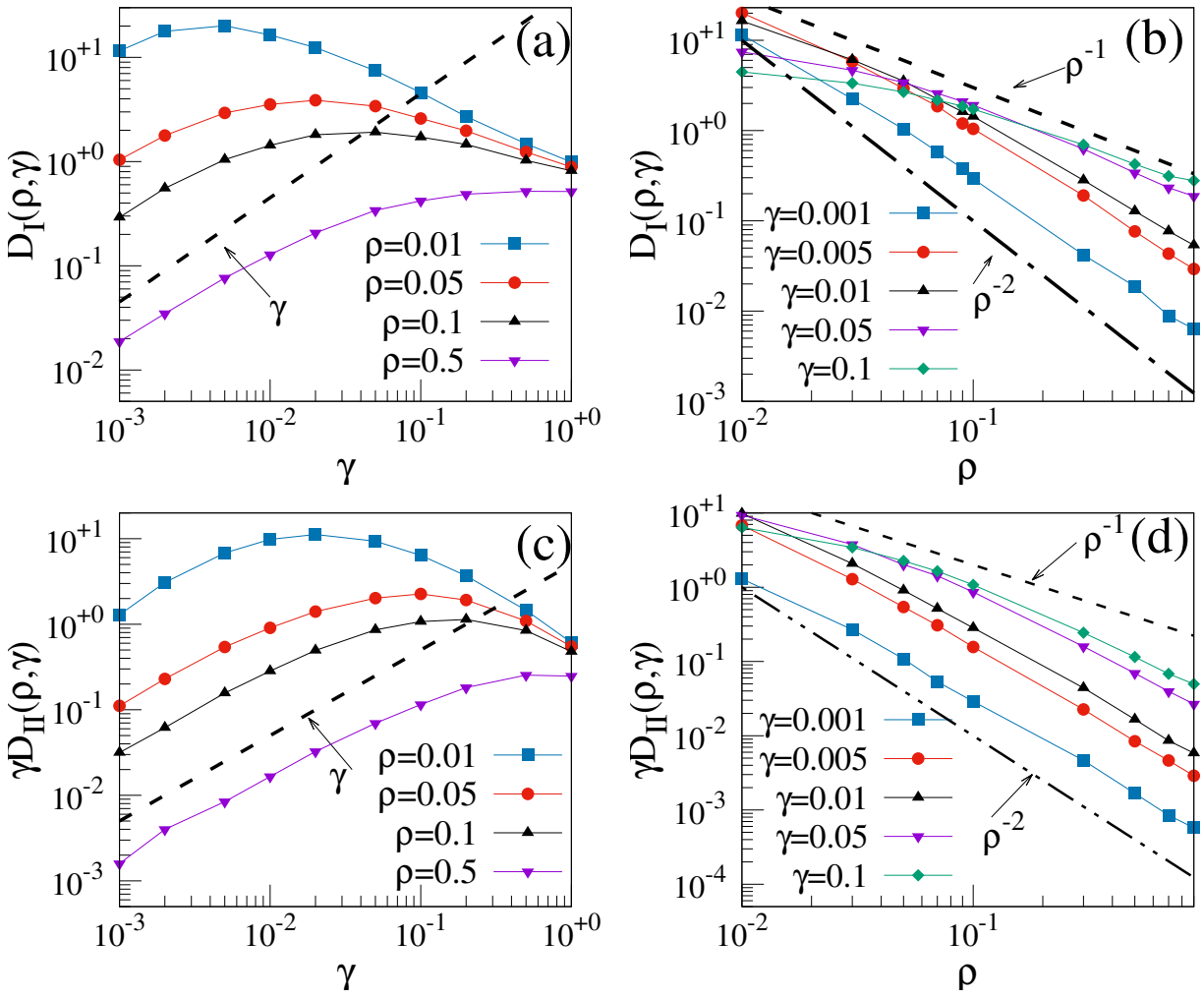

Figure 2.5: We show here the parameter dependence of the bulk-diffusion coefficient in one dimension. We plot $D_I(\rho,\gamma)$ and $\gamma D_{II}(\rho,\gamma)$, as a function of γ at various densities $\rho = 0.01$ (blue square), 0.05 (red circle), 0.1 (black up triangle) and 0.5 (magenta down triangle) for model I [panel (a)] and model II [panel (c)], respectively. In panels (b) and (d), we plot $D_I(\rho,\gamma)$ and $\gamma D_{II}(\rho,\gamma)$, respectively as a function of ρ at various $\gamma = 0.001$ (blue square), 0.005 (red circle), 0.01 (black up triangle), 0.05 (magenta down triangle) and 0.1 (green diamond).

parameter values; the corresponding numerical solution obtained from our theory Eq. (2.8) is plotted as a black solid line. Remarkably, the simulation points exhibit a notable convergence onto each other, and the curve representing the collapsed data aligns very closely with the theoretical solution. This alignment strongly indicates the immediate existence of a diffusive scaling limit for model I.

2.5 Simulation results

2.5.1 Bulk-diffusion coefficients in models I and II

Applying the methodologies outlined in the preceding section, we compute the bulk diffusion coefficient $D(\rho, \gamma)$ for both models within the parameter ranges $0.01 \leq \rho \leq 0.9$ and $0.001 \leq \gamma \leq 1$. For model II, we employ the numerically obtained steady-state gap distribution $P(g)$ in Eq. (2.26). In the case of model I, we adopt the approach detailed in Section 2.4.2. In this section, we analyze the parameter dependence of $D(\rho, \gamma)$ for these two models.

In Fig. 2.5a, we plot $D(\rho, \gamma)$ for model I, as a function of the tumbling rate γ at different densities shown in figure. Notably, the bulk diffusion coefficient $D(\rho, \gamma)$ has a non-monotonic relationship with γ, reaching an optimal diffusion condition when $\gamma \simeq \rho$. This behavior is consistent with previous observations in the context of the self-diffusion coefficient for self-propelled particles (SPPs) reported in Refs. [42, 58, 94]. Indeed, this nonmonotonicity clearly describes the intricate interplay between persistence and hard-core interactions within the system. When $\gamma \gg \rho$, a reduction in γ introduces greater persistence among particles, leading to an increase in $D(\rho, \gamma)$. Conversely, in the regime where $\gamma \ll \rho$, particles exhibit strong interactions, resulting in jammed configurations. Here, a decrease in γ enhances the jamming condition, causing a reduction in $D(\rho, \gamma)$. Furthermore, we observe that $D(\rho, \gamma) \sim \gamma$ goes linearly with the tumbling rate γ in this regime. The observed linear behavior in γ indicates that diffusion occurs on the timescale $\tau_p = 1/\gamma$. This is evident because diffusion occurs only when a boundary particle within a cluster flips, and this local spin-flipping event happens at a timescale $\tau_p = 1/\gamma$, causing $D(\rho, \gamma)$ to scale as $1/\tau_p = \gamma$.

To analyze the density dependence, in Fig. 2.5b, we depict $D(\rho, \gamma)$ for model I, varying with density ρ, across different tumbling rates shown in the figure. Unlike the previous scenario, here we observe that $D(\rho, \gamma)$ consistently decreases with ρ and displays a power-law tail, i.e., $D(\rho, \gamma) \sim \rho^{-\alpha}$, where the exponent α depends on the parameters. Interestingly, for model II, we find $\gamma D(\rho, \gamma)$ to exhibit similar qualitative features. This is illustrated by plotting $\gamma D(\rho, \gamma)$ for model II as a function of γ and ρ in Figs. 2.5(c) and 2.5(d), respectively, while maintaining the other parameter values identical to model I.

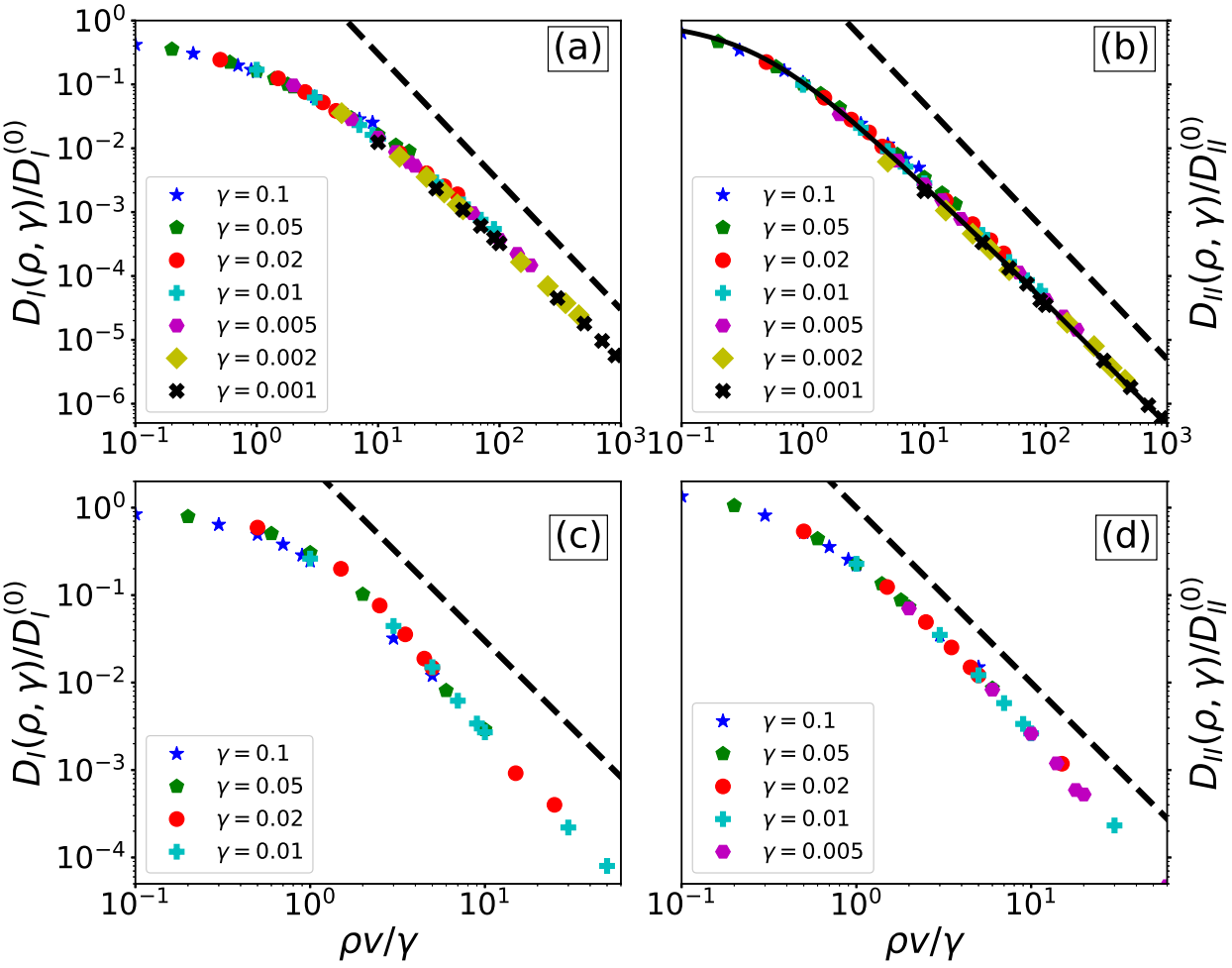

Figure 2.6: The scaled bulk-diffusion coefficients $D(\rho,\gamma)/D^{(0)}$ are plotted against the scaling variable $\psi = \rho v/\gamma$ (with $v = 1$) for model I ((a) - 1D and (c) - 2D) and model II ((b) - 1D and (d) - 2D). The solid line in panel (b) represents the theory as in Eq. (2.36); the black dotted guiding lines represent $1/\psi^2$ behavior at large ψ.

Scaling collapse of the bulk-diffusion coefficient for small density and tumbling rate

We have already observed the competing effects of persistence and hard-core interaction: while the former enhances diffusion, the latter diminishes it, leading to a nonmonotonic variation of the bulk diffusion coefficient concerning the tumbling rate, see Figs. 2.5(a) and 2.5(c). Notably, we have analytically characterized this competing effect for model II via a scaling law satisfied by $D(\rho,\gamma)$ as given in Eq. (2.34); also we have explicitly calculated the scaling function $\mathcal{F}(\psi)$ for $1D$ in Eq. (2.36). The scaling variable $\psi = \rho v/\gamma$ provides a quantitative measure of the intriguing interplay between persistence and interaction. Importantly, similar to model II, this fascinating interplay can be quantified using the same scaling variable ψ for

model I as well. We proceed to validate these findings in Fig. 2.6.

In Figs. 2.6(b) and 2.6(d), we plot the ratio $D_{II}(\rho,\gamma)/D_{II}^{(0)}$ for model II as a function of ψ, in one and two dimensions, respectively. We observe a nice scaling collapse of simulation points in both dimensions. In one dimension, the collapsed data points excellently follow the scaling function $\mathcal{F}_{II}(\psi)$ in Eq. (2.36) [see the black solid line in Fig. 2.6b]. For the model I, in Figs. 2.6a and 2.6c, we plot $D_I(\rho,\gamma)/D_I^{(0)} \equiv \mathcal{F}_I(\psi)$ as a function of ψ with $D_I^{(0)} = v^2/\gamma d$ for both one and two dimensional cases, respectively. We notice a remarkable scaling collapse in both dimensions, validating the presence of the scaling regime of $D(\rho,\gamma)$ for model I. Interestingly, the distinction in the microscopic time unit between models I and II is evident in the ratio $D^{(0)}I/D^{(0)}II = \gamma$. Additionally, similar to model II, we observe that $\mathcal{F}_I(0) = \text{const.}$ and $\mathcal{F}_I(\psi) \simeq 1/\psi^2$ for $\psi \gg 1$. This indicates that both model I and II share remarkably similar characteristics, which become immediately apparent upon time rescaling for model I (standard RTPs): $\gamma t \to t$, where time is measured in units of the persistence time $\tau_p = \gamma^{-1}$.

2.5.2 Diffusive density relaxation

In this section, we explicitly investigate the long-time hydrodynamic description, for simplicity only in one dimension, as shown in Eq. (2.8). This involves the relaxation of initial density perturbations using the previously determined bulk-diffusion coefficients $D_I(\rho,\gamma)$ and $D_{II}(\rho,\gamma)$ for models I and II, respectively. To this end, we consider the initial density perturbation $\rho_{in}(x) = \rho(x,0)$ to be a step-function characterized by a step height ρ_1 and width w over a uniform background density ρ_b. This mathematical expression is given by,

$$\rho_{in}(x) = \begin{cases} \rho_b + \rho_1 & \text{for } |x - \frac{1}{2}| \leq \frac{w}{2}, \\ \rho_b & \text{otherwise.} \end{cases} \tag{2.43}$$

We choose $\rho_1 = 0.4$, $\rho_b = 0.5$, $w = 0.1$ and $L = 1000$ for both the models. To verify Eq. (2.8), we plot the excess density $\delta\rho(x,\tau) = \rho(x,\tau) - \rho_b$ in Fig. 2.7, obtained from simulation (points), as a function of x at various times τ for $\gamma = 0.05$ [panel (a) for model I, panel (c) for model II] and 0.01 [panel (b) for model I, panel (d) for model II]. In order to obtain the theoretical predictions (line), we perform numerical integration of Eq. (2.8) by using the above initial condition and the numerically calculated bulk-diffusion coefficients [$D_I(\rho,\gamma)$ for model I and $D_{II}(\rho,\gamma)$ for model II]. In the case of both γ values, we observe that the hydrodynamic theory (represented by the line) excellently follows the simulation data points. The remarkable agreement between the theoretical predictions and simulations provides strong evidence for the accuracy of the calculated bulk-diffusion coefficients and, consequently, supports the validity of the diffusive description, as outlined in Eq. (2.8), for

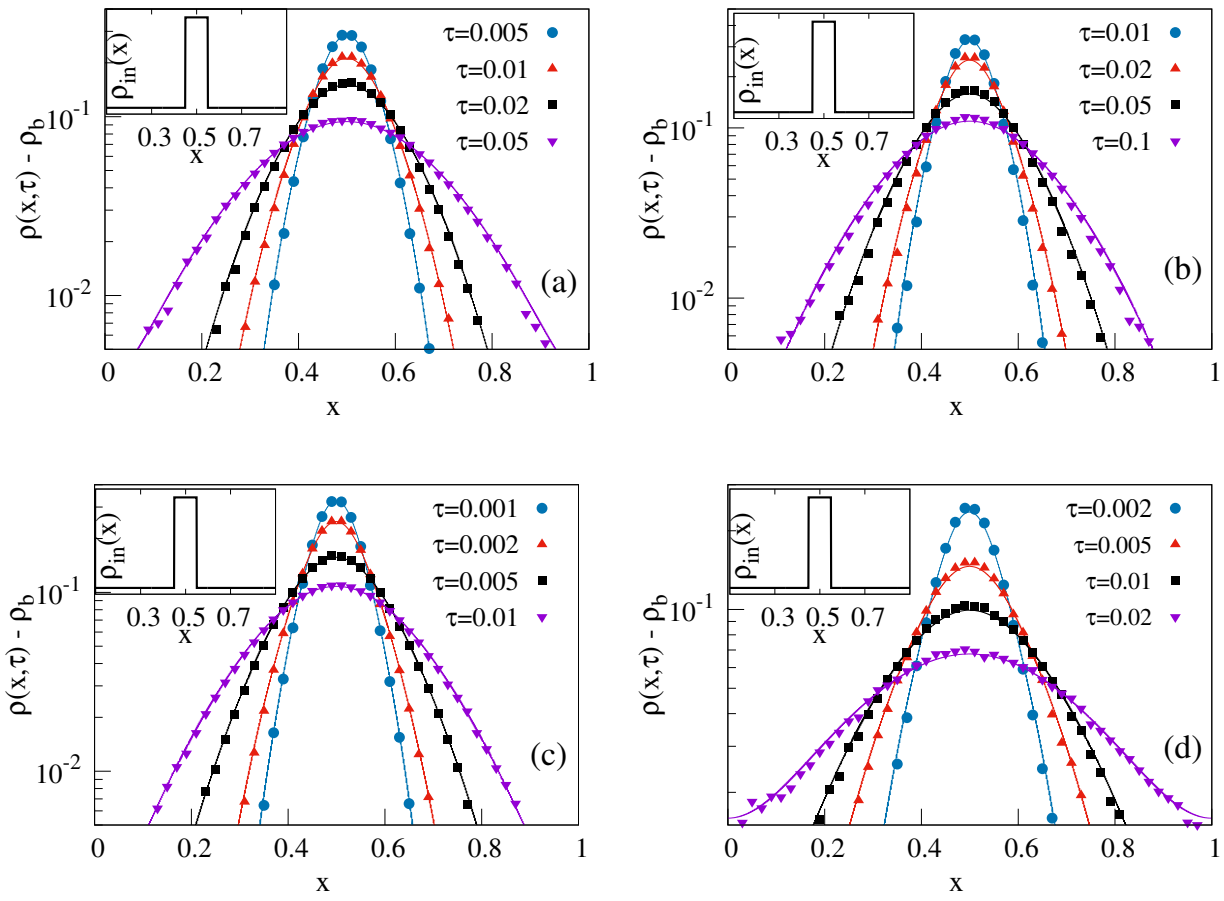

Figure 2.7: The excess density profile $\delta\rho(x,\tau) = \rho(x,\tau) - \rho_b$, obtained from simulations in one dimension, are plotted against the scaled position x at different hydrodynamic times τ for two different $\gamma = 0.05$ [model I (a) and model II (c)] and 0.01 [model I (b) and model II (d)]. In each of these panels, the matching curves are generated by integrating the hydrodynamic equation described in Eq. (2.8), employing the same initial condition (illustrated in the inset) as specified in Eq. (2.43), with parameters set as $\rho_b = 0.5$, $\rho_1 = 0.4$, and $w = 0.1$.

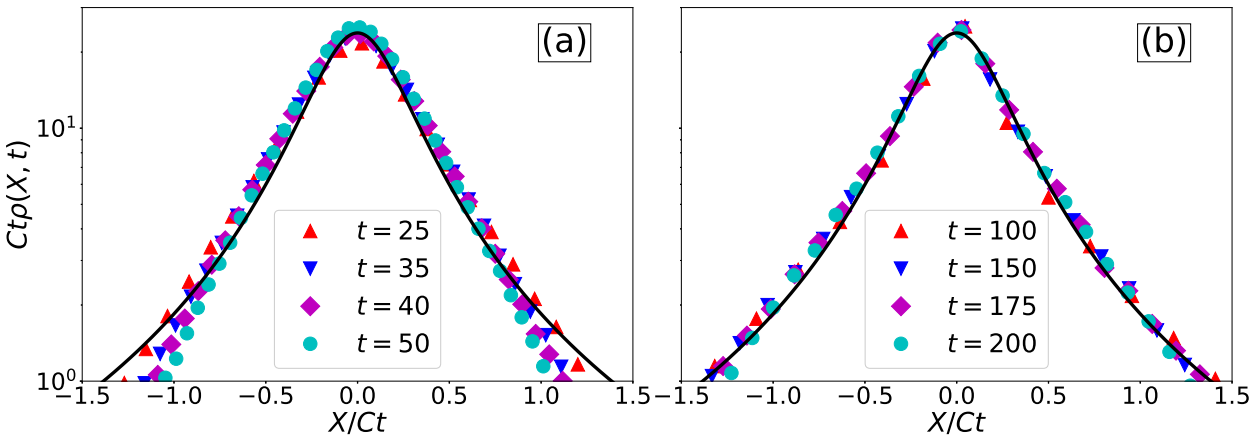

Figure 2.8: We plot the scaled density profile $Ct\rho(X,t)$ as a function of $\xi = X/Ct$ for models I (panel a) and II (panel b). Notably, the time unit in panel (a) is represented by the scale of $\tau_p = 1/\gamma$. We consider $\gamma = 0.05$ ($l_p = 20$), $N = 20$ with $C = 3.2$ (for model I) and 2.2 (for model II); the black solid lines are the scaling solution $\mathcal{R}(\xi)$ in Eq. (2.48).

both models I and II.

2.5.3 Anomalous transport

We now examine the "early-time" anomalous transport in both models I and II of hardcore RTPs by studying a localized initial density distribution. Initially, for model I (standard RTPs), we rescale time $\gamma t \to t$ (resulting in $D \to \gamma D$), thus establishing an equivalent framework with model II (LLG). Now, during the initiation of diffusion, specifically at *early yet sufficiently long* times, where $1 \ll t \ll L^2/D$, particles have experienced numerous collisions, allowing the local density to evolve reliably according to Equation (2.7). It is crucial to note that, in the limit of strong persistence, the bulk-diffusion coefficient $D(\rho,\gamma)$ exhibits a power-law decay with density, i.e.,

$$D(\rho,\gamma) \simeq \frac{C}{\rho^\alpha}, \tag{2.44}$$

where the constant C and exponent α ($0 \le \alpha \le 2$) depend on the parameter regime under consideration (see Sec. 2.5.1). Interesting, for $D(\rho,\gamma)$ in Eq. (2.44) and *delta* initial condition $\rho(X,0) = N\delta(X)$, Eq. (2.7) can be exactly solved using the following scaling ansatz,

$$\rho(X,t) = \frac{1}{(Ct)^\omega}\mathcal{R}\left(\xi\right). \tag{2.45}$$

Here, $\xi = X/(Ct)^\omega$ serves as the scaling variable, with ω representing the growth exponent and $\mathcal{R}(\xi)$ denoting the scaling function, both of which can be computed as elaborated below.

Upon inserting the above scaling ansatz in the density evolution equation Eq. (2.7) and following the transformation $X \to \xi = X/(Ct)^{\omega}$, we can immediately obtain the time-evolution for the scaling function $\mathcal{R}(\xi)$,

$$\omega \frac{d\left(\xi \mathcal{R}\right)}{d\xi} = -\left(Ct\right)^{1-(2-\alpha)\omega} \frac{d}{d\xi}\left[\mathcal{R}^{-\alpha}\frac{d\mathcal{R}}{d\xi}\right]. \tag{2.46}$$

However, for a self-similar solution to emerge, Eq. (2.46) should not have explicit t dependence, indicating $1-(2-\alpha)\omega = 0$, or

$$\omega = \frac{1}{2-\alpha}. \tag{2.47}$$

It is important to highlight that Eq. (2.47) establishes a direct connection between the growth exponent ω and the parameter-dependent exponent α. We now proceed by choosing a parameter range where $\alpha = 1$, resulting in $\omega = 1$ (and hence a dynamic exponent $z = 1/\omega = 1$), indicating ballistic transport, which is remarkably observed within the context of a diffusion equation (2.7), albeit a nonlinear one. By choosing $\mathcal{R}(0) = 2/\xi_0^2$ and $\mathcal{R}'(0) = 0$, we exactly obtain,

$$\mathcal{R}(\xi) = \frac{2}{\xi_0^2 + \xi^2}, \tag{2.48}$$

where we determine the constant ξ_0 by using the conservation condition $\int_{-\infty}^{\infty} \mathcal{R}(\xi)d\xi = \text{const.}$. Thus, the density relaxation exhibits anomalous space-time scaling characterized by a non-Gaussian spreading, which eventually transitions to Gaussian behavior (thus leading to normal diffusion with $z = 2$). In the simulation, we generate the delta-like initial profile by employing the step initial condition described in Eq. (2.43), with the assumption of a narrow width limit, i.e., $w/L \ll 1$. We consider the following parameters: $L = 1000$, $w = 20$, $\rho_0 = 0$, $\rho_1 = 1$, $\gamma = 0.05$. In Fig. 2.8, we depict the numerically obtained scaled density profile $Ct\rho(X,t)$ for model I (panel a) and II (panel b) plotted against the scaling variable X/Ct. We observe a quite good scaling collapse and reasonably good agreement with the theory (illustrated by the solid black line). Deviations at the tails occur due to the power-law behavior of $D(\rho,\gamma)$ being truncated at very low densities.

2.6 Summary and concluding remarks

This chapter investigates the relaxation of density in models of conventional hardcore run-and-tumble particles (RTPs) on a d-dimensional periodic lattice with volume L^d, for arbitrary density ρ and tumbling rate $\gamma = \tau_p^{-1}$. We focus on two minimalistic variants: The first

is the standard version, model I, which is similar to the one studied in Ref. [36]. The second is model II, which is characterized as a hardcore long-ranged lattice gas (LLG) and represents an analytically amenable variant of model I. It is important to note that the class of RTPs we examine here differ from those analyzed in Ref. [57], where dynamics is thermal diffusion dominated and the tumbling rate depends on system size L and diminishes in the thermodynamic limit $L \to \infty$. Consequently, in the latter case, the large-scale behavior of the system is precisely captured by mean-field hydrodynamics, derived by computing various averages using a product Bernoulli measure. In contrast, the models discussed in this work exhibit nontrivial spatial correlations, and the nonequilibrium steady-state measures are unknown.

Using models I and II, we propose that the collective diffusion observed in RTPs results from subtle many-body effects, stemming from a complex interplay between their interactions and persistence. We aim to characterize the relaxation of density in these systems by precisely determining the parameter (density and tumbling rate) dependent bulk diffusion coefficient. For this purpose, we rescale the original position $\mathbf{X}$ and time t as $\mathbf{x} = \mathbf{X}/L$ and $\tau = t/L^2$, respectively, and proceed to take the thermodynamic limit (where the system size L tends to infinity and the particle number N increases to infinity while maintaining a fixed global density N/L^d). Subsequently, we demonstrate that the coarse-grained density field $\rho(\mathbf{x}, \tau)$ adheres to a nonlinear diffusion equation $\partial_\tau \rho(\mathbf{x}, \tau) = \nabla[D(\rho, \gamma)\nabla\rho(\mathbf{x}, \tau)]$, where $D(\rho, \gamma)$ is the bulk-diffusion coefficient. We compute $D(\rho, \gamma)$, analytically for model II and through efficient Monte Carlo simulations for model I. Additionally, we validate our analytical findings for model II using simulations.

The presence of many-body correlation, caused by the competing effects of persistence and interaction, produces fascinating transport characteristics in hardcore RTPs. Indeed, we characterize their nontrivial interplay in terms of two relevant length scales in the system: the persistence length $l_p = 1/\gamma$ and the "mean free path" $\langle g \rangle = 1/\rho$, defined as the average gap size in the hopping direction. Moreover, in the regime of dilute gas and strong persistence, when both length scales are diverging with the ratio $\psi = l_p/\langle g \rangle = \rho/\gamma$ finite, there exists a scaling relation, $D(\rho, \gamma) = D^{(0)}\mathcal{F}(\rho/\gamma)$ as shown in Eq. (2.5). Additionally, for model II in one dimension, we derive the scaling function $\mathcal{F}(\psi)$ analytically, and it closely matches the results obtained from simulations.

We also observe that over a broad spectrum of parameter values, $D(\rho, \gamma)$ demonstrates a power-law decay with density, specifically $D \sim \rho^{-\alpha}$, where $0 < \alpha \leq 2$. This specific observation carries two significant implications. Firstly, this suggests that local structural relaxations are highly sensitive to local densities, with regions of lower density relaxing more rapidly than those of higher density. Consequently, a diverse range of time scales (distributed according to

a power law) emerges, giving rise to dynamic heterogeneity and anomalous transport within the systems. Secondly, there is no diffusive instability in the system. This particular observation is of crucial importance in the context of motility-induced phase separation (MIPS). Notably, the theory of MIPS relies on vanishing instability in the bulk-diffusion coefficient [see Sec. 1.2]. However, in our case with hardcore RTPs, we do not observe the same phenomenon. In fact, in the regime characterized by strong persistence and high density, where MIPS would typically occur, $D(\rho, \gamma)$ exhibits a smooth power-law decay $D \sim 1/\rho^2$ and does not vanish at all. In this situation, it would be intriguing to directly compute the bulk diffusion coefficient, as a function of density and activity (tumbling rate for RTPs), aiming to investigate whether other types of conventional self-propelled particles (SPPs) display any diffusive instability. We anticipate that our proposed mechanism involving density relaxations could offer valuable insights into collective transport within SPPs and could pave the way for exploring new research directions in the future.

3

Current fluctuations in athermal hardcore run-and-tumble particles

3.1 Introduction

As previously discussed in Sec. 1.4.1, for nonequilibrium diffusive systems, there is a theoretical framework of fluctuating hydrodynamics known as macroscopic fluctuation theory (MFT) [118]. According to this theory, the dynamic evolution of local density $\rho(x,\tau)$, defined on the appropriate coarse-grained level, is governed by the following equation:

$$\frac{\partial\rho(x,\tau)}{\partial\tau} = \frac{\partial}{\partial x}\left[D(\rho)\frac{\partial\rho}{\partial x} + \sqrt{\frac{2\chi(\rho)}{L}}\zeta_x(\tau)\right], \tag{3.1}$$

where $D(\rho)$ and $\chi(\rho)$ are the density- and other parameter-dependent macroscopic transport coefficients, the bulk-diffusion coefficient and mobility, respectively. Notably, L represents the system size, and $\zeta_x(\tau)$ is the uncorrelated Gaussian white noise with unit noise strength. The relaxation phenomena are governed by the bulk-diffusion coefficient $D(\rho)$, whereas fluctuations are encoded in the mobility $\chi(\rho)$. Therefore, in order to establish a framework for fluctuating hydrodynamics applicable to many-body systems, it is necessary to determine

This chapter is based on the paper "Time-dependent properties of run-and-tumble particles. II. Current fluctuations", Tanmoy Chakraborty and Punyabrata Pradhan, Phys. Rev. E **109**, 044135 (2024).

both $D(\rho)$ and $\chi(\rho)$. However, calculating them for systems with many-body correlations is difficult, particularly in scenarios where the system is in nonequilibrium condition and the steady-state measure is not known beforehand.

In the previous chapter, we investigated the relaxation of local density $\rho(x,\tau)$ by calculating the density and tumbling-rate dependent bulk-diffusion coefficient $D(\rho,\gamma)$ for a class of hardcore run-and-tumble particles (RTPs). In this chapter, we aim to characterize the other transport coefficient, the density- and tumbling-rate-dependent collective mobility $\chi(\rho,\gamma)$, which is directly related to the fluctuation of the space-time integrated current over the entire system [117], for the same class of RTPs. Thus, the determination of $\chi(\rho,\gamma)$ demands calculating the current fluctuations in hardcore RTPs for arbitrary density ρ and tumbling rate γ, which is the primary focus of this chapter. Another objective is to understand the spatial correlations of the current (suitably coarse-grained) or, equivalently, the "velocity" within such systems. In fact, investigation into velocity correlations in active matter has recently received a lot of attention in a variety of contexts, including phenomena like coarsening in the Vicsek model [140], ordering dynamics in active Brownian particles (ABPs) [141–144], and other active-matter systems [145–148].

Numerous analytical investigations have been conducted in the past on current fluctuations, particularly focusing on passive lattice gases, both using the framework of microscopic [149–153] as well as hydrodynamic calculations [117, 154, 155]. Nonetheless, their adaptation to interacting self-propelled particles (SPPs) remains an ongoing task. Indeed, unlike investigations into fluctuations in tagged particle displacement [42, 94, 99, 156], except for a few cases, the exploration of current fluctuations in conventional SPPs is considerably less extensive. Current fluctuations have been calculated exactly in noninteracting RTPs [157] and approximately for interacting ABPs [158]. In recent times, there have been efforts to characterize fluctuations through exact mean-field level calculations in Refs. [89, 159], on "weakly-interacting" run-and-tumble particles (RTPs) [57]. Notably, the dynamics of weakly interacting RTPs in Ref. [57] involves interaction-independent thermal diffusion occurring at a finite rate, while run-and-tumble events take place at system-size-dependent vanishingly small rates. Consequently, for large system sizes, the dynamics are dominated by thermal diffusion, allowing for the solution of fluctuations using mean-field hydrodynamics. However, the conventional RTPs are considered "strongly interacting," featuring long-range many-body correlations. In such cases, the approach to characterizing fluctuations through the mean-field framework outlined in Refs. [89, 159] is not applicable. Instead, a comprehensive microscopic framework that incorporates both interaction and persistence of conventional RTPs is essential.

In this chapter, we characterize the space-time correlation and fluctuations of current in

two conventional models of strongly interacting run-and-tumble particles (RTPs): Model I is a system of standard hardcore RTPs, while Model II is a hardcore long-ranged lattice gas that is an analytically tractable idealized variant of Model I [112]. Both models are defined in the previous chapter in Sec. 2.2. We proceed with numerical simulation for model I, while characterization for model II is done using microscopic calculations. Our microscopic theory is based on an approximation of current decomposition and a truncation scheme introduced in Ref. [114]. While the decomposition method decomposes the instantaneous current into diffusive (slow) and fluctuating (fast) components, the truncation method helps to avoid the otherwise involved infinite hierarchy of many-body correlations, allowing the calculation to be performed despite the presence of long-range correlation in model II. We microscopically demonstrate that large-scale fluctuations and correlations of current in both models can be characterized in terms of the density- and tumbling-rate-dependent macroscopic transport coefficients, the bulk-diffusion coefficient $D(\rho,\gamma)$ and the collective particle mobility $\chi(\rho,\gamma)$. We characterize the mobility through the fluctuation of the scaled space-time integrated current or the total current $Q_{tot}(L,T)$ in the system of size L and observation time T via the following relation: $\chi(\rho,\gamma) \equiv \lim_{L\to\infty}(1/2LT)\langle Q_{tot}^2\rangle$. Notably, similar to $D(\rho,\gamma)$, the nontrivial interplay between persistence and interaction corresponds to a scaling regime for $\chi(\rho,\gamma)$. In the regime of small density and strong persistence, the mobility $\chi(\rho,\gamma)$ satisfies a scaling relation, $\gamma^a\chi(\rho,\gamma)/\chi^{(0)} \equiv \mathcal{H}(\psi=\rho/\gamma)$. $\chi^{(0)}=\rho(1-\rho)$ is the mobility of symmetric simple exclusion process (SSEP) [117] and $a=1$ for model I, and 2 for model II. Our theory also allows for the characterization of the spatial correlation of the instantaneous current, which decays exponentially with separation distance, and the corresponding correlation length diverges as $\sqrt{l_p}\simeq 1/\sqrt{\gamma}$ in the strong persistence limit, thus providing a theoretical explanation of the findings in recent simulations and experiments [141, 147].

The chapter is structured as follows: In Sec. 3.2.1, we outline the method of decomposing the current into "slow" (diffusive) and "fast" (noise-like) components. Following that, in Sec. 3.2.2, we introduce a truncation technique enabling us to compute spatiotemporal correlations of time-integrated currents. Secs. 3.2.3 and 3.2.4 are dedicated to examining spatiotemporal correlations of instantaneous and fluctuating currents, respectively. Subsequently, in Sec. 3.2.5, we analyze the total current fluctuations, leading to the characterization of collective particle mobility $\chi(\rho,\gamma)$; within this discussion, we also explore a scaling law applicable in the regime of strong persistence and low density. Moving on to Sec. 3.2.6, we delve into characterizing bond-current fluctuations and uncover another scaling law applicable to the bond current; notably, we find that the scaling function remains consistent across both models. Finally, we encapsulate the chapter's findings in Sec. 3.3, offering some

concluding remarks.

3.2 Theory: Model II

Here, we introduce a microscopic dynamic framework to compute current fluctuations analytically for the long-ranged variant of run-and-tumble particles (RTPs), i.e., for model II. Additionally, we support the theoretical results with numerical simulations for both model I and model II.

3.2.1 Current decomposition into slow and fast components

To begin, we recall the cumulative (time-integrated) bond current $Q_i(T)$ introduced in the previous chapter, which represents the total current flowing through a bond $(i, i+1)$ over time-interval T. On the contrary, the instantaneous current $J_i(t)$ is defined as:

$$J_i(t) \equiv \lim_{\Delta t \to 0} \frac{\Delta Q_i}{\Delta t}, \tag{3.2}$$

where $\Delta Q_i = \int_t^{t+\Delta t} dt J_i(t)$ is cumulative bond current during the time-period Δt. Note that, in this chapter, we want to characterize the two-point space-time correlation and fluctuation properties of both the quantities $Q_i(t)$ and $J_i(t)$. However, before analyzing the second moment (fluctuations) of currents, it is necessary to characterize their first moments (averages), which, as derived in chapter 2, has been shown to possess the following *gradient* structure:

$$\langle J_i(t)\rangle = \frac{1}{2}\sum_{l=1}^{\infty}\phi(l)\left[\sum_{g=1}^{l-1}\left(\langle \mathcal{V}_{i+g+1}^{(g+2)}\rangle - \langle \mathcal{V}_{i+1}^{(g+2)}\rangle\right) + \left(\langle \mathcal{U}_{i+l}^{(l)}\rangle - \langle \mathcal{U}_{i}^{(l)}\rangle\right)\right], \tag{3.3}$$

where the multi-point correlators $\langle \mathcal{V}^{(g+2)}\rangle$ and $\langle \mathcal{U}_i^{(l)}\rangle$, defined in Eq. (2.12), can be connected to the gap-distribution function $P(g)$ as follows:

$$\langle \mathcal{V}^{(g+2)}\rangle = \rho P(g), \tag{3.4}$$

$$\langle \mathcal{U}^{(l)}\rangle = \rho \sum_{g=l}^{\infty}(g-l+1)P(g). \tag{3.5}$$

Now, by employing the assumption of a *local-equilibrium* like steady state achieved by the system at long time and further applying gradient expansions, the average current is explicitly expressed in terms of the discrete gradient of the local density [112],

$$\langle J_i(t)\rangle \simeq -D(\rho,\gamma)[\langle \eta_{i+1}(t)\rangle - \langle \eta_i(t)\rangle] \tag{3.6}$$

where $\rho_i(t) = \langle \eta_i(t) \rangle$ is the local density and the density and tumbling-rate dependent bulk-diffusion coefficient $D(\rho, \gamma)$ is given by [112]

$$D(\rho,\gamma) \;=\; -\frac{1}{2}\frac{\partial}{\partial\rho}\left[\rho\sum_{l=1}^{\infty}\phi(l)\left(\sum_{g=1}^{l-1} gP(g) + l\sum_{g=l-1}^{\infty}(g-l+1)P(g)\right)\right]. \tag{3.7}$$

Since the system is homogeneous in the steady state, the gradients in Eq. (3.3) vanish, indicating the steady-state average current to be *zero*. However, at the level of fluctuations, the (stochastic) instantaneous current remains *nonzero* even in the steady state. Therefore, to appropriately characterize these fluctuations [117,118], we decompose the total instantaneous current into two parts: a (hydrodynamic) diffusive current $J_i^{(D)}$, despite being stochastic, relaxes very slowly, and a fluctuating or noise current $J_i^{(fl)}$ which relaxes very rapidly. In other words, we express the instantaneous current as the sum of these slow and fast components,

$$J_i(t) = J_i^{(D)}(t) + J_i^{(fl)}(t), \tag{3.8}$$

where we identify, by using Eq. (3.3), the stochastic diffusive current

$$J_i^{(D)} \equiv \frac{1}{2}\sum_{l=1}^{\infty}\phi(l)\left[\sum_{g=1}^{l-1}\left(\mathcal{V}_{i+g+1}^{(g+2)} - \mathcal{V}_{i+1}^{(g+2)}\right) + \left(\mathcal{U}_{i+l}^{(l)} - \mathcal{U}_{i}^{(l)}\right)\right]. \tag{3.9}$$

Indeed, as we derive later [see Eqs. (3.53) and (3.60)], the time-dependent correlation function for the diffusive current $J_i^{(D)}$ (as well as the total current J_i) exhibits a power-law tail, while the correlation function for the fluctuating (noise) current $J_i^{(fl)}$ is delta-correlated. Additionally, upon comparing Eqs. (3.3), (3.8), and (3.9), we observe that the average fluctuating current is simply zero,

$$\langle J_i^{fl}(t) \rangle = 0. \tag{3.10}$$

However, the space-time correlations of J_i^{fl} have nontrivial spatial structures [see Eq. (3.60)] and, in the subsequent section, they are analytically calculated by using a truncation scheme, which we discuss next.

3.2.2 Spatio-temporal correlations of current

We consider the time-integrated currents $Q_r(t')$ and $Q_0(t)$, which are measured up to times t' and t ($t' > t$) across bonds $(r, r+1)$ and $(0, 1)$, respectively, where the bonds are spatially separated by a distance r. In this section, we calculate the two-point unequal space and

unequal time correlation function $\mathcal{C}_r^{QQ}(t',t)$, which is expressed as:

$$\begin{aligned}\mathcal{C}_r^{QQ}(t',t) &= \langle Q_r(t')Q_0(t)\rangle_c\,,\\ &= \langle Q_r(t')Q_0(t)\rangle - \langle Q_r(t')\rangle\langle Q_0(t)\rangle\,.\end{aligned} \tag{3.11}$$

It is quite evident that, in the regime of $t' > t$, within an infinitesimal time period $[t', t'+dt']$, $Q_0(t)$ remains constant, and any variation in $\mathcal{C}_r^{QQ}(t',t)$ derives only from the change in $Q_r(t')$. Now, using the infinitesimal update rules in Eq. (2.10), the time-evolution equation for $\mathcal{C}_r^{QQ}(t',t)$ as follows (see Appendix B.1 for details):

$$\frac{d}{dt'}\mathcal{C}_r^{QQ}(t',t) = \frac{1}{2}\sum_{l=1}^{\infty}\phi(l)\Big[\Big\{\mathcal{C}_{r+l}^{\mathcal{U}^{(l)}Q}(t',t) - \mathcal{C}_r^{\mathcal{U}^{(l)}Q}(t',t)\Big\} + \sum_{g=1}^{l-1}\Big\{\mathcal{C}_{r+g+1}^{\mathcal{V}^{(g+2)}Q}(t',t) - \mathcal{C}_{r+1}^{\mathcal{V}^{(g+2)}Q}(t',t)\Big\}\Big]. \tag{3.12}$$

In other words, we obtain the following identity,

$$\frac{d}{dt'}\mathcal{C}_r^{QQ}(t',t) = \left\langle J_r^{(D)}(t')Q_0(t)\right\rangle_c, \tag{3.13}$$

where $J_r^{(D)}$ is the stochastic diffusive current across the rth bond at time t, as defined in Eq. (3.9). Note that Eq. (3.12) governing the two-point current correlation is exact and has been expressed in terms of the gradients of two nontrivial multi-point correlation functions,

$$\mathcal{C}_r^{\mathcal{U}^{(l)}Q}(t',t) = \langle \mathcal{U}_r^{(l)}(t')Q_0(t)\rangle_c, \tag{3.14}$$

$$\mathcal{C}_r^{\mathcal{V}^{(g+2)}Q}(t',t) = \langle \mathcal{V}_r^{(g+2)}(t')Q_0(t)\rangle_c. \tag{3.15}$$

Hence, to compute the two-point correlation $\mathcal{C}_r^{QQ}(t',t)$ as outlined in Eq. (3.12), one needs to evaluate the associated multi-point correlators, $\mathcal{C}_r^{\mathcal{U}^{(l)}Q}(t',t)$ and $\mathcal{C}_r^{\mathcal{V}^{(g+2)}Q}(t',t)$. Not surprisingly, the hierarchy involving the time evolution of these correlation functions does not close, posing significant challenges for exact calculations.

To overcome the aforementioned challenge, we introduce a truncation scheme that, while approximate, enables the closure of the mentioned hierarchy. This approach allows us to express the time evolution of two-point current correlations in a form involving only current and density correlations, which, interestingly, are close to themselves. Indeed, when the fluctuations of local density around the steady state are small, on a long time scale the variables $\mathcal{V}^{(g+2)}$ and $\mathcal{U}^{(l)}$ at a particular time, appearing in Eq. (3.9), are "slave" to the local density and, as a result, the diffusive current could be approximately written in the form of

a "microscopic" version of the Fick's law [153], which is evident from Eq. (3.6),

$$J_r^{(D)}(t') \simeq D(\rho,\gamma)[\eta_r(t') - \eta_{r+1}(t')], \tag{3.16}$$

where we have simply used $D[\rho_r(t),\gamma] \simeq D(\rho,\gamma)$; the symbol "$\simeq$" in Eq. (3.16) should rather be interpreted as an "equivalence", not an "equality", between the random variables there, unless one takes explicit averages. This straightforwardly implies that we can express the correlation function for the stochastic diffusive current $J_r^{(D)}(t')$ and any other stochastic variable $B(t)$ directly in terms of the correlation between the local density and the variable B,

$$\left\langle J_r^{(D)}(t')B(t)\right\rangle_c \simeq -D(\rho,\gamma)\Delta_r \left\langle \eta_r(t')B(t)\right\rangle_c, \tag{3.17}$$

where $\Delta_r h_r = h_{r+1} - h_r$ is the forward difference operator. Following the above truncation scheme Eq. (3.17), the time evolution of the current correlations in Eq. (3.13) greatly simplifies as the gradient of two-point density-current correlation function $\mathcal{C}_r^{\eta Q}(t',t) = \langle \eta_r(t')Q_0(t)\rangle_c$, which, as shown below, immediately closes the hierarchy. We thus rewrite Eq. (3.13) as

$$\frac{d}{dt'}\mathcal{C}_r^{QQ}(t',t) \simeq -D(\rho,\gamma)\Delta_r \mathcal{C}_r^{\eta Q}(t',t), \tag{3.18}$$

whereas the time-evolution of the density-current correlation $\mathcal{C}_r^{\eta Q}(t',t)$ can be written as [for details see Appendix B.2],

$$\frac{d}{dt'}\mathcal{C}_r^{\eta Q}(t',t) = D(\rho,\gamma)\Delta_r^2 \mathcal{C}_r^{\eta Q}(t',t). \tag{3.19}$$

Surprisingly, the SSEP, despite having a product-measure steady state and density-independent bulk-diffusion coefficient [153], exhibits a similar structure in density and current correlations to the LLG, which have nonzero spatial correlations, albeit. To further simplify the time-evolution equations governing two-point correlations, we represent the correlation functions in Fourier space using the following transformation:

$$\tilde{\mathcal{C}}_{q_n}^{AB}(t',t) = \sum_{r=0}^{L-1} \mathcal{C}_r^{AB}(t',t)e^{iq_n r}. \tag{3.20}$$

The inverse Fourier transform is given by

$$\mathcal{C}_r^{AB}(t',t) = \frac{1}{L}\sum_n \tilde{\mathcal{C}}_{q_n}^{AB}(t',t)e^{-iq_n r}, \tag{3.21}$$

where

$$q_n = \frac{2\pi n}{L}, \tag{3.22}$$

and $n = 0, 1, 2, \ldots, (L-1)$. Using Eq. (3.21), we now rewrite Eqs. (3.18) and (3.19) in terms of the time evolution of the respective Fourier modes,

$$\frac{d}{dt'}\tilde{\mathcal{C}}_q^{QQ}(t', t) = D(\rho, \gamma)\left(1 - e^{-iq}\right)\tilde{\mathcal{C}}_q^{QQ}(t', t), \tag{3.23}$$

and

$$\frac{d}{dt'}\tilde{\mathcal{C}}_q^{\eta Q}(t', t) = -D(\rho, \gamma)\lambda_q \tilde{\mathcal{C}}_q^{\eta Q}(t', t), \tag{3.24}$$

where λ_q is given by

$$\lambda_q = 2\left(1 - \cos q\right). \tag{3.25}$$

By integrating Eqs. (3.23) and (3.24), we express the unequal-time correlation functions in the following forms,

$$\tilde{\mathcal{C}}_q^{QQ}(t', t) = D(\rho, \gamma)\int_t^{t'} dt''\left(1 - e^{-iq}\right)\tilde{\mathcal{C}}_q^{\eta Q}(t'', t) + \tilde{\mathcal{C}}_q^{QQ}(t, t), \tag{3.26}$$

$$\tilde{\mathcal{C}}_q^{\eta Q}(t'', t) = e^{-\lambda_q D(\rho,\gamma)(t''-t)}\tilde{\mathcal{C}}_q^{\eta Q}(t, t), \tag{3.27}$$

where $t'' \geq t$. It is now clear that, in order to evaluate the unequal-time correlation functions, $\mathcal{C}_r^{QQ}(t', t)$ and $\mathcal{C}_r^{\eta Q}(t', t)$, one must first calculate their equal-time counterparts, which we do next.

Equal-time density-current correlation $\tilde{\mathcal{C}}_q^{\eta Q}(t, t)$

In this section, we calculate the equal-time density-current correlation function $\tilde{\mathcal{C}}_q^{\eta Q}(t, t)$, which is crucial in calculating $\tilde{\mathcal{C}}_q^{QQ}$. To this end, we begin with the microscopic dynamical rules and obtain the time-evolution of $\mathcal{C}_r^{\eta Q}(t, t)$, which, in terms of the Fourier modes, satisfies the following equation [see Appendix B.3 for details],

$$\left(\frac{d}{dt} + D(\rho, \gamma)\lambda_q\right)\tilde{\mathcal{C}}_q^{\eta Q}(t, t) = \tilde{\mathcal{S}}_q^{\eta Q}(t). \tag{3.28}$$

Here the source term $\tilde{\mathcal{S}}_q^{\eta Q}(t)$ is given by

$$\tilde{\mathcal{S}}_q^{\eta Q}(t) \;=\; \frac{1}{(1-e^{-iq})}\left[D(\rho,\gamma)\lambda_q\tilde{\mathcal{C}}_q^{\eta\eta}(t,t) - f_q(t)\right], \tag{3.29}$$

where $f_q(t)$ is directly related to the gap-distribution $P(g,t)$ of the system and is given by

$$f_q(t) = \rho\sum_{l=1}^{\infty}\phi(l)\left[\sum_{g=1}^{l-1}\lambda_{gq}P(g,t) + \lambda_{lq}\sum_{g=l}^{\infty}P(g,t)\right]. \tag{3.30}$$

We can now solve for $\tilde{\mathcal{C}}_q^{\eta Q}(t,t)$ by integrating Eq. (3.28) and the solution is given by

$$\tilde{\mathcal{C}}_q^{\eta Q}(t,t) = \int_0^t dt''' e^{-\lambda_q D(\rho,\gamma)(t-t''')}\tilde{\mathcal{S}}_q^{\eta Q}(t'''), \tag{3.31}$$

which, upon substitution in Eq. (3.27), leads to the unequal-time density-current correlation function,

$$\tilde{\mathcal{C}}_q^{\eta Q}(t'',t) = \int_0^t dt''' e^{-\lambda_q D(\rho,\gamma)(t''-t''')}\tilde{\mathcal{S}}_q^{\eta Q}(t'''). \tag{3.32}$$

In the above analysis, it is important to note that $\tilde{\mathcal{S}}_q^{\eta Q}(t)$, and consequently $\tilde{\mathcal{C}}_q^{\eta Q}(t,t)$ and $\tilde{\mathcal{C}}_q^{\eta Q}(t'',t)$, depend on the equal-time density-density correlation function $\tilde{\mathcal{C}}_q^{\eta\eta}(t,t)$, which is the sole unknown quantity at this stage and requires determination. To achieve this, we first derive the time-evolution equation for the correlation function $\mathcal{C}_r^{\eta\eta}(t,t) = \langle\eta_r(t)\eta_0(t)\rangle_c$ in real space; see Appendix B.4 for details. Finally, we use the Fourier transform of Eq. (3.20) to derive the following time-evolution equation for the Fourier modes $\tilde{\mathcal{C}}_q^{\eta\eta}(t,t)$,

$$\left(\frac{d}{dt} + 2D(\rho,\gamma)\lambda_q\right)\tilde{\mathcal{C}}_q^{\eta\eta}(t,t) = \tilde{\mathcal{S}}_q^{\eta\eta}(t), \tag{3.33}$$

where the source term $\tilde{\mathcal{S}}_q^{\eta\eta}(t) = f_q(t)$. Eq. (3.33) can now be solved to obtain the time-dependent solution of $\tilde{\mathcal{C}}_q^{\eta\eta}(t,t)$. However, as we are interested in evaluating the dynamic density-density correlation function in the steady state, we simply remove its time dependence and set $d\tilde{\mathcal{C}}_q^{\eta\eta}(t,t)/dt = 0$. As a result, we have from Eq. (3.33),

$$2D(\rho,\gamma)\lambda_q\tilde{\mathcal{C}}_q^{\eta\eta} = \tilde{\mathcal{S}}_q^{\eta\eta} = f_q. \tag{3.34}$$

The above Eq. (3.34) provides the solution for the static density-density correlation function and f_q is then obtained by replacing $P(g,t)$ by its steady-state value $P(g)$ in Eq. (3.30). Upon

substituting the static $\tilde{\mathcal{C}}_q^{\eta\eta}$ in Eq. (3.29), the source term $\tilde{\mathcal{S}}_q^{\eta Q}$ also becomes time-independent and thus the solution is given by

$$\tilde{\mathcal{S}}_q^{\eta Q} = -\frac{f_q}{2(1-e^{-iq})}. \tag{3.35}$$

Using this particular form of $\tilde{\mathcal{S}}_q^{\eta Q}$ in Eq. (3.32), we finally obtain the equal- as well as unequal-time density-current correlation function $\tilde{\mathcal{C}}_q^{\eta Q}$ in the steady state,

$$\tilde{\mathcal{C}}_q^{\eta Q}(t,t) = \frac{-f_q}{2D(\rho,\gamma)\lambda_q(1-e^{-iq})}\left(1-e^{-\lambda_q D(\rho,\gamma)t}\right), \tag{3.36}$$

$$\tilde{\mathcal{C}}_q^{\eta Q}(t'',t) = \frac{-f_q e^{-\lambda_q D(\rho,\gamma)t''}}{2D(\rho,\gamma)\lambda_q(1-e^{-iq})}\left(e^{\lambda_q D(\rho,\gamma)t}-1\right), \tag{3.37}$$

where $t'' \geq t$. It is worth noting that by inserting Eq. (3.37) into Eq. (3.26), one can immediately derive the first term of the unequal-time current-current correlation function $\tilde{\mathcal{C}}_q^{QQ}(t'',t)$. In the subsequent section, our focus shifts to another equal-time correlation function $\mathcal{C}^{QQ}r(t,t)$, a crucial quantity in the calculation of the two-point space-time correlation function $\mathcal{C}_r^{QQ}(t',t)$.

Equal-time current-current correlation $\mathcal{C}_r^{QQ}(t,t)$

In order to compute the equal-time current-current correlation $\mathcal{C}_r^{QQ}(t,t)$, we begin by deriving its time-evolution equation. Upon employing the closure scheme, as outlined in Eq. (3.16), the resulting solution for $\mathcal{C}_r^{QQ}(t,t)$ takes on a closed-form expression given by:

$$\mathcal{C}_r^{QQ}(t,t) = \frac{D}{L}\sum_q \left(1-e^{-iq}\right)(2-\lambda_{qr})\int_0^t \tilde{\mathcal{C}}_q^{\eta Q}(t,t)dt + \Gamma_r t. \tag{3.38}$$

On the right-hand side of the above equation, the first term involving $\tilde{\mathcal{C}}_q^{\eta Q}(t,t)$ is easily derived from Eq. (3.36). While for the second term, Γ_r can be expressed in terms of the gap distribution as shown below:

$$\Gamma_r = \rho\sum_{l=|r|+1}^{\infty}\phi(l)\left[(l-\mid r\mid)\sum_{g=l}^{\infty}P(g) + \sum_{g=|r|}^{l-1}(g-\mid r\mid)P(g)\right]; \tag{3.39}$$

see Appendix B.5 for calculation details. The quantity Γ_r represents the strength of the "noise current" and is shown to be realted to the two-point space-time correlation of the fluctuating current, expressed as $\langle J_r^{(fl)}(t)J_0^{(fl)}(0)\rangle = \Gamma_r\delta(t)$ (see Eq. (3.60)). Later we also show that the

steady-state fluctuation of the space-time integrated current $Q_{tot}(L,T) = \int_0^T dt \sum_{i=0}^{L-1} J_i^{(fl)}(t)$ [see Eq. (3.67)] satisfies, in the thermodynamic limit, a fluctuation relation,

$$2\chi(\rho,\gamma) \equiv \lim_{L\to\infty} \frac{1}{LT}\langle Q_{tot}^2(L,T)\rangle = \sum_r \Gamma_r, \tag{3.40}$$

where the particle mobility $\chi(\rho,\gamma)$ has the following expression,

$$\chi(\rho,\gamma) = \frac{\rho}{2}\sum_{l=1}^{\infty}\phi(l)\left[\sum_{g=1}^{l-1} g^2 P(g) + l^2\sum_{g=l}^{\infty} P(g)\right]. \tag{3.41}$$

The mobility can be written explicitly as a function of density and tumbling rate, provided that the gap distribution $P(g)$ is known (see the $\rho,\gamma\to 0$ limit and the corresponding scaling regime, discussed later in Sec. 3.2.5). Note that the sum rule, as in Eq. (3.40), states that the scaled space-time integrated current fluctuation is equal to the spatially integrated correlation function for fluctuating current and can be directly tested in simulations [see Fig. (3.3)].

We now perform inverse Fourier transform of Eq. (3.26) and finally obtain the desired solution for the steady-state unequal-time two-point current-current correlation function $\mathcal{C}_r^{QQ}(t',t)$ in real space,

$$\mathcal{C}_r^{QQ}(t',t) = -\frac{1}{2LD}\sum_q \frac{f_q}{\lambda_q^2}\left(e^{-\lambda_q Dt} - e^{-\lambda_q Dt'}\right)\left(e^{-\lambda_q Dt}-1\right)e^{-iqr} - \frac{1}{2L}\sum_q \frac{f_q}{\lambda_q}\left\{t - \frac{\left(1-e^{-\lambda_q Dt}\right)}{\lambda_q D}\right\} \times(2-\lambda_{qr}) + \Gamma_r t. \tag{3.42}$$

Now onwards, to keep the notations simple, we drop the argument of $D(\rho,\gamma)$ in Eq. (3.42) and elsewhere.

3.2.3 Spatio-temporal correlation of the instantaneous current

In this section, we compute the two-point unequal-time correlation function of the instantaneous current, denoted as $\mathcal{C}_r^{JJ}(t',t)$, in the steady state. This is achieved by taking the derivative of the steady-state integrated current correlation function $\mathcal{C}_r^{QQ}(t',t)$ with respect to the times t' and t. However, the expression for $\mathcal{C}_r^{QQ}(t',t)$ given in Eq. (3.42) is only valid for $t' \geq t$. Therefore, to obtain $\mathcal{C}_r^{JJ}(t',t)$ for arbitrary t' and t, the appropriate formula is derived by incorporating the Heaviside-Theta function $\Theta(t)$,

$$\mathcal{C}_r^{JJ}(t,t') = \frac{d}{dt}\frac{d}{dt'}\left[\mathcal{C}_r^{QQ}(t',t)\Theta(t'-t) + \mathcal{C}_r^{QQ}(t,t')\Theta(t-t')\right], \tag{3.43}$$

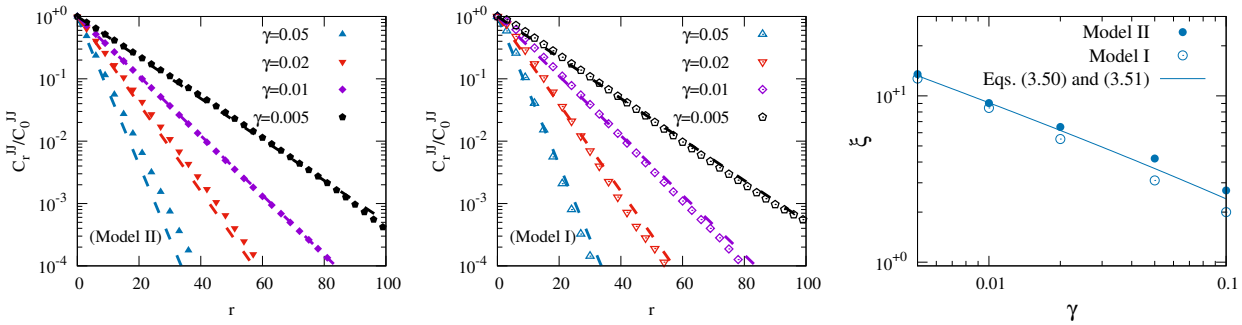

Figure 3.1: *Verification of Eqs.* (3.49), (3.50) *and* (3.51)- We plot the scaled equal-time spatial correlation $\mathcal{C}_r^{JJ}/\mathcal{C}_0^{JJ}$ for models II (LLG, left panel) and I (standard RTPs, middle panel), extracted from simulations (data points), as a function of spatial separation r with a fixed $\rho = 0.5$, and varying γ values: 0.05 (upper triangle), 0.02 (lower triangle), and 0.01 (diamond). Additionally, we compare the simulation results from both models with the analytical solution for strong persistence (dotted line), as provided by Eqs. (3.49), (3.50), and (3.51). In the rightmost panel, we illustrate the correlation length ξ against γ at $\rho = 0.5$ for models II (LLG, solid points) and I (RTPs, open points), and contrast them with the analytical solution for strong persistence (line), as given by Equations (3.50) and (3.51).

where $\mathcal{C}_r^{QQ}(t,t')$ is obtained directly from Eq. (3.42) by interchanging t' and t. Using Eq. (3.43), we straightforwardly compute $\mathcal{C}_r^{JJ}(t',t)$. After doing some algebraic manipulations and setting $t' = 0$, we eventually arrive at the following expression,

$$\mathcal{C}_r^{JJ}(t,t') = \Gamma_r \delta(t-t') - \frac{D}{4L}\sum_q (2-\lambda_{qr})\, f_q e^{-\lambda_q D|t-t'|}\Big\{\Theta(t-t') + \Theta(t'-t)\Big\}. \tag{3.44}$$

where f_q is obtained by substituting the steady-state gap-distribution $P(g)$ in Eq. (3.30). Evidently, $\mathcal{C}_r^{JJ}(t,t')$ can be decomposed into two components. The initial part consists of a space-dependent prefactor that is delta-correlated in time, representing the equal-time two-point correlation determined by the fluctuating current correlations Γ_r. The second part encompasses correlations at unequal space and time points. In the subsequent analysis, we investigate the contribution of each of these terms.

Equal-time unequal-space correlation

To obtain the equal-time spatial correlations of the instantaneous current, we consider the case in Eq. (3.44) with $t = t' = 0$, yielding the leading order contribution,

$$\mathcal{C}_r^{JJ} \simeq \left(\frac{\mathcal{C}_0^{JJ}}{\Gamma_0}\right)\Gamma_r, \tag{3.45}$$

Notably, the spatial correlation function $\mathcal{C}_r^{JJ}$ is governed by Γ_r,which, as indicated in Eq. (3.39), depends entirely on the steady-state gap distribution function $P(g)$. As a result,

it is not surprising that the spatial correlations of the current are governed by the statistics of the gap-size, and one would expect the correlation length to be determined by the typical gap size in the system. However, obtaining an explicit expression for $P(g)$ as a function of ρ and γ is a challenging task. We can still proceed with the following generic asymptotic analysis: for larger gap size, we expect $P(g)$ to be an exponential function (which can be shown to be indeed the case for $\gamma \ll 1$ [139]),

$$P(g) \simeq N_* \exp(-g/g_*), \tag{3.46}$$

where g_* is the typcal gap size. Now, using the conservation relation $\langle g \rangle = \sum_{g=1}^{\infty} gP(g) = 1/\rho - 1$, one can immediately obtain the prefactor

$$N_* \simeq \left(\frac{1}{\rho} - 1\right) \frac{(e^{1/g_*} - 1)^2}{e^{1/g_*}}. \tag{3.47}$$

Upon substituting the above expression of $P(g)$ into Eq. (3.39), we obtain the following simplified expression

$$\Gamma_r \simeq (1-\rho) \frac{(e^{1/g_*} - 1)}{(e^{(\gamma + 1/g_*)} - 1)} e^{-r/\xi} = \Gamma_0 e^{-r/\xi}, \tag{3.48}$$

which immediately leads to the spation correlation function of current,

$$\mathcal{C}_r^{JJ} = \mathcal{C}_0^{JJ} e^{-r/\xi}, \tag{3.49}$$

where the correlation length ξ is given by

$$\xi = \frac{1}{\gamma + g_*^{-1}}. \tag{3.50}$$

Eqs. (3.48) and (3.50) indicate that the typical gap size g_* significantly influences the determination of Γ_r and ξ. While it is relatively straightforward to numerically obtain g_*, calculating its exact analytical form for arbitrary parameter regimes is a nontrivial task. Nevertheless, in the limit of strong persistence, where $l_p = \gamma^{-1} \to \infty$, there exists an analytical expression for the typical gap size [139],

$$g_* \simeq \sqrt{\frac{1-\rho}{\gamma\rho}}, \tag{3.51}$$

which leads to the explicit solution of Γ_r and hence the correlation function C_r^{JJ}. Importantly, in the particular regime of strong persistence, the correlation length ξ is predominantly

influenced by g_* alone. This directly leads to the conclusion that $\xi \sim 1/\sqrt{\gamma} = \sqrt{\tau_p}$. In other words, the correlation length ξ diverges with the square root of the persistence time τ_p, offering a straightforward theoretical explanation for recent observations in simulations and experiments [141, 147].

To validate the theoretical predictions expressed in Eqs. (3.49), (3.50), and (3.51), we numerically compute, for enhanced statistical accuracy, the correlation function $C^{\bar{J}\bar{J}}(r) = \lim_{t\to\infty}\langle \bar{J}_0(t)\bar{J}_r(t)\rangle$. Here, the coarse-grained current is defined as $\bar{J}_i(t) = (1/\Delta t)\int_t^{t+\Delta t} dt J_i(t)$, and the averaging is carried out over a reasonably small time window $(t, t+\Delta t)$. The correlation function is then evaluated at two spatial points separated by a distance r. In Fig. (3.1), we plot the scaled correlation function $\mathcal{C}_r^{JJ}/\mathcal{C}_0^{JJ}$ for models II (LLG, represented by closed points; left panel) and I (standard RTPs, depicted by open points; middle panel). The data is obtained from Monte Carlo simulations conducted at various tumbling rates $\gamma = 0.05$ (upper triangle), 0.02 (lower triangle), 0.01 (diamond), and 0.005 (pentagon), while maintaining a constant density of $\rho = 0.5$. We also compare the simulation data with the strong-persistence analytical solution (dotted lines), obtained using Eqs. (3.49), (3.50) and (3.51). We observe a notable agreement between simulations and analytical results, particularly in the regime of small γ. Finally, in the right panel of Fig. (3.1), we present the numerically determined correlation length ξ as a function of γ for models II (LLG, represented by closed points) and I (standard RTPs, depicted by open points) at a constant density $\rho = 0.5$. Additionally, we compare these results with the analytical solution for the strong-persistence scenario, obtained using Eqs. (3.50) and (3.51). In both cases - models I and II, we find in simulations that the correlation functions decay exponentially, $C^{\bar{J}\bar{J}}(r) \sim \exp(-r/\xi)$ and agree reasonably well with the analytical results. Notably, at small γ, the correlation lengths for models I and II asymptotically converge to each other as implied by our theory Eqs. (3.49), (3.50) and (3.51).

Equal-space unequal-time correlation function

We now proceed to evaluate the steady-state dynamic two-point correlation function for the instantaneous current. To this end, we set $r = 0$ and investigate the case $t' = 0$ and $t > 0$ in Eq. (3.44) and derive the following expression,

$$\mathcal{C}_0^{JJ}(t, 0) = -\frac{D}{2L}\sum_q f_q(t)e^{-\lambda_q Dt}. \tag{3.52}$$

It is interesting note that the order of applying large space and large time limits in Eq. (3.52) does not commute. In particular, when we initially take the large time limit, i.e., $t \to \infty$, followed by the large space limit, i.e., $L \to \infty$, we immediately obtain vanishing temporal

correlation $\mathcal{C}_0^{JJ}(t,0)$. On the contrary, in the opposite scenario, where we initiate by taking the limit $L \to \infty$ and then proceed to the limit $t \to \infty$ (specifically, when $L^2/D \gg t \gg 1/D$), we observe the system to develop long-ranged temporal correlation $\mathcal{C}_0^{JJ}(t,0)$, which we elaborate on in the subsequent analysis. Notably, in this temporal range, $\mathcal{C}_0^{JJ}(t,0)$ as described in Eq. (3.52) is primarily governed by the relaxations of small-q Fourier modes. Therefore, to elucidate the behavior for large values of t, a small q analysis can be employed by implementing the transformations $\lambda_q \to q^2$ and $f_q \to \chi(\rho,\gamma)q^2$. Furthermore, for significantly large values of $L \gg 1$, the summation can be converted into an integral, resulting in the expression:

$$\mathcal{C}_0^{JJ}(t) \simeq -\frac{\chi(\rho,\gamma)}{4\sqrt{\pi D(\rho,\gamma)}} t^{-3/2}; \tag{3.53}$$

see Appendix B.6 for calculation details. The correlation function $\mathcal{C}_0^{JJ}(t,0)$ indicates a negative correlation for $t > 0$, with a delta function at $t = 0$ and a power-law decay. Interestingly, with proper rearrangements of Eq. (3.53), one readily obtains the following scaling relationship:

$$\frac{1}{\chi D}\mathcal{C}_0^{JJ}(t) = -\frac{1}{4\sqrt{\pi}}(Dt)^{-3/2}, \tag{3.54}$$

where $\chi \equiv \chi(\rho,\gamma)$ and $D \equiv D(\rho,\gamma)$ are the density- and tumbling-rate-dependent collective mobility, defined in Eq. (3.41), and the bulk-diffusion coefficient, as in Eq. (3.7), respectively. Interestingly, in a somewhat different context, similar power-law scaling was observed in the dynamic fluctuations of the "force" acting on a "passive" tracer within a hardcore RTP bath, as demonstrated in Ref. [95].

To verify the scaling relationship presented in Eq. (3.54), the initial step involves computing the parameter-dependent transport coefficients $D(\rho,\gamma)$ and $\chi(\rho,\gamma)$ for models I and II. We determine $D(\rho,\gamma)$ and $\chi(\rho,\gamma)$ for model II (LLG) by numerically evaluating $P(g)$ in the steady state and applying it in Eqs. (3.7) and (3.41), respectively. In contrast, for model I (standard RTPs), analytical expressions for the transport coefficients are unavailable, which forces us to rely on direct simulations. For the computation of $D(\rho,\gamma)$ in model I, we investigate the relaxation of long-wavelength perturbations using the approach provided in our earlier work [112]. To numerically determine the mobility $\chi(\rho,\gamma)$, we evaluate the scaled space-time integrated current fluctuation, as specified in Eq. (3.67). We validate the scaling relationship in Eq.(3.54) by plotting the ratio $-\mathcal{C}_0^{JJ}(t)/\chi D$ (extracted from simulations) in Fig. (3.2), against the scaling variable Dt, for model II (solid points) and model I (empty

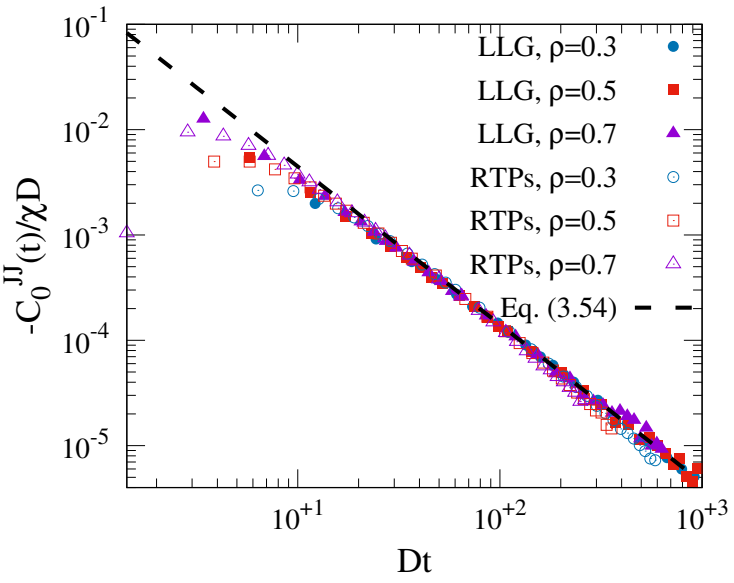

Figure 3.2: *Verification of Eq.* (3.54)- The negative scaled temporal (equal-space) correlations $-\mathcal{C}_0^{JJ}(t)/\chi D$, obtained from simulations, are plotted against Dt for models II (LLG, closed symbols) and I (standard RTPs, open symbols). To this end, we consider a constant $\gamma = 0.1$ and various densities $\rho = 0.3$ (blue circle), 0.5 (red square) and 0.7 (magenta triangle). The numerical data points are also compared with the corresponding theory (black dotted line) as shown in Eq. (3.54).

points) across various densities $\rho = 0.3$ (circle), 0.5 (square), and 0.7 (triangle) at a constant tumbling rate $\gamma = 0.1$. Additionally, we compare the simulation results (points) with the analytical solution provided in Eq. (3.54). The excellent agreement between our theory and simulation data at large time scales immediately verifies Eq. (3.54).

3.2.4 Space-time correlations of fluctuating ("noise") current

In this section, we are directed towards the calculation of the two-point spatiotemporal correlation for the fluctuating current $J^{fl}(t)$ in the steady state. Put differently, our goal is to establish the expression for $\mathcal{C}_r^{J^{fl}J^{fl}}(t,0)$ where $t \geq 0$. Employing the current decomposition given in Eq. (3.8), we can express the following relation,

$$\mathcal{C}_r^{J^{fl}J^{fl}}(t,0) = \mathcal{C}_r^{JJ}(t,0) - \mathcal{C}_r^{J^D J}(t,0) - \mathcal{C}_r^{J^{fl}J^D}(t,0). \tag{3.55}$$

Notably, there is no correlation between the fluctuation current $J_r^{fl}(t)$ at time t and the diffusive current $J_0^D(0)$, which occured at a preceding time, i.e.,

$$\mathcal{C}_r^{J^{fl}J^D}(t,0) = \langle J_r^{fl}(t) J_0^D(0) \rangle = 0. \tag{3.56}$$

Subsequently, the third term in Eq. (3.55) is dropped out. Furthermore, to compute the second term $\mathcal{C}_r^{J^D J}(t,0)$, we employ the following relation:

$$\mathcal{C}_r^{J^D J}(t,0) = \left[\frac{d}{dt'}\mathcal{C}_r^{J^D Q}(t,t')\right]_{t'=0}, \tag{3.57}$$

$$\simeq D\frac{d}{dt'}\left[\mathcal{C}_r^{\eta Q}(t,t') - \mathcal{C}_{r+1}^{\eta Q}(t,t')\right]_{t'=0}, \tag{3.58}$$

where we have used the truncation approximation as in Eq. (3.16), to arrive at Eq. (3.58) by using Eq. (3.57). Following Eq. (3.20), we now expand the correlators $\mathcal{C}_r^{\eta Q}(t,t')$ in the Fourier basis, and then using Eq. (3.37), we obtain the desired solution,

$$\mathcal{C}_r^{J^D J}(t,0) = -\frac{D}{4L}\sum_q (2-\lambda_{qr}) f_q(t) e^{-\lambda_q D t}. \tag{3.59}$$

Notably, the above solution aligns with the two-point unequal-time correlation of $\mathcal{C}_r^{JJ}(t,0)$, as shown in the second term of Eq. (3.44) for $t \geq t' = 0$. Finally, using Eqs. (3.44), (3.56) and (3.59) in Eq. (3.55), we easily obtain

$$\mathcal{C}_r^{J^{fl}J^{fl}}(t,0) = \langle J_r^{fl}(t) J_0^{fl}(0)\rangle = \delta(t)\Gamma_r. \tag{3.60}$$

3.2.5 Fluctuation of the space-time integrated current

The space-time integrated current $Q_{tot}(L,T)$ of the system is defined as

$$Q_{tot}(L,T) = \sum_{i=0}^{L-1} Q_i(T) = \int_0^T dt \sum_{i=0}^{L-1} J_i(t). \tag{3.61}$$

Note that, $Q_{tot}(L,T)$ quantifies the total current in the system upto the observation time T. Alternatively, $Q_{tot}(L,T)$ is related to the cumulative tagged particle displacements in the following way:

$$Q_{tot}(L,T) = \sum_{i=1}^{N} X_i(T). \tag{3.62}$$

Here, $X_i(T)$ represents the displacement of the ith particle over the time interval T. In this section, we will examine the fluctuation properties of $Q_{tot}(L,T)$, which essentially quantifies the fluctuations in the cumulative displacements of active particles within the system.

It is important to highlight that, based on the decomposition presented in Eq. (3.8), we can break down $J_i(t)$ in Eq.(3.61) into diffusive $J_i^{(D)}(t)$ and fluctuating $J_i^{(fl)}(t)$ components.

However, for periodic systems, as considered here, we employ the identity:

$$\sum_{i=0}^{L-1} J_i^{(D)}(t) = 0. \tag{3.63}$$

Consequently, the diffusive component does not contribute to $Q_{tot}(L,T)$, resulting in:

$$Q_{tot}(L,T) = \int_0^T dt \sum_{i=0}^{L-1} J_i^{fl}(t). \tag{3.64}$$

The equation above clearly shows that the fluctuating component $J_i^{(fl)}(t)$ is solely responsible for the system's total current, $Q_{tot}(L,T)$. This immediately implies the average current,

$$\langle Q_{tot}(L,T)\rangle = \int_0^T dt \sum_{i=0}^{L-1} \langle J_i^{fl}(t)\rangle = 0, \tag{3.65}$$

since $\langle J_i^{fl}(t)\rangle = 0$. In a similar way, we write the expression for the fluctuation

$$\langle Q_{tot}^2(L,T)\rangle \;\; = \;\; \int_0^T dt' \int_0^T dt \sum_{i=0}^{L-1} \sum_r \langle J_i^{fl}(t) J_{i+r}^{fl}(t')\rangle. \tag{3.66}$$

By employing Eq. (3.60) in the above equation, it becomes straightforward to determine that the total current fluctuation satisfies the following relation:

$$\frac{1}{LT}\langle Q_{tot}^2(L,T)\rangle = \sum_r \Gamma_r = 2\chi(\rho,\gamma), \tag{3.67}$$

where $\chi(\rho,\gamma)$ is explicitly expressed as a function of $P(g)$ in Eq. (3.41). To validate the above fluctuation relation for model II (LLG), we calculate $\langle Q_{tot}^2(L,T)\rangle$ through numerical simulations with system size $L = 1000$ and observation time $T = 50$, within the parameter range of $0.01 \leq \rho \leq 0.9$ and $0.005 \leq \gamma \leq 1$. We also numerically determine $P(g)$ and apply it in Eq. (3.41) to obtain $\chi(\rho,\gamma)$ for the same set of parameter values. In panels (a) and (b) of Fig.(3.3), we depict the numerically obtained scaled fluctuation $\gamma\langle Q_{tot}^2(L,T)\rangle/2LT$ as a function of ρ and γ, respectively. The previously calculated $\gamma\chi(\rho,\gamma)$ is also plotted and represented by dotted lines. The remarkable agreement between $\gamma\langle Q^2 tot(L,T)\rangle/2LT$ and $\gamma\chi(\rho,\gamma)$ serves as immediate confirmation of Eq.(3.67) for model II. For model I, we also plot the numerically obtained $\langle Q_{tot}^2(L,T)\rangle/2LT$, , which is also identified as $\chi(\rho,\gamma)$ according to Eq. (3.67), with respect to ρ (panel c) and γ (panel d), respectively. It is observed that the scaled fluctuation exhibits a non-monotonic behavior in both ρ and γ. Qualitative similarities

between panels (a) and (c), as well as panels (b) and (d), are identified, indicating the presence of the same underlying mechanism of particle transport in models I (standard RTPs) and II (LLG).

Scaling regime for the particle mobility $\chi(\rho,\gamma)$

In this section, we closely examine the particle mobility $\chi(\rho,\gamma)$ by exploring two distinct limiting cases: *Case I,* $\rho \to 0$ *and* $\gamma \to \infty$, and *Case II,* $\rho \to 0$ *and* $\gamma \to 0$. While Case I exhibits qualitative similarities to the SSEP limit, Case II remarkably captures the intricate interplay of interaction and persistence through the scaling variable $\psi = \rho/\gamma$. In our previous study, detailed in chapter 2 and in Ref. [112], we investigated the scaling regime for the bulk-diffusion coefficient $D(\rho,\gamma)$ in Case II. Additionally, in this limit, we analytically determined the associated scaling function for model II. Employing the truncation scheme outlined in Eq. (3.16), we have successfully computed the same for the mobility $\chi(\rho,\gamma)$.

We have previously represented $\chi(\rho,\gamma)$ using the steady-state gap-distribution $P(g)$ in Eq.(3.41). By substituting the assumed exponential form of $P(g)$, as specified in Eq.(3.46), into Eq. (3.41), we derive the following simplified expression for the mobility $\chi(\rho,\gamma)$:

$$\chi(\rho,\gamma) \simeq \frac{(1-\rho)}{2}\frac{(e^{1/g_*}-1)(e^{\gamma+1/g_*}+1)}{(e^{\gamma+1/g_*}-1)^2}. \tag{3.68}$$

Note that, the above expression of $\chi(\rho,\gamma)$ is valid for any arbitrary ρ and γ, with the $\simeq$ signifying the substitution of $P(g)$ with an approximate exponential distribution. However, in the following discussion, we analyze the limiting cases mentioned in the beginning.

Case I, $\rho \to 0$ *and* $\gamma \to \infty$.– In the limit of low density and small persistence, the steady-state distribution takes the form of a product measure: $P(g) \sim (1-\rho)^g \simeq e^{-\rho g}$, resulting in $g_* = 1/\rho$. Ultimately, by employing this g_* and imposing the condition $\gamma \gg 1 \gg \rho$ in Eq. (3.68), we derive the following:

$$\chi(\rho,\gamma) \simeq \frac{e^{-\gamma}}{2}\rho(1-\rho) = \frac{e^{-\gamma}}{2}\chi^{(0)}, \tag{3.69}$$

which, up to a scaling factor of $\exp(-\gamma)$ resulting from time scaling, corresponds to the particle mobility $\chi^{(0)} = \rho(1-\rho)$ in the SSEP. The exponential prefactor $e^{-\gamma}$ in the earlier equation originates from the same physical considerations discussed in chapter 2. For further details, we direct the reader to Sec. 2.4.1.

Case II, $\rho \to 0$ *and* $\gamma \to 0$: Similar to the investigation of the bulk-diffusion coefficient

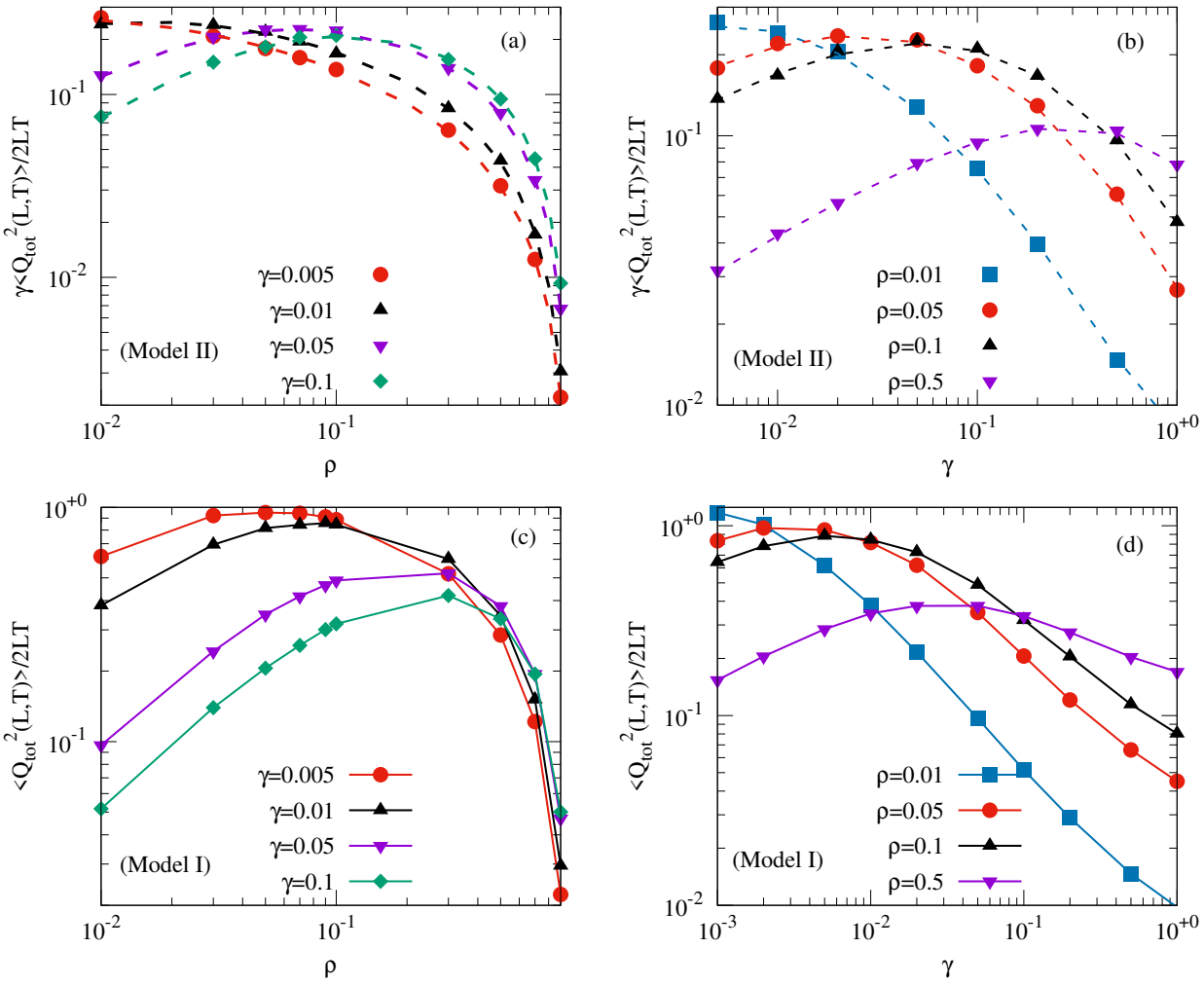

Figure 3.3: In panels (a) and (b), we plot the scaled space-time integrated current fluctuation $\gamma\langle Q^2_{tot}(L,T)\rangle/2LT$ for the LLG, obtained from simulation (points), as a function of ρ [at different $\gamma = 0.001$ (blue square), 0.005 (red circle), 0.01 (black upper-triangle), 0.05 (magenta down-triangle), and 0.1 (green diamond)] and γ [at various $\rho = 0.01$ (blue square), 0.05 (red circle), 0.1 (black upper-triangle) and 0.5 (magenta down-triangle)], respectively. Corresponding dotted lines are $\gamma\chi(\rho,\gamma)$ calculated by using the numerically obtained $P(g)$ in Eq. (3.41). The excellent match between these two quantities verifies Eq. (3.67). In panels (c) and (d), we plot $\langle Q^2_{tot}(L,T)\rangle/2LT$ for model I (standard RTPs), obtained from numerical simulation (line-point), as a function of ρ and γ, respectively for the aforementioned parameters.

$D(\rho,\gamma)$ in hardcore RTPs presented in chapter 2 as well as in Ref. [112], collective particle mobility $\chi(\rho,\gamma)$ exhibits remarkable scaling characteristics. Indeed, following the discussion in Sec. 2.3, in the strong-persistence and low-density limit, the problem is characterized by only two relevant length scales: the persistence length $l_p = v/\gamma$ and the "mean free path" or average gap $\langle g\rangle \simeq 1/\rho$. As a result, their ratio $\psi = l_p/\langle g\rangle$ is expected to serve as a scaling variable that effectively captures the interplay between persistence and interaction. In the limit of strong persistence, $\psi \to \infty$ signifies the strongly interacting limit, while $\psi \to 0$ corresponds to the noninteracting limit. Now as argued previously in chapter 2 and in Ref. [112], we have the typical gap-length g_* satisfing the following scaling law - $g_* \simeq \mathcal{G}(\psi)/\rho$. In the limit as $\psi \to 0$, the model converges to the well-known SSEP, where $\mathcal{G}(\psi) = 1$. On the contrary, in the opposite extreme as $\psi \to \infty$, the system enters a strongly interacting regime, and the previous computations in Ref. [139] indicate $\mathcal{G}(\psi) = \sqrt{\psi}$. By combining these two limiting cases, we can express $\mathcal{G}(\psi) \simeq \sqrt{1+\psi}$. Lastly, by substituting the assumed form of $g_* = \mathcal{G}(\psi)/\rho$ into Eq.(3.68), and following some algebraic manipulations, we arrive at the following scaling law:

$$\chi_{II}(\rho,\gamma) \equiv \frac{\chi^{(0)}}{\gamma^2}\mathcal{H}_{II}\left(\psi = \frac{\rho}{\gamma}\right), \tag{3.70}$$

where $\chi^{(0)} = \rho(1-\rho)$ is the particle mobility in the SSEP and the expression for the scaling function can be explicitly written as

$$\mathcal{H}_{II}(\psi) \;=\; \frac{\mathcal{G}(\psi)}{(\psi+\mathcal{G}(\psi))^2}. \tag{3.71}$$

Finally, by replacing the above form of $\mathcal{G}(\psi) \simeq \sqrt{1+\psi}$, we immediately obtain

$$\mathcal{H}_{II}(\psi) \;=\; \frac{\sqrt{1+\psi}}{(\psi+\sqrt{1+\psi})^2}; \tag{3.72}$$

for calculation details, see Appendix B.9. Thus, we successfully obtained the scaling relation stated in Eq. (3.70) and computed the scaling function as defined in Eq. (3.72) for the mobility $\chi(\rho,\gamma)$ in model II (LLG). However, for model I (hardcore RTPs), following a similar methodology as mentioned for bulk-diffusion coefficients in chapter 2, we expect that collective particle mobility will satisfy the following scaling relationship:

$$\chi_{I}(\rho,\gamma) \equiv \frac{\chi^{(0)}}{\gamma}\mathcal{H}_{I}\left(\psi = \frac{\rho}{\gamma}\right), \tag{3.73}$$

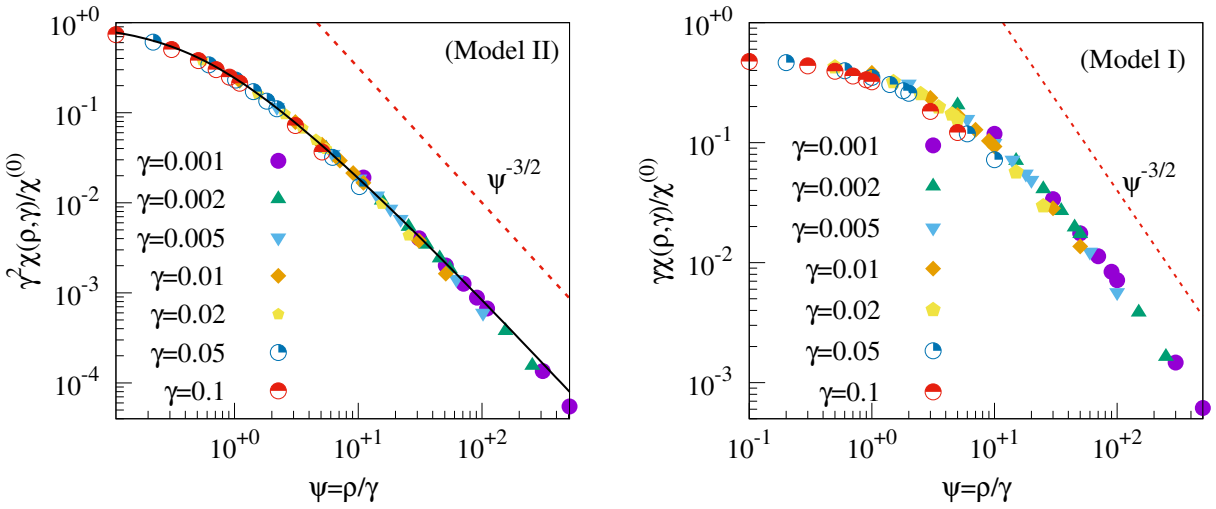

Figure 3.4: *Verification of Eqs.* (3.70) *and* (3.72)- We plot the ratio $\gamma^a \chi(\rho,\gamma)/\chi^{(0)}$ for model II (LLG, top-panel, $a = 2$) and model I (RTPs, bottom-panel, $a = 1$), as a function of scaling variable $\psi = \rho/\gamma$ in the parameter ranges $0.01 \leq \rho \leq 0.5$ and $0.001 \leq \gamma \leq 0.1$. For LLG, we compare the collapsed simulation data points with the analytic scaling function $\mathcal{H}_{LLG}(\psi)$ (solid balck line) shown in Eq. (3.72). For both the models, the collapsed data points exhibit $\psi^{-3/2}$ decay in the asymptotic limit, which is shown here by the red-dotted line.

where, unlike model II, the analytic form of the scaling function $\mathcal{H}_I(\psi)$ is not known at this stage.

We now validate the scaling relationships for the mobility $\chi(\rho,\gamma)$, as expressed in Eqs.(3.73) and (3.70), for both model I and II. In the left panel of Fig.3.4, we depict the scaled mobility $\gamma^2\chi_{II}(\rho,\gamma)/\chi^{(0)}$ for model II, obtained from simulation (data points), as a function of the scaling variable $\psi = \rho/\gamma$ within the parameter ranges $0.01 \leq \rho \leq 0.5$ and $0.001 \leq \gamma \leq 0.1$. Additionally, in the right panel of Fig.3.4, we present the numerically obtained $\gamma\chi_I(\rho,\gamma)/\chi^{(0)}$ for model I against ψ, covering the same parameter range as model II. In both panels, the data points exhibit a remarkable collapse onto each other. Furthermore, for model II (left panel), the collapsed data points closely follows the analytically derived scaling function $\mathcal{H}_{II}(\psi)$ (solid line), as derived in Eq. (3.72). This observation effectively confirms the scaling relationship expressed in Eqs.(3.70) and (3.73) for model II and I, respectively, and supports the validity of the scaling function in Eq. (3.72) for model II.

3.2.6 Time-Integrated Bond-Current fluctuation

To compute the time-integrated bond-current fluctuation in the steady state, we substitute $r = 0$ and $t' = t = T$ in Eq. (3.42) and obtain

$$\mathcal{C}_0^{QQ}(T,T) = \Gamma_0 T - \frac{1}{L}\sum_q \frac{f_q}{\lambda_q}\left\{t - \frac{\left(1-e^{-\lambda_q DT}\right)}{\lambda_q D}\right\}, \tag{3.74}$$

$$= \frac{2\chi}{L}T + \frac{1}{DL}\sum_q \frac{f_q}{\lambda_q^2}\left(1-e^{-\lambda_q DT}\right); \tag{3.75}$$

see Appendix B.7 for the derivation of Eq. (3.75). It is worth noting that $\mathcal{C}_0^{QQ}(T,T)$, described by the comprehensive expressions in Eqs. (3.74) and (3.75), displays intriguing characteristics in various time regimes. In the following analysis, we explore these properties by examining the limiting cases.

Case I : Small-time regime $DT \ll 1$

In this scenario, we linearly expand the exponential function in the second term of Eq. (3.74) with respect to DT, leading to $e^{-\lambda_q DT} \approx 1 - \lambda_q DT$. Consequently, this term is eliminated, and we are left with:

$$\mathcal{C}_0^{QQ}(T,T) \simeq \Gamma_0 T, \tag{3.76}$$

where Γ_0 is simply obtained by putting $r = 0$ in Eq. (3.39).

Case II : Intermediate- and long-time regime $DT \gg 1$

In general, solving the summation in the second term of Eq.(3.75) is a challenging task. However, in this particular case, it is important to note that the summand contributes solely when $q \to 0$ and becomes negligible otherwise. In this limit, the eigenvalues exhibit quadratic behavior, i.e., $\lambda_q \to q^2$, $\lambda_{gq} \to g^2q^2$ and $\lambda_{lq} \to l^2q^2$. This leads to a simplified version of Eq.(3.75):

$$\mathcal{C}_0^{QQ}(T,T) = \frac{2\chi}{L}\left[T + \frac{1}{D}\sum_q \frac{1}{\lambda_q^2}\left(1-e^{-\lambda_q DT}\right)\right]. \tag{3.77}$$

Considering case I and II, the limiting behavior of $\mathcal{C}_0^{QQ}(T,T) = \langle Q^2(t)\rangle$ can be obtained to be

$$\langle Q^2(T)\rangle \simeq \begin{cases} \Gamma_0 T, & \text{for } DT \ll 1, \\ \frac{2\chi(\rho,\gamma)}{\sqrt{\pi D(\rho,\gamma)}}\sqrt{T}, & \text{for } 1 \ll DT \ll L^2, \\ \frac{2\chi(\rho,\gamma)}{L}T, & \text{for } DT \gg L^2, \end{cases} \tag{3.78}$$

where the first term simply corresponds to Eq. (3.76), while the other two are obtained using Eq. (3.77); for details, see Appendix B.8. Hence, the time-integrated bond-current fluctuation $\langle Q_i^2(T)\rangle$ undergoes an initial linear growth over time before crossing over to a subdiffusive scaling within the intermediate regime $L^2/D \gg T \gg 1/D$. Subsequently, at larger time scales $T \gg L^2/D$, it reverts to diffusive or linear scaling behavior, where the strength of the fluctuation is dictated by $\chi(\rho,\gamma)$. To validate these observations, we plot the numerically obtained bond-current fluctuation $\langle Q_i^2(T)\rangle$ as a function of the observation time T in the left panel of Fig.3.5 for model II, at various parameter values [shown in figure], and compare them with our analytical solution provided in Eq.(3.75). The numerical data points distinctly exhibit the three different regimes mentioned earlier and align well with the analytical solution. For model I (standard RTPs), we obtain the same quantity from simulation and plot at the right panel of Fig. 3.5. We observe that the data points exhibit similar characteristics to model II (LLG) in the time regime much larger than its microscopic time scale, i.e., when $DT \gg 1$.

Remarkably, the intermediate and long-time regimes for time-dependent bond-current fluctuations can be unified through a single scaling function. Moreover, the scaling function appears to be universal, as it does not depend on the specific details of the dynamical rules in the considered models. In the limit of $L \to \infty$ and $DT \to \infty$ such that $y = DT/L^2$ is finite, we find $\mathcal{C}_0^{QQ}(T,T) = \langle Q^2(T)\rangle$, as expressed in Eq. (3.77), to satisfy the following scaling relation,

$$\frac{D}{2\chi L}\langle Q^2(T)\rangle = \mathcal{W}\left(\frac{DT}{L^2}\right). \tag{3.79}$$

For model II (LLG), the scaling function is calculated exactly within the truncation scheme and is given by the following series,

$$\mathcal{W}(y) = y + \lim_{L\to\infty}\frac{1}{L^2}\sum_q \frac{1}{\lambda_q}\left(1 - e^{-\lambda_q y L^2}\right). \tag{3.80}$$

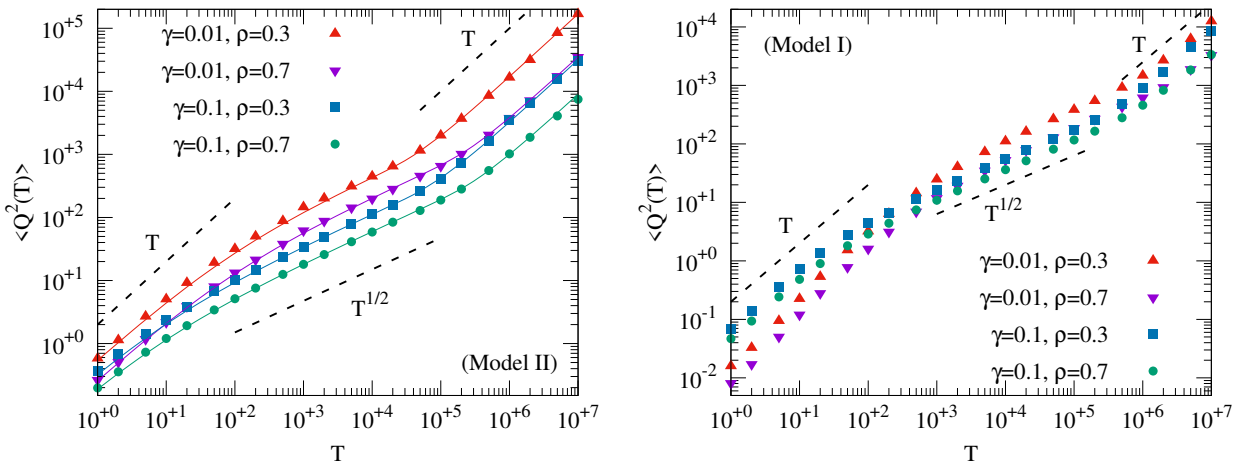

Figure 3.5: We plot the time-integrated bond-current fluctuation $\langle Q_i^2(T)\rangle$, as a function of time T, obtained from simulations (points) for model II (LLG, top-panel) and model I (standard RTPs, bottom-panel) at $\rho = 0.3,\ 0.7$ and $\gamma = 0.1,\ 0.01$. In case of model I, we also compare the simulation data points with the analytical solution shown in Eq. (3.75) (line). For both these models, $\langle Q_i^2(T)\rangle$ exhibits subdiffusive growth at the intermediate time regime, followed by a diffusive (linear) growth, as shown by the dotted lines.

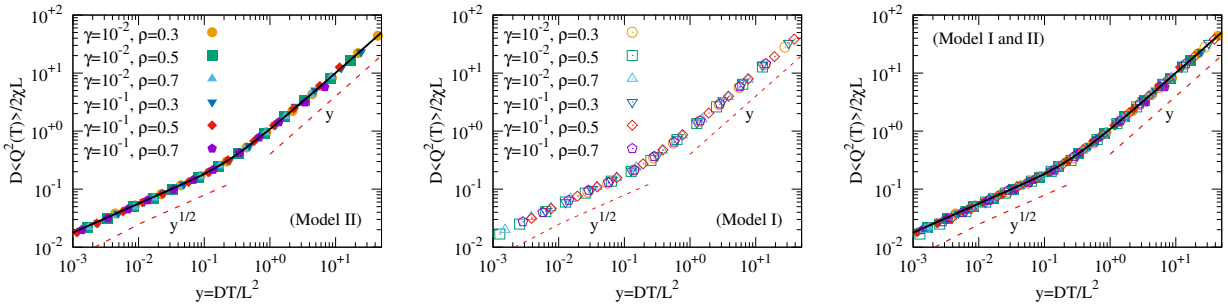

Figure 3.6: *Verification of Eqs.* (3.79) *and* (3.80)- We plot the scaled bond-current fluctuation $D\langle Q_i^2(T)\rangle/2\chi L$ for model II (LLG, left-panel) and model I (standard RTPs, middle-panel), obtained from simulations (points) at various ρ and γ, as a function of the rescaled hydrodynamic time $y = D(\rho,\gamma)T/L^2$. For LLG, we compare the scaled data points with the analytic scaling function $\mathcal{W}(y)$ shown in Eq. (3.80) (black line). In the right-panel, we check the universality of $\mathcal{W}(y)$ by plotting these numerically obtained scaled current fluctuation $D\langle Q_i^2(T)\rangle/2\chi L$ for model II (LLG, closed points) and model I (standard RTPs, open points) together and compare them with the analytically obtained $\mathcal{W}(y)$. In all three panels, the red dotted guiding lines reflect the early time subdiffusive ($\sim \sqrt{y}$), followed by the diffusive growth of $\mathcal{W}(y) \sim y$ as derived in Eq. (3.82).

The above discrete summation can be approximated in terms of known functions [160],

$$\mathcal{W}(y) \simeq y + \left(\frac{y}{\pi}\right)^{1/2} \mathrm{erfc}\left(2\pi\sqrt{y}\right) + \frac{1-\exp(-4\pi^2 y)}{4\pi^2}, \tag{3.81}$$

where $\mathrm{erfc}(y) = 1 - \mathrm{erf}(y)$ and the error function is defined as $\mathrm{erf}(y) = (2/\sqrt{\pi})\int_0^y \exp(-t^2)dt$. Notably, both models I and II bear identical scaling functions as shown in Fig. 3.6. Upon performing asymptotic analysis, one can get the limiting behavior of the scaling function $\mathcal{W}(y)$, as shown below,

$$\mathcal{W}(y) \simeq \begin{cases} \sqrt{y/\pi}, & \text{for } y \ll 1, \\ y, & \text{for } y \gg 1. \end{cases} \tag{3.82}$$

We validate the theoretical findings, as expressed in Eqs. (3.79), (3.80), and (3.82), for both model I and II in Fig. 3.6. The left panel depicts the numerically obtained steady-state scaled current fluctuation $D\langle Q^2(T)\rangle/2\chi L$ (denoted as closed points) for model II, against the rescaled time $y = DT/L^2$, for various ρ and γ. Data points exhibit excellent collapse with each other, and the collapsed data initially grows subdiffusively and then crosses over to linear or diffusive growth, and follows the analytic scaling function $\mathcal{W}(y)$ (solid line), as derived in Eq. (3.80). Simulation data points for model I show a similar trend, as shown in the middle panel of Fig. 3.6. In fact, they are identical to model II, which we verify by plotting numerically obtained data points for model I (open points) and II (closed points) together, in the right-most panel, and comparing them with the already derived $\mathcal{W}(y)$ (solid line) in Eq. (3.80). These observations confirm Eqs. (3.79), (3.80), and (3.82) for models I and II simultaneously.

3.3 Summary and concluding remarks

This chapter calculates the dynamic correlation and current fluctuations, in the steady-state, for two minimal model systems of hardcore (athermal) run-and-tumble particles (RTPs) in a one-dimensional periodic lattice. For model I - the conventional model of hardcore RTPs [36] - we employ an efficient Monte Carlo algorithm, and for model II - the long-ranged analytically tractable variant of hardcore RTPs - we incorporate a microscopic theoretical approach by introducing a closure or truncation scheme. We contrast our theoretical findings with results derived from direct Monte Carlo simulations of models I and II and find a striking resemblance in the characteristics shared by the two models of RTPs.

We now summarize the main findings of the chapter. Our microscopic theory analytically calculates the total or space-time-integrated current fluctuation (similar to the fluctu-

ation of the total displacement of the entire number of particles) in the long-range variant (i.e., for model II). In the large space-time limit, the fluctuation is found to exhibit linear growth with system size L and observation time T. We therefore define the collective particle mobility $\chi(\rho,\gamma)$ in terms of the properly scaled fluctuation of the total current, i.e., $\chi(\rho,\gamma) \equiv \lim_{T\to\infty}\lim_{L\to\infty}(1/2LT)\langle[\sum_{i=1}^{L} Q_i(T)]^2\rangle$ [see Eq. 3.67], where $Q_i(T)$ is the time-integrated current across bond $(i, i+1)$ upto time T. Indeed, the regime where the system is both highly persistent and dilute, as set by $\gamma \to 0$ and $\rho \to 0$, such that the ratio ρ/γ finite, we observe a distinct scaling pattern in the mobility function. This regime reveals an intriguing relationship between persistence and interaction, influencing the fluctuations within the system.

Our analysis also yields an interesting growth pattern of the fluctuation of the time-integrated bond current $Q_i(T)$. In the moderate time regime $1/D \ll T \ll L^2/D$, $\langle Q_i^2(T)\rangle$ exhibits a $\sqrt{T}$ (subdiffusive) growth and then makes a crossover to a linear or diffusive growth at large time $T \gg L^2/D$, where $D \equiv D(\rho,\gamma)$ is the density and tumbling-rate dependent bulk-diffusion coefficient [112]. Notably, the prefactors of the above growth laws are model-dependent through the macroscopic transport coefficients $D(\rho,\gamma)$ and $\chi(\rho,\gamma)$. Interestingly, we find a new scaling regime for $\langle Q_i^2(T)\rangle$; for large system size L and large times T such that DT/L^2 remains finite, the above growth laws can be connected through a presumably universal single scaling function [see Eq. (3.79)].

Apart from time-integrated currents, we have been able to microscopically characterize the spatiotemporal properties of the instantaneous currents in the system. We find the equal-space temporal correlation of instantaneous current to show a negative power-law decay for large times $t \gg 1$, i.e., $\sim -t^{-3/2}$, along with a delta-correlated part at the origin $t = 0$. Additionally, our analysis captures the characteristic long-range spatial correlation observed in active matter. We demonstrate that the spatial correlation of currents at equal times follows an exponential pattern, with a correlation length denoted as ξ, which extends over large distances. In fact, in the scenario of strong persistence $\gamma \to 0$, ξ diverges with the square root of the inverse tumbling rate γ, expressed as $\xi \sim \gamma^{-1/2}$. This outcome offers a microscopic theoretical interpretation of the fundamental characteristics of velocity correlations noted in recent experiments and simulations [141, 147].

All the results mentioned above, derived from our microscopic calculations for model II, have been thoroughly validated numerically for both models I and II. This confirms that the dynamic properties of hardcore athermal RTPs can be fully described by macroscopic transport coefficients - $D(\rho,\gamma)$ and $\chi(\rho,\gamma)$ - alone. This is a significant achievement of our work, and to the best of our knowledge, such a precise characterization of dynamic properties of RTPs through $D(\rho,\gamma)$ and $\chi(\rho,\gamma)$ has not been reported so far. Certainly, the dynamic

fluctuations within interacting SPPs have not been comprehensively understood, and there remains a notable absence of a general theoretical framework to address such systems. In this context, our research could offer valuable insights into the broader large-scale structure of interacting SPPs.

4

Hydrodynamics, "superfluidity", and giant number fluctuations in a model of self-propelled particles

4.1 Introduction

In the preceding two chapters, we investigated collective relaxation and dynamic correlations in a class of athermal hardcore run-and-tumble particles (RTPs) using two density and tumbling-rate dependent macroscopic transport coefficients, the bulk diffusion coefficient, and collective mobility. Because these model systems are athermal, their dynamics are defined by a single length scale, the persistence length l_p of each RTP. In this chapter, we investigate the presence of another length scale, perhaps arising from thermal noise in the surrounding environment, and characterize the hydrodynamic behavior and fluctuations in the system.

Indeed, introducing thermal noise can have interesting consequences on collective steady-state behaviors in self-propelled particles (SPPs). The nontrivial interplay between per-

This chapter is based on the papers "Hydrodynamics, superfluidity, and giant number fluctuations in a model of self-propelled particles", Tanmoy Chakraborty, Subhadip Chakraborti, Arghya Das, and Punyabrata Pradhan, Phys. Rev. E **101**, 052611 (2020), and "Transport and fluctuations in mass aggregation processes: Mobility-driven clustering", Subhadip Chakraborti, Tanmoy Chakraborty, Arghya Das, Rahul Dandekar, and Punyabrata Pradhan, Phys. Rev. E **103**, 042133 (2021).

sistence, interaction, and thermal fluctuation has been shown to induce a nonequilibrium clustering transition in *conventional* hardcore SPPs [58]. Recently, in a slightly different setting, noise-induced phase separation has been reported in a model of "weakly interacting" RTPs [57]. In order to provide a dynamic characterization of such nonequilibrium phase transitions, it is instructive to derive the hydrodynamic structure and identify the above-mentioned macroscopic transport coefficients. Although an effort in this regard was made in Ref. [57] for weakly interacting RTPs, having a product measure steady-state, to derive the hydrodynamic structure, an exact first principle derivation of the hydrodynamics of interacting SPPs, accounting for long-ranged correlations as manifest in the anomalous behaviors of fluctuation and transport, has been elusive so far.

To bridge this gap, we introduce a generalized version of the long-ranged lattice gas (gLLG) that undergoes phase transition. Motivated by the direct correspondence between conventional hardcore RTPs [36] and the hardcore long-ranged lattice gas (LLG), where hop lengths follow a distribution $\phi(l)$, as demonstrated in Chapters. 2 and 3, we introduce gLLG as a minimalistic variant of thermal RTPs. We consider here the simplest possible generalization by incorporating $\phi(l)$ as a superposition of two localized distribution functions: $\phi(l) = \alpha\delta_{l,1} + \beta\delta_{l,l_p}$. This generalized model emphasizes an important aspect: competition between two mechanisms of long- and short-ranged hopping. while the long hops correspond to persistence in RTPs, short hops imitate thermal diffusion. The relative strength of long-range hopping is referred to as activity.

In this chapter, we derive, from first principles, an exact hydrodynamic structure of gLLG in the diffusive scaling limit. Moreover, in a special case when the typical long-range hop-length diverges, we explicitly obtain in one dimension the analytic expressions of two transport coefficients - the bulk diffusion coefficient $D_{l_p}(\rho)$ and the mobility, or the inverse resistivity, $\chi_{l_p}(\rho)$, which, in general, are nonlinear functions of density ρ. Remarkably, even in the absence of detailed balance, we find an equilibrium-like Einstein relation $\sigma^2(\rho) = \chi_{l_p}(\rho)/D_{l_p}(\rho)$, which relates scaled variance $\sigma^2(\rho)$ of subsystem particle-number to the ratio of the two transport coefficients. Indeed, the competition between the two hopping mechanisms induces, beyond a critical density ρ_c (or activity $\tilde{q}_c$), a first-order condensation transition from a *homogeneous* fluid phase to an *inhomogeneous* translational-symmetry-broken "ordered" phase with coexisting fluid of density ρ_c and a condensate of vacancies or "holes". Near criticality, the bulk behaves like a "superfluid" where the mobility diverges as $\chi(\rho) \sim (\rho - \rho_c)^{-1}$ (i.e., the resistivity vanishes), implying giant-number fluctuation (GNF), which, along with the diverging mobility, persists even in the ordered phase; interestingly, the bulk-diffusion coefficient remains finite throughout.

The chapter is organized as follows. In Sec. 4.2, we define the generalized long-ranged

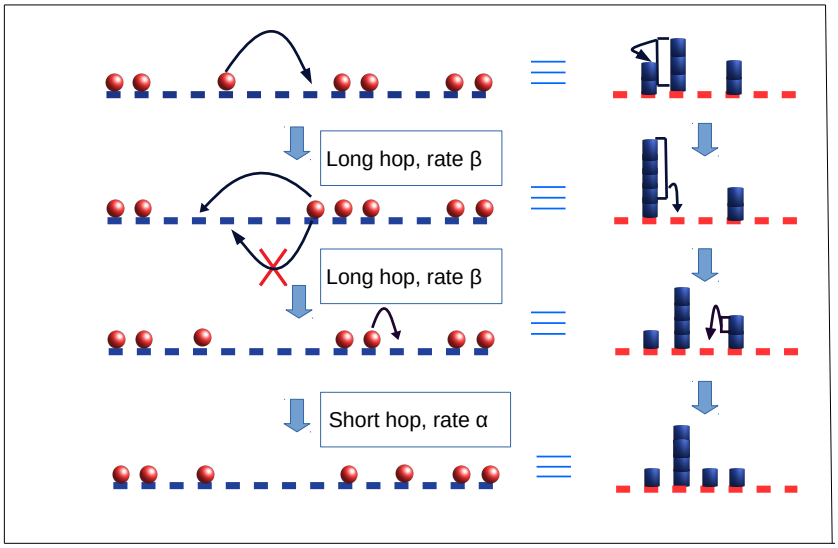

Figure 4.1: Schematic diagram to illustrate the mapping between gLLG and UgLLG in one dimension in a few successive time-steps; we consider here gLLG with localized hop-length distribution $\phi(l) = \alpha\delta_{l,1} + \beta\delta_{l,l_p}$ with $l_p = 4$. The filled circles (red) are particles in gLLG and filled blue squares are masses in UgLLG (gaps in gLLG). The maximum possible hop-length in gLLG in this particular case is $l = 4$, which, in UgLLG, corresponds to the maximum amount of mass, which can be transferred at any time. The "crossed" arrow indicates the impossibility of the time-reversed hopping process, demonstrating a violation of detailed balance in the system.

lattice gas (gLLG). In section 4.3, we derive the hydrodynamic structure of the model in terms of the bulk-diffusion coefficient and the mobility: Hydrodynamics for finite range hopping in Sec. 4.3.1 and for infinite range hopping in Sec. 4.3.2; we verify density relaxation governed by the above hydrodynamics in Sec. 4.3.3 and the existence of an Einstein relation in Sec. 4.3.4, we discuss the connection between "superfluid" transition and "giant" number fluctuation in Sec. 4.3.5. In Sec. 4.4, we summarize with some concluding remarks.

4.2 Model

This section introduces the generalized long-ranged lattice gas, consisting of N hardcore particles moving across a one-dimensional periodic lattice with L sites. The hardcore condition sets the maximum number of particles that can occupy a lattice site to one and prohibits particle crossing. Particles undergo continuous time stochastic evolution and follow the dynamical laws listed below,

(A) Short-range hop: The short-range hopping occurs at rate α and during this event, a particle hops towards the right or left nearest neighboring site with equal probability 1/2, given that the destination site is unoccupied.

(B) Long-range hop: Particles also perform long-range hopping at rate β. Notably, this particular dynamics is already introduced in Chapters 2 and 3. In this case, a particle attempts a long-range hop of length l_p to the left or right with equal probability 1/2. The hopping event is successful if the empty lane of vacancies, or *gap* g, along the hopping direction, exceeds l_p; otherwise, conforming to the hardcore constraint, the particle explores the entire gap of length g and resides behind the next particle along the same direction. Based on the nature of the typical hopping length l_p, we categorize long-range hops into two: Finite-range hops (FRH) have a finite typical long-hop length, whereas infinite-range hops (IRH) are characterized by infinite typical long-hop length.

We specify a microscopic configuration $\{\eta_i\}$ using the occupation variable η_i at each site $i = 1, \ldots, L$, where $\eta_i = 1$ indicates occupation and $\eta_i = 0$ signifies vacancy. The total particle number is a conserved quantity, and the constant global density is defined as $\rho = N/L$. We introduce a dimensionless parameter $\tilde{\beta} = \beta/(\alpha + \beta)$, referred to as the activity, which enables the quantification of the interplay between short and long jumps. Notably, when $\beta = 0$ (absence of long-range hopping), the generalized long-ranged lattice gas (gLLG) simplifies to the extensively studied model of the Simple Symmetric Exclusion Process (SSEP) [161], while for $\alpha = 0$, it simply transforms into the long-ranged lattice gas (LLG) studied in Chapters 2 and 3, also in Refs. [112, 162].

Interestingly, a one-dimensional gLLG comprising L sites and N particles can be transformed into an unbounded one-dimensional model referred to as unbounded generalized long-ranged lattice gas (UgLLG), as introduced in [163]. In UgLLG, there are N "sites" and $(L - N)$ "particles", and there is no hardcore constraint, meaning that the occupation number at a site in UgLLG is not restricted. This specific mapping is later employed in Section 4.3.2 when we perform a detailed calculation of transport coefficients for infinite-range hopping. According to the adopted convention, the kth particle in gLLG is treated as the kth lattice site in UgLLG. Additionally, the gap or the count of "holes" between the kth and $(k + 1)$th particles in gLLG is regarded as the occupancy number or mass at the kth site in UgLLG. Thus density ρ in gLLG is related to density $\tilde{\rho}$ in UgLLG as

$$\tilde{\rho} = \frac{L - N}{N} = \left(\frac{1}{\rho} - 1\right). \tag{4.1}$$

Consequently, the dynamic rules in gLLG can be mapped into UgLLG as follows: At a rate p, a single unit of mass in UgLLG (equivalent to a "hole" in gLLG) is removed and transferred, with equal probabilities of 1/2 to the right or left, to the nearest neighbor site. This specific dynamical rule corresponds to a short-range hop in gLLG. At a rate of β, two types of

dynamics could occur: (i) If the mass (number of "particles") at a site in UgLLG exceeds l_p, only l_p units of mass are fragmented and transferred to the right or left neighbor with a probability of 1/2. The fragments eventually coalesce with the mass at the destination site. (ii) If the mass at a site is less than or equal to l_p, the entire mass is transferred to the right or left neighbor with a probability of 1/2 and coalesces with the mass at the destination site.

We refer to the schematic diagram in Fig. 4.1 for an illustration of the updated rules in both models and their correspondence. It is important to note that, for generic parameter values, these models violate the Kolmogorov criterion and, consequently, detailed balance due to certain hopping events that cannot be time-reversed. For instance, consider a gLLG with a hop-length distribution $\phi(l) = \alpha\delta_{l,1} + \beta\delta_{l,l_p}$ where $l_p = 4$. The impossibility of a time-reversed path in a specific hopping event is depicted in Fig. 4.1 by a "crossed" arrow. The violation of the Kolmogorov criterion is demonstrated by constructing a closed loop in the trajectory space, containing at least one event that cannot be time-reversed. Therefore, long-range hops contribute to breaking time-reversibility and driving the system out of equilibrium.

4.3 Hydrodynamics

The hydrodynamic time evolution reveals complex large-scale spatiotemporal behaviors of slow variables in a system. Given the conservation of total particle number in the generalized long-ranged lattice gas (gLLG), the slow variable in this problem becomes the local particle-number density, denoted by $\rho(x,t)$ at position x and time t. This chapter aims to provide a macroscopic hydrodynamic representation of the temporal evolution of the density field $rho(x,t)$, which is governed by a continuity equation,

$$\frac{\partial\rho(x,\tau)}{\partial\tau} = -\frac{\partial}{\partial x}\left[-D(\rho)\frac{\partial\rho}{\partial x} + \chi(\rho)F\right] \equiv -\frac{\partial J}{\partial x}, \tag{4.2}$$

through a constitutive relation between local density $\rho(x,t)$ and hydrodynamic current $J(\rho) = -D(\rho)\partial\rho/\partial x + \chi(\rho)F$, defined using two transport coefficients - the bulk-diffusion coefficient $D(\rho)$ and the mobility $\chi(\rho)$. The first component of the current emerges following Fick's law, where a nonuniform density distribution contributes to a diffusive current $J_D(\rho(x,t)) = -D(\rho)\partial\rho(x,t)/\partial x$. The subsequent part of the current yields a drift current $J_d = \chi(\rho)F$, essentially representing the linear response to a small perturbation induced by an externally applied biasing force with magnitude F.

In determining the mobility $\chi(\rho)$ under the influence of a small biasing force F (assumed to be counterclockwise along the ring), we first modify the initial (unbiased) hopping rate $c_{i\to j}$

from the site i to j using macroscopic fluctuation theory [115] in the following manner:

$$c^F_{i\to j} = c_{i\to j} \exp\left(\frac{\Delta e_{ij}}{2}\right) \simeq c_{i\to j}\left[1 + \frac{F(j-i)a}{2}\right], \tag{4.3}$$

which is linearized in the limit of small force F, with $\Delta e_{ij} = \Delta m_{i\to j} F(j-i)a/2$ being an "energy cost" for transferring $\Delta m_{i\to j}$ number of particles from the site i to j; for gLLG, $\Delta m_{i\to j} = 1$, which is the number of particles transferred at a time, and $a = 1$ the lattice spacing. Due to these modified hopping rates, defined in Eq. (4.3), particles now hop with rates that are slightly greater in the direction of the applied force compared to those in the opposite direction.

We now distinguish the modified (or biased) hop rates in each direction, naming the modified long-hop rates as $\beta^F_R(l_p)$ and $\beta^F_L(l_p)$, and similarly, the modified short-hop rates as α^F_R and α^F_L. Here, the subscripts "R" and "L" signify anti-clockwise (aligned with the biasing force) and clockwise (opposite to the biasing force) hopping directions of particles, respectively. To determine the rate of change of average occupancy $\rho_i = \langle \eta_i(t) \rangle$ or the local density at site i, we consider all possible ways of gaining and losing a particle at site i. At a given site i, there are four contributions in total. Two of these are linked to the loss of a particle, i.e., outward fluxes $J^-_R(i)$ towards the right and $J^-_L(i)$ towards the left. The remaining two contributions involve the gain of a particle, i.e., inward fluxes $J^+_R(i)$ towards the right and $J^+_L(i)$ towards the left. The rate of change of average occupation $\langle \eta_i(t) \rangle$ can now be expressed as:

$$\frac{\partial \langle \eta_i(t) \rangle}{\partial t} = \frac{\partial \rho_i(t)}{\partial t} = J^+_R(i) + J^+_L(i) - J^-_R(i) - J^-_L(i). \tag{4.4}$$

Therefore, to proceed further, we have to calculate these flux terms in Eq. (4.4). To calculate $J^-_R(i)$, we explicitly examine the particle hopping events from site i towards its right direction. Notably, this term encompasses two contributions: the flux contribution $J^-_{R,sh}(i)$ arising from short-hop and another, $J^-_{R,l}(i)$, stemming from long-hop, as calculated below.

Short-hop contribution.– In the case of short-range hopping, a particle moves a unit distance, provided the destination site is unoccupied. Consequently, the ith site can acquire a particle from its nearest neighbors, either $(i+1)$ or $(i-1)$. Conversely, site i can experience a particle loss when a particle hops to either $(i+1)$ or $(i-1)$. Therefore, the corresponding

rate of loss for a particle moving to the right from the site i to $(i+1)$ is expressed as:

$$\begin{aligned} J^{-}_{R,sh}(i) &= \frac{1}{2}\alpha^{F}_{R}\langle \eta_i \overline{\eta}_{i+1}\rangle \\ &= \frac{\alpha}{2}\left(1+\frac{Fa}{2}\right)\langle \eta_i(1-\eta_{i+1})\rangle + \mathcal{O}(F^2), \end{aligned}$$

where angular brackets denote steady-state averages.

Long hop contribution.– In this scenario, based on the number of consecutive unoccupied sites or the gap size g, two distinct types of hopping events can occur from site i, as outlined below.

Case I.– If $g < l_p$, the particle at site i can only hop a distance of g since the nearest occupied site is situated at $(i+g+1)$. Consequently, the corresponding rate of loss is determined by:

$$J^{-}_{R,<}(i \to i+g) = \frac{1}{2}\beta^{F}_{R}(g)\langle \eta_i \overline{\eta}_{i+1}\overline{\eta}_{i+2}\ldots\overline{\eta}_{i+g}\eta_{i+g+1}\rangle.$$

Case II.– If $g \geq l_p$, the particle covers the maximum distance of l_p and then settles at the $(i+l)$th site, and the associated rate of loss is expressed as:

$$J^{-}_{R,\geq}(i \to i+l_p) = \frac{1}{2}\beta^{F}_{R}(l_p)\langle \eta_i \overline{\eta}_{i+1}\overline{\eta}_{i+2}\ldots\overline{\eta}_{i+l_p}\rangle.$$

The overall rate of loss, corresponding to the outward movement of particles to the right from the site i, taking into account all conceivable gap sizes, can now be formulated as:

$$J^{-}_{R,l_p}(i) = \sum_{g=1}^{l_p-1} J^{-}_{R,<}(i \to i+g) + J^{-}_{R,\geq}(i \to i+l_p).$$

By revisiting the correlation functions $\mathcal{U}^{(l_p)}$ and $\mathcal{V}^{(l_p+2)}$ defined in Eq. (2.12), we now express various rightward fluxes at linear order $\mathcal{O}(F)$ of the biasing force F as follows:

$$J^{-}_{R,sh}(i) = \frac{\alpha}{2}\left(1+\frac{Fa}{2}\right)(\rho_i - \mathcal{V}^{(2)}_{i+1}) + \mathcal{O}(F^2), \tag{4.5}$$

$$J^{-}_{R,<}(i \to i+g) = \frac{\beta}{2}\left(1+\frac{Fga}{2}\right)\mathcal{V}^{(g+2)}_{i+g+1} + \mathcal{O}(F^2), \tag{4.6}$$

$$J^{-}_{R,\geq}(i \to i+l_p) = \frac{\beta}{2}\left(1+\frac{Fla}{2}\right)\left(\mathcal{U}^{(l_p)}_{i+l_p} - \mathcal{U}^{(l_p+1)}_{i+l_p}\right) + \mathcal{O}(F^2) \tag{4.7}$$

The net loss rate $J_R^-(i)$ due to both short-range and long-range hop is given by

$$J_R^-(i) = J_{R,sh}^-(i) + J_{R,l_p}^-(i). \tag{4.8}$$

We can calculate other loss and gain rates similarly; for detailed calculations of $J_L^-(i)$, $J_R^+(i)$ and $J_L^+(i)$, see the Appendix C.1.

4.3.1 Finite range hopping

In this section, we establish the continuity equation for the density field for gLLG with finite range hopping, i.e., we are interested in the regime of finite l_p. As derived in Eq. (4.8), the rightward loss rate from site i is given by, upto linear order $\mathcal{O}(F)$ of force,

$$J_R^-(i) \simeq \frac{\alpha}{2}(1+\frac{Fa}{2})(\rho_i - \mathcal{V}_{i+1}^{(2)}) + \sum_{g=1}^{l_p-1}\frac{\beta}{2}(1+\frac{Fga}{2})\mathcal{V}_{i+g+1}^{(g+2)} + \frac{\beta}{2}(1+\frac{Fl_pa}{2})\left(\mathcal{U}_{i+l_p}^{(l_p)} - \mathcal{U}_{i+l_p}^{(l_p+1)}\right). \tag{4.9}$$

Similarly, as shown in the Appendix C.1, we write the leftward gain rate,

$$J_L^+(i) \simeq \frac{\alpha}{2}(1-\frac{Fa}{2})(\rho_{i+1} - \mathcal{V}_{i+1}^{(2)}) + \sum_{g=1}^{l_p-1}\frac{\beta}{2}(1-\frac{Fga}{2})\mathcal{V}_{i+g}^{(g+2)} + \frac{\beta}{2}\left(1-\frac{Fl_pa}{2}\right)\left(\mathcal{U}_{i+l_p-1}^{(l_p)} - \mathcal{U}_{i+l_p}^{(l_p+1)}\right), \tag{4.10}$$

the rightward gain rate,

$$J_R^+(i) \simeq \frac{\alpha}{2}(1+\frac{Fa}{2})(\rho_{i-1} - \mathcal{V}_{i}^{(2)}) + \sum_{g=1}^{l_p-1}\frac{\beta}{2}(1+\frac{Fga}{2})\mathcal{V}_{i+1}^{(g+2)} + \frac{\beta}{2}(1+\frac{Fl_pa}{2})\left(\mathcal{U}_{i}^{(l_p)} - \mathcal{U}_{i}^{(l_p+1)}\right), \tag{4.11}$$

and the leftward loss rate,

$$J_L^-(i) \simeq \frac{\alpha}{2}(1-\frac{Fa}{2})(\rho_i - \mathcal{V}_{i}^{(2)}) + \sum_{g=1}^{l_p-1}\frac{\beta}{2}(1-\frac{Fga}{2})\mathcal{V}_{i}^{(g+2)} + \frac{\beta}{2}(1-\frac{Fl_pa}{2})\left(\mathcal{U}_{i-1}^{(l_p)} - \mathcal{U}_{i}^{(l_p)}\right). \tag{4.12}$$

Substituting all loss and gain rates from Eqs. (4.9), (4.10), (4.11) and (4.12) into Eq. (4.4), we obtain the time-evolution of local density, which, in the leading order $\mathcal{O}(F)$ of the biasing

force F, is recast below in a somewhat long, but an interesting form,

$$\begin{aligned}\frac{\partial \rho_i}{\partial t} \simeq & \frac{\beta}{2}\Big[\Big\{\mathcal{U}^{(l_p)}_{i+l_p-1}-\mathcal{U}^{(l_p)}_{i+l_p}\Big\}-\Big\{\mathcal{U}^{(l_p)}_{i-1}-\mathcal{U}^{(l_p)}_{i}\Big\}\Big]-\frac{\beta F l_p}{4}\Big[\Big\{\mathcal{U}^{(l_p)}_{i+l_p-1}+\mathcal{U}^{(l_p)}_{i+l_p}\Big\}-\Big\{\mathcal{U}^{(l_p)}_{i-1}+\mathcal{U}^{(l_p)}_{i}\Big\} \\ & -2\Big\{\mathcal{U}^{(l_p+1)}_{i+l_p}-\mathcal{U}^{(l_p+1)}_{i}\Big\}\Big]+\sum_{g=1}^{l_p-1}\frac{\beta}{2}\Big[\Big\{\mathcal{V}^{(g+2)}_{i+1}-\mathcal{V}^{(g+2)}_{i}\Big\}-\Big\{\mathcal{V}^{(g+2)}_{i+g+1}-\mathcal{V}^{(g+2)}_{i+g}\Big\}\Big] \\ & -\sum_{g=1}^{l_p-1}\frac{\beta F g}{4}\Big[\Big\{\mathcal{V}^{(l_p+2)}_{i+g+1}+\mathcal{V}^{g+2}_{i+g}\Big\}-\Big\{\mathcal{V}^{(g+2)}_{i+1}+\mathcal{V}^{(g+2)}_{i}\Big\}\Big]+\frac{\alpha}{2}\Big[\rho_{i+1}-2\rho_i+\rho_{i-1}\Big] \\ & +\frac{\alpha F}{4}\Big[\Big\{\rho_{i-1}-\rho_{i+1}\Big\}+2\Big\{\mathcal{V}^{(2)}_{i+1}-\mathcal{V}^{(2)}_{i}\Big\}\Big]. \end{aligned} \tag{4.13}$$

In the above expression, terms within the curly brackets are arranged in a gradient form. This arrangement leads to a continuity equation for local density as follows. By adopting the diffusive scaling limit $i \to x = i/L$, $t \to \tau = t/L^2$, and $a \to 1/L$, where the observables are assumed to exhibit slow variations in both space and time, taking on *local steady-state* values [115,136], we expand $\mathcal{U}^{(l_p)}_i(t) \equiv \mathcal{U}^{(l_p)}[\rho(x,\tau)]$ in a Taylor series around the local density $\rho_i(t) \equiv \rho(x,\tau)$. The expansion is carried out up to $\mathcal{O}[(1/L)^2]$, resulting in:

$$\mathcal{U}^{(l_p)}_{i+l} \simeq \mathcal{U}^{(l_p)}[\rho(x,\tau)] + \frac{l_p}{L}\frac{\partial \mathcal{U}^{(l_p)}[\rho(x,\tau)]}{\partial x} + \frac{l_p^2}{2L^2}\frac{\partial^2 \mathcal{U}^{(l_p)}[\rho(x,\tau)]}{\partial x^2}. \tag{4.14}$$

We now extend a similar expansion to other correlators, $\mathcal{V}^{(l_p+2)}_{i+l_p}$ and $\mathcal{V}^{(2)}_{i+1}$. Ultimately, by applying the Taylor series expansions mentioned above in Eq. (4.13) and considering terms up to $\mathcal{O}(1/L^2)$, we derive the desired hydrodynamics of the gLLG in the diffusive scaling limit:

$$\frac{\partial \rho(x,\tau)}{\partial \tau} = -\frac{\partial}{\partial x}\left[-D_{l_p}(\rho)\frac{\partial \rho}{\partial x} + \chi_{l_p}(\rho)F\right]. \tag{4.15}$$

Notably, the obtained hydrodynamic structure, as shown in Eq. (4.15), is characterized by the two macroscopic transport coefficients: the bulk-diffusion coefficient $D_{l_p}(\rho)$ and the mobility $\chi_{l_p}(\rho)$, which we identify as,

$$D_{l_p}(\rho) = \frac{\alpha}{2} - \frac{\beta}{2}\sum_{g=1}^{l_p-1} g\frac{\partial \mathcal{V}^{(g+2)}(\rho)}{\partial \rho} - \frac{\beta l_p}{2}\frac{\partial \mathcal{U}^{(l_p)}(\rho)}{\partial \rho}, \tag{4.16}$$

$$\chi_{l_p}(\rho) = \frac{1}{2}\left[\beta\sum_{g=1}^{l_p-1} g^2 \mathcal{V}^{(g+2)}(\rho) + \alpha\left(\rho - \mathcal{V}^{(2)}(\rho)\right)\right] + \frac{\beta l_p^2}{2}\left[\mathcal{U}^{(l_p)}(\rho) - \mathcal{U}^{(l_p+1)}(\rho)\right], \tag{4.17}$$

respectively; for details, see the Appendix C.1. Importantly, the calculated transport coefficients $D_{l_p}(\rho)$ and $\chi_{l_p}(\rho)$, as presented in Eqs. (4.16) and (4.17) respectively, involve the

nontrivial many-point correlators $\mathcal{U}^{(l)}$ and $\mathcal{V}^{(l+2)}$. The calculation of these correlators, guided by the following identities,

$$\langle \mathcal{V}^{(g+2)} \rangle(\rho) = \rho P(g|\rho), \tag{4.18}$$

$$\langle \mathcal{U}^{(l)} \rangle(\rho) = \rho \sum_{g=l}^{\infty} (g-l+1) P(g|\rho), \tag{4.19}$$

essentially boils down to determining the steady-state distribution of consecutive clusters of holes or gap sizes, denoted as $P(g|\rho)$. However, the explicit analytical formulations for the gap-distribution $P(g|\rho)$ and thus the transport coefficients for arbitrary hopping range l_p are out of the scope of this thesis. Indeed, they can be computed numerically quite efficiently to validate the hydrodynamic structure described in Eq. (4.15). Notably, in the simplest nontrivial case of $l_p = 2$, upon mapping the exclusion model gLLG to the corresponding unbounded version UgLLG [139], as defined in Sec. 4.2, exact determination of the gap-distribution function is possible, allowing for analytic derivation of the transport coefficients, which we derive below.

Exactly solvable case, $l_p = 2$: We consider here the simplest non-trivial case with $l_p = 2$; this model can be mapped to the unbounded variant UgLLG, where each site fragments a single unit of mass at rate α to the symmetrically chosen nearest neighbor, while at rate β, if the site has masses larger than $l_p = 2$, it chips off 2 units of masses; otherwise, the entire block of masses at that site (which is 1 or 2 in this case) is transferred to the randomly chosen neighboring site. As shown in Ref. [139], the neighboring correlations in this model vanish in the limit of large system sizes, thus we can calculate the steady-state single-site mass distribution $P(g)$ by employing a mean-field theory, where the joint mass distribution is assumed to have a product form. Now taking into account all possible ways of mass transfer, we can write the time evolution equations of $P(g,t)$ for an arbitrary l_p as given below,

$$\left.\frac{dP(g,t)}{dt}\right|_{g>0} = -(\alpha+\beta)[1+\sum_{g'=1}^{\infty} P(g',t)]P(g,t) + \beta P(g+l_p,t) + \alpha P(g+1,t) + \alpha P(g-1,t)\sum_{g'=1}^{\infty} P(g',t)$$
$$+\beta P(g-l_p,t)\theta(g-l_p)\sum_{g'=l_p}^{\infty} P(g',t) + \beta\sum_{g'=1}^{m} P(g-g',t)P(g',t) - \beta\sum_{g'=l_p}^{m} P(g-g',t)P(g',t)\theta(g-l_p), \tag{4.20}$$

$$\frac{dP(0,t)}{dt} = -(\alpha+\beta)\sum_{g'=1}^{\infty} P(g',t)P(0,t) + \alpha P(1,t) + \beta\sum_{g'=1}^{\infty} P(g',t) + \beta P(l_p,t) - \beta\sum_{g'=l_p}^{\infty} P(g',t), \tag{4.21}$$

where the Heaviside theta function $\theta(g-l_p)=0$ if $g<l_p$ and $\theta(g-l_p)=1$ otherwise. We now solve the master equations (4.20) and (4.21) for a particular value of $l_p=2$ in the steady state by setting the left-hand sides of Eqs. (4.20) and (4.21) to zero. Now multiplying the right-hand side of Eq. (4.20) by z^g, summing g from 1 to ∞, and by combining Eq. (4.21) in the steady state, we solve for the generating function $Q(z)=\sum_{g=1}^{\infty} P(g)z^g$ as given below,

$$Q(z) = \frac{z\left[\beta P_1 + P_0(1-P_0)(\alpha+\beta+\beta z)z - \beta P_1 P_0 z^2\right]}{\beta + (\alpha+\beta)\{z-(1-P_0)z^2\} - \beta(1-P_1-P_0)z^3}. \tag{4.22}$$

We further simplify the problem by choosing $\alpha=\beta=1/2$ and in this case, we obtain,

$$Q(z) = z\frac{P_1 + P_0(1-P_0)(2+z)z - P_1P_0z^2}{1+2z-2(1-P_0)z^2-(1-P_1-P_0)z^3}, \tag{4.23}$$

where we denote the undetermined parameters $P_0=P(g=0)$ and $P_1=P(g=1)$. By definition, we have $Q(0)=0$ and $Q(1)=1-P_0$, both of which are satisfied by Eq. (4.23), implying that the above expression for $Q(z)$ is indeed consistent. To determine the two unknown parameters P_0 and P_1 in the generating function $Q(z)$, we need to put two conditions on $Q(z)$. One condition can be found in the identity

$$\left.\frac{dQ}{dz}\right|_{z=1} = \sum_{g=1}^{\infty} gP(g) = \tilde{\rho}, \tag{4.24}$$

which leads to

$$P_1 = \frac{5-P_0(5+3\tilde{\rho})}{\tilde{\rho}+2}, \tag{4.25}$$

where the mass density $\tilde{\rho}$ in UgLLG is defined as a function of the particle density in gLLG in Eq. (4.1). The second condition is obtained as follows. From the definition, $Q(z)$ converges only if $|z|\leq 1$ since $0\leq P(g)\leq 1$. However, if the denominator of $Q(z)$ has a root at $z=z^*$ with $|z^*|\leq 1$, $Q(z)$ will diverge at that root z^* which is not allowed. So to avoid a diverging $Q(z)$, both the denominator and the numerator of $Q(z)$ in Eq. (4.23) should share a common root at $z=z^*$ so that $Q(z)$ remains finite. This condition helps us to determine the probability P_1 in terms of probability P_0 and the mass density $\tilde{\rho}$. As the numerator of

$Q(z)$ is a quadratic function of z, we explicitly find the two roots,

$$z_{\pm} = \frac{1-P_0}{1-P_1-P_0}\left[-1 \pm \sqrt{1 - \frac{P_1(1-P_1-P_0)}{P_0(1-P_0)^2}}\right]. \tag{4.26}$$

Since $0 < P_1,\ P_0 < 1$, the pre-factor $(1-P_0)/(1-P_1-P_0)$ is always greater than 1. Moreover, one can check that the term inside the square root is always positive, implying that both the roots are real and $z_- \leq -1$. So the root of physical interest is $z = z_+$. Furthermore, the denominator of $Q(z)$ in Eq. (4.23) should vanish at $z = z^* = z_+$. Using this condition and the relation in Eq. (4.25) together, we express the probabilities P_0 and P_1 as a function of mass density $\tilde{\rho}$,

$$P_0 = \frac{9 + 5\tilde{\rho} - \sqrt{1 + 10\tilde{\rho} + 5\tilde{\rho}^2}}{2(2+\tilde{\rho})^2}, \tag{4.27}$$

$$P_1 = \frac{(3\tilde{\rho}+5)\sqrt{1 + 10\tilde{\rho} + 5\tilde{\rho}^2} - (5\tilde{\rho}^2 + 12\tilde{\rho} + 5)}{2(2+\tilde{\rho})^3}. \tag{4.28}$$

Next we expand the generating function $Q(z)$ as Eq. (4.23) in power series of z,

$$Q(z) = \sum_{g=1}^{\infty} \left(\frac{P_1}{P_0}\right)^g P_0 F_{g+1} z^g, \tag{4.29}$$

where F_{g+1} is the $(g+1)$th element of the Fibonacci series, which is defined as the following [164]:

$$F_g = \begin{cases} 0 & \text{for g} = 0, \\ 1 & \text{for g} = 1, \\ F_{g-1} + F_{g-2} & \text{for g} \geq 2. \end{cases} \tag{4.30}$$

Comparing the power series expansion in Eq. (4.29) and the definition of the generating function $Q(z)$, we immediately find $P(g)$ as a function of g for any particle density ρ,

$$P(g) = \left(\frac{P_1}{P_0}\right)^g P_0 F_{g+1}, \tag{4.31}$$

where P_0 and P_1 both depend on the mass density $\tilde{\rho}$, hence on particle density ρ via Eq. (4.1), and are provided by Eqs. (4.27) and (4.28), respectively.

By utilizing the identities presented in Eqs.(4.18) and (4.19), we apply the obtained expression for the gap-distribution function $P(g|\rho)$ from Eq.(4.31) to derive the transport

coefficients for $l_p = 2$ in Eqs. (4.16) and (4.17), and the resulting expressions are give by,

$$D_2(\rho) = \frac{\alpha}{2} + \frac{\beta}{2}\frac{\partial}{\partial\rho}\left[\rho\left(4 - 2P_0 - P_1\right)\right], \tag{4.32}$$

$$\chi_2(\rho) = \frac{\alpha}{2}\rho\left(1 - P_0\right) + \frac{\beta}{2}\rho\left(4 - 4P_0 - 3P_1\right). \tag{4.33}$$

Next, in the limit of $\alpha = \beta = 1/2$, we substitute P_0 and P_1 from Eqs. (4.27) and (4.28), respectively, in the above two equations, which after using the relation in Eq. (4.1), we obtain the following explicit expression of the transport coefficients:

$$D_2(\rho) = \frac{1}{8(1+\rho)^4}\left[10\left(1 - \frac{\rho}{\sqrt{5-4\rho^2}}\right) + 5\rho\left(6 + \frac{\rho}{\sqrt{5-4\rho^2}}\right) + \rho^2\left(17 + \frac{12\rho}{\sqrt{5-4\rho^2}}\right)\right], \tag{4.34}$$

$$\chi_2(\rho) = \frac{\rho}{8(1+\rho)^3}\left[10 + 4\rho\left(5 - \sqrt{5-4\rho^2}\right) - \rho^2\left(9 + \sqrt{5-4\rho^2}\right) - 16\rho^3\right]. \tag{4.35}$$

Importantly, the above explicit form of $D_2(\rho)$ and $\chi_2(\rho)$ immediately suggest that transport coefficients remain finite and bounded for any ρ, so the model does not exhibit any interesting feature in this finite-ranged hopping of $l_p = 2$. In the subsequent section, we delve into the intriguing special scenario of gLLG with infinite-range hopping (IRH). This particular case of IRH is analytically amenable, featuring a phase transition, and allows for the explicit calculation of the two transport coefficients in terms of density.

4.3.2 Infinite range hopping

In the case of finite-range hopping (FRH), the transport coefficients, as outlined in Eqs. (4.16) and (4.17), remain finite, and there is no occurrence of a phase transition. However, the scenario undergoes a significant transformation when the typical length scale associated with long-range hopping becomes divergent, leading to a phase transition in the system. To illustrate this, we investigate a particular case of infinite-range hopping, where the typical hop-length l_p approaches infinity.

In this situation, the dynamics for short-range hopping are identical to those described in the preceding section. However, the long-range hopping process is slightly altered, as the hopping range is now indefinitely large. Specifically, during a long-range hop, a particle located at site i always jumps, symmetrically in either direction with probability $1/2$, the longest distance feasible along an empty lane in its hopping direction. In other words, in the long-ranged hopping dynamics, the particle travels a distance g, which represents the gap size in the hopping direction.

Below, we provide an overview of the calculation techniques; for details, see Appendix C.2. Notably, in the infinite-range hopping with $l_p \to \infty$, certain simplifications emerge as the terms involving $\mathcal{U}_i^{(l_p)}$ are eliminated from Eqs. (4.16) and (4.17). This results in the expressions for the bulk-diffusion coefficient $D(\rho)$ and the mobility $\chi(\rho)$ as presented below:

$$D_\infty(\rho) = \frac{\alpha}{2} - \frac{\beta}{2}\sum_{g=1}^{\infty} g\frac{\partial \mathcal{V}^{(g+2)}(\rho)}{\partial \rho}, \tag{4.36}$$

$$\chi_\infty(\rho) = \frac{\alpha}{2}(\rho - \mathcal{V}^{(2)}(\rho)) + \frac{\beta}{2}\sum_{g=1}^{\infty} g^2 \mathcal{V}^{(g+2)}(\rho). \tag{4.37}$$

To progress further, it is necessary to determine $\mathcal{V}^{g+2}(\rho)$ and $\mathcal{V}^{(2)}(\rho)$ in terms of ρ. To achieve this, we again utilize the mapping previously described between the gLLG and its "unbounded" counterpart, UgLLG. In UgLLG, the infinite-range hopping is analogous to the diffusion of individual masses as a collective entity, encompassing the complete aggregation of neighboring masses.

We now proceed by noting that the gap distribution in gLLG at density ρ is identical to the single-site mass distribution in the corresponding UgLLG with mass density $\tilde{\rho} = 1/\rho - 1$. This identity together with Eq. (4.18) enable us to write the correlator $\mathcal{V}^{g+2}(\rho)$, appearing in Eqs. (4.36) and (4.37), as a function of the mass distribution $\tilde{P}(g|\tilde{\rho})$ in UgLLG as

$$\mathcal{V}^{(g+2)}(\rho) = \rho P(g|\rho), \tag{4.38}$$

and

$$\mathcal{V}^{(2)}(\rho) = \rho P(g=0|\rho) = \rho\{1 - \tilde{c}[\tilde{\rho}(\rho)]\}, \tag{4.39}$$

where $\tilde{c}(\tilde{\rho})$ is the occupation probability in UgLLG. We notice that the bulk-diffusion coefficient $D(\rho)$ depends on the average or the first moment of the distribution $\tilde{P}(g|\tilde{\rho})$

$$\langle g \rangle = \sum_{g=1}^{\infty} g P(g|\rho) = \tilde{\rho} = \frac{1}{\rho} - 1. \tag{4.40}$$

Upon plugging the above relation in Eq. (4.36), we simply find the bulk-diffusion coefficient

$$D_\infty(\rho) = \frac{\alpha + \beta}{2}, \tag{4.41}$$

to be independent of density, i.e., constant. Notably, Eqs. (4.38) and (4.39) suggest that the other transport coefficient, i.e., the mobility is dependent on the occupation probability $\tilde{c}(\tilde{\rho})$

and the second moment $\theta_2(\tilde{\rho}) = \sum_g g^2 P(g|\rho)$ of the $P(g|\rho)$ in the following manner:

$$\chi_\infty(\rho) = \frac{\alpha}{2}\rho\tilde{c}(\tilde{\rho}) + \frac{\beta}{2}\rho\theta_2(\tilde{\rho}). \tag{4.42}$$

Now, as prescribed in Refs. [139, 165], one can immediately calculate $\tilde{c}(\tilde{\rho})$ and $\theta_2(\tilde{\rho})$ by assuming a statistical independence between neighboring masses in UgLLG, which is shown to have the following forms: $\tilde{c}(\tilde{\rho}) = \tilde{\rho}(\alpha-\beta\tilde{\rho})/\alpha(1+\tilde{\rho})$, $\theta_2(\tilde{\rho}) = \alpha\tilde{\rho}[1+\tilde{c}(\tilde{\rho})]/[\alpha\{1-\tilde{c}(\tilde{\rho})-2\beta\tilde{\rho}\}]$. Finally, using the relation $\tilde{\rho} = 1/\rho - 1$, the explicit expression of the mobility is calculated to be,

$$\chi_\infty(\rho) \;=\; \frac{\rho(1-\rho)[(\alpha+\beta)\rho^2 - 2\beta\rho + \beta]}{2[\rho^2 - \beta/(\alpha+\beta)]}, \tag{4.43}$$

for calculation details, see the Appendix C.3. Therefore, in gLLG with infinite-range hopping, it is notable that despite the bulk-diffusion coefficient remaining constant and finite, as the system approaches a critical density (or activity), the mobility experiences a singularity, characterized by a first-order pole, indicating a phase transition beyond a critical density $\rho_c(q) = \tilde{\beta}^{1/2}$ [or a critical activity $\tilde{\beta}_c(\rho) = \rho^2$]. As elaborated later in Section 4.3.5, when the system reaches criticality and beyond (i.e., for $\rho \leq \rho_c$ or $\tilde{\beta} \geq \tilde{\beta}_c$), the bulk exhibits characteristics reminiscent of a "superfluid". This is marked by the divergence of mobility, represented by $\chi_\infty(\rho) \sim \theta_2(\rho) \sim (\rho - \rho_c)^{-1}$ (or equivalently, the reduction of resistivity $\sim (\rho - \rho_c)$ to zero). Such behavior is a direct consequence of the diverging fluctuations in gap or vacancy size, giving rise to cooperativity within the system.

4.3.3 Density Relaxation

In this section, we investigate the relaxation of density profiles following an initial density perturbation in the generalized long-ranged lattice gas, considering the original unbiased hopping rates ($F = 0$). As established in the preceding sections, the dynamics of density relaxation are determined by Equation (4.2) with $F = 0$, i.e.,

$$\frac{\partial\rho(x,\tau)}{\partial\tau} = \frac{\partial}{\partial x}\left(D(\rho)\frac{\partial\rho(x,\tau)}{\partial x}\right), \tag{4.44}$$

where $x = i/L$ is rescaled position and $\tau = t/L^2$ is hydrodynamic rescaled time. We validate the hydrodynamic temporal evolution under two scenarios: hopping with a finite range ($l_p = 2$) and hopping with an infinite range ($l_p \to \infty$). This is achieved by using a suitable initial condition $\rho(x, \tau = 0)$ and employing the respective bulk-diffusion coefficients $D_2(\rho)$ [as derived in Eq. (4.34)] and $D_\infty(\rho)$ [as derived in Eq. (4.41)] in Eq. (4.44), which we solve

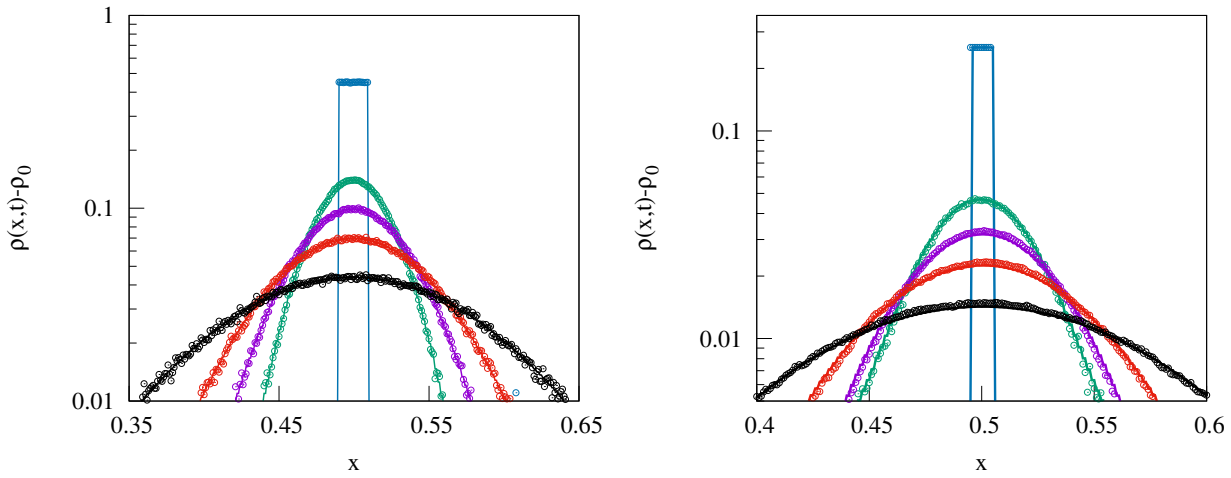

Figure 4.2: Density relaxation in gLLG from a two-step initial condition. Density profiles $\delta\rho(x,t) = \rho(x,t) - \rho_0$ (line) obtained by numerically integrating Eq. (4.44) are compared with those obtained from microscopic simulations (points) at $t = 0$ (blue points, initial profile), $t = 0.5 \times 10^{-3}$ (green), 10^{-3} (gagenta), 2×10^{-3} (red) and 5×10^{-3} (black). Left panel: finite range hopping with $l_p = 2$, $\rho_0 = 0.5$ and $\rho_1 = 0.5$; right panel: infinite range hopping with $l_p \to \infty$, $\rho_0 = 0.75$, $\rho_1 = 0.25$. We take $w = 0.1$ and $L = 1000$ in both cases.

through numerical integration using the Euler scheme. To this end, we consider a step-like initial density perturbation of height ρ_1 and width w over a uniform density profile ρ_0, i.e., the initial density profile is given by

$$\rho(x,0) = \begin{cases} \rho_0 + \rho_1 & \text{for } |\mathrm{x} - \frac{1}{2}| < \frac{\mathrm{w}}{2}, \\ \rho_0 & \text{otherwise.} \end{cases} \tag{4.45}$$

In Fig. 4.2, we present the numerically obtained excess density profile $\delta\rho(x,\tau) = \rho(x,\tau) - \rho_0$, as a function of rescaled position $x = i/L$ at different hydrodynamic times: $\tau = 0$ (blue points, the initial profile), $\tau = 0.5 \times 10^{-3}$ (green), $\tau = 10^{-3}$ (gagenta), $\tau = 2 \times 10^{-3}$ (red), and $\tau = 5 \times 10^{-3}$ (black). This is illustrated for both finite-range hopping ($l_p = 2$, $\rho_0 = 0.5$, left panel) and infinite-range hopping ($l_p \to \infty$, $\rho_0 = 0.75$, right panel). In both scenarios, we set $L = 1000$ and $\alpha = \beta = 1/2$. The simulation results (depicted as points) exhibit a strong agreement with the hydrodynamic theory predictions (represented by lines). This excellent alignment between simulation and theory collectively validates the hydrodynamic density evolution described in Eq. (4.44) and the bulk-diffusion coefficients of the model in the cases of $l_p = 2$ and $l_p \to \infty$.

4.3.4 Verification of Einstein Relation for gLLG

In the introduction section (see Sec. 1.4.1), we show how one can formulate an effective equilibrium-like fluctuating hydrodynamic description using the framework of the macro-

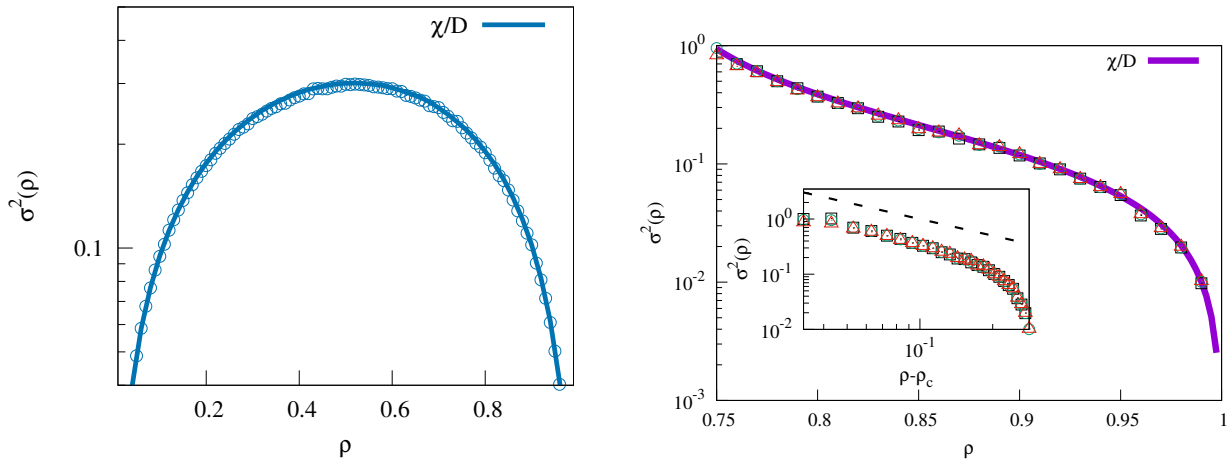

Figure 4.3: *Verification of Einstein relation Eq. (4.46) in gLLG.* Scaled variance $\sigma^2(\rho)$ of subsystem particle number obtained from simulations (points) and the ratio $\chi(\rho)/D(\rho)$ of transport coefficients obtained from hydrodynamic theory (lines) is plotted as a function of density ρ. For $l_p = 2$ (left-panel), system size $L = 5000$ and subsystem of size $l_{sub} = 50$; for $l_p \to \infty$ (right-panel), $L = 10000$ and subsystem sizes $l_{sub} = 50$ (red triangles), 100 (green circles) and 200 (black rectangles); we throughout take $\alpha = \beta = 1/2$ and thus $\rho_c = 1/\sqrt{2}$. Inset, right panel: We plot scaled variance $\sigma^2(\rho)$ as a function of $(\rho - \rho_c)$, where the guiding dashed line shows the simple-pole singularity $\sigma^2 \sim (\rho - \rho_c)^{-1}$ as predicted by Einstein relation Eq. (4.46).

scopic fluctuation theory (MFT) [115, 118]. Indeed, one of the most important achievements of MFT is the prediction of the existence of equilibrium-like Einstein Relation (ER) for nonequilibrium diffusive systems. According to the ER, for periodic driven-diffusive systems, there exists a one-to-one correspondence between the macroscopic transport coefficients and particle number fluctuation. More specifically, the ratio between the macroscopic transport coefficients, the mobility $\chi(\rho)$, and the bulk-diffusion coefficient $D(\rho)$ is identically equal to the scaled subsystem particle number fluctuation $\sigma^2(\rho)$, i.e.,

$$\frac{\chi(\rho)}{D(\rho)} = \sigma^2(\rho), \tag{4.46}$$

where ρ is the global density and we define $\sigma^2(\rho)$ as the following:

$$\sigma^2(\rho) = \lim_{1 \ll l_{sub} \ll L} \frac{\langle (\Delta n)^2 \rangle}{l_{sub}}. \tag{4.47}$$

Here l_{sub} is the subsystem size and $\langle (\Delta n)^2 \rangle$ is the particle number fluctuation within it.

For the analytical proof of Eq. (4.46) for gLLG, we urge the reader to look at the next Chapter in Sec. 5.2.6. In this section, we provide the numerical verification of ER for gLLG in Fig. 4.3, both in the limit of finite ($l_p = 2$, left panel) and infinite ($l_p \to \infty$, right panel)

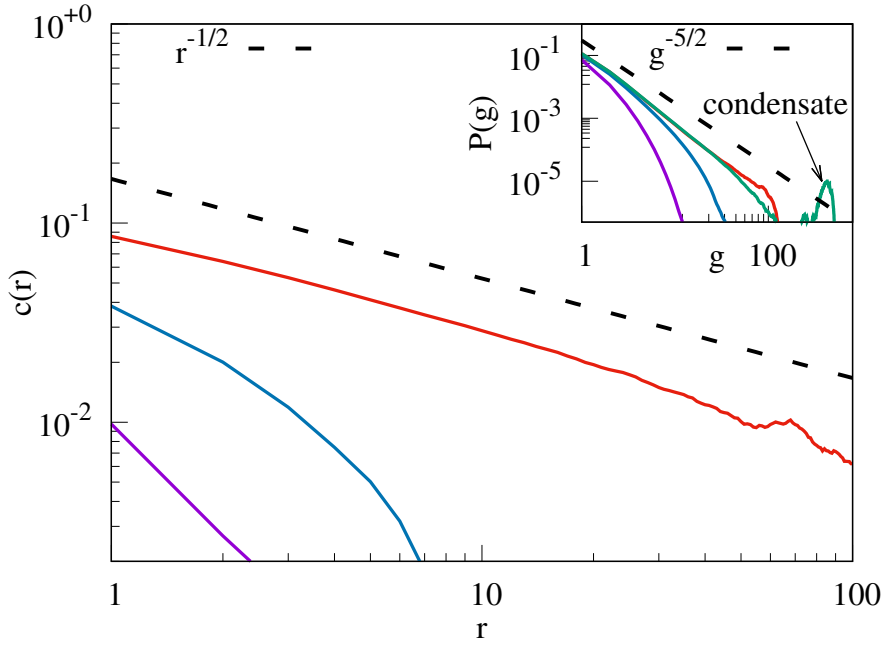

Figure 4.4: Two-point correlation function $c(r) = (\langle \eta_i \eta_{i+r} \rangle - \rho^2)$, in the limit $l_p \to \infty$, is plotted as a function of distance r is plotted for densities $\rho = 0.9$ (magenta), 0.8 (sky-blue), and 0.71 (red, near criticality). The power-law tail of $c(r) \sim r^{-1/2}$ near critical point $\rho = 0.71$ demonstrates the presence of long-ranged spatial correlation in the system. Inset: Gap distribution $P(g)$ is plotted as a function of gap size g is for densities $\rho = 0.9$ (magenta), 0.8 (sky-blue), 0.71 (red, near criticality) and 0.5 (green).

hopping range. We plot the numerically obtained scaled particle number fluctuation $\sigma^2(\rho)$, depicted as points, and analytically derived ratio $\chi(\rho)/D(\rho)$ [using Eqs. (4.34) and (4.35) for $l_p = 2$ and Eqs. (4.41) and (4.43) for $l_p \to \infty$], represented as lines, against global density ρ for finite ($l_p = 2$, left panel) and infinite ($l_p \to \infty$, right panel) range hopping. We throughout fix the hopping rates as $\alpha = \beta = 1/2$. For both hopping ranges, we find a remarkable agreement between the L.H.S (lines) and R.H.S (points) of Eq. (4.46), thereby suggesting the existence of ER in gLLG. It is important to note that while the number fluctuation remains finite for any density and activity in the scenario of finite range hopping, it diverges for infinite range hopping as the critical density ρ_c is approached, with $\rho_c = 1/\sqrt{2}$, and continues to diverge thereafter. In the inset of the right panel of Fig. 4.3, we illustrate the scaled number fluctuation $\sigma^2(\rho)$ for infinite range hopping plotted against $\Delta = (\rho - \rho_c)$, revealing that, akin to mobility, the number fluctuation also exhibits a straightforward pole singularity $\sigma^2 \sim \Delta^{-1}$, in accordance with the prediction of the Einstein relation.

4.3.5 "Superfluid"-like transition and "giant" number fluctuation for infinite range hopping

As indicated in Sec. 4.3.2, when considering the generalized long-ranged lattice gas (gLLG) with infinite range hopping, it exhibits a "superfluid"-like transition once the density surpasses a critical threshold, given by $\rho \leq \rho_c = \tilde{q}^{1/2}$ or when the scaled activity exceeds $\tilde{q} \geq \tilde{q}_c = \rho^2$, where $\tilde{q} = q/(\alpha + \beta)$. Examining this phase transition in the light of a previously investigated mass aggregation model [166], which represents the unbounded counterpart of gLLG with infinite range hopping, provides valuable insights by analyzing the dynamics of gaps or vacancies. Consider two neighboring gaps that are initially separated by a particle. As the particle undergoes a long-range hop, the two gaps merge to form a larger gap. The inability of the reverse process, where a larger gap splits into two smaller gaps upon a particle's long-range hop, is the specific cause for the violation of detailed balance within the system. It is evident that the irreversibility of the coalescence process described above promotes the creation of larger gaps. Conversely, short-range hops have the opposite effect, diminishing a gap as particles from either side invade inside and consequently fragment the vacancy cluster. When the density is below the critical value $\rho_c = \tilde{q}^{1/2}$, the system undergoes self-organization where long-hops prevail over short-hops. This results in the emergence of a macroscopic gap, essentially a "condensate" of vacancies or holes. The formation of such a vacancy cluster with a macroscopic size breaks down the translational symmetry of the system, leading to the formation of an "ordered" phase in the system. Conversely, when the density is equal to or exceeds ρ_c (or when $q \leq \tilde{q}_c$), the system maintains homogeneity and the associated phase is termed "disordered".

Notably, the simple-pole singularity in the mobility $\chi(\rho)$ associated with the ordered phase has interesting implications, listed as follows:

(i) *Simple-pole singularity in number/density fluctuation.*– As shown in the right panel of Fig. 4.3 for infinite range hopping, particle-number fluctuation diverges near criticality (and remains diverging beyond). This can be understood from the Einstein relation $\sigma^2(\rho) = \chi(\rho)/D(\rho)$ as in Eq. (4.46), which immediately implies a simple pole in the scaled subsystem particle-number fluctuation $\sigma^2(\rho) \sim (\rho - \rho_c)^{-1}$, leading to diverging particle-number fluctuation near criticality (see inset of Fig. 4.3).

(ii) *Gap distribution.*– For densities below the critical value ρ_c (or $\tilde{q} > \tilde{q}_c$), the system enters the ordered phase with a bimodal gap distribution, implying a condensation tran-

sition (CT) [166]. In accordance with Ref. [129] and utilizing the fluctuation-response relation given in Eq. (4.46), it can be demonstrated that the simple-pole singularity structure of the scaled number fluctuation $\sigma^2(\rho) \sim (\rho - \rho_c)^{-1}$ corresponds to a gap distribution $P(g) \sim \text{const.} g^{-5/2} + \text{const.} \delta[g - (\tilde{\rho} - \tilde{\rho_c})N]$, exhibiting a power-law tail near criticality and a "delta-peak" at a macroscopic gap of size $(\tilde{\rho} - \tilde{\rho_c})N$ in the ordered phase. Here, $\tilde{\rho}$ represents the corresponding mass density in UgLLG, as defined in Equation (4.1). We refer to Appendix C.4 for details. In the inset of Figure 4.4, the gap distribution $P(g)$ is plotted against the gap size g for various densities: $\rho = 0.9$ (gagenta), 0.8 (sky-blue), 0.71 (red, near criticality), and 0.5 (green, ordered phase). It is evident that near criticality (red line) and beyond criticality ($\rho < 1/\sqrt{2}$), there is a power-law tail, and in addition to that, a peak emerges at a large gap, indicating the formation of a macroscopic-sized vacancy (hole) cluster in the system. Importantly, the transition from the homogeneous fluid phase to the translational-symmetry-broken ordered phase, characterized by the coexistence of two distinct densities, is of the first order.

(iii) *Long-ranged spatial correlations.*– Not surprisingly, as the system achieves infinite mobility, long-ranged spatial correlations are expected to develop within it. These correlations are not only present near the critical point but also in the ordered phase. Following Refs. [129] and [167], we calculate the two-point density correlation $c(r)$ for gLLG in the near-critical regimes, see Appendix C.5 for details. We find $c(r)$ exhibits a power-law tail with an exponent of 1/2 and a cutoff distance known as the correlation length, denoted as $\xi \sim (\rho - \rho_c)^{-\nu}$ with $\nu = 2$ (as indicated below using simple scaling arguments), i.e., $c(r) = (\langle \eta_i \eta_{i+r} \rangle - \rho^2) \sim r^{-1/2} \exp(-r/\xi)$. In Fig. 4.4, we plot the numerically obtained correlation function $c(r)$ against distance r for different densities $\rho = 0.9$ (gagenta), 0.8 (sky-blue), and 0.71 (red). As we approach criticality, it becomes evident that the system does exhibit long-ranged correlations. Specifically, at a density of $\rho = 0.71$ (near criticality, indicated by the red line), the correlation function $c(r)$ follows the theoretically derived $r^{-1/2}$ power-law tail, as illustrated by the black-dotted line in the plot.

(iv) *Giant number fluctuations.*– The existence of long-ranged correlations results in significant fluctuations in the number of particles, often referred to as "giant" number fluctuations, both near criticality and in the ordered phase of the system. In the case of infinite-range hopping, we can derive, using straightforward scaling arguments, the standard deviation of the subsystem particle number near criticality as $\sqrt{\langle (\Delta n)^2 \rangle} \sim \langle n \rangle^{\alpha'}$, where $\alpha' > 1/2$. These diverging fluctuations persist in the bulk even in the ordered phase, as altering the global density in this phase only impacts the condensate size while leaving the density of

the bulk "superfluid" unchanged. Indeed, we can connect the power-law tail to the density correlation with the diverging number fluctuation in the following way. Near criticality as $\Delta = (\rho - \rho_c) \to 0$ and correlation length $\xi \sim \Delta^{-\nu}$, the scaled variance $\sigma^2(\rho)$ is related to the integrated correlation function as $\sigma^2(\rho) \simeq \int c(r)dr \sim \int_0^\xi r^{-1/2}dr \sim \xi^{1/2} \sim \Delta^{-\nu/2}$. Now explicitly using simple-pole singularity of scaled number fluctuation $\sigma^2 \sim \Delta^{-1} \sim \Delta^{-\nu/2}$, we obtain $\nu = 2$. Moreover, taking the correlation length $\xi \sim l_{sub} \gg 1$ (but, assuming $l_{sub} \ll L$), the standard deviation of subsystem particle-number n in a subsystem of length l_{sub} is given by $\sqrt{\langle(\Delta n)^2\rangle} = \sqrt{(\langle n^2\rangle - \langle n\rangle^2)} \sim \sqrt{l_{sub}\xi^{1/2}} \sim (l_{sub})^{\alpha'}$, leading to the scaling exponent $\alpha' = 3/4$ corresponding to "giant" number fluctuation with the standard deviation $\sqrt{\langle(\Delta n)^2\rangle} \sim \langle n\rangle^{\alpha'}$. However, when the subsystem size $l_{sub} \sim L$ is of order system size, there is a strong finite-size effect, and the correlation length, which is related to the width of mass fluctuation in UgLLG, has a scaling $\xi \sim L^{2/3}$ [168]. Interestingly, in that case, the standard deviation of subsystem particle-number scales slightly differently and crosses over to the following scaling of the giant number fluctuation $\sqrt{\langle(\Delta n)^2\rangle} \sim \sqrt{L\xi^{1/2}} \sim L^{\alpha'}$ with exponent $\alpha' = 2/3$. As evident from the above discussions, diverging mobility, through Einstein relation between the transport coefficients and fluctuation, is intimately connected to the giant number fluctuation in the system.

4.4 Summary and concluding remarks

In this study, we obtained an exact hydrodynamic structure in one dimension for a minimal model of hardcore SPPs known as the generalized long-ranged lattice gas (gLLG). Despite violating detailed balance at the microscopic level, this model is suitable for analytic studies. The model is defined by two length scales that employ short- (nearest neighbor) and long-ranged symmetric hopping while adhering to the hardcore constraint. Notably, nearest-neighbor hopping is reminiscent of thermal or passive diffusion and long-ranged hopping corresponds to the ballistic or active motion of RTPs on the persistence time scale. As a result, we propose gLLG as the simplest nontrivial variant of thermal RTPs that is analytically accessible.

We investigate the response of the system to a small perturbation by applying a small biasing force following macroscopic fluctuation theory (MFT), which causes particle movement to be slightly asymmetric: slightly biased toward the force direction and vice versa. As a result, the hydrodynamic evolution of local density can be expressed by two density- and activity-dependent macroscopic transport coefficients: the bulk-diffusion coefficient and the mobility. If the typical length of long hops is finite, these transport coefficients remain finite and bounded, indicating no anomalies within the system. However, when the typical long-range hop length diverges, as considered in Sec. 4.3.2, we obtain an explicit analytical

density- and activity-dependent form of transport coefficients and find the mobility has a pole, it *diverges* upon tuning global density and activity, while the bulk-diffusion coefficient remains finite throughout. This diverging instability in mobility has a rich consequence: it indicates an emerging "superfluidity", which further causes "giant" number fluctuation in this minimal model system. The latter is supplemented by the existence of an equilibrium-like Einstein Relation (ER), relating number fluctuation $\sigma^2(\rho)$ to the ratio of the transport coefficients $\sigma^2(\rho) = \chi(\rho)/D(\rho)$, which we have shown to exist in gLLG despite it violates detailed balance at the microscopic level.

Physically, the emerging "superfluidity" corresponds to a condensation transition in the system resulting from the opposing effects of short- and long-range hopping. Indeed, in the diverging hop length regime, an entire vacancy cluster can move in unison and merge with neighboring vacancies to form a larger cluster, introducing clustering, or cooperativity, into the system. Short-range hops, on the other hand, favor cluster fragmentation and homogenize the system. Thus, in the limit of infinite-ranged hopping and beyond the critical values of density and activity, long-hop dominates over short-hop, which results in vacancy clusters growing to macroscopic size and forming a "condensate" with a diverging instability of mobility at the critical point, resulting in "superfluidity" in the system, while the bulk-diffusion coefficient remains finite throughout. Interestingly, this stands in stark contrast to the equilibrium (second-order) phase transition, which is characterized by the vanishing instability of the bulk-diffusion coefficient and thus results in *critical slowing down* in the system [169, 170]. Notably, similar to equilibrium systems, the phenomenology of motility-induced phase separation (MIPS) [22] is also based on the same concept of diffusive instability at the critical point. Therefore, our first principle theory opens up the possibility of a new mechanism of clustering transition in SPPs.

Our study could be relevant in the context of collective behaviors of micro-organisms as in a bacterial colony. It is interesting to note that superfluidlike transitions have been observed in the past experimentally in bacterial suspensions [171], where viscous resistance to the bacteria moving in the surrounding solvent medium is shown to be highly reduced. Though the bacterial superfluidity is influenced by various fluid dynamical interactions between swimming bacteria and the solvent [172], our hydrodynamic theory could provide another route to understanding the experimentally observed reduced viscosity in bacterial colonies. Overall, we believe our analytic results provide a fresh perspective on the collective behaviors in self-propelled particle systems, which are often seen in the light of motility-induced phase separation [20, 22].

5

Dynamic characterization of "superfluid"-like transition in a model of self-propelled particles

5.1 Introduction

In the previous chapter, we studied a condensation transition in a prototypical variant of thermal interacting run-and-tumble particles (RTPs), called generalized long-ranged lattice gas (gLLG), arising due to the intricate interplay between the *passive* or thermal diffusion, *active* or ballistic long-range motion and interaction. Interestingly, the mechanism of this nonequilibrium transition does not have an equilibrium counterpart. The latter is usually characterized by the vanishing bulk-diffusion coefficient, thus leading to the critical slowing down in the system and eventually forming phase separation. On the contrary, the former is triggered by a diverging instability of the mobility, which leads to a "superfluid"-like critical state; notably, the bulk-diffusion coefficient remains finite at the critical point. Not surprisingly, there is no generic mechanism to account for such a nonequilibrium phase transition. It is therefore instructive to explore the consequences of the diverging instability in mobility which could help in understanding the mechanism of the observed transition better.

In this chapter, we investigate the mechanism for the mobility-driven clustering tran-

sition in gLLG by characterizing the fluctuations of the system's time-integrated currents. To this end, we employ the microscopic theory described in Chapter 3. When the typical long-range hopping length is finite, the time-integrated current fluctuation exhibits the usual characteristics as observed in the case of long-ranged lattice gas (LLG) in Chapter 3. However, in the case of infinite-range hopping, the divergence in the mobility in the system shows anomalous current fluctuations at the critical phase: the fluctuation of time-integrated current across a bond is *enhanced*, and the scaled fluctuation of the space-time integrated current across the entire system is shown to be *divergent*. Moreover, we analytically establish a direct correspondence between the scaled space-time integrated current fluctuation and the density fluctuation of the system through an equilibrium-like Einstein relation. Therefore, our microscopic theory captures the anomalous current fluctuation through the diverging instability in the mobility, which further accounts for the diverging fluctuation in the density of the system. Although diverging density fluctuation is also observed in typical equilibrium phase transitions, occurring through the mechanism of *critical slowing down* of the system, however, such a diverging current fluctuation is a distinct feature of nonequilibrium systems. Thus, our microscopic analysis in this chapter provides a new mechanism of current fluctuation-induced phase transition in the system.

We organize the chapter as follows. We calculate the first moment of time-integrated bond-current and identify the transport coefficients, bulk-diffusion coefficient, and mobility in Sec. 5.2.1. We next decompose the bond-current into slow and fast components in Sec. 5.2.2, followed by introducing the closure or truncation scheme to calculate dynamic correlation in Sec. 5.2.3. We then proceed to calculate the fluctuation of time-integrated bond-current in Secs. 5.2.4. In Sec. 5.3, we verify the theoretical predictions both for finite as well as infinite range hopping. Finally, we summarize the chapter with some concluding remarks in Sec. 5.4.

5.2 Theory for bond-current fluctuation

In this section, we use the recently developed microscopic theoretical framework [114], also discussed in Chapter 3, to calculate current fluctuations in gLLG, defined in Sec. 4.2, analytically. We also supplement our analytic results with direct Monte Carlo simulation results.

5.2.1 Average bond-current

To begin with, let us first define the time-integrated current $Q_i(t)$ across a bond $[i, i+1]$, which quantifies the net flow of particles to the right via the same bond up to time t. Notably, $Q_i(t)$ is a macroscopic and experimentally realizable quantity that is linked to its microscopic

equivalent, instantaneous current $J_i(t)$, as follows:

$$J_i(t) \equiv \lim_{\Delta t \to 0} \frac{\Delta Q_i}{\Delta t}, \tag{5.1}$$

where $\Delta Q_i(t) = \int_t^{t+\Delta t} J_i(t)dt$ is the time-integrated bond-current in the time interval Δt. This section will characterize the average instantaneous current $\langle J_i(t)\rangle$. It is important to note that, as the model dynamics incorporates particle hopping that is symmetric or unbiased, we expect that $\langle J_i(t)\rangle$ will be generated solely by the density gradient, which will lead to the determination of the bulk-diffusion coefficient $D(\rho)$ of the system, as followed by the Fick's law. However, to determine the other transport coefficient, i.e., collective mobility $\chi(\rho)$, we suitably bias the system following the prescription of the macroscopic fluctuation theory (MFT) which we applied in Chapter 4 and also discussed in the introduction. In that case, the average instantaneous current of the biased system takes the drift-diffusion form of Eq. (1.23), which would enable the determination of the mobility $\chi(\rho)$ of the system. Although, we have already determined $D(\rho)$ and $\chi(\rho)$ for gLLG using the local density update dynamics in the previous chapter, this chapter implements a different strategy to characterize them from the update dynamics of bond-currents, i.e., $Q_i(t)$.

Before delving into the calculational details, we now define the following stochastic variables,

$$\mathcal{U}_{i+l}^{(l)} \equiv \overline{\eta}_{i+1}\overline{\eta}_{i+2}\ldots\overline{\eta}_{i+l}, \tag{5.2}$$

$$\mathcal{V}_{i+l+1}^{(l+2)} \equiv \eta_i\overline{\eta}_{i+1}\overline{\eta}_{i+2}\ldots\overline{\eta}_{i+l}\eta_{i+l+1}, \tag{5.3}$$

where $\bar{\eta}_i = (1-\eta_i)$, $\mathcal{U}^{(l)}$ and $\mathcal{V}^{(l+2)}$ are indicator functions for a single site being vacant, l consecutive sites being vacant and a vacancy cluster to be of size l, respectively. Notably, for a particle moving rightward (leftward) across a bond, current across the bond is increased (decreased) by unity. By considering this, the continuous-time evolution for time-integrated current $Q_i(t)$ in an infinitesimal time interval $[t, t+dt]$ can be written as

$$Q_i(t+dt) = \begin{cases} Q_i(t)+1, & \text{prob.} \quad \mathcal{P}_i^R(t)dt, \\ Q_i(t)-1, & \text{prob.} \quad \mathcal{P}_i^L(t)dt, \\ Q_i(t), & \text{prob.} \quad 1-(\mathcal{P}_i^R+\mathcal{P}_i^L)dt, \end{cases} \tag{5.4}$$

where $\mathcal{P}_i^R dt$ and $\mathcal{P}_i^L dt$ are probabilities of the hopping events which we will determine now. To compute the hopping rate $\mathcal{P}_i^R$, we consider below all possible rightward hopping events

which generate unit increment in Q_i across the bond $[i, i+1]$:

Short-range hop: With rate α, a particle from the site i hops symmetrically to the right neighboring site, i.e., $i+1$, provided the site is unoccupied. In this case, the corresponding probability term is given by $\mathcal{P}_i^{R,sh}dt$, where

$$\mathcal{P}_i^{R,sh} = \frac{\alpha}{2}\eta_i(1-\eta_{i+1}) = \frac{\alpha}{2}\left(\eta_i - \mathcal{V}_{i+1}^{(2)}\right). \tag{5.5}$$

Long-range hop: In this case, particle symmetrically hops with rate β and depending on the gap size g along the hopping direction and the attempted hop-length l_p, we consider the following two cases:

I. $g < l_p$: In this particular case of gap size being smaller than the attempted hopping length, a particle traverses the entire gap of length g and crosses the bond $[i, i+1]$ only when the bond resides within the vacancy or gap cluster. We also realize that, for a fixed g, current across a particular bond $[i, i+1]$ can be contributed by translating the entire cluster in g possible ways. The corresponding contribution to the probability is given by $P_i^{R,g<l_p}dt$ where,

$$P_i^{R,g<l_p} = \frac{\beta}{2}\sum_{k=1}^{g}\mathcal{V}_{i+k+1}^{(g+2)}. \tag{5.6}$$

II. $g \geq l_p$: In the opposite scenario, the particle hops by length l_p, and for the contribution of Q_i caused by the above move, the particle must cross the bond $[i, i+1]$. Following the preceding argument, we obtain current contribution across the bond $[i, i+1]$ in l_p in different ways. The corresponding contribution to the probability is given by $P_i^{R,g\geq l_p}dt$ where,

$$P_i^{R,g\geq l_p} = \frac{\beta}{2}\sum_{k=1}^{l_p}\left(\mathcal{U}_{i+k}^{(l_p)} - \mathcal{U}_{i+k}^{(l_p+1)}\right). \tag{5.7}$$

Now, considering all possible gap sizes and using the above contributions in Eqs. (5.5), (5.6), and, (5.7), the total rightward hopping rate is calculated to be

$$\mathcal{P}_i^R \equiv \frac{\beta}{2}\left[\sum_{k=1}^{l_p}\left(\mathcal{U}_{i+k}^{(l_p)} - \mathcal{U}_{i+k}^{(l_p+1)}\right) + \sum_{g=1}^{l_p-1}\sum_{k=1}^{g}\mathcal{V}_{i+k+1}^{(g+2)}\right] + \frac{\alpha}{2}\left(\eta_i - \mathcal{V}_{i+1}^{(2)}\right). \tag{5.8}$$

Similarly, considering the leftward hopping events, we directly obtain the leftward hopping rate

$$\mathcal{P}_i^L \equiv \frac{\beta}{2}\left[\sum_{k=1}^{l_p}\left(\mathcal{U}_{i+k-1}^{(l_p)}-\mathcal{U}_{i+k}^{(l_p+1)}\right)+\sum_{g=1}^{l_p-1}\sum_{k=1}^{g}\mathcal{V}_{i+k}^{(g+2)}\right]+\frac{\alpha}{2}\left(\eta_{i+1}-\mathcal{V}_{i+1}^{(2)}\right). \tag{5.9}$$

By using the above microscopic update rules and doing some straightforward algebraic manipulations, the average instantaneous current $\langle J_i(t)\rangle$ can be written as [112]

$$\langle J_i(t)\rangle = \frac{\alpha}{2}(\langle\eta_i\rangle-\langle\eta_{i+1}\rangle)+\frac{\beta}{2}\left[\sum_{g=1}^{l_p-1}\left(\langle\mathcal{V}_{i+g+1}^{(g+2)}\rangle-\langle\mathcal{V}_{i+1}^{(g+2)}\rangle\right)+\left(\langle\mathcal{U}_{i+l}^{(l_p)}\rangle-\langle\mathcal{U}_{i}^{(l_p)}\rangle\right)\right]. \tag{5.10}$$

It is important to note that $\langle J_i(t)\rangle$ in Eq. (5.10) is expressed as the gradient of the local observables $\langle\eta\rangle$, $\langle\mathcal{V}^{(g+2)}\rangle$, and, $\langle\mathcal{U}^{(l_p)}\rangle$, which clearly suggests the system to be of *gradient* type [113, 119]. Now, at large time, we may assume the system to attain a *local steady state*, which implies that the time evolution of the above observables is effectively governed by the evolution of the conserved local density field. In that case, using Taylor's series expansion, one can write the average instantaneous current in the form of diffusive current in the following manner:

$$\langle J_i(t)\rangle \simeq -D(\rho)[\langle\eta_{i+1}(t)\rangle-\langle\eta_i(t)\rangle] \tag{5.11}$$

where the bulk-diffusion coefficient $D(\rho)$ is a function of the global density ρ and is given by,

$$D(\rho) = \frac{\alpha}{2}-\frac{\beta}{2}\frac{\partial}{\partial\rho}\left[\sum_{g=1}^{l_p-1}g\langle\mathcal{V}^{(g+2)}\rangle(\rho)+l_p\langle\mathcal{U}^{(l_p)}\rangle(\rho)\right], \tag{5.12}$$

$$= \frac{\alpha}{2}-\frac{\beta}{2}\frac{\partial}{\partial\rho}\left[\rho\left(\sum_{g=1}^{l_p-1}gP(g)+l_p\sum_{g=l_p-1}^{\infty}(g-l+1)P(g)\right)\right]. \tag{5.13}$$

Note that, we have arrived at Eq. (5.13) by using the following identities,

$$\langle\mathcal{V}^{(g+2)}\rangle(\rho) = \rho P(g|\rho), \tag{5.14}$$

$$\langle\mathcal{U}^{(l)}\rangle(\rho) = \rho\sum_{g=l}^{\infty}(g-l+1)P(g|\rho), \tag{5.15}$$

expressing the correlation functions $\langle\mathcal{V}^{(g+2)}\rangle(\rho)$ and $\langle\mathcal{U}^{(l)}\rangle(\rho)$ as a function of the gap-distribution function $P(g)$. Notably, Eq. (5.11) is the microscopic Fick's law that connects the instanta-

neous bond-current and the density gradient through the bulk-diffusion coefficient $D(\rho)$ of the system. However, the application of a small bias will modify the bond-current to possess the drift-diffusion structure of Eq. (1.23), which allows for the determination of the linear response function or mobility $\chi(\rho)$ of the system. This method is outlined below.

Current in presence of small bias: calculation of mobility

To calculate the mobility $\chi(\rho)$ for gLLG, we study the system when subject to a vanishingly small biasing force F along a particular direction [say rightward]. Notably, due to the applied force, particle hopping along the same direction is biased slightly, which in turn induces a drift current in addition to the diffusive current in Eq. (5.11). In the spirit of local detailed balance, we now incorporate the effect of bias in the modified rate of microscopic hopping event from the site i to j in the following manner [118]:

$$c_{i\to j}^{(F)} \simeq c_{i\to j}\exp\left(\frac{F(j-i)}{2}\right), \tag{5.16}$$

$$= c_{i\to j}\left[1+\frac{F(j-i)}{2}\right]+\mathcal{O}(F^2), \tag{5.17}$$

where $c_{i\to j}$ is the corresponding unbiased hopping rate, with values α and β for short- and long-range hopping, respectively. Furthermore, the exponential term in Eq. (5.16) is the extra energy cost due to the applied force F for the abovementioned hopping event, which we retain up to linear order in Eq. (5.17) because F is vanishingly small. Using the modified hopping rates in Eq. (5.17), the net rightward and leftward hopping rates that contribute to the unit increment and decrement of $Q_i(t)$ are given by,

$$\mathcal{P}_i^{R,F} \equiv \frac{\beta}{2}[(1+\frac{Fl_p}{2})\sum_{k=1}^{l_p}(\mathcal{U}_{i+k}^{(l_p)}-\mathcal{U}_{i+k}^{(l_p+1)})+\sum_{g=1}^{l_p-1}(1+\frac{Fg}{2})\sum_{k=1}^{g}\mathcal{V}_{i+k+1}^{(g+2)}]+\frac{\alpha}{2}(1+\frac{F}{2})(\eta_i-\mathcal{V}_{i+1}^{(2)}), \tag{5.18}$$

$$\mathcal{P}_i^{L,F} \equiv \frac{\beta}{2}[(1-\frac{Fl_p}{2})\sum_{k=1}^{l_p}(\mathcal{U}_{i+k-1}^{(l_p)}-\mathcal{U}_{i+k}^{(l_p+1)})+\sum_{g=1}^{l_p-1}(1-\frac{Fg}{2})\sum_{k=1}^{g}\mathcal{V}_{i+k}^{(g+2)}]+\frac{\alpha}{2}(1-\frac{F}{2})(\eta_{i+1}-\mathcal{V}_{i+1}^{(2)}). \tag{5.19}$$

Using the above-modified rates $\mathcal{P}_i^{R,F}$ and $\mathcal{P}_i^{L,F}$, the average instantaneous bond-current in the presence of bias is given by,

$$\begin{aligned}\left\langle J_i^{(F)}(t)\right\rangle &= \left[\frac{\alpha}{2}\Big(\langle\eta_i\rangle - \langle\eta_{i+1}\rangle\Big) + \frac{\beta}{2}\left\{\sum_{g=1}^{l_p-1}\Big(\langle\mathcal{V}_{i+g+1}^{(g+2)}\rangle - \langle\mathcal{V}_{i+1}^{(g+2)}\rangle\Big) + \Big(\langle\mathcal{U}_{i+l}^{(l_p)}\rangle - \langle\mathcal{U}_i^{(l_p)}\rangle\Big)\right\}\right] \\ &\quad + \frac{F}{4}\left[\alpha\Big(\langle\eta_i\rangle + \langle\eta_{i+1}\rangle - 2\langle\mathcal{V}_{i+1}^{(2)}\rangle\Big) + \beta\left\{\sum_{g=1}^{l_p-1} g\sum_{k=1}^{g}\Big(\langle\mathcal{V}_{i+k+1}^{(g+2)}\rangle + \langle\mathcal{V}_{i+k}^{(g+2)}\rangle\Big)\right.\right. \\ &\quad \left.\left. + l_p\sum_{k=1}^{l_p}\Big(\langle\mathcal{U}_{i+k}^{(l_p)}\rangle + \langle\mathcal{U}_{i+k-1}^{(l_p)}\rangle - 2\langle\mathcal{U}_{i+k}^{(l_p+1)}\rangle\Big)\right\}\right]. \qquad (5.20)\end{aligned}$$

It is worth noting that by setting $F = 0$, the above expression of $\left\langle J_i^{(F)}(t)\right\rangle$ is reduced to the same for the unbiased case, as shown in Eq. (5.10). Now, using the previously mentioned assumption of local steady-state achieved by the system at large-time, we recover the following expression of the average instantaneous bond-current:

$$\left\langle J_i^{(F)}(t)\right\rangle = -D(\rho)\left[\langle\eta_{i+1}\rangle - \langle\eta_i\rangle\right] + \chi(\rho)F, \qquad (5.21)$$

where $D(\rho)$ is the bulk-diffusion coefficient as derived in Eq. (5.13), while the response function or the mobility $\chi(\rho)$ is defined as,

$$\begin{aligned}\lim_{F\to 0}\frac{\delta\langle J_i^{(F)}\rangle}{\delta F} = \chi(\rho) &= \frac{\alpha}{2}\Big(\rho - \langle\mathcal{V}^{(2)}\rangle(\rho)\Big) + \frac{\beta}{2}\left[\sum_{g=1}^{l_p-1} g^2\langle\mathcal{V}^{(g+2)}\rangle(\rho) + l_p^2\Big(\langle\mathcal{U}^{(l_p)}\rangle(\rho) - \langle\mathcal{U}^{(l_p+1)}\rangle(\rho)\Big)\right], \\ &= \frac{\rho}{2}\left[\alpha\left(1 - P(0)\right) + \beta\left(\sum_{g=1}^{l_p-1} g^2 P(g) + l_p^2\sum_{g=l_p}^{\infty} P(g)\right)\right]. \qquad (5.22)\end{aligned}$$

Notably, in the last line of Eq. (5.22), we have expressed the correlation functions $\langle\mathcal{V}^{(g+2)}\rangle$ and $\langle\mathcal{U}^{(l_p)}\rangle$ in terms of the gap-distribution function $P(g)$ using the transformation relation shown in Eq. (5.14). It should be emphasized that the sole purpose of applying small bias F was to calculate the mobility $\chi(\rho)$, and we will now return to our original unbiased model, defined in Sec. 4.2, for which we want to calculate the current fluctuation.

5.2.2 Bond-current decomposition

Let us first rewrite the average instantaneous bond-current $\langle J_i(t)\rangle$, in the original (unbiased) model, from Eqs. (5.10) and (5.11) as follows:

$$\begin{aligned}\langle J_i(t)\rangle &= \frac{\alpha}{2}(\langle\eta_i\rangle - \langle\eta_{i+1}\rangle) + \frac{\beta}{2}\left[\sum_{g=1}^{l_p-1}\left(\langle\mathcal{V}_{i+g+1}^{(g+2)}\rangle - \langle\mathcal{V}_{i+1}^{(g+2)}\rangle\right) + \left(\langle\mathcal{U}_{i+l}^{(l_p)}\rangle - \langle\mathcal{U}_{i}^{(l_p)}\rangle\right)\right] \\ &\simeq -D(\rho)\left[\langle\eta_{i+1}\rangle - \langle\eta_i\rangle\right], \end{aligned} \tag{5.23}$$

where the bulk-diffusion coefficient $D(\rho)$ is defined in Eq. (5.13). Notably, the gradient structure of Eq. (5.23) implies that the average current $\langle J_i(t)\rangle$ is zero at the steady state when the system achieves homogeneous configuration. However, due to the stochasticity of the dynamics, we still expect a non-zero contribution of the variable $J_i(t)$ on the level of fluctuations. Therefore, to properly incorporate fluctuations, we resort to the decomposition of $J_i(t)$ into the following slow and fast components:

$$J_i(t) = J_i^D(t) + J_i^{fl}(t), \tag{5.24}$$

where $J_i^D(t)$ is the stochastic diffusive current, which is characterized by very slow relaxation, and thus governs the hydrodynamic behavior of the system. We identify $J_i^D(t)$ as,

$$J_i^D \equiv \frac{\alpha}{2}(\eta_i - \eta_{i+1}) + \frac{\beta}{2}\left[\sum_{g=1}^{l_p-1}\left(\mathcal{V}_{i+g+1}^{(g+2)} - \mathcal{V}_{i+1}^{(g+2)}\right) + \left(\mathcal{U}_{i+l_p}^{(l_p)} - \mathcal{U}_{i}^{(l_p)}\right)\right]. \tag{5.25}$$

On the other hand, the fluctuating component $J_i^{fl}(t)$, which is originated due to the stochasticity in the dynamics, exhibits very fast relaxation [in fact, it is *delta* correlated in time as shown in Eq. (5.66)]. Notably, the identification of $J_i^{(D)}(t)$ in Eq. (5.25) along with Eq. (5.23) immediately implies that the average fluctuating component is identically zero, that is,

$$\langle J_i^{fl}(t)\rangle = 0. \tag{5.26}$$

It should be noted that, although $J_i^{fl}(t)$ does not contribute to the average level, it exhibits nontrivial spatiotemporal correlation and plays a crucial role in calculating the correlation and fluctuation of currents in the system. We will now analytically determine the same in the next section.

5.2.3 Correlations and fluctuations of bond-current

To begin with, we define the spatiotemporal correlation of two stochastic variables $A_r(t')$ and $B_0(t)$ in the following:

$$\begin{aligned} \mathcal{C}_r^{AB}(t',t) &= \langle A_r(t')B_0(t)\rangle_c\,, \\ &= \langle A_r(t')B_0(t)\rangle - \langle A_r(t')\rangle\,\langle B_0(t)\rangle\,. \end{aligned} \tag{5.27}$$

Let us now consider, $Q_r(t')$ and $Q_0(t)$ are the stochastic time-integrated currents, measured across bonds $(r, r+1)$ and $(0,1)$ up to times t' and t $(t' > t)$, respectively. In this section, we are going to calculate the spatio-temporal correlation between them, i.e., $\mathcal{C}_r^{QQ}(t',t)$. As we choose $t' > t$, it is easy to see that $\mathcal{C}_r^{QQ}(t',t)$ satisfies the following exact identity [114, 162]:

$$\frac{d}{dt'}\mathcal{C}_r^{QQ}(t',t) = \left\langle J_r^{(D)}(t')Q_0(t)\right\rangle_c\,, \tag{5.28}$$

where $J_r^{(D)}$ is the stochastic diffusive-current across rth bond at time t. Moreover, according to the expression of $J_r^{(D)}$ in Eq. (5.25), one finds that the calculation of two-point current-current correlation function $\mathcal{C}_r^{QQ}(t',t)$ demands to calculate two-point density-current correlator $\mathcal{C}_r^{\eta Q}(t',t)$ and two multi-point correlators $\mathcal{C}_r^{\mathcal{U}^{(l)}Q}(t',t)$ and $\mathcal{C}_r^{\mathcal{V}^{(g+2)}Q}(t',t)$, all of which are among the unknowns in the problem. However, it can be shown that the time-evolution of $\mathcal{C}_r^{\mathcal{U}^{(l)}Q}(t',t)$ and $\mathcal{C}_r^{\mathcal{V}^{(g+2)}Q}(t',t)$ depends on the higher order correlations, whose time-evolution would then throw even higher order terms, and so on. As a result, calculating these correlation functions involves solving an infinite hierarchy of equations that cannot be closed, thus making the exact determination of $\mathcal{C}_r^{QQ}(t',t)$ not possible at this stage.

To address the aforementioned difficulty, we apply here the truncation (closure) scheme, introduced in Chapter 3, that allows us to efficiently handle Eq. (5.28) and to calculate the desired quantities quite accurately. According to the scheme, on the hydrodynamic (i.e., large space-time) scale, when the fluctuations of density around the global steady-state profile are small, the gradients of the non-conserved variables $\mathcal{V}^{(g+2)}$ and $\mathcal{U}^{(l)}$ appearing in the local stochastic diffusive-current J_r^D in Eq. (5.25), can be assumed to be governed by the gradient of the conserved stochastic density or occupation variable, i.e.,

$$J_r^D(t') \simeq D(\rho)[\eta_r(t') - \eta_{r+1}(t')]. \tag{5.29}$$

A straightforward consequence of Eq. (5.29) is that, we can now simply replace the correlation between the stochastic diffusive current $J_r^D(t')$ and any arbitrary variable $B_0(t)$ as the gradient

of correlations between the stochastic density and the variable $B_0(t)$, i.e.,

$$\left\langle J_r^D(t')B_0(t)\right\rangle_c \simeq -D(\rho)\Delta_r \left\langle \eta_r(t')B_0(t)\right\rangle_c, \tag{5.30}$$

where $\Delta_r\eta_r = \eta_{r+1} - \eta_r$ is the forward difference of η_r. Now, following the above truncation scheme in Eq. (5.28), we immediately get rid of the unclosed multi-point correlators $\mathcal{C}_r^{\mathcal{U}^{(l)}Q}(t',t)$ and $\mathcal{C}_r^{\mathcal{V}^{(g+2)}Q}(t',t)$ and, the resulting time-evolution of $\mathcal{C}_r^{QQ}(t',t)$ reduces to the gradient of density-current correlation function $\mathcal{C}_r^{\eta Q}(t',t)$ as follows,

$$\frac{d}{dt'}\mathcal{C}_r^{QQ}(t',t) \simeq -D(\rho)\Delta_r\mathcal{C}_r^{\eta Q}(t',t). \tag{5.31}$$

Notably, the time-evolution of $\mathcal{C}_r^{\eta Q}(t',t)$ can be easily shown to possess a closed structure, which has the following form:

$$\frac{d}{dt'}\mathcal{C}_r^{\eta Q}(t',t) = D(\rho)\Delta_r^2\mathcal{C}_r^{\eta Q}(t',t). \tag{5.32}$$

Thus, our proposed truncation scheme in Eq. (5.30) successfully closes the hierarchy and, makes the calculation of $\mathcal{C}_r^{QQ}(t',t)$ possible. For calculational convenience, we now represent the correlators in the Fourier space by using the following transformation,

$$\tilde{\mathcal{C}}_{q_n}^{AB}(t',t) = \sum_{r=0}^{L-1}\mathcal{C}_r^{AB}(t',t)e^{iq_nr}, \tag{5.33}$$

while the inverse Fourier transform is given by

$$\mathcal{C}_r^{AB}(t',t) = \frac{1}{L}\sum_{n=0}^{L-1}\tilde{\mathcal{C}}_{q_n}^{AB}(t',t)e^{-iq_nr}, \tag{5.34}$$

where

$$q_n = \frac{2\pi n}{L}. \tag{5.35}$$

Indeed, applying the above transformation of Eq. (5.34) in Eqs. (5.31) and (5.32), we obtain greatly simplified forms of time-evolution equations for the respective correlation functions in the Fourier space, i.e., for $\tilde{\mathcal{C}}_{q_n}^{QQ}(t',t)$ and $\tilde{\mathcal{C}}_{q_n}^{\eta Q}(t'',t)$. We write the corresponding solutions

in the following:

$$\tilde{\mathcal{C}}^{QQ}_{q_n}(t',t) = D(\rho)\int_t^{t'} dt''\left(1-e^{-iq_n}\right)\tilde{\mathcal{C}}^{\eta Q}_{q_n}(t'',t)+\tilde{\mathcal{C}}^{QQ}_{q_n}(t,t), \tag{5.36}$$

$$\tilde{\mathcal{C}}^{\eta Q}_{q_n}(t'',t) = e^{-\lambda_{q_n}D(\rho)(t''-t)}\tilde{\mathcal{C}}^{\eta Q}_{q_n}(t,t), \tag{5.37}$$

where $t' \geq t'' \geq t$ and λ_{q_n} is the eigenvalue of the negative discrete Laplacian operator, which is given by

$$\lambda_{q_n} = 2\left(1-\cos q_n\right). \tag{5.38}$$

Eqs. (5.36) and (5.37) clearly suggest that diiferent time correlation functions $\tilde{\mathcal{C}}^{QQ}_{q_n}(t',t)$ and $\tilde{\mathcal{C}}^{\eta Q}_{q_n}(t'',t)$ solely depend on their equal-time counterparts. To calculate the equal-time density-current correlation function $\tilde{\mathcal{C}}^{\eta Q}$, we first derive its infinitesimal time-evolution equation in the real space. Then performing Fourier transformation, as defined in Eq. (5.33), we obtain the time-evolution equation for $\tilde{\mathcal{C}}^{\eta Q}_{q_n}(t,t)$, and the corresponding solution is given by,

$$\tilde{\mathcal{C}}^{\eta Q}_{q_n}(t,t) = \int_0^t dt''' e^{-\lambda_{q_n}D(\rho)(t-t''')}\tilde{\mathcal{S}}^{\eta Q}_{q_n}(t'''), \tag{5.39}$$

where the term $\tilde{\mathcal{S}}^{\eta Q}_{q}(t''')$ takes the following form:

$$\tilde{\mathcal{S}}^{\eta Q}_{q_n}(t) = \frac{1}{\left(1-e^{-iq_n}\right)}\Big[D(\rho)\lambda_{q_n}\tilde{\mathcal{C}}^{\eta\eta}_{q_n}(t,t)-f_{q_n}(t)\Big]. \tag{5.40}$$

Notably, $f_q(t)$ is directly related to the gap-distribution $P(g,t)$ of the system and is given by

$$f_{q_n}(t) = \rho\Big[\alpha\lambda_{q_n}\Big\{1-P(0,t)\Big\}+\beta\Big\{\sum_{g=1}^{l_p-1}\lambda_{gq_n}P(g,t)+\lambda_{l_pq_n}\sum_{g=l_p}^{\infty}P(g,t)\Big\}\Big], \tag{5.41}$$

and $\tilde{\mathcal{C}}^{\eta\eta}_{q_n}(t,t)$ is the equal-time density-density correlation function, which at steady-state can be shown to satisfy the following identity:

$$\tilde{\mathcal{C}}^{\eta\eta}_{q_n} = \frac{f_{q_n}}{2D(\rho)\lambda_{q_n}}. \tag{5.42}$$

Here, the steady-state (i.e., time-independent) f_{q_n} is simply obtained by substituting the time-dependent gap distribution function $P(g,t)$ with their steady-state values in Eq. (5.41). Now, replacing the steady-state $\tilde{\mathcal{C}}^{\eta\eta}_{q_n}$ of Eq. (5.42) in Eq. (5.40) and then substituting $\tilde{\mathcal{S}}^{\eta Q}_{q_n}$ in

Eq. (5.39), we finally obtain the steady-state equal-time density-current correlation $\tilde{\mathcal{C}}^{\eta Q}_{q_n}(t,t)$ as follows:

$$\tilde{\mathcal{C}}^{\eta Q}_{q_n}(t,t) = \frac{-f_{q_n}}{2D(\rho)\lambda_{q_n}(1-e^{-iq_n})}\left(1-e^{-\lambda_{q_n}D(\rho)t}\right). \tag{5.43}$$

We now use this equal-time correlation function $\tilde{\mathcal{C}}^{\eta Q}_{q_n}(t,t)$ in Eq. (5.37) to calculate its different-time counterpart, which is given by,

$$\tilde{\mathcal{C}}^{\eta Q}_{q_n}(t'',t) = \frac{-f_{q_n}e^{-\lambda_{q_n}D(\rho)t''}}{2D(\rho)\lambda_{q_n}(1-e^{-iq_n})}\left(e^{\lambda_{q_n}D(\rho)t}-1\right), \tag{5.44}$$

where $t'' \geq t$. By plugging in the calculated $\tilde{\mathcal{C}}^{\eta Q}_{q}(t'',t)$ into Eq. (5.36), we obtain the required most general correlation function $\tilde{\mathcal{C}}^{QQ}_{q_n}(t',t)$ in terms of the equal-time correlation $\tilde{\mathcal{C}}^{QQ}_{q_n}(t,t)$, which takes the following form after inverse Fourier transform:

$$\mathcal{C}^{QQ}_{r}(t',t) \;=\; \mathcal{C}^{QQ}_{r}(t,t) - \frac{1}{2LD}\sum_{n=0}^{L-1}\frac{f_{q_n}}{\lambda^2_{q_n}}\left(e^{-\lambda_{q_n}Dt}-e^{-\lambda_{q_n}Dt'}\right)\left(e^{-\lambda_{q_n}Dt}-1\right)e^{-iq_nr}. \tag{5.45}$$

We are now at the final step of our analysis, where the only unknown quantity is the equal-time current-current correlation function $\mathcal{C}^{QQ}_{r}(t,t)$. We calculate it by deriving the infinitesimal time-evolution equation, which, when applied to the truncation approximation of Eq. (5.29), yields the following closed-form expression:

$$\mathcal{C}^{QQ}_{r}(t,t) \;=\; \Gamma_r t + \frac{D}{L}\sum_{n=0}^{L-1}\left(1-e^{-iq_n}\right)\left(2-\lambda_{rq_n}\right)\int_0^t \tilde{\mathcal{C}}^{\eta Q}_{q_n}(t,t)dt. \tag{5.46}$$

Notably, $\mathcal{C}^{QQ}_{r}(t,t)$ depends on the equal-time density-current correlation $\tilde{\mathcal{C}}^{\eta Q}_{q_n}(t,t)$, as defined in Eq. (5.43), and the other term Γ_r, which can be written in terms of the steady-state gap distribution $P(g)$, is given by

$$\Gamma_r = \rho\left[\alpha\Big\{1-P(0)\Big\}\delta_{r,0} + \beta\sum_{l=|r|+1}^{\infty}\delta_{l,l_p}\Big\{(l-\mid r\mid)\sum_{g=l}^{\infty}P(g) + \sum_{g=|r|}^{l-1}(g-\mid r\mid)P(g)\Big\}\right]; \tag{5.47}$$

It is important to note that, Γ_r physically corresponds to the strength of spatiotemporal correlation of the fluctuating component J^{fl}_r, i.e., $\langle J^{fl}_r(t)J^{fl}_0(0)\rangle = \Gamma_r\delta(t)$. Also, it is spatially extended, which is a consequence of the long-range nature of the dynamics. Now, using Eqs. (5.43) and (5.46) in Eq. (5.45), we finally obtain the following closed-form expression of

the spatiotemporal correlation of the time-integrated current for $t' > t$:

$$\begin{aligned}\mathcal{C}_r^{QQ}(t',t) &= \Gamma_r t - \frac{1}{2LD}\sum_{n=0}^{L-1}\frac{f_q}{\lambda_q^2}\left(e^{-\lambda_q Dt} - e^{-\lambda_q Dt'}\right)\left(e^{-\lambda_q Dt}-1\right)e^{-iqr}. \\ &\quad -\frac{1}{2L}\sum_{n=0}^{L-1}\frac{f_q}{\lambda_q}\left\{t - \frac{\left(1-e^{-\lambda_q Dt}\right)}{\lambda_q D}\right\}(2-\lambda_{qr}). \end{aligned} \tag{5.48}$$

5.2.4 Fluctuation of time-integrated bond-current

We immediately obtain the time-integrated bond-current fluctuation $\mathcal{C}_0^{QQ}(T,T)$ by putting $r = 0$ and $t' = t = T$ in Eq. (5.48), and the resulting expression is given by,

$$\mathcal{C}_0^{QQ}(T,T) = \Gamma_0 T - \frac{1}{L}\sum_q \frac{f_q}{\lambda_q}\left\{T - \frac{\left(1-e^{-\lambda_q DT}\right)}{\lambda_q D}\right\}, \tag{5.49}$$

which, upon using the identity

$$\sum_q \left(\frac{f_q}{\lambda_q}\right) = L\Gamma_0 - 2\chi(\rho,\gamma), \tag{5.50}$$

can be immediately written in the following form:

$$\mathcal{C}_0^{QQ}(T,T) = \frac{2\chi(\rho)}{L}T + \frac{1}{D(\rho)L}\sum_q \frac{f_q}{\lambda_q^2}\left(1-e^{-\lambda_q D(\rho)T}\right). \tag{5.51}$$

Notably, $\mathcal{C}_0^{QQ}(T,T) = \langle Q^2(T)\rangle$ in Eqs. (5.49) and (5.51) share the identical form with the one derived for the long-ranged lattice gas (LLG) in Chapter 3 [see Eq. (3.74) and (3.75)]. Therefore, to obtain the limiting behaviors of $\langle Q^2(T)\rangle$ for gLLG, we apply the same technique employed for LLG in Sec. 3.2.6, which immediately yields the following behaviors to those akin to the already derived in Eq. (3.78):

$$\langle Q^2(T)\rangle \simeq \begin{cases} \Gamma_0 T, & \text{for } DT \ll 1, \\ \frac{2\chi(\rho)}{\sqrt{\pi D(\rho)}}\sqrt{T}, & \text{for } 1 \ll DT \ll L^2, \\ \frac{2\chi(\rho)}{L}T, & \text{for } DT \gg L^2 \end{cases} \tag{5.52}$$

The above equation clearly indicates the existence of three distinct time regimes: (a) in the initial regime, $T \ll 1/D$, $\langle Q^2(T)\rangle$ follows linear growth, and the prefactor Γ_0 is readily determined from Eq. (5.47) by setting $r = 0$, (b) within the intermediate regime, $1/D \ll T \ll$

L^2/D, $\langle Q^2(T)\rangle$ exhibits subdiffusive growth, with the prefactor dependent on the mobility $\chi(\rho)$ and the bulk-diffusion coefficient $D(\rho)$, (c) in the final regime, $T \gg L^2/D$, the subdiffusive growth transitions to a linear or diffusive one, where the growth law is solely governed by the mobility $\chi(\rho)$ and the system size L.

Interestingly, at large times $T \gg 1/D$ and large system sizes, the R.H.S of Eq. (5.51) contributes in the $q \to 0$ limit. Therefore, in order to characterize fluctuation at large times, we need to perform a small q expansion in Eq. (5.51). This is done by simply putting $\lambda_q \simeq q^2$, which quite strikingly yields $f_q/\lambda_q = \chi$ and the resulting equation can be expressed as the following scaling form:

$$\frac{D}{2\chi L}\langle Q^2(T)\rangle = \mathcal{W}\left(\frac{DT}{L^2}\right). \tag{5.53}$$

The scaling function is calculated exactly within the truncation scheme and is given by the following series,

$$\mathcal{W}(y) = y + \lim_{L\to\infty} \frac{1}{L^2}\sum_q \frac{1}{\lambda_q}\left(1 - e^{-\lambda_q y L^2}\right). \tag{5.54}$$

Upon performing an asymptotic analysis to obtain the behavior of $\mathcal{W}(y)$ in the two limiting cases when $y \ll 1$ and $y \gg 1$, we find the following relation,

$$\mathcal{W}(y) \simeq \begin{cases} \sqrt{y/\pi}, & \text{for } y \ll 1, \\ y, & \text{for } y \gg 1. \end{cases} \tag{5.55}$$

Undoubtedly, Eqs. (5.52), (5.53), (5.54), and (5.55) constitute the main results in our analysis so far. We will explicitly verify them for gLLG with finite-range hopping ($l_p = 2$), as well as characterize their fate when hopping with infinite-range, particularly at the critical point in sections 5.3.1 and 5.3.2, respectively.

5.2.5 Space-time integrated current fluctuation

So far in our analysis, we have restricted ourselves to the fluctuation of time-integrated current across a bond. However, in this section, we shift our attention towards describing the fluctuation characteristics of the total space-time integrated current $Q_{tot}(L,T)$ of the system, as defined by

$$Q_{tot}(L,T) = \sum_{i=0}^{L-1} Q_i(T) = \int_0^T dt \sum_{i=0}^{L-1} J_i(t). \tag{5.56}$$

Now, utilizing the decomposition scheme outlined in Eq. (5.24), we can break down the instantaneous bond current $J_i(t)$ into its diffusive component $J_i^{(D)}(t)$ and fluctuating component $J_i^{(fl)}(t)$. Additionally, since the system under consideration here is periodic, we can further utilize the identity $\sum_{i=0}^{L-1} J_i^{(D)}(t) = 0$. This immediately enables us to express $Q_{tot}(L,T)$ as a function of $J_i^{(fl)}(t)$ in the following manner:

$$Q_{tot}(L,T) = \int_0^T dt \sum_{i=0}^{L-1} J_i^{fl}(t). \tag{5.57}$$

The above equation implies the average current $\langle Q_{tot}(L,T)\rangle = \int_0^T dt \sum_{i=0}^{L-1} \langle J_i^{fl}(t)\rangle = 0$. Similarly, we write the expression for the fluctuation

$$\langle Q_{tot}^2(L,T)\rangle_c = \int_0^T dt_1 \int_0^T dt_2 \sum_{i=0}^{L-1} \sum_r \langle J_{i+r}^{fl}(t_1) J_i^{fl}(t_2)\rangle_c = LT \int_0^T dt \mathcal{C}_r^{J^{fl}J^{fl}}(t,0). \tag{5.58}$$

Therefore, to characterize total current fluctuation, we must first calculate the space-time correlation of the fluctuating current $\mathcal{C}_r^{J^{fl}J^{fl}}(t,0) = \langle J_r^{fl}(t) J_0^{fl}(0)\rangle_c$, which using Eq. (5.24) can be expressed in terms of the following correlation functions:

$$\mathcal{C}_r^{J^{fl}J^{fl}}(t,0) = \mathcal{C}_r^{JJ}(t,0) - \mathcal{C}_r^{J^D J}(t,0) - \mathcal{C}_r^{J^{fl}J^D}(t,0). \tag{5.59}$$

Notably, the fluctuation current $J^{(fl)}(t)$ at time t is not correlated with the diffusive current $J_0^D(0)$ at an earlier time $t = 0$, i.e.,

$$\mathcal{C}_r^{J^{fl}J^D}(t,0) = \langle J_r^{fl}(t) J_0^D(0)\rangle = 0. \tag{5.60}$$

Then the third term in Eq. (5.59) immediately drops out. To solve for the first term, i.e., the two-point instantaneous current correlation function $\mathcal{C}_r^{JJ}(t,0)$, we simply use the following formula:

$$\mathcal{C}_r^{JJ}(t,0) = \frac{d}{dt}\frac{d}{dt''}\left[\mathcal{C}_r^{QQ}(t,t'')\Theta(t-t'')\right]_{t''=0}. \tag{5.61}$$

Upon plugging in $\mathcal{C}_r^{QQ}(t,t'')$ from Eq. (5.48), the above equation simply yields the following form:

$$\mathcal{C}_r^{JJ}(t,0) = \Gamma_r \delta(t) - \frac{D}{4L} \sum_q (2 - \lambda_{qr})\, f_q e^{-\lambda_q D t}. \tag{5.62}$$

Moreover, in order to determine the second term $\mathcal{C}_r^{J^D J}(t,0)$, we use the following relation

$$\mathcal{C}_r^{J^D J}(t,0) = \left[\frac{d}{dt''}\mathcal{C}_r^{J^D Q}(t,t'')\right]_{t''=0}, \tag{5.63}$$

$$\simeq D\frac{d}{dt''}\left[\mathcal{C}_r^{\eta Q}(t,t'') - \mathcal{C}_{r+1}^{\eta Q}(t,t'')\right]_{t''=0}, \tag{5.64}$$

where we have used the truncation approximation as in Eq. (5.29), to arrive at Eq. (5.64) by using Eq. (5.63). Following Eq. (5.33), we now expand the correlators $\mathcal{C}_r^{\eta Q}(t,t')$ in the Fourier basis, and then using Eq. (5.44), we obtain the desired solution,

$$\mathcal{C}_r^{J^D J}(t,0) = -\frac{D}{4L}\sum_q (2-\lambda_{qr}) f_q(t) e^{-\lambda_q D t}. \tag{5.65}$$

Importantly, the above solution coincides with the two-point unequal-time correlation of $\mathcal{C}_r^{JJ}(t,0)$ which is displayed in the second term of Eq. (5.62) with $t \geq t' = 0$. Finally using Eqs. (5.62), (5.60) and (5.65) in Eq. (5.59), we readily obtain

$$\mathcal{C}_r^{J^{fl}J^{fl}}(t,0) = \langle J_r^{fl}(t) J_0^{fl}(0)\rangle = \delta(t)\Gamma_r, \tag{5.66}$$

i.e., the fluctuating component relaxes instantaneously and the spatial correlation is determined by Γ_r. Finally, using Eq. (5.66) in Eq. (5.58), we find that the total current fluctuation satisfies the following relation

$$\frac{1}{LT}\langle Q_{tot}^2(L,T)\rangle = \sum_r \Gamma_r. \tag{5.67}$$

By employing the identity,

$$\sum_r \Gamma_r(\rho) = \rho\left[\alpha\left(1-P(0)\right) + \beta\left(\sum_{g=1}^{l_p-1} g^2 P(g) + l_p^2 \sum_{g=l_p}^{\infty} P(g)\right)\right] = 2\chi(\rho), \tag{5.68}$$

in Eq. (5.67) and comparing the resulting equation with Eq. (5.22), we immediately obtain the following *fluctuation-response* relation for gLLG:

$$\frac{1}{2LT}\langle Q_{tot}^2(L,T)\rangle_c = \chi(\rho) = \lim_{F\to 0}\frac{\delta\langle J_i^{(F)}\rangle}{\delta F}. \tag{5.69}$$

The above equation establishes a relation between the space-time integrated current fluctuation and the response function, i.e., the mobility $\chi(\rho)$. We explicitly verify Eq. (5.69) with our numerical simulation data in sections 5.3.1 and 5.3.2.

5.2.6 Density fluctuation and current fluctuation: Einstein relation

In the preceding section, we demonstrated the relationship between total current fluctuation $\langle Q_{tot}^2(L,T)\rangle$ at the steady-state and the transport coefficient mobility $\chi(\rho)$ of the system. Additionally, in Chapter 4 [see Sec. 4.3.4], we numerically showed that the steady-state density fluctuation $\sigma^2(\rho)$ can be expressed in terms of $\chi(\rho)$ and the bulk-dffusion coefficient $D(\rho)$ using an equilibrium-like Einstein relation (ER). Consequently, a natural question arises regarding the interconnection of steady-state density and current fluctuations in such systems. In this section, starting from the microscopic dynamical rules and employing our proposed closure approximation in Eq. (5.29), we analytically derive the existence of ER for the generalized long-range lattice gas (gLLG). Finally, we demonstrate that by using ER, one may construct a one-to-one correspondence between the density and current fluctuations in these systems.

In order to calculate the single-site particle number or density fluctuation at the steady-state, we first look into the relevant correlation function, i.e., the two-point density correlation $\mathcal{C}_r^{\eta\eta}(t,t)$. Using the microscopic dynamical rules and employing the closure scheme in Eq. (5.29), we characterize the time-evolution of $\mathcal{C}_r^{\eta\eta}(t,t)$, which in the steady state, we evaluate the static correlation in the Fourier space in Eq. (5.42), which has the following structure:

$$\tilde{\mathcal{C}}_q^{\eta\eta} = \frac{\rho}{2D(\rho)}\Big[\alpha\Big\{1-P(0)\Big\} + \beta\Big\{\sum_{g=1}^{l_p-1}\left(\frac{\lambda_{gq}}{\lambda_q}\right)P(g) + \left(\frac{\lambda_{l_pq}}{\lambda_q}\right)\sum_{g=l_p}^{\infty}P(g)\Big\}\Big]. \tag{5.70}$$

To obtain the correlation function in the real space $\mathcal{C}_r^{\eta\eta}$, we simply perform the inverse Fourier transformation [as shown in Eq. (5.34)] of the above equation.

$$\mathcal{C}_r^{\eta\eta} = \frac{\rho}{2D(\rho)L}\sum_q\Big[\alpha\Big\{1-P(0)\Big\} + \beta\Big\{\sum_{g=1}^{l_p-1}\left(\frac{\lambda_{gq}}{\lambda_q}\right)P(g) + \left(\frac{\lambda_{l_pq}}{\lambda_q}\right)\sum_{g=l_p}^{\infty}P(g)\Big\}\Big]e^{-iqr}. \tag{5.71}$$

Next, by using the concept of translational invariance in gLLG, we may immediately write $\mathcal{C}_r^{\eta\eta} = \mathcal{C}_{-r}^{\eta\eta}$. This identity helps us to get rid of the term e^{-iqr} in the above equation and the resulting equation becomes,

$$\mathcal{C}_r^{\eta\eta} = \frac{\rho}{4D(\rho)L}\sum_q\Big[\alpha\Big\{1-P(0)\Big\} + \beta\Big\{\sum_{g=1}^{l_p-1}\left(\frac{\lambda_{gq}}{\lambda_q}\right)P(g) + \left(\frac{\lambda_{l_pq}}{\lambda_q}\right)\sum_{g=l_p}^{\infty}P(g)\Big\}\Big](2-\lambda_{qr}). \tag{5.72}$$

where $q = 0, 2\pi/L, 4\pi/L, 6\pi/L, \ldots, 2\pi(L-1)/L$. In order to proceed further, we introduce here the following identities satisfied by the eigenvalue λ_q:

$$\sum_q \lambda_{nq} = 2L(1-\delta_{n,0}), \tag{5.73}$$

$$\sum_q \frac{\lambda_{nq}}{\lambda_q} = n(L-n), \tag{5.74}$$

$$\sum_q \frac{\lambda_{nq}\lambda_{mq}}{\lambda_q} = 2L\left[m\Theta(n-m) + n\Theta(m-n)\right], \tag{5.75}$$

where $\Theta(X)$ is the heaviside theta function. Employing the above identities in Eq. (5.72) and after some algebraic manipulation, we obtain

$$\mathcal{C}_r^{\eta\eta}(\rho) = \frac{\rho}{2D(\rho)}\left[\alpha\Big\{1-P(0)\Big\}\delta_{|r|,0} + \beta\Theta(l_p-r)\Big\{\sum_{g=|r|+1}^{l_p-1}(g-|r|)P(g) + (l_p-|r|)\sum_{g=l_p}^{\infty}P(g)\Big\}\right] - \frac{1}{D(\rho)L}\left[\chi(\rho) - \frac{\rho\alpha}{2}\Big\{1-P(0)\Big\}\right]. \tag{5.76}$$

The equation above distinctly represents the two-point density correlation in terms of the steady-state gap distribution $P(g)$ and the system's transport coefficients $D(\rho)$ and $\chi(\rho)$. Now, we compute the scaled subsystem particle number fluctuation (coarse-grained density fluctuation), as previously defined in Eq. (4.47), which is essentially the integrated two-point density correlation function, employing the following formula:

$$\sigma^2(\rho) = \mathcal{C}_0^{\eta\eta}(\rho) + 2\sum_{r=1}^{(L-1)/2}\mathcal{C}_r^{\eta\eta}(\rho). \tag{5.77}$$

Upon employing $\mathcal{C}_r^{\eta\eta}(\rho)$ from Eq. (5.76) and performing some algebraic manipulations, the above formula easily transforms into:

$$\sigma^2(\rho) = \frac{1}{D(\rho)}\sum_r \Gamma_r(\rho) - \frac{\chi(\rho)}{D(\rho)} = \frac{\chi(\rho)}{D(\rho)}. \tag{5.78}$$

In the last line, we have used the identity in Eq. (5.68). Notably, Eq. (5.78) is the celebrated Einstein relation, linking the density fluctuation to the ratio of mobility and bulk-diffusion coefficient. Here, we derive this relation for gLLG from a microscopic dynamical viewpoint. Furthermore, by comparing Eqs. (5.78) and (5.69), we readily identify the direct correspondence between the steady-state density and total current fluctuation, as expressed by the

following relation:

$$\sigma^2(\rho) = \frac{1}{2LTD(\rho)} \langle Q_{tot}^2(L,T) \rangle_c. \tag{5.79}$$

Eq. (5.79) is of crucial importance because it relates to the fluctuation of static quantities like density with the same dynamic quantities like currents, which we derive from a microscopic dynamical perspective.

5.3 Results

In the previous section, using a microscopic dynamical framework, we have calculated current fluctuations in gLLG in terms of two macroscopic transport coefficients - the bulk-diffusion coefficient $D(\rho)$ and the mobility $\chi(\rho)$. We have also been successful in establishing an intimate equilibrium-like relation between current and density fluctuation in our model system which is far from equilibrium. In this section, we will validate the analytical predictions with simulation results for the following two special cases that have known analytical forms for the transport coefficients.

5.3.1 Finite-range hopping, $l_p = 2$

In case of finite-range hopping, one readily obtains transport coefficients: the bulk-diffusion coefficient $D(\rho)$ and the mobility $\chi(\rho)$ in terms of the steady-state gap-distribution function $P(g)$, as derived in Eqs. (5.13) and (5.22), respectively. Although numerical determination is possible for arbitrary but finite hopping range l_p, the exact analytical formulation of transport coefficients is limited to the simplest nontrivial scenario of $l_p = 2$ [see Sec. 4.3.1]. In this section, we will thus be restricted to this particular limit and verify our analytical findings of current fluctuations with numerical simulation.

To begin with, we first recall the already calculated bulk-diffusion coefficient $D(\rho) \equiv D_2(\rho)$ and the mobility $\chi(\rho) \equiv \chi_2(\rho)$ from Eqs. (4.34) and (4.35),

$$D_2(\rho) = \frac{1}{8(1+\rho)^4}\left[10\left(1-\frac{\rho}{\sqrt{5-4\rho^2}}\right)+5\rho\left(6+\frac{\rho}{\sqrt{5-4\rho^2}}\right)+\rho^2\left(17+\frac{12\rho}{\sqrt{5-4\rho^2}}\right)\right], \tag{5.80}$$

$$\chi_2(\rho) = \frac{\rho}{8(1+\rho)^3}\left[10+4\rho\left(5-\sqrt{5-4\rho^2}\right)-\rho^2\left(9+\sqrt{5-4\rho^2}\right)-16\rho^3\right]. \tag{5.81}$$

It is important to highlight that both $D_2(\rho)$ and $\chi_2(\rho)$ remain finite and bounded within the entire density range, from 0 to 1. Therefore, our analytical framework for the current fluctuation should remain valid in the finite-range hopping. We are going to validate each of

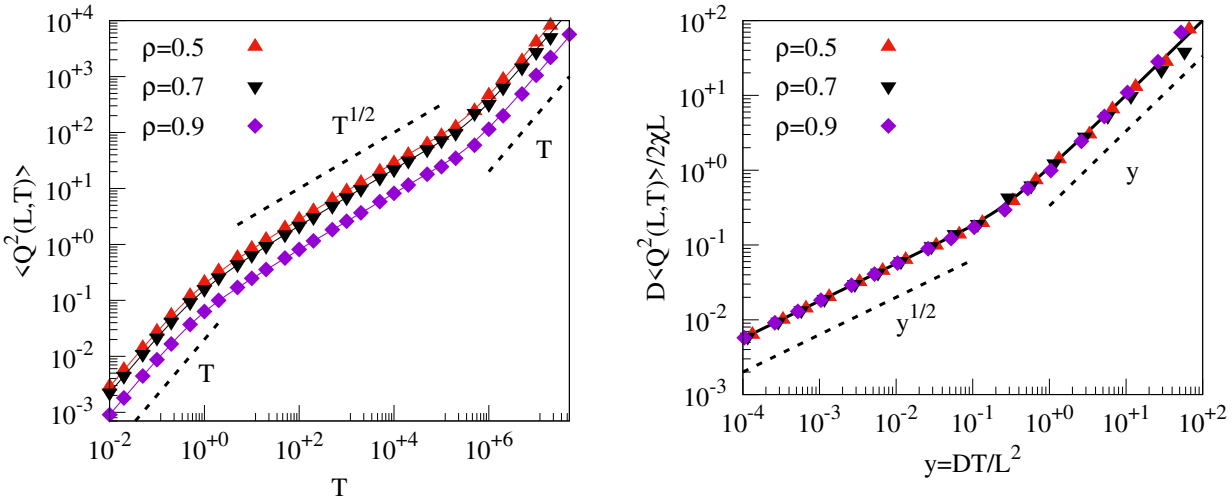

Figure 5.1: Left: We plot the time-integrated bond-current fluctuation $\langle Q^2(T)\rangle$, as a function of time T, obtained from simulations (points) for $l_p = 2$ at $\rho = 0.5$, 0.7, and 0.9. We also compare the simulation data points with the analytical solution shown in Eq. (5.51) (line). $\langle Q^2(T)\rangle$ exhibits diffusive growth at early times, subdiffusive growth at the intermediate time regime, followed by a diffusive (linear) growth, as shown by the dotted lines. Right: The scaled bond-current fluctuation $D_2\langle Q^2(T)\rangle/2\chi_2 L$ is plotted against the rescaled hydrodynamic time $y = D_2(\rho)T/L^2$ for the abovementioned combination of densities. We also compare the scaled data points with the analytic scaling function $\mathcal{W}(y)$ shown in Eq. (5.54) (black line).

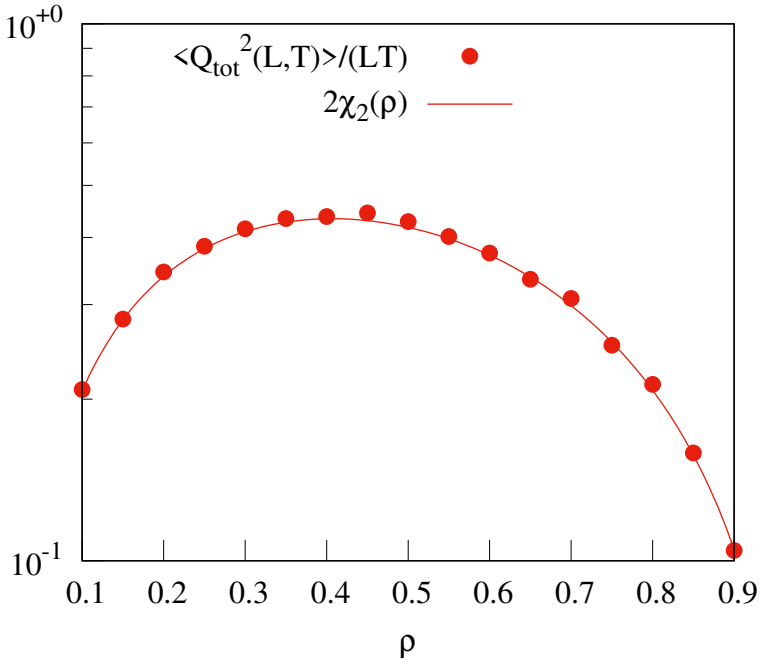

Figure 5.2: *Verification of Eq.* (5.69) *for* $l_p = 2$*:* We plot the numerically obtained scaled fluctuation of the space-time integrated current as a function of ρ and compare the numerical data with theoretically calculated $\chi_2(\rho)$ (line), as shown in Eq. (5.81).

the main analytic results in the subsequent analysis.

We verify the time-integrated bond-current fluctuations $\langle Q^2(T)\rangle_c$, derived in Eqs. (5.51) and (5.52), for $l_p = 2$ in Fig. 5.1 (left-panel) by plotting the numerically obtained $\langle Q^2(T)\rangle_c$ as a function of the observation time T for various densities $\rho = 0.5$, 0.7, and 0.9. We observe that the data points initially display diffusive growth, transitioning to a subdiffusive (i.e., $\sqrt{T}$) one, and eventually returning to diffusive growth, as shown in Eq. (5.52). We also complement the simulation data points with the theoretical lines obtained from Eq. (5.51), where we substitute the transport coefficients from Eqs. (5.80) and (5.81), and solve for f_q utilizing the steady-state gap distribution $P(g)$ obtained from Eq. (4.31) in Eq. (5.41). Certainly, we observe a remarkable agreement between the simulation data and theoretical curves. These findings collectively verify Eqs. (5.51) and (5.52) for gLLG with finite-ranged hopping ($l_p = 2$).

We next plot the numerically obtained scaled current fluctuation, i.e., $D_2\langle Q^2(T)\rangle/2\chi_2 L$ against the scaled hydrodynamic time $y = D_2 T/L^2$ in Fig. 5.1 (right-panel) to verify the scaling relationship in Eq. (5.53). To this end, we consider the following set of densities: $\rho = 0.5$, 0.7, and 0.9. We find the simulation data points collapse onto each other remarkably well, and the collapsed data points excellently follow the theoretically derived scaling function $\mathcal{W}(y)$ (black solid line) in Eq. (5.54). Moreover, we observe the scaling function, as well as the collapsed data points make a crossover from the $\sqrt{y}$ growth at small times to the linear or y behavior at very large times. Therefore, our observations altogether verifies Eqs. (5.53), (5.54), and (5.55).

We also verify the equilibrium-like fluctuation-response relation in Eq. (5.69) by numerically computing the space-time integrated current fluctuation $\langle Q^2_{tot}(L,T)\rangle_c$ in the steady state. We calculate $\langle Q^2_{tot}(L,T)\rangle_c$ numerically for system size $L = 1000$ and observation time $T = 100$. To verify Eq. (5.69), we now plot the numerically obtained scaled total current fluctuation $\langle Q^2_{tot}(L,T)\rangle/2LT$ (close points), as a function of density ρ, in Fig. 5.2. We compare the simulation findings with the analytical solution $2\chi_2(\rho)$ from Eq. (5.81), which is represented as the corresponding lines. We again find great agreement between all of the simulation data points and theoretical lines, confirming the presence of Eq. (5.69) in this system.

5.3.2 Infinite-range hopping, $l_p = \infty$

In this special scenario of $l_p = \infty$, we first set the hopping rates $\alpha = \beta = 1/2$ and rewrite here the explicit density-dependent form of the transport coefficients, that we derived in

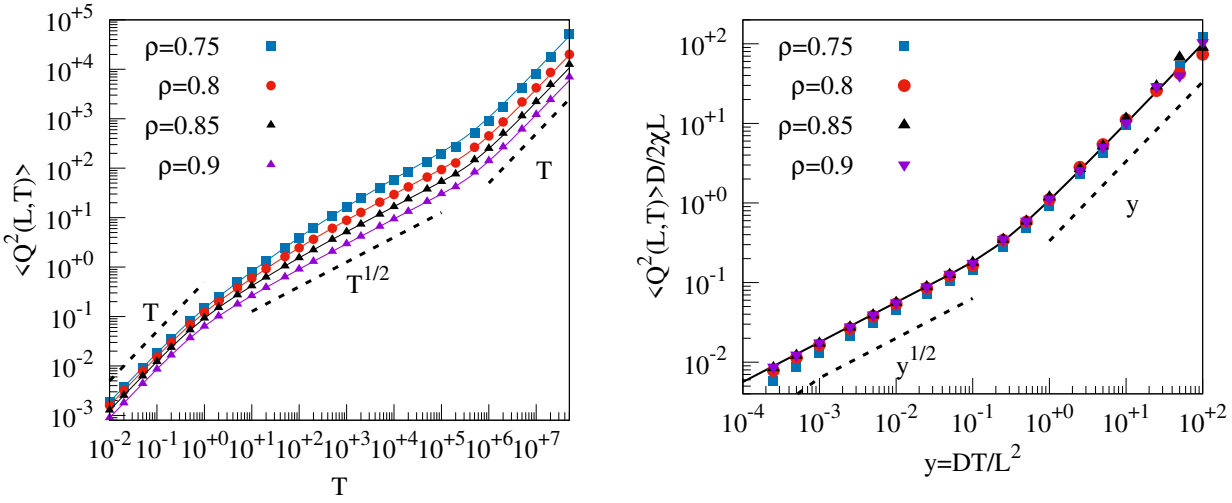

Figure 5.3: Left: We plot the time-integrated bond-current fluctuation $\langle Q^2(T)\rangle$, as a function of time T, obtained from simulations (points) for $l_p = \infty$ at the normal phase with densities $\rho = 0.75$, 0.8, 0.85 and 0.9. We also compare the simulation data points with the analytical solution shown in Eq. (5.51) (line). $\langle Q^2(T)\rangle$ exhibits diffusive growth at early times, subdiffusive growth at the intermediate time regime, followed by a diffusive (linear) growth, as shown by the dotted lines. Right: The scaled bond-current fluctuation $D_\infty\langle Q^2(T)\rangle/2\chi_\infty L$ is plotted against the rescaled hydrodynamic time $y = D_\infty(\rho)T/L^2$ for the abovementioned combination of densities. We also compare the scaled data points with the analytic scaling function $\mathcal{W}(y)$ shown in Eq. (5.54) (black line).

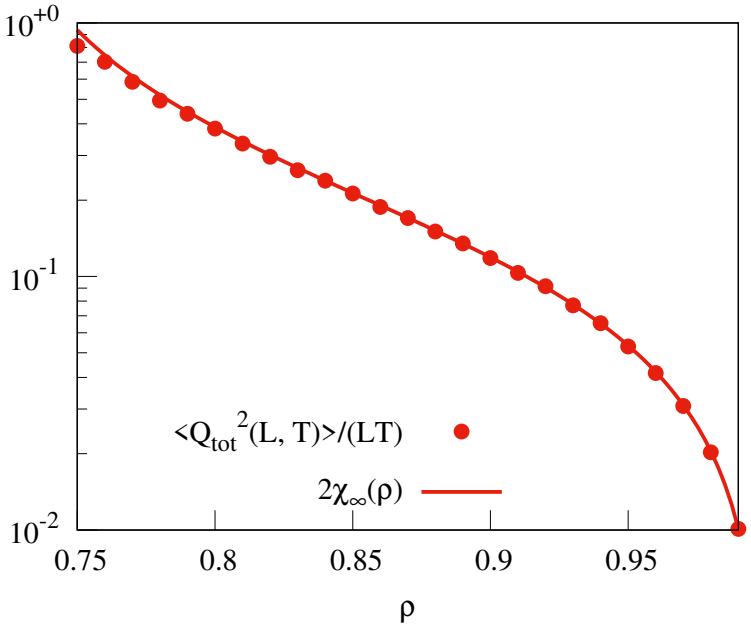

Figure 5.4: *Verification of Eq.* (5.69) *for* $l_p \to \infty$ *at normal phase (i.e.,* $\rho > \rho_c$*):* We plot the numerically obtained scaled fluctuation of the space-time integrated current as a function of ρ in the normal phase and compare the numerical data with the theoretically calculated $\chi_\infty(\rho)$ (line), as shown in Eq. (5.83).

Chapter 4,

$$D_\infty(\rho) = \frac{1}{2}, \tag{5.82}$$

$$\chi_\infty(\rho) = \frac{\rho(1-\rho)(2\rho^2-2\rho+1)}{2(2\rho^2-1)}. \tag{5.83}$$

Notably, unlike the previous case of finite range hopping, the mobility $\chi_\infty(\rho)$ has a singularity at $\rho = \rho_c = 1/\sqrt{2}$. As discussed already in Chapter 4, this diverging instability in the mobility gives rise to a nonequilibrium phase transition in the system: for $\rho > \rho_c$, the system is in the normal or the disordered phase, while in the other limit of $\rho < \rho_c$, the system spontaneously phase separates into a critical fluid at density ρ_c and a macroscopic vacancy or gap cluster of typical size $(\rho_c - \rho)L$. It is therefore instructive to study the current fluctuation in this limit, especially at the critical density at which the mobility diverges. In this section, we will first verify our analytical findings with numerical simulations at the normal phase, i.e., for $\rho > \rho_c$, and subsequently delve into the most intriguing critical phase $\rho = \rho_c$.

Verification in the normal phase, $\rho > \rho_c$: In the left-panel of Fig.5.3, we validate the time-integrated bond-current fluctuations $\langle Q^2(T)\rangle$ derived in Eqs.(5.51) and (5.52) in the normal phase by plotting numerically obtained $\langle Q^2(T)\rangle$ against observation time T across various densities $\rho = 0.75$, 0.8, 0.85, and 0.9. Initially, the data points exhibit diffusive growth, transitioning to subdiffusive behavior ($\sqrt{T}$) before returning to diffusive growth, consistent with Eq.(5.52). To complement the simulation data, we also plot theoretical lines derived from Eq.(5.51), substituting transport coefficients from Eqs.(5.82) and (5.83), and solving for f_q using the numerically obtained steady-state gap distribution $P(g)$ in Eq.(5.41). Notably, we observe a significant agreement between simulation data and theoretical curves, collectively validating Eqs. (5.51) and (5.52) within the normal phase of infinite-ranged hopping.

To verify the scaling relationship outlined in Eq.(5.53), we proceed to plot the numerically derived scaled current fluctuation, expressed as $D_\infty\langle Q^2(T)\rangle/2\chi_\infty L$, against the scaled hydrodynamic time $y = D_\infty T/L^2$ in the right-panel of Fig.5.3. For this purpose, we consider a series of densities: $\rho = 0.75$, 0.8, 0.85, and 0.9. Remarkably, we observe that the simulation data points collapse onto one another exceptionally well, adhering closely to the theoretically derived scaling function $\mathcal{W}(y)$ (represented by the solid black line) as described in Eq.(5.54). Furthermore, we note a transition in both the scaling function and the collapsed data points from $\sqrt{y}$ growth at smaller times to linear or y behavior at significantly larger times. Consequently, our observations collectively confirm the validity of Eqs.(5.53), (5.54), and (5.55) in this normal phase.

We further validate the derived fluctuation-response relation in Eq.(5.69) by numerically evaluating the space-time integrated current fluctuation $\langle Q^2_{tot}(L,T)\rangle$ in the steady state. For $\langle Q^2_{tot}(L,T)\rangle$, we conduct numerical calculations using a system size of $L = 1000$ and an observation time of $T = 1000$. To confirm Eq.(5.69), we plot the numerically obtained scaled total current fluctuation $\langle Q^2_{tot}(L,T)\rangle/2LT$ (represented by points) against density ρ in Fig.5.4. We also compare the numerical data points with the analytical solution $\chi_\infty(\rho)/D_\infty(\rho)$ derived from Eq. (5.83), illustrated as corresponding lines. Once again, we observe excellent agreement between all simulation data points and theoretical lines, confirming the validity of Eq.(5.69) within this nonequilibrium system.

Current fluctuation at the critical phase, $\rho = \rho_c$: As previously mentioned, while the bulk-diffusion coefficient $D_\infty(\rho_c)$ at the transition point remains constant and finite, the mobility $\chi_\infty(\rho_c)$ however diverges in the thermodynamic limit, leading to an anomalous scaling of the current fluctuations. At this stage, it would be quite interesting to inquire how $\chi_\infty(\rho_c, L)$ grows with system sizes L when they are large but finite. Given the gap distribution function $P(g) \sim g^{-5/2}e^{-g/g_0}$ with $g_0 \propto L$ in the critical phase, as depicted in Chapter 4, by directly incorporating this into Eq. (5.22), we immediately obtain,

$$\chi_\infty(\rho_c, L) \sim \langle g^2\rangle \sim \sqrt{L}. \tag{5.84}$$

Therefore, at the phase transition point (at criticality), the mobility diverges as $\sqrt{L}$ with the system size in the thermodynamic limit. It is worth highlighting that the equation above, along with Eq. (5.69), suggests that the space-time integrated current fluctuations exhibit anomalous feature: $\langle Q^2_{tot}(L,T)\rangle \sim L^{3/2}$, which is qualitatively different from the behavior observed in the normal phase, where $\langle Q^2_{tot}(L,T)\rangle \sim L$. Note that we have already verified the latter in Fig. 5.4. To validate the former observation, we plot the numerically computed $\langle Q^2_{tot}(L,T)\rangle/(LT)$, as functions of system size L, at the critical density $\rho = \rho_c = 1/\sqrt{2}$ in the right panel of Fig.5.5. Notably, for all system sizes, we have fixed the observation time at $T = L^2/10$. It is evident that the simulation data points exhibit $\sqrt{L}$ growth in the critical phase, thereby leading to diverging total or space-time integrated current fluctuation at the critical phase.

Not surprisingly, akin to the fluctuations observed in the total current, we expect that the time-integrated fluctuation of bond currents, denoted as $\langle Q^2(L,T)\rangle$, will also exhibit anomalous characteristics. This is solely because the mobility $\chi_\infty(\rho_c)$ is not finite and it diverges in the thermodynamic limit. However, from Eq. (5.84), we expect $\chi_\infty(\rho_c)$ to diverge as $\sqrt{L}$ in the limit of large system size L, but the bulk-diffusion coefficient $D_\infty(\rho_c)$ still remains constant and finite. Now inspired by the theoretically obtained scaling relation in Eq. (5.53)

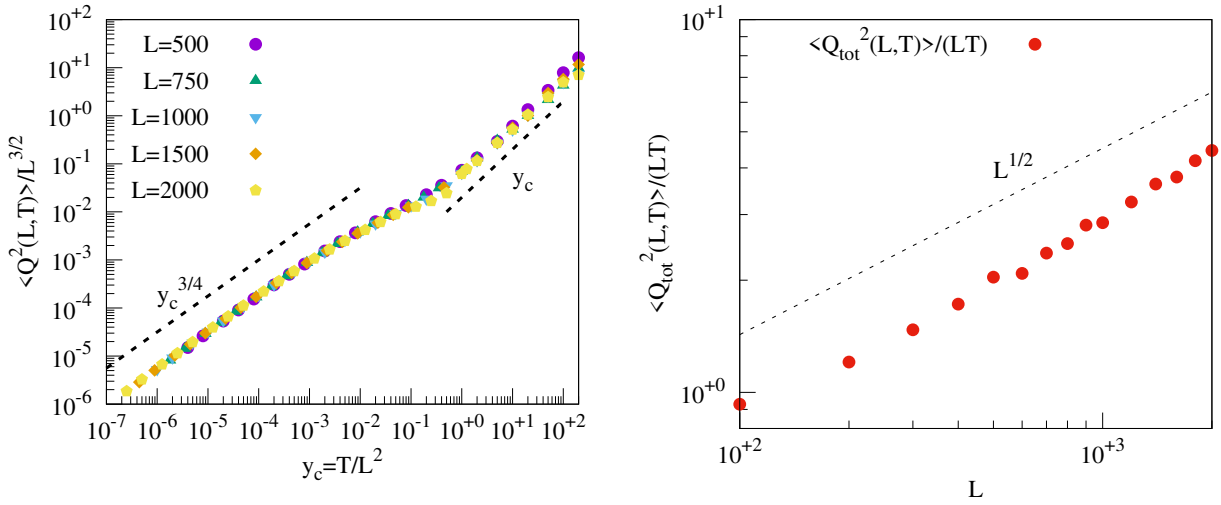

Figure 5.5: *Left:* We plot the scaled time-integrated bond-current fluctuation $\langle Q(L,T)^2\rangle/L^{3/2}$, as a function of the scaled time $y_c = T/L^2$ at the critical phase (i.e., $l_p \to \infty$ and $\rho = \rho_c$). The collapsed data points are shown to exhibit a short-time subdiffusive growth $\sim y_c^{3/4}$ followed by a diffusive growth $\sim y_c$ at large times. *Right:* We plot the growth of scaled space-time integrated current fluctuation with system size L. The dotted line compares the simulation data points with the theoretically obtained $\sqrt{L}$ growth at the critical phase.

and considering the possibility of system-size dependent mobility at the critical point, we assume the following scaling ansatz for the time-integrated bond-current fluctuation,

$$\langle Q^2(L,T)\rangle \simeq L^{3/2}\mathcal{W}_c\left(y_c = \frac{T}{L^2}\right). \tag{5.85}$$

Though the full scaling function $\mathcal{W}_c\,(y_c)$ is not known, we can calculate the asymptotic form of the scaling function by using the following scaling arguments. We expect that in the intermediate time regime ($T \ll L^2$), the bond-current fluctuation exhibits L-independent growth $\langle Q^2\rangle \sim T^\nu$, with an exponent $\nu < 1$; this growth law then crosses over to L-dependent diffusive (linear) one $\langle Q^2\rangle \sim T/L^\delta$ at large times, where $\delta > 0$ is another exponent. Interestingly, the exact determination of the exponents ν and δ is possible from our scaling ansatz in Eq. (5.85). Using the fact that $\langle Q^2(L,T)\rangle$ is L-independent for $y_c \to 0$, we immediately obtain $\lim_{y_c\to 0}\mathcal{W}_c(y_c) \sim y_c^{3/4}$ and thus the exponent $\nu = 3/4$. Moreover, the diffusive growth of $\langle Q^2(L,T)\rangle$ in the large y_c limit suggests $\lim_{y_c\to\infty}\mathcal{W}_c(y_c) \sim y_c$ and the exponent $\delta = 1/2$. Therefore the asymptotic behavior of the scaling function at criticality is given by,

$$\mathcal{W}_c\,(y_c) \sim \begin{cases} y_c^{3/4}, & \text{for } y_c \ll 1, \\ y_c, & \text{for } y_c \gg 1. \end{cases} \tag{5.86}$$

Now, using the above solution in the scaling ansatz in Eq. (5.85), we immediately obtain the limiting behaviors of the time-integrated bond-current fluctuation $\langle Q^2(L,T)\rangle$ at criticality as follows:

$$\langle Q^2(L,T)\rangle \sim \begin{cases} T^{3/4}, & \text{for} \quad 1/D_\infty(\rho_c) \ll T \ll L^2/D_\infty(\rho_c), \\ T/\sqrt{L}, & \text{for} \quad T \gg L^2/D_\infty(\rho_c). \end{cases} \tag{5.87}$$

By comparing the limiting behavior of $\langle Q^2(L,T)\rangle$ at the critical phase as shown above with that in the normal phase, as depicted in Eq. (5.52), we immediately observe an enhancement in the current fluctuation across each bond within the system at criticality: it increases as $T^{3/4}$ during the moderate time-regime instead of the $\sqrt{T}$ growth observed in the normal phase. Subsequently, there is a transition to diffusive growth with a system-size dependent prefactor of $1/\sqrt{L}$ instead of $1/L$ as seen in the normal phase. Interestingly, such an enhancement of current fluctuation on the level of each bond collectively causes divergence of fluctuation of space-time integrated current at the critical phase, as observed in the right panel of Fig. 5.5.

Notably, all the above arguments are based on our scaling ansatz in Eq. (5.85) which we verify now in the left panel of Fig. 5.5 by plotting the numerically obtained scaled fluctuation of the time-integrated bond-current $\langle Q^2(L,T)\rangle/L^{3/2}$, as a function of the scaled hydrodynamic time $y_c = T/L^2$, at the critical density $\rho = \rho_c = 1/\sqrt{2}$ for various system sizes $L = 500$, 750, 1000, 1500, and 2000. We observe the data points collapse on each other remarkably well, and the growth laws in the small and large time limits are consistent with Eq. (5.86), as compared with the black-dotted lines. The above observations clearly serve for the verification of our proposed scaling ansatz in Eq. (5.85).

5.4 Summary and concluding remarks

In this chapter, we provide a dynamic characterization of the nonequilibrium condensation transition observed earlier in Chapter 4 within the prototypical variant of thermal RTPs, called generalized long-ranged lattice gas (gLLG). We accomplish this by directly computing current fluctuations through microscopic dynamical calculations outlined in Chapter 3. Our approach is based on two key assumptions: firstly, we decompose the instantaneous bond-current into two parts—a slowly decaying diffusive component and a rapidly fluctuating component that relaxes instantly. Secondly, we assume that the instantaneous diffusive component adheres to a microscopic version of Fick's law on large time scale, enabling us to express it as the product of the bulk diffusion coefficient and the local density gradient. Importantly, both assumptions are required to avoid the otherwise infinite hierarchical evolution equations and enable precise determination of current fluctuations in the system.

For the finite-range hopping, as characterized by the finite long-range hopping length l_p, we find the time-integrated bond-current fluctuation for gLLG exhibits typical characteristics of diffusive systems, as reported in Chapter 3 also in Refs. [114, 153, 162]. In this case, the growth of the fluctuation of time-integrated bond-current exhibits three distinct regimes. Initially, in regime I, the fluctuation grows in proportion to the observation time t. Then, it transitions to regime II, where the fluctuation exhibits growth proportional to $\sqrt{t}$ (referred to as subdiffusive growth). Finally, it returns to linear growth with the observation time and diminishes with the system size L in regime III, characterized by $\langle Q^2(t)\rangle \sim t/L$. Notably, the prefactors of $\langle Q^2(t)\rangle$ in regimes II and III can be expressed as the density-dependent macroscopic transport coefficients–the bulk-diffusion coefficient and the mobility. Interestingly, after suitable scale transformations, $\langle Q^2(t)\rangle$ is shown to satisfy a scaling law with a presumably universal scaling function.

In the most interesting scenario of infinite range hopping, the observed condensation transition is found to manifest anomalous current fluctuations in the system at the critical point. In the moderately large but much less than the hydrodynamic timescale, the time-integrated bond-current fluctuation is found to exhibit subdiffusive growth with an exponent of 3/4, i.e., $\langle Q^2(t)\rangle \sim t^{3/4}$. This is strikingly different from the typical subdiffusive growth of the current fluctuation in the normal phase discussed above, where the growth is considerably suppressed with an exponent of 1/2. Lastly, in the time regime significantly larger than the hydrodynamic scales, the time-integrated bond-current fluctuation demonstrates diffusive growth. While the growth pattern resembles that found in the normal phase discussed above, the peculiarity in the critical phase is linked to the atypical system size dependence: $\langle Q^2(t)\rangle$ shows a dependence of $1/\sqrt{L}$ at the critical phase, as opposed to $1/L$ dependence in the normal phase.

The observations above clearly indicate that the system displays enhanced growth of bond-current fluctuations at the critical point. Interestingly, the enhancement of current fluctuation across each bond collectively causes the scaled space-time integrated current across the entire system to exhibit anomalous fluctuation: it *diverges* as $\sqrt{L}$ in the limit of large L in the critical phase, in contrast to the behavior in the normal phase where it is finite (i.e., independent of L). Indeed, such an anomaly in current fluctuations is an immediate consequence of the diverging instability in mobility at the critical point, as demonstrated by deriving an equilibrium-like fluctuation-response relation that connects the scaled fluctuations of the space-time integrated current in the entire system to the linear response function, collective particle mobility. Furthermore, our microscopic study also demonstrates the existence of the Einstein relation (ER) for all hopping ranges relating density fluctuations to the system's mobility-to-diffusivity ratio. Therefore, the Einstein relation, coupled with the fluctuation

response relation, suggests the diverging fluctuations in space-time integrated current giving rise to the diverging density fluctuations at the critical point. Although diverging density fluctuation can be associated with equilibrium phase transitions, the mechanism in that case is exactly the opposite of what is observed in this study. In the equilibrium scenario, the bulk-diffusion coefficient vanishes, slowing down dynamics at criticality. In contrast, the dynamics in such a nonequilibrium setup do not slow down, and the phase transition is triggered by diverging current fluctuations in the system. We believe this novel mechanism is unique for nonequilibrium setups and could provide a fresh perspective to study phase transitions in such systems, especially for self-propelled particles that are usually perceived from the viewpoint of motility-induced phase separation (MIPS) [22].

6

Summary and concluding remarks of the thesis

In this thesis, we present a microscopic dynamical theory, that characterizes large-scale fluctuation and transport properties of a broad class of hardcore run-and-tumble particles (RTPs), an archetypal lattice model of self-propelled particles (a subclass of active-matter systems). Our theoretical formulation elucidates various fascinating aspects of collective phenomena observed in active matter, in the light of the perhaps simplest class of nonequilibrium systems - the driven-diffusive systems, which has been intensively studied in the past decades [117,118]. Indeed, we show that the nontrivial collective properties of such systems, arising due to the subtle interplay between interaction and persistence, are encoded in the density- and activity-dependent macroscopic transport coefficients, the bulk-diffusion coefficient $D(\rho, \gamma)$ and the collective particle mobility $\chi(\rho, \gamma)$ where ρ and γ are density and tumbling rate of RTPs, respectively. Our theoretical formalism enables us to precisely calculate the transport coefficients and demonstrate how these transport coefficients play a crucial role in understanding current and density fluctuations, and even phase transitions, in the context of the model systems studied here. Before summarizing the main findings, we briefly describe the models studied in the thesis.

I. Models of hardcore athermal RTPs - The conventional model of hardcore RTPs, such as that defined in Ref. [36], consists of particles, having a spin variable and executing

persistent hopping (i.e., *run*) with unit rate to the nearest-neighbor vacant site along its spin direction. Particles also change their spin orientation (called *tumbles*) spontaneously, without the influence of other particles, with rate γ. One can therefore define the persistence length as $l_p = 1/\gamma$. Due to the internal spin variable associated with each particle, this model becomes quite difficult to handle analytically. To bypass the difficulty, we introduce an analytically tractable variant of the standard hardcore RTPs - the hardcore long-ranged lattice gas (LLG). In the latter model, particles simply perform symmetric long-range hopping, with hop length chosen from a distribution $\phi(l)$, while abiding by the hardcore constraint. The hopping event is successful only if the empty stretch or the gap in the hopping direction is at least of length l; else, the particle traverses the entire stretch and sits adjacent to its nearest occupied site. Notably, the long-range hopping in LLG is analogous to the ballistic run of RTPs between successive tumbling events. Considering $\phi(l)$ to be exponentially distributed with the typical length-scale l_p [i.e., $\phi(l) \sim \exp(-l/l_p)$], we demonstrate that the long-ranged lattice gas model qualitatively captures the large-scale transport and fluctuation properties of the standard hardcore RTPs. To show this, we conduct parallel investigations into both models in Chapters 2 and 3, designated them as models I and II of (athermal) hardcore RTPs, respectively.

II. Model of hardcore thermal SPPs - It is important to note that the dynamics of the above two models are defined in terms of a single length scale, namely the persistence length, and the effect of *thermal* fluctuations has not been taken into consideration. We next investigate the presence of another length scale in the system, arising from the thermal noise in the surrounding environment. To address the issue, we made the simplest possible generalization of the model II (LLG) by incorporating $\phi(l)$ as a combination of two localized distribution functions: $\phi(l) = \alpha\delta_{l,l_s} + \beta\delta_{l,l_p}$ with $\alpha + \beta = 1$. The generalized LLG (gLLG) model now encompasses two distinct length scales, denoted by l_s being a short-ranged hopping-lengh scale (say, $l_s = a$ being simply equal to the lattice spacing a) and l_p being a long-ranged hopping-length scale. Without loss of generality, the two length scales $l_s = a = 1$ and l_p are measured in the unit of lattice spacing a, which we set to unity and they represent short-ranged thermal (or, in other words, passive) diffusion and long-ranged ballistic (or, active) motion of SPPs, respectively. The interplay between these two competing length scales manifests themselves through intriguing collective behavior in the steady state, as explored in Chapters 4 and 5. We now summarize below the main findings of the thesis.

1. Collective diffusion of hardcore athermal RTPs - In Chapter 2, we study density relaxation in conventional models of hardcore RTPs for arbitrary density ρ and persistence length $l_p = \gamma^{-1}$, where γ is the tumbling rate. To this end, we consider model I (standard hardcore RTPs) and model II (LLG version) as mentioned above, on a d dimensional periodic

lattice of volume L^d. Our study reveals that over time scales significantly longer than those of microscopic events, RTPs exhibit collective (typically nonlinear) diffusive relaxation. We characterize the relaxation phenomena by determining the density- and activity-dependent bulk-diffusion coefficient $D(\rho, \gamma)$ analytically for model II and numerically in model I using an efficient Monte Carlo simulation algorithm. Indeed, characterizing the density dependence of the bulk-diffusion coefficient is of crucial interest in the physics of active matter. In the limit of strong persistence, the bulk-diffusion coefficient is found to have a power-law density dependence: $D(\rho, \gamma) \sim \rho^{-\alpha}$, with the parameter-dependent exponent $0 < \alpha \leq 2$. This particular result has the following important implications:

(a) The local structural relaxations, influenced by $D[\rho(\mathbf{x}, \tau), \gamma]$, are sensitive to local density. This characteristic causes diverse relaxation time scales (distributed as a power-law), resulting in dynamical heterogeneity and anomalous transport in the system.

(b) There is no evidence of MIPS-like diffusive instability in RTPs, whether in one or higher dimensions. Instead, in the regime of strong persistence and high density, where MIPS would typically occur, $D(\rho, \gamma)$ does not vanish; rather, it decreases as a power-law with an exponent of 2, i.e., $D \sim \rho^{-2}$.

We also observe that subtle interplay between persistence and interaction causes collective transport in RTPs to manifest themselves through the competition between two length scales - the persistence length l_p and a "mean free path", which is a measure of the average size of an empty stretch, or the mean *gap* $\langle g \rangle \sim 1/(\rho\sigma)$ [where σ is the particle cross-section, which is set to unity], in the direction of particle hopping. Consequently, in the regime of strong persistence and low density, as set by $l_p^{-1} = \gamma \to 0$ and $\langle g \rangle^{-1} = \rho \to 0$, while maintaining the ratio $\psi = \rho/\gamma$ finite, the bulk diffusion coefficient follows a scaling relationship $D(\rho, \gamma) = D^{(0)}\mathcal{F}(\rho/\gamma)$ as described in Equation (2.5), $D^{(0)}$ is the diffusivity of RTPs in the noninteracting limit. Here, we analytically determine the scaling function $\mathcal{F}(\psi)$ for model II in one dimension and numerically identify it in all other cases. Despite the quantitative differences, we see qualitative similarities in the scaling functions across models and dimensions.

2. Current fluctuations in hardcore athermal RTPs - After exploring the relaxation properties, we delve into characterizing dynamic fluctuation in hardcore athermal RTPs in Chapter 3. We quantify steady-state current fluctuations numerically in model I and analytically in model II in one dimension, for arbitrary density ρ and persistence length $l_p = \gamma^{-1}$. Our analytic theory is based on a truncation (closure) method that allows us to close the otherwise infinite hierarchy of many-body correlations appearing in the dynamical evolution

equation and solve for current fluctuations exactly within the closure approximation in a system of hardcore RTPs. Using this scheme, we find the fluctuation of the space-time integrated current $Q_{tot}(L,T) = \sum_{i=1}^{L} Q_i(T)$ (where $Q_i(T)$ and L are the time-integrated bond-current measured up to time T and system size, respectively) can be related to another transport coefficient, collective mobility $\chi(\rho,\gamma)$ through the equilibrium-like fluctuation-response relation $\chi(\rho,\gamma) \equiv \lim_{L\to\infty}(1/2LT)\langle[\sum_{i=1}^{L} Q_i^2(T)]\rangle_c$. Interestingly, in the limit of small density and strong persistence, i.e., $\rho,\gamma \to 0$ with scaling variable $\psi = \rho/\gamma$ fixed, we show that, similar to the bulk-diffusion coefficient $D(\rho,\gamma)$ previously studied in Chapter 2, *there exists a scaling regime for the mobility* $\chi(\rho,\gamma)$ *too.* Therefore, our investigation demonstrates how persistence and interaction contribute to collective relaxation and current fluctuations within typical hardcore models of athermal RTPs. Furthermore, we compute the time-integrated bond-current fluctuation $\langle Q_i^2(T)\rangle$ and observe its intriguing evolution patterns. Specifically, we observe subdiffusive growth during moderately large timescales $r_0^2/D \ll T \ll L^2/D$ (where r_0 denotes the lattice spacing or particle diameter, assumed to be unity throughout), characterized by $\langle Q_i^2(T)\rangle \sim T^{1/2}$. This behavior transitions to a diffusive growth regime for significantly longer durations $T \gg L^2/D$, where $D(\rho,\gamma)$ represents the bulk-diffusion coefficient dependent on the density and tumbling rate [112]. Notably, the prefactors associated with the growth laws can be expressed in terms of the calculated macroscopic transport coefficients: the bulk-diffusion coefficient $D(\rho,\gamma)$ and the mobility $\chi(\rho,\gamma)$. Interestingly, in the limit of L, T is large, with the dimensionless scaling variable DT/L^2 finite, we show that the growth of time-integrated bond-current fluctuation obeys a scaling law, that is presumably *universal*, i.e., independent of the dynamical rules of the models and parameter values [see Eq. (3.79)]. Moreover, our theoretical scheme readily allows for calculating the spatial properties of the instantaneous current in model II (LLG). Using our microscopic calculations, we derive that, the spatial correlations of current in both models decay exponentially $\exp(-r/\xi)$ with spatial separation r. Interestingly, in the strong-persistence regime, we find that correlation length ξ *diverges* as the square root of persistence time τ_p, i.e., $\xi \sim \sqrt{\tau_p}$, the behavior which we derive analytically for model II (LLG). This result provides a microscopic theoretical explanation of the qualitative features of velocity correlations, which is somewhat related to the spatial correlation of instantaneous current, observed in the recent experiments and simulations [141, 147].

3. Mobility-driven clustering in hardcore thermal SPPs - So far in Chapters. 2 and 3, we have investigated the relaxation and fluctuation characteristics of athermal RTPs. In the following chapters, we incorporate thermal fluctuations by generalizing (one-dimensional) model II of RTPs, which now include short- and long-range hopping, thus reducing the dynamics to passive or thermal diffusion and active or ballistic motion of typical active matter

in contact with a heat bath. In this generalized version, starting from the microscopic dynamical description, we derive the hydrodynamic structure in Chapter 4 and identify the density- and activity-dependent macroscopic transport coefficients, the bulk-diffusion coefficient $D_{l_p}(\rho)$ and mobility $\chi_{l_p}(\rho)$. When the typical long-range hop length l_p is finite, the two transport coefficients remain finite as a function of density, indicating no anomaly in the system. However, in the limit of diverging typical long-range hop length, the competing effects of long- and short-ranged hopping result in a condensation transition of holes or vacancies in the system. Unlike the typical equilibrium scenario, the phase transition does not cause the vanishing instability of the bulk-diffusion coefficient. Instead, the transition is triggered by the diverging instability in the mobility $\chi_\infty(\rho)$, while the bulk-diffusion coefficient $D_\infty(\rho)$ remains finite at the transition point. Notably, such a divergence in mobility leads to diminishing resistance to particle flow, resulting in a "superfluid"-like state in the system of thermal SPPs. Such an anomaly in transport characteristics also results in anomalous fluctuations in the system, which we will discuss now.

3a. Anomalous density fluctuation - Although the system is driven out of equilibrium at the microscopic level, we discovered that the transport coefficients are related to density fluctuations via the equilibrium-like Einstein Relation (ER): $\chi_{l_p}(\rho)/D_{l_p}(\rho) = \sigma^2(\rho)$. This observation aligns with the findings of the macroscopic fluctuation theory (MFT) [118], which we have verified numerically in Chapter 4 and analytically derived from microscopic calculations in Chapter 5. Because the phase transition is caused by diverging mobility instability, the intimate connection between transport coefficients and density fluctuation, as found by ER, immediately results in diverging number fluctuation in the system at the critical point. It is noteworthy that such diverging fluctuation in numbers, often termed "giant" number fluctuations (GNF) at criticality, is a distinctive feature in active systems. It is interesting that our microscopic theory, which focuses on such a simplistic active system, validates this feature.

3b. Anomalous current fluctuation - To investigate the dynamical origin of the condensation transition, we calculate the current fluctuation for gLLG in Chapter 5. For finite typical long-range hop length l_p and in the normal phase (i.e., $\rho > \rho_c$) for infinite range hopping, i.e., $l_p \to \infty$, the system exhibits usual characteristics of the current fluctuations as found in Chapter 3. However, at the critical phase (i.e., $l_p \to \infty$, $\rho = \rho_c$), the onset of the condensation transition is characterized by atypical growth in current fluctuation, as briefly described below.

(i) *The bond-current exhibits enhanced fluctuation at the critical point.* For moderate

observation time T, it grows as $T^{3/4}$ (compared to $\sqrt{T}$ growth at the normal phase), while at large times, it transitions into diffusive or linear growth with less suppressed system size-dependent prefactor $1/\sqrt{L}$ (compared to $1/L$ growth at the normal phase).

(ii) *The scaled space-time integrated current fluctuation diverges at the critical point.* Our microscopic theory allows us to relate the scaled space-time integrated current fluctuation to the system's mobility, which, according to the ER, links with the density fluctuation of the system [see Eq. (5.79)]. Thus, at the critical point, mobility instability leads to divergent scaled space-time integrated current fluctuation, resulting in "giant" density fluctuation in the system in the thermodynamic limit. Notably, for finite systems, we determine both (scaled) current and density fluctuations and mobility diverge as $\sqrt{L}$ with the system size.

Interestingly, such diverging current fluctuations at criticality provide a unique and novel mechanism for "superfluid"-like nonequilibrium phase transitions in SPPs, which contrasts sharply with the equilibrium scenario. The latter is identified by a vanishing bulk-diffusion coefficient and finite mobility, implying that density perturbations caused by typical current fluctuations would undergo slow relaxation at the critical point. Because current fluctuations are finite, they cause more perturbation to the density, which eventually grows indefinitely due to the slow relaxation process, causing phase transition. Notably, the phenomenology of motility-induced phase separation (MIPS) [22] also relies on a similar equilibrium-like mechanism. However, in the mobility-driven nonequilibrium clustering transition studied here, as described by the finite bulk-diffusion coefficient and diverging mobility, density perturbation would relax at a finite rate; however, due to the diverging current fluctuations, the system exhibits instability in density fluctuations, resulting in a "superfluid"-like phase transition. Notably, "superfluidity" has already been reported in bacterial suspension, as characterized by vanishing viscosity [171]. Remarkably, the reduction in viscosity in dense bacterial suspensions is qualitatively similar to the mobility-driven clustering observed in our minimal setup. We, therefore, believe our proposed mechanism of current fluctuation-induced phase transition could provide a new perspective to understand the phase transition in SPPs, which is usually perceived in the light of MIPS [22].

A

Appendix for Chapter 2

In the appendix section, we provide additional calculation and derivation details, as well as simulation results used in the main text.

A.1 Verification of the scaling form of gap distribution $P(g)$

In this section, we numerically verify the scaling law satisfied by the typical gap size g_* in the regime of low density and strong persistence used in the main text in Eq. (2.31), i.e.,

$$g_* = \frac{1}{\rho}\mathcal{G}(\psi). \tag{A.1}$$

Note that, using the assumed exponential form of the gap distribution, i.e.,

$$P(g) \simeq N_* e^{-g/g_*} \tag{A.2}$$

and the above scaling form of g_* in the following conservation equation

$$\langle g \rangle = \sum_{g=1}^{\infty} gP(g) = 1/\rho, \tag{A.3}$$

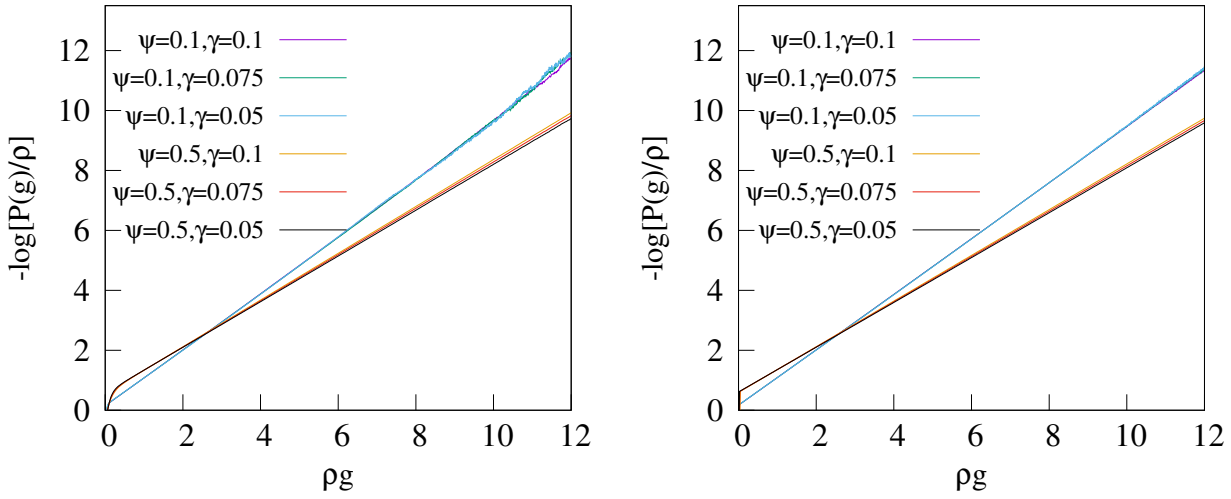

Figure A.1: *Verification of Eq.* (A.5) . We plot $-\ln(P(g)/\rho)$ as a function of ρg for model I (left-panel) and model II (right-panel) in $1D$, for various combinations of ρ and γ such that the scaling variable ψ remains fixed at 0.1 and 0.5. In both these panels, for $\psi = 0.1$, we have used $\gamma = 0.1$ (magenta line), 0.05 (green line) and 0.01 (sky blue line); while the same for $\psi = 0.5$ are shown in orange line, black line and blue line respectively.

which is exact in the low-density limit, we straightforwardly obtain the proportionality constant

$$N_* = \frac{1}{\rho}\frac{[\exp(\rho/\mathcal{G}(\psi)) - 1]^2}{\exp(\rho/\mathcal{G}(\psi))}. \tag{A.4}$$

Now, inserting g_* and N_*, as shown in Eqs. (A.1) and (A.4), in the expression of $P(g)$ in Eq. (A.2), we obtain the following scaling law for $P(g)$,

$$-\ln\left(\frac{P(g)}{\rho}\right) = \frac{\rho g}{\mathcal{G}(\psi)} + 2\ln\left(\mathcal{G}(\psi)\right). \tag{A.5}$$

Clearly, the above scaling law is a direct consequence of the assumed scaling form of g_* in Eq. (A.1). Hence, verifying Eq. (A.5) yields the existence of the proposed scaling law of $g*$ right away. In order to do so, we compute and plot the steady-state $P(g)$ for model I (left panel) and model II (right panel) in $1D$ at various tumbling rates γ (various persistent lengths for model II) and densities ρ, while keeping the ratio $\psi = \rho v/\gamma$ constant. The scaling law would be verified if data points corresponding to different ρ and γ at a fixed ψ collapse with each other.

To check this, in Fig. A.1, we plot $-\ln(P(g)/\rho)$ as a function of the scaled gap size ρg for model I (left) and model II (right) at two different $\psi = 0.1$ and 0.5. For each ψ, we have used three different tumbling rates $\gamma = 0.05$, 0.075, and 0.1 and the corresponding density ρ is chosen from the relation $\rho = \gamma\psi/v$ (where $v = 1$). Data belonging to different parameter

spaces (ρ, γ) corresponding to the same ψ collapse quite well, as shown in the figure. This observation immediately validates the scaling form of g_* for both models I and II.

A.2 Derivation of scaling function $\mathcal{F}_{II}(\psi)$ of the bulk-diffusion coefficient in model II

In this section, we derive the analytic expressions for the bulk-diffusion coefficient $D_{II}(\rho, \gamma)$ and the corresponding scaling function $\mathcal{F}_{II}(\psi)$, presented in the main text in Eq. (2.35). Using the gap distribution function given in Eq. (A.2) in the calculated expression of the bulk-diffusion coefficient $D_{II}(\rho, \gamma)$, shown in the main text in Eq (2.26), we obtain,

$$D_{II}(\rho,\gamma) = -\frac{1}{2d}\frac{\partial}{\partial\rho}\Big[N_*\rho\sum_{l=1}^{\infty}\phi(l)\Big(\sum_{g=1}^{\infty}ge^{-g/g_*} + (l-1)\sum_{g=l}^{\infty}(g-l)e^{-g/g_*}\Big)\Big]. \tag{A.6}$$

We now note the following identities:

$$\sum_{g=1}^{\infty}ge^{-g/g_*} = \frac{\langle g\rangle}{N_*}, \tag{A.7}$$

$$\sum_{g=l}^{\infty}(g-l)e^{-g/g_*} = e^{-l/g_*}\frac{\langle g\rangle}{N_*}, \tag{A.8}$$

$$\langle g\rangle = \frac{1}{\rho} - 1. \tag{A.9}$$

Here $\langle g\rangle$ is the mean gap length at density ρ. Now, using these identities and $\phi(l) = Be^{-l/l_p}$ in Eq. (A.6), we obtain

$$D_{II}(\rho,\gamma) = -\frac{B}{2d}\frac{\partial}{\partial\rho}\left[(1-\rho)\left\{\sum_{l=1}^{\infty}e^{-l/l_p} + \sum_{l=1}^{\infty}(l-1)e^{-l/\xi}\right\}\right], \tag{A.10}$$

where we define $\xi = 1/\left(1/l_p + 1/g_*\right)$. It is now easy to perform the summations appearing in Eq. (A.10), which are given by,

$$\sum_{l=1}^{\infty}e^{-l/l_p} = \frac{1}{e^{1/l_p}-1}, \tag{A.11}$$

$$\sum_{l=1}^{\infty}(l-1)e^{-l/\xi} = \frac{1}{(e^{1/\xi}-1)^2}. \tag{A.12}$$

Finally, replacing Eqs. (A.11) and (A.13) in Eq. (A.10), we obtain the following simplified form:

$$D_{II}(\rho,\gamma) = -\frac{B}{2d}\frac{\partial}{\partial\rho}\left[(1-\rho)\left\{\frac{1}{e^{1/l_p}-1}+\frac{1}{(e^{1/\xi}-1)^2}\right\}\right]. \tag{A.13}$$

Notably, the above form of $D_{II}(\rho,\gamma)$ is used in the main text in Eq. (2.27) and is valid for arbitrary values of ρ and γ. However, in the subsequent analysis, we consider the following special cases:

- Case I, ρ arbitrary, $\gamma \to \infty$: In this case, we have $B = 1$ and the typical gap size g_* is given by,

$$g_* = -\frac{1}{\log(1-\rho)}. \tag{A.14}$$

  Using this particular g_* and $\gamma \to \infty$ or $l_p \to 0$ in Eq. (A.13), it is straighforward to show that the second term in the curly bracket does not contribute, and the resulting expression of $D_{II}(\rho,\gamma)$ is given by,

$$D_{II}(\rho,\gamma) = e^{-1/l_p} D_{SSEP}, \tag{A.15}$$

  where $D_{SSEP} = 1/2d$ is the bulk-diffusion coefficient for SSEP in d dimension.

- Case II, ρ finite and large, $\gamma \to 0$: In this case, we have $B = 1/l_p$ and the typical gap size, as calculated in Ref. [139], is given by

$$g_* = \sqrt{l_p \langle g \rangle}, \tag{A.16}$$

  which immediately implies,

$$\frac{\partial g_*}{\partial \rho} = -\frac{1}{2\rho^2}\sqrt{\frac{l_p}{\langle g \rangle}}. \tag{A.17}$$

  Moreover, using the g_* mentioned above, we obtain

$$\xi = \frac{l_p}{1+\sqrt{\frac{l_p}{\langle g \rangle}}}. \tag{A.18}$$

  Notably, in this regime, l_p, g_* and ξ are infinitely large. Using all of the above relations in Eq. (A.13) and after some algebraic manipulations, we finally obtain a simplified

expression of $D(\rho,\gamma)$ in this regime, which is given by,

$$D_{II}(\rho,\gamma) = \frac{1}{2\rho^2}. \tag{A.19}$$

- Case III, $\rho \to 0$, $\gamma \to 0$: In this particular regime of interest, the typical gap size g_* obeys the following scaling law,

$$g_* = \frac{1}{\rho}\mathcal{G}(\psi), \tag{A.20}$$

where $\psi = \rho/\gamma$. Using the above expression of g_*, we can easily caluclate

$$\frac{\partial g_*}{\partial \rho} = -\frac{g_*}{\rho}\left(1 - \psi\frac{\mathcal{G}'(\psi)}{\mathcal{G}(\psi)}\right). \tag{A.21}$$

Note that, since $\rho \to 0$, we can easily write $1-\rho \simeq 1$, which simplifies Eq. (A.13) substantially. Finally, substituting all of the results in Eq. (A.13), some algebraic manipulations leads to the following expression of the bulk-diffusion coefficient:

$$D_{II}(\rho,\gamma) = \frac{e^{1/\xi}}{l_p d(e^{1/\xi}-1)^3}\frac{1}{\mathcal{G}(\psi)}\left(1 - \psi\frac{\mathcal{G}'(\psi)}{\mathcal{G}(\psi)}\right). \tag{A.22}$$

Asymptotic expansion of $D_{II}(\rho,\gamma)$: We further expand the bulk-diffusion coefficient $D_{II}(\rho,\gamma)$, obtained in Eq. (A.22), in the limit of $\gamma \to 0$ and $\rho \to 0$, such that the dimensionless quantity $\psi = \rho v/\gamma$ remains finite. Let us first make the replacement,

$$\frac{1}{\xi} = n = \frac{1}{l_p} + \frac{\rho}{\mathcal{G}(\psi)} = \frac{1}{l_p}\left(1 + \frac{\psi}{\mathcal{G}(\psi)}\right). \tag{A.23}$$

Note that this particular limit of interest automatically implies $n \to 0$. We now expand the following expression as

$$\begin{aligned}\frac{e^n}{l_p(e^n-1)^3} &= \frac{\left(1+n+\frac{n^2}{2}\dots\right)}{l_p n^3\left(1+\frac{n}{2}+\frac{n^2}{6}\dots\right)^3} \\ &\simeq \frac{1}{l_p}\left(\frac{1}{n^3} - \frac{1}{2n^2} - \frac{3}{2n}\dots\right).\end{aligned} \tag{A.24}$$

Since we are working in the regime $n \to 0$, the leading order contribution to Eq. (A.24) emerges from $1/n^3$ term only and consequently the bulk-diffusion coefficient can be written as

$$D_{II}(\rho,\gamma) = \frac{1}{l_p d n^3 \mathcal{G}(\psi)}\left(1-\psi\frac{\mathcal{G}'(\psi)}{\mathcal{G}(\psi)}\right)+\mathcal{O}\left(\frac{\gamma}{n^2}\right),$$
$$\simeq \frac{l_p^2\mathcal{G}^2(\psi)}{d\left(\mathcal{G}(\psi)+\psi\right)^3}\left(1-\psi\frac{\mathcal{G}'(\psi)}{\mathcal{G}(\psi)}\right)+\mathcal{O}\left(l_p\right). \tag{A.25}$$

From the above equation, it is quite evident that $D_{II}(\rho,\gamma)$ satisfies a scaling law and the corresponding scaling function can be written as

$$\mathcal{F}_{II}(\rho,\gamma) = \frac{1}{d}\left(\frac{\gamma}{v}\right)^2 D_{II}(\rho,\gamma) \simeq \frac{\mathcal{G}^2(\psi)}{\left(\mathcal{G}(\psi)+\psi\right)^3}\left(1-\psi\frac{G'(\psi)}{\mathcal{G}(\psi)}\right), \tag{A.26}$$

which we have used in the main text in Eq. (2.35).

B

Appendix for Chapter 3

B.1 Time evolution of equal-time current correlation $\mathcal{C}_r^{QQ}(t', t)$

$$Q_r(t'+dt')Q_0(t) = \begin{cases} (Q_r(t')+1)Q_0(t), & \text{prob.} \quad \mathcal{P}_r^R dt', \\ (Q_r(t')-1)Q_0(t), & \text{prob.} \quad \mathcal{P}_r^L dt', \\ Q_r(t')Q_0(t), & \text{prob.} \quad 1-(\mathcal{P}_r^R+\mathcal{P}_r^L)dt'. \end{cases} \tag{B.1}$$

Using the update rules in Eq. (B.1) and substituting the expressions of $\mathcal{P}_r^R$ and $\mathcal{P}_r^L$, as shown in Eqs. (2.16) and (2.17), respectively, the corresponding time-evolution equation can be written as

$$\frac{d}{dt'}\langle Q_r(t')Q_0(t)\rangle = \frac{1}{2}\sum_{l=1}^{\infty}\phi(l)\Bigg[\Big\{\Big\langle \hat{\mathcal{U}}_{r+l}^{(l)}(t')Q_0(t)\Big\rangle - \Big\langle \hat{\mathcal{U}}_r^{(l)}(t')Q_0(t)\Big\rangle\Big\} + \sum_{g=1}^{l-1}\Big\{\Big\langle \hat{\mathcal{V}}_{r+g+1}^{(g+2)}(t')Q_0(t)\Big\rangle - \Big\langle \hat{\mathcal{V}}_{r+1}^{(g+2)}(t')Q_0(t)\Big\rangle\Big\}\Bigg], \tag{B.2}$$

Finally using the definition of $\mathcal{C}_r^{QQ}(t',t)$ as provided in Eq. (3.11), we immediately obtain

$$\frac{d}{dt'}\mathcal{C}_r^{QQ}(t',t) = \frac{1}{2}\sum_{l=1}^{\infty}\phi(l)\Big[\Big\{\mathcal{C}_{r+l}^{\mathcal{U}^{(l)}Q}(t',t)-\mathcal{C}_r^{\mathcal{U}^{(l)}Q}(t',t)\Big\}+\sum_{g=1}^{l-1}\Big\{\mathcal{C}_{r+g+1}^{\mathcal{V}^{(g+2)}Q}(t',t)-\mathcal{C}_{r+1}^{\mathcal{V}^{(g+2)}Q}(t',t)\Big\}\Big], \tag{B.3}$$

$$= \left\langle J_r^{(D)}(t')Q_0(t)\right\rangle_c. \tag{B.4}$$

Here we have used the expression for $J_r^{(D)}(t')$ as given in Eq. (3.9). Note that the above two equations are expressed in the main text as Eqs. (3.12) and (3.13).

B.2 Time evolution of unequal-space-time density-current correlation $\mathcal{C}_r^{\eta Q}(t',t)$

In this section, we derive the time-evolution equation for the two-point unequal-time density-current correlation $\mathcal{C}_r^{\eta Q}(t',t)$ as shown in Eq. (3.19) in the main text. To do so, we first derive the time-evolution equation of the local density $\rho_r(t)$, which is defined as the average occupancy at site r and time t, i.e., $\rho_r(t)=\langle\eta_r(t)\rangle$.
Recall, the average instantaneous bond-current $\langle J_r(t)\rangle$ across the bond $(r,r+1)$ at time t (as given by Eq. (3.3) in the main text) is given by,

$$\langle J_r(t)\rangle = \frac{1}{2}\sum_{l=1}^{\infty}\phi(l)\left[\sum_{g=1}^{l-1}\left(\mathcal{V}_{r+g+1}^{(g+2)}-\mathcal{V}_{r+1}^{(g+2)}\right)+\left(\mathcal{U}_{r+l}^{(l)}-\mathcal{U}_r^{(l)}\right)\right]. \tag{B.5}$$

Since the total number of particles is a conserved quantity, the corresponding local density is a slow variable and its time-evolution must be related to $\langle J_r(t)\rangle$ via the following continuity equation:

$$\frac{d\rho_r(t)}{dt} = \langle J_{r-1}(t)\rangle - \langle J_r(t)\rangle. \tag{B.6}$$

Using Eq. (B.5) in Eq. (B.6), it is now straightforward to obtain the corresponding time-evolution equation in the form of the following balance equation:

$$\frac{d\rho_r(t)}{dt} = \left\langle \mathcal{P}_r^{+}(t)\right\rangle - \left\langle \mathcal{P}_r^{-}(t)\right\rangle, \tag{B.7}$$

where the gain and loss terms are respectively given by,

$$\mathcal{P}_r^+(t) = \frac{1}{2}\sum_{l=1}^{\infty}\phi(l)\left[\sum_{g=1}^{l-1}\left\{\mathcal{V}_{r+g}^{(g+2)} + \mathcal{V}_{r+1}^{(g+2)}\right\} + \left\{\left(\mathcal{U}_{r+l-1}^{(l)} - \mathcal{U}_{r+l}^{(l+1)}\right) + \left(\mathcal{U}_r^{(l)} - \mathcal{U}_r^{(l+1)}\right)\right\}\right], \tag{B.8}$$

$$\mathcal{P}_r^-(t) = \frac{1}{2}\sum_{l=1}^{\infty}\phi(l)\left[\sum_{g=1}^{l-1}\left\{\mathcal{V}_{r+g+1}^{(g+2)} + \mathcal{V}_{r}^{(g+2)}\right\} + \left\{\left(\mathcal{U}_{r+l}^{(l)} - \mathcal{U}_{r+l}^{(l+1)}\right) + \left(\mathcal{U}_{r-1}^{(l)} - \mathcal{U}_{r}^{(l+1)}\right)\right\}\right]. \tag{B.9}$$

We now use the expression of the local diffusive current operator, as shown in Eq. (3.9) in the main text, to arrive at the following identity:

$$\begin{aligned}\mathcal{P}_r^+(t) - \mathcal{P}_r^-(t) &= J_{r-1}^{(D)}(t) - J_r^{(D)}(t), &\text{(B.10)}\\ &\simeq D(\rho,\gamma)\left[\eta_{r+1}(t) + \eta_{r-1}(t) - 2\eta_r(t)\right], &\text{(B.11)}\end{aligned}$$

where Eq. (B.11) is a direct consequence of the proposed closure approximation, as shown in Eq. (3.16) in the main text. Finally using Eqs. (B.11) and (B.7) together, we arrive at the desired time-evolution equation,

$$\frac{d\rho_r(t)}{dt} \simeq D(\rho,\gamma)\left[\rho_{r+1}(t) + \rho_{r-1}(t) - 2\rho_r(t)\right] = D(\rho,\gamma)\Delta_r^2\rho_r(t), \tag{B.12}$$

where Δ_r^2 is the discrete laplacian operator. We will now deduce the desired time-evolution of $\mathcal{C}_r^{\eta Q}(t',t)$ by writing the following update rules:

$$\eta_r(t'+dt')Q_0(t) = \begin{cases} 1\times Q_0(t), & \text{prob.} \quad \mathcal{P}_r^+(t')dt', \\ 0\times Q_0(t), & \text{prob.} \quad \mathcal{P}_r^-(t')dt', \\ \eta_r(t)Q_0(t), & \text{prob.} \quad 1-\Sigma dt, \end{cases} \tag{B.13}$$

Using the update equation, as shown above in Eq. (B.13), we write down the corresponding time-evolution equation as,

$$\begin{aligned}\frac{d}{dt'}\left\langle\eta_r(t')Q_0(t)\right\rangle &= \left\langle\left(\mathcal{P}_r^+(t') - \mathcal{P}_r^-(t')\right)Q_0(t)\right\rangle. &\text{(B.14)}\\ &\simeq D(\rho,\gamma)\Delta_r^2\left\langle\eta_r(t')Q_0(t)\right\rangle, &\text{(B.15)}\end{aligned}$$

where in the last equation, we have used the identity displayed in Eq. (B.11). Now, by using the definition of $\mathcal{C}_r^{\eta Q}(t',t) = \langle \eta_r(t')Q_0(t)\rangle - \langle \eta_r(t')\rangle Q_0(t)\rangle$, we directly obtain

$$\frac{d}{dt'}\mathcal{C}_r^{\eta Q}(t',t) \simeq D(\rho,\gamma)\Delta_r^2 \mathcal{C}_r^{\eta Q}(t',t). \tag{B.16}$$

Note that Eq. (B.16) is the desired time-evolution equation which we have used in Eq. (3.19) in the main text.

B.3 Time evolution of equal time density-current correlation $\mathcal{C}_r^{\eta Q}(t,t)$

Here we will derive the time-evolution equation for the equal time density-current correlation $\mathcal{C}_r^{\eta Q}(t,t)$, which is presented in Eq. (3.28) of the main text. We write down all of the possible ways that the product $\eta_r Q_0$ can change in the infinitesimal time interval $[t, t+dt]$, as given by

$$\eta_r(t+dt)Q_0(t+dt) = \begin{cases} 1\times(Q_0(t)+1), & \text{prob.} \quad \mathcal{P}_r^3(t)dt, \\ 1\times(Q_0(t)-1), & \text{prob.} \quad \mathcal{P}_r^4(t)dt, \\ 0\times(Q_0(t)+1), & \text{prob.} \quad \mathcal{P}_r^5(t)dt, \\ 0\times(Q_0(t)-1), & \text{prob.} \quad \mathcal{P}_r^6(t)dt, \\ \eta_r(t)(Q_0(t)+1), & \text{prob.} \quad [\mathcal{P}_0^R(t)-\mathcal{P}_r^3(t)-\mathcal{P}_r^5(t)]dt, \\ \eta_r(t)(Q_0(t)-1), & \text{prob.} \quad [\mathcal{P}_0^L(t)-\mathcal{P}_r^4(t)-\mathcal{P}_r^6(t)]dt, \\ 1\times Q_0(t), & \text{prob.} \quad [\mathcal{P}_r^+(t)-\mathcal{P}_r^3(t)-\mathcal{P}_r^4(t)]dt, \\ 0\times Q_0(t), & \text{prob.} \quad [\mathcal{P}_r^-(t)-\mathcal{P}_r^5(t)-\mathcal{P}_r^6(t)]dt, \\ \eta_r(t)Q_0(t), & \text{prob.} \quad 1-\hat{\Sigma}(t)dt, \end{cases} \tag{B.17}$$

where $\hat{\Sigma}(t)dt$ is the sum of probability operators corresponding to the all possible ways in which the product $\eta_r(t)Q_0(t)$ can change in the infinitesimal time interval dt and is given by

$$\hat{\Sigma}(t) = \mathcal{P}_r^+(t) + \mathcal{P}_r^-(t) + \mathcal{P}_0^R(t) + \mathcal{P}_0^L(t) + \mathcal{P}_r^3(t) + \mathcal{P}_r^4(t) + \mathcal{P}_r^5(t) + \mathcal{P}_r^6(t), \tag{B.18}$$

and the operators $\mathcal{P}_r^3(t)$, $\mathcal{P}_r^4(t)$, $\mathcal{P}_r^5(t)$ and $\mathcal{P}_r^6(t)$ are defined as,

$$\mathcal{P}_r^3(t) = \frac{1}{2}\sum_{l=1}^{\infty}\phi(l)\left[\left(\mathcal{U}_r^{(l)} - \mathcal{U}_r^{(l+1)}\right)\sum_{k=1}^{l}\delta_{r,k} + \sum_{g=1}^{l-1}\mathcal{V}_{r+1}^{(g+2)}\sum_{k=1}^{g}\delta_{r,k}\right], \tag{B.19}$$

$$\mathcal{P}_r^4(t) = \frac{1}{2}\sum_{l=1}^{\infty}\phi(l)\left[\left(\mathcal{U}_{r+l-1}^{(l)} - \mathcal{U}_{r+l}^{(l+1)}\right)\sum_{k=1}^{l}\delta_{r,-k+1} + \sum_{g=1}^{l-1}\mathcal{V}_{r+g}^{(g+2)}\sum_{k=1}^{g}\delta_{r,-k+1}\right], \tag{B.20}$$

$$\mathcal{P}_r^5(t) = \frac{1}{2}\sum_{l=1}^{\infty}\phi(l)\left[\left(\mathcal{U}_{r+l}^{(l)} - \mathcal{U}_{r+l}^{(l+1)}\right)\sum_{k=1}^{l}\delta_{r,-k+1} + \sum_{g=1}^{l-1}\mathcal{V}_{r+g+1}^{(g+2)}\sum_{k=1}^{g}\delta_{r,-k+1}\right], \tag{B.21}$$

$$\mathcal{P}_r^6(t) = \frac{1}{2}\sum_{l=1}^{\infty}\phi(l)\left[\left(\mathcal{U}_{r-1}^{(l)} - \mathcal{U}_{r}^{(l+1)}\right)\sum_{k=1}^{l}\delta_{r,k} + \sum_{g=1}^{l-1}\mathcal{V}_{r}^{(g+2)}\sum_{k=1}^{g}\delta_{r,k}\right]. \tag{B.22}$$

Using the above update rules, shown in Eq. (B.17), the time-evolution of the quantity $\langle\eta_r(t)Q_0(t)\rangle$ is given by,

$$\begin{aligned}\frac{d}{dt}\langle\eta_r(t)Q_0(t)\rangle &= \left[\langle\mathcal{P}_r^3(t)\rangle - \langle\mathcal{P}_r^4(t)\rangle - \langle\mathcal{P}_r^5(t)\rangle + \langle\mathcal{P}_r^6(t)\rangle\right] + \left\langle\left[\mathcal{P}_r^+(t) - \mathcal{P}_r^-(t)\right]Q_0(t)\right\rangle \\ &\quad + \left\langle\eta_r(t)\left[\mathcal{P}_0^R(t) - \mathcal{P}_0^L(t)\right]\right\rangle.\end{aligned} \tag{B.23}$$

At the steady-state, we can disregard the spatial dependence in the average quantities $\langle\mathcal{U}^{(l)}\rangle$ and $\langle\mathcal{V}^{(g+2)}\rangle$, which essentially leads to the simplification of the first term in Eq. (B.23) in the following manner:

$$\begin{aligned}\langle\mathcal{P}_r^3(t)\rangle - \langle\mathcal{P}_r^4(t)\rangle - \langle\mathcal{P}_r^5(t)\rangle + \langle\mathcal{P}_r^6(t)\rangle &= \sum_{l=1}^{\infty}\phi(l)\Bigg[\left(\mathcal{U}^{(l)} - \mathcal{U}^{(l+1)}\right)\sum_{k=1}^{l}(\delta_{r,k} - \delta_{r,-k+1}) + \\ &\quad \sum_{g=1}^{l-1}\mathcal{V}^{(g+2)}\sum_{k=1}^{g}(\delta_{r,k} - \delta_{r,-k+1})\Bigg].\end{aligned} \tag{B.24}$$

Moreover, using the identity shown in Eq. (B.11), the second term in Eq. (B.23) can be transformed into

$$\left\langle\left[\mathcal{P}_r^+(t) - \mathcal{P}_r^-(t)\right]Q_0(t)\right\rangle \simeq D(\rho,\gamma)\Delta_r^2\langle\eta_r(t)Q_0(t)\rangle. \tag{B.25}$$

Furthermore, using the following relation: $\mathcal{P}_0^R(t) - \mathcal{P}_0^L(t) = J_0^{(D)}(t) \simeq D(\rho,\gamma)(\eta_0 - \eta_1)$, we rewrite the third term in Eq. (B.23) in the following way:

$$\left\langle\eta_r(t)\left[\mathcal{P}_0^R(t) - \mathcal{P}_0^L(t)\right]\right\rangle \simeq D(\rho,\gamma)\left[\langle\eta_r(t)\eta_0(t)\rangle - \langle\eta_r(t)\eta_1(t)\rangle\right] = D(\rho,\gamma)\Delta_r\langle\eta_r(t)\eta_0(t)\rangle \tag{B.26}$$

Finally using the last three transformations, the time-evolution equation of $\mathcal{C}_r^{\eta Q}(t,t)$ can be written as the following inhomogeneous differential equation:

$$\frac{d}{dt}\mathcal{C}_r^{\eta Q}(t,t) \simeq D(\rho,\gamma)\Delta_r^2\mathcal{C}_r^{\eta Q}(t,t) + \mathcal{S}_r^{\eta Q}(t), \tag{B.27}$$

where the source term is given by

$$\begin{aligned}\mathcal{S}_r^{\eta Q}(t) &= \sum_{l=1}^{\infty}\phi(l)\left[\left(\mathcal{U}^{(l)} - \mathcal{U}^{(l+1)}\right)\sum_{k=1}^{l}(\delta_{r,k} - \delta_{r,-k+1}) + \sum_{g=1}^{l-1}\mathcal{V}^{(g+2)}\sum_{k=1}^{g}(\delta_{r,k} - \delta_{r,-k+1})\right] \\ &\quad + D(\rho,\gamma)\Delta_r\mathcal{C}_r^{\eta\eta}(t,t).\end{aligned} \tag{B.28}$$

Eq. (B.27) describes the time-evolution of $\mathcal{C}_r^{\eta Q}(t,t)$ in the real space, which in the Fourier space is simply transformed into the following equation:

$$\left(\frac{d}{dt} + D(\rho,\gamma)\lambda_q\right)\tilde{\mathcal{C}}_q^{\eta Q}(t,t) = \tilde{\mathcal{S}}_q^{\eta Q}(t). \tag{B.29}$$

Note that, the above equation appears in Eq. (3.28) in the main text. Here $-\lambda_q$ is the eigenvalue of the discrete Laplacian operator, which is given by,

$$\lambda_q = 2\left(1 - \cos(q)\right), \tag{B.30}$$

and $\tilde{\mathcal{S}}_q^{\eta Q}(t)$ is the source term in the Fourier space which is trivially obtained to be,

$$\tilde{\mathcal{S}}_q^{\eta Q}(t) = \frac{1}{(1-e^{-iq})}\left[D(\rho,\gamma)\lambda_q\tilde{\mathcal{C}}_q^{\eta\eta}(t,t) - \sum_{l=1}^{\infty}\phi(l)\Big\{\left(\mathcal{U}^{(l)} - \mathcal{U}^{(l+1)}\right)\lambda_{lq} + \sum_{g=1}^{l-1}\mathcal{V}^{(g+2)}\lambda_{gq}\Big\}\right]. \tag{B.31}$$

Finally using the following identities that relates the correlators $\mathcal{U}^{(l)}$, $\mathcal{V}^{(g+2)}$ with the gap-distrbution function $P(g)$ as given by

$$\begin{aligned}\mathcal{U}^{(l)}(t) &= \rho\sum_{g=l-1}^{\infty}(g-l+1)P(g,t), \\ \mathcal{V}^{(g+2)}(t) &= \rho P(g,t),\end{aligned} \tag{B.32}$$

we obtain simpler structure of $\tilde{\mathcal{S}}_q^{\eta Q}(t)$, which is given by

$$\tilde{\mathcal{S}}_q^{\eta Q}(t) = \frac{1}{(1-e^{-iq})}\Big[D(\rho,\gamma)\lambda_q\tilde{\mathcal{C}}_q^{\eta\eta}(t,t) - f_q(t)\Big], \tag{B.33}$$

where $f_q(t)$ is given by

$$f_q(t) = \rho \sum_{l=1}^{\infty} \phi(l) \left[\sum_{g=1}^{l-1} \lambda_{gq} P(g,t) + \lambda_{lq} \sum_{g=l}^{\infty} P(g,t) \right]. \tag{B.34}$$

The last two equations compositely express the source term corresponding to the equal time density-current correlation function and they appear in the main text in Eqs. (3.29) and (3.30), respectively.

B.4 Time evolution of equal-time density correlation $\mathcal{C}_r^{\eta\eta}(t,t)$

$$\eta_r(t+dt)\eta_0(t+dt) = \begin{cases} 1 \times 1, & \text{prob.} \quad \mathcal{P}_r^7(t)dt, \\ 0 \times 0, & \text{prob.} \quad \mathcal{P}_r^8(t)dt, \\ 1 \times 0, & \text{prob.} \quad \mathcal{P}_r^9(t)dt, \\ 0 \times 1, & \text{prob.} \quad \mathcal{P}_r^{10}(t)dt, \\ 1 \times \eta_0(t), & \text{prob.} \quad [\mathcal{P}_r^+(t) - \mathcal{P}_r^7(t) - \mathcal{P}_r^9(t)]dt, \\ 0 \times \eta_0(t), & \text{prob.} \quad [\mathcal{P}_r^-(t) - \mathcal{P}_r^8(t) - \mathcal{P}_r^{10}(t)]dt, \\ \eta_r(t) \times 1, & \text{prob.} \quad [\mathcal{P}_0^+(t) - \mathcal{P}_r^7(t) - \mathcal{P}_r^{10}(t)]dt, \\ \eta_r(t) \times 0, & \text{prob.} \quad [\mathcal{P}_0^-(t) - \mathcal{P}_r^8(t) - \mathcal{P}_r^9(t)]dt, \\ \eta_r(t)\eta_0(t), & \text{prob.} \quad 1 - \hat{\Sigma}(t)dt, \end{cases} \tag{B.35}$$

where $\hat{\Sigma}(t)dt$ corresponds to the total probability with which the product of occupations at sites r and 0 changes in the infinitesimal time interval dt with

$$\hat{\Sigma}(t) = \mathcal{P}_r^+(t) + \mathcal{P}_r^-(t) + \mathcal{P}_0^+(t) + \mathcal{P}_0^-(t) - \mathcal{P}_r^7(t) - \mathcal{P}_r^8(t) - \mathcal{P}_r^9(t) - \mathcal{P}_r^{10}(t), \tag{B.36}$$

and the operators $\mathcal{P}_r^7(t)$, $\mathcal{P}_r^8(t)$, $\mathcal{P}_r^9(t)$ and $\mathcal{P}_r^{10}(t)$ are defined as,

$$\mathcal{P}_r^7(t) = \frac{1}{2}\sum_{l=1}^{\infty}\phi(l)\left[\sum_{g=1}^{l-1}\left(\mathcal{V}_{r+1}^{(g+2)}+\mathcal{V}_{r+g}^{(g+2)}\right)\delta_{r,0}+\left\{\left(\mathcal{U}_r^{(l)}-\mathcal{U}_r^{(l+1)}\right)+\left(\mathcal{U}_{r+l-1}^{(l)}-\mathcal{U}_{r+l}^{(l+1)}\right)\right\}\delta_{r,0}\right], \quad \text{(B.37)}$$

$$\mathcal{P}_r^8(t) = \frac{1}{2}\sum_{l=1}^{\infty}\phi(l)\left[\sum_{g=1}^{l-1}\left(\mathcal{V}_{r}^{(g+2)}+\mathcal{V}_{r+g+1}^{(g+2)}\right)\delta_{r,0}+\left\{\left(\mathcal{U}_{r+l}^{(l)}-\mathcal{U}_{r+l}^{(l+1)}\right)+\left(\mathcal{U}_{r-1}^{(l)}-\mathcal{U}_{r}^{(l+1)}\right)\right\}\delta_{r,0}\right], \quad \text{(B.38)}$$

$$\mathcal{P}_r^9(t) = \frac{1}{2}\sum_{l=1}^{\infty}\phi(l)\left[\sum_{g=1}^{l-1}\left(\mathcal{V}_{g+1}^{(g+2)}\delta_{r,g}+\mathcal{V}_{0}^{(g+2)}\delta_{r,-g}\right)+\left\{\left(\mathcal{U}_{l}^{(l)}-\mathcal{U}_{l}^{(l+1)}\right)\delta_{r,l}+\left(\mathcal{U}_{-1}^{(l)}-\mathcal{U}_{0}^{(l+1)}\right)\delta_{r,-l}\right\}\right], \quad \text{(B.39)}$$

$$\mathcal{P}_r^{10}(t) = \frac{1}{2}\sum_{l=1}^{\infty}\phi(l)\left[\sum_{g=1}^{l-1}\left(\mathcal{V}_{r+g+1}^{(g+2)}\delta_{r,-g}+\mathcal{V}_{r}^{(g+2)}\delta_{r,g}\right)+\left\{\left(\mathcal{U}_{r+l}^{(l)}-\mathcal{U}_{r+l}^{(l+1)}\right)\delta_{r,-l}+\left(\mathcal{U}_{r-1}^{(l)}-\mathcal{U}_{r}^{(l+1)}\right)\delta_{r,l}\right\}\right]. \quad \text{(B.40)}$$

Finally using the above update rules in Eq. (B.35), we can straightforwardly write down the corresponding time-evolution equation, which is given by,

$$\frac{d}{dt}\langle\eta_r(t)\eta_0(t)\rangle = \left(\langle\mathcal{P}_r^7(t)\rangle+\langle\mathcal{P}_r^8(t)\rangle-\langle\mathcal{P}_r^9(t)\rangle-\langle\mathcal{P}_r^{10}(t)\rangle\right)+\left\langle\eta_r(t)\left(\mathcal{P}_0^+(t)-\mathcal{P}_0^-(t)\right)\right\rangle + \left\langle\left(\mathcal{P}_r^+(t)-\mathcal{P}_r^-(t)\right)\eta_0(t)\right\rangle. \quad \text{(B.41)}$$

Using the concept of spatial homogeneity at the steady-state, we can now ignore the spatial dependence in the averages $\langle\mathcal{U}^{(l)}\rangle$ and $\langle\mathcal{V}^{(g+2)}\rangle$, which leads to the following simplification of the first term in Eq. (B.41):

$$\begin{aligned}\mathcal{S}_r^{\eta\eta}(t) &= \langle\mathcal{P}_r^7(t)\rangle+\langle\mathcal{P}_r^8(t)\rangle-\langle\mathcal{P}_r^9(t)\rangle-\langle\mathcal{P}_r^{10}(t)\rangle,\\ &= \sum_{l=1}^{\infty}\phi(l)\left[\sum_{g=1}^{l-1}\mathcal{V}^{(g+2)}(t)\left(2\delta_{r,0}-\delta_{r,g}-\delta_{r,-g}\right)+\left(\mathcal{U}^{(l)}(t)-\mathcal{U}^{(l+1)}(t)\right)\left(2\delta_{r,0}-\delta_{r,l}-\delta_{r,-l}\right)\right],\\ &= \rho\sum_{l=1}^{\infty}\phi(l)\left[\sum_{g=1}^{l-1}P(g,t)\left(2\delta_{r,0}-\delta_{r,g}-\delta_{r,-g}\right)+\sum_{g=l}^{\infty}P(g,t)\left(2\delta_{r,0}-\delta_{r,l}-\delta_{r,-l}\right)\right]. \quad \text{(B.42)}\end{aligned}$$

Note that, in the last line we have used the identities in Eq. (B.32) to replace the correlators $\mathcal{V}^{(g+2)}(t)$ and $\mathcal{U}^{(l)}(t)$ in terms of the gap-distribution function $P(g,t)$. Furthermore, using the second identity, shown in Eq. (B.11), and the definition of $\mathcal{C}_r^{\eta\eta}(t,t)$, we can write down the corresponding time-evolution equation in real space in the following manner:

$$\frac{d}{dt}\mathcal{C}_r^{\eta\eta}(t,t) = 2D(\rho,\gamma)\Delta_r^2\mathcal{C}_r^{\eta\eta}(t,t)+\mathcal{S}_r^{\eta\eta}(t). \quad \text{(B.43)}$$

Using Eq. (3.20) in the above equation, we immediately obtain the corresponding evolution equation in the Fourier space, which is given by,

$$\frac{d}{dt}\tilde{\mathcal{C}}_q^{\eta\eta}(t,t) + 2D(\rho,\gamma)\lambda_q \tilde{\mathcal{C}}_q^{\eta\eta}(t,t) = \tilde{\mathcal{S}}_q^{\eta\eta}(t), \tag{B.44}$$

where $\tilde{\mathcal{S}}_q^{\eta\eta}(t)$ is the corresponding source-term in the Fourier space, which is simply obtained by using Eq. (3.20) in Eq. (B.42) and is given by,

$$\tilde{\mathcal{S}}_q^{\eta\eta}(t) = \rho \sum_{l=1}^{\infty} \phi(l) \left[\sum_{g=1}^{l-1} \lambda_{gq} P(g,t) + \lambda_{lq} \sum_{g=l}^{\infty} P(g,t) \right]. \tag{B.45}$$

It is worth noting that Eqs. (B.44) is the desired equation used in the main text as Eq. (3.33).

B.5 Time evolution of equal-time current correlation $\mathcal{C}_r^{QQ}(t,t)$

Here we provide the derivation details of Eq. (3.38) in the main text, which describes the time-evolution of $\mathcal{C}_r^{QQ}(t,t)$. We begin with the update rules corresponding to $Q_r(t)Q_0(t)$, as written below,

$$Q_r(t+dt)Q_0(t+dt) = \begin{cases} (Q_r(t)+1)(Q_0(t)+1), & \text{prob.} \quad \mathcal{P}_r^1(t)dt, \\ (Q_r(t)+1)Q_0(t), & \text{prob.} \quad [\mathcal{P}_r^R(t) - \mathcal{P}_r^1(t)]dt, \\ Q_r(t)(Q_0(t)+1), & \text{prob.} \quad [\mathcal{P}_0^R(t) - \mathcal{P}_r^1(t)]dt, \\ (Q_r(t)-1)(Q_0(t)-1), & \text{prob.} \quad \mathcal{P}_r^2(t)dt, \\ (Q_r(t)-1)Q_0(t), & \text{prob.} \quad [\mathcal{P}_r^L(t) - \mathcal{P}_r^2]dt, \\ Q_r(t)(Q_0(t)-1), & \text{prob.} \quad [\mathcal{P}_0^L(t) - \mathcal{P}_r^2(t)]dt, \\ Q_r(t)Q_0(t), & \text{prob.} \quad 1 - \hat{\Sigma}(t)dt, \end{cases} \tag{B.46}$$

where $\hat{\Sigma}(t)dt$ corresponds to the total probability with which the product of currents across bonds $(r, r+1)$ and $(0,1)$ changes in the infinitesimal time interval dt with

$$\hat{\Sigma} = \mathcal{P}_r^R(t) + \mathcal{P}_0^R(t)) + \mathcal{P}_r^L(t) + \mathcal{P}_0^L(t)) - \mathcal{P}_r^1(t) - \mathcal{P}_r^2(t), \tag{B.47}$$

and the operators $\mathcal{P}_r^1$ and $\mathcal{P}_r^2$ are defined as,

$$\mathcal{P}_r^1 = \frac{1}{2}\sum_{l=1}^{\infty}\phi(l)\Bigg\{\sum_{k=1}^{l}\left(\mathcal{U}_{r+k}^{(l)} - \mathcal{U}_{r+k}^{(l+1)}\right)\Theta(k+r)\Theta(l-r-k+1) + \sum_{g=1}^{l-1}\sum_{k=1}^{g}\mathcal{V}_{r+k+1}^{(g+2)}\Theta(k+r)\Theta(g-r-k+1)\Bigg\},$$

$$\mathcal{P}_r^2 = \frac{1}{2}\sum_{l=1}^{\infty}\phi(l)\Bigg\{\sum_{k=1}^{l}\left(\mathcal{U}_{r+k-1}^{(l)} - \mathcal{U}_{r+k}^{(l+1)}\right)\Theta(k+r)\Theta(l-r-k+1) + \sum_{g=1}^{l-1}\sum_{k=1}^{g}\mathcal{V}_{r+k}^{(g+2)}\Theta(k+r)\Theta(g-r-k+1)\Bigg\}.$$

Here $\Theta(r)$ is the Heaviside theta function, which is defined as

$$\Theta(r) = \begin{cases} 1, & \text{for } r > 0, \\ 0, & \text{otherwise.} \end{cases} \tag{B.48}$$

Using the update rules shown in Eq. (B.46), we write the evolution of two-point equal-time current-current correlation as,

$$\frac{d}{dt}\langle Q_r(t)Q_0(t)\rangle = \left[\left\langle \mathcal{P}_r^1\right\rangle + \left\langle \mathcal{P}_r^2\right\rangle\right] + \left\langle J_r^{(D)}(t)Q_0(t)\right\rangle + \left\langle J_0^{(D)}(t)Q_r(t)\right\rangle. \tag{B.49}$$

At the steady state, we can ignore the position dependence in the averages $\langle\mathcal{P}_r^1\rangle$ and $\langle\mathcal{P}_r^2\rangle$, which leads us to write the first term in a simplified manner through the following quantity:

$$\begin{aligned}
\Gamma_r &= \left\langle \mathcal{P}_r^1\right\rangle + \left\langle \mathcal{P}_r^2\right\rangle, \\
&= \sum_{l=|r|+1}^{\infty}\phi(l)\Bigg\{\left(\mathcal{U}^{(l)} - \mathcal{U}^{(l+1)}\right)(l- \mid r \mid) + \sum_{g=1}^{l-1}\mathcal{V}^{(g+2)}(g- \mid r \mid)\Bigg\} &\text{(B.50)}\\
&= \rho\sum_{l=|r|+1}^{\infty}\phi(l)\Bigg\{(l- \mid r \mid)\sum_{g=l}^{\infty}P(g) + \sum_{g=1}^{l-1}(g- \mid r \mid)P(g)\Bigg\}, &\text{(B.51)}
\end{aligned}$$

where to arrive at the last equation, which is presented as Eq. (3.39) in the main text, we have used the identities shown in Eq. (B.32). Finally using the definition of $\mathcal{C}_r^{QQ}(t,t)$ and the closure approximation scheme, as shown in Eq. (3.16), we obtain the desired time-evolution equation,

$$\frac{d}{dt}\mathcal{C}_r^{QQ}(t,t) = \Gamma_r - D(\rho,\gamma)\Delta_r\mathcal{C}_r^{\eta Q}(t,t) - D(\rho,\gamma)\Delta_{-r}\mathcal{C}_{-r}^{\eta Q}(t,t). \tag{B.52}$$

By using Fourier transform in Eq. (3.21) in the main text, we now invert the $\mathcal{C}_r^{\eta Q}(t,t)$ and $\mathcal{C}_{-r}^{\eta Q}(t,t)$ in Eq. (B.52) in their Fourier basis, and as a result, the corresponding steady-state

time-evolution equation of $\mathcal{C}_r^{QQ}(t,t)$ takes the following form:

$$\frac{d}{dt}\mathcal{C}_r^{QQ}(t,t) = \Gamma_r + \frac{D(\rho,\gamma)}{L}\sum_q (2-\lambda_{qr})\left(1-e^{-iq}\right)\tilde{\mathcal{C}}_q^{\eta Q}(t,t). \tag{B.53}$$

Eq. (B.53) is the resulting time-evolution equation, which is presented in the main text as Eq. (3.38) after integration.

B.6 Temporal correlation of instantaneous bond-current

Our aim in this section is to derive the expression of the steady-state temporal correlation of the instantaneous current $\mathcal{C}_0^{JJ}(t)$ in the long-time regime, which is presented in the main text in Eq. (3.53). Note that, for any time $t > 0$, we have already derived $\mathcal{C}_0^{JJ}(t)$ to obey the following equation (Eq. (3.52) in the main text):

$$\mathcal{C}_0^{JJ}(t,0) = -\frac{D(\rho,\gamma)}{2L}\sum_q f_q e^{-\lambda_q D(\rho,\gamma)t}, \tag{B.54}$$

where $q = 2\pi n/L$ with $n = 1, 2, \ldots, L-1$ and the quantity f_q at the steady state is defined as,

$$f_q = \rho\sum_{l=1}^{\infty}\phi(l)\left[\sum_{g=1}^{l-1}\lambda_{gq}P(g) + \lambda_{lq}\sum_{g=l}^{\infty}P(g)\right], \tag{B.55}$$

here $P(g)$ is the steady-state gap-distribution function of the system. Now, if we first take the infinite system size limit, i.e. $L \to \infty$, we have the following transformations: $q \to q(x) = 2\pi x$, $\lambda_q \to \lambda(x)$ and $f_q \to f(x)$. As a result, we can convert the summation into an integration, as shown in the following:

$$\lim_{L\to\infty}\mathcal{C}_0^{JJ}(t) \simeq -D(\rho,\gamma)\int_0^{1/2} dx f(x) e^{-\lambda(x)D(\rho,\gamma)t} \tag{B.56}$$

Interestingly, if we now take the large-time limit, i.e. $L^2/D \gg t \gg 1/D$ for $x > 0$, the integrand in Eq. (B.56) contributes only in the limit $x \to 0$, while it becomes vanishingly small for any other x values. This effectively leads to perform a small x analysis of Eq. (B.56). Note that, in this limit of $x \to 0$, $\lambda(x)$ is quadratic, i.e. $\lambda(x) \to 4\pi^2x^2$, $\lambda(lx) \to 4\pi^2l^2x^2$ and $\lambda(gx) \to 4\pi^2g^2x^2$. These transformations straighforwardly yield $f(x) \to 8\pi^2x^2\chi$ where χ is defined in Eq. (3.41) in the main text. Following all of the aforementioned transformations, Eq. (B.56) in terms of a new variable $z = 4\pi^2x^2Dt$ is directly reduced to the following in the

limit of large t:

$$\lim_{L\to\infty} \mathcal{C}_0^{JJ}(t) \simeq -\frac{\chi(\rho,\gamma)}{2\pi\sqrt{D(\rho,\gamma)}} t^{-3/2} \int_0^\infty dz\sqrt{z}e^{-z}. \tag{B.57}$$

Finally, using $\int_0^\infty dz\sqrt{z}e^{-z} = \sqrt{\pi}/2$, we get the desired result presented in the main text in Eq. (3.53),

$$\mathcal{C}_0^{JJ}(t) \simeq -\frac{\chi(\rho,\gamma)}{4\sqrt{\pi D(\rho,\gamma)}} t^{-3/2}. \tag{B.58}$$

B.7 Derivation of the time-integrated bond-current fluctuation $\mathcal{C}_0^{QQ}(t,t)$

According to Eq. (3.74) in the main text, the steady-state bond-current fluctuation for LLG is given by,

$$\mathcal{C}_0^{QQ}(t,t) = \left[\Gamma_0 - \frac{1}{L}\sum_q \left(\frac{f_q}{\lambda_q}\right)\right] t + \frac{1}{LD}\sum_q \left(\frac{f_q}{\lambda_q^2}\right)\left(1 - e^{-\lambda_q D t}\right), \tag{B.59}$$

where we have defined f_q and λ_q in the main text in Eqs. (3.30) and (3.25), respectively. Moreover, in order to obtain Γ_0, we put $r = 0$ in Eq. (3.39) in the main text, and get

$$\Gamma_0 = \rho \sum_{l=1}^{\infty} \phi(l) \left\{ l \sum_{g=l}^{\infty} P(g) + \sum_{g=1}^{l-1} g P(g) \right\}. \tag{B.60}$$

In order to simplify Eq. (B.59), we first expand f_q write

$$\sum_q \left(\frac{f_q}{\lambda_q}\right) = \rho \sum_{l=1}^{\infty} \phi(l) \left[\sum_{g=1}^{l-1} P(g) \sum_q \left(\frac{\lambda_{gq}}{\lambda_q}\right) + \left(\sum_q \frac{\lambda_{lq}}{\lambda_q}\right) \sum_{g=l}^{\infty} P(g) \right]. \tag{B.61}$$

Note that, the wave vector is given by $q = 2\pi n/L$ where $n = 1, 2, 3, \ldots, L-1$. Therefore, the above summation over q, appearing at the R.H.S of the above equation, can be equivalently transformed over the integer variable n, which can be solved easily using MATHEMATICA

to have the following simplified form:

$$\sum_q \left(\frac{\lambda_{gq}}{\lambda_q}\right) = \sum_{n=1}^{L-1} \left(\frac{1-\cos\left(\frac{2\pi gn}{L}\right)}{1-\cos\left(\frac{2\pi n}{L}\right)}\right) = g(L-g), \tag{B.62}$$

$$\sum_q \left(\frac{\lambda_{lq}}{\lambda_q}\right) = \sum_{n=1}^{L-1} \left(\frac{1-\cos\left(\frac{2\pi ln}{L}\right)}{1-\cos\left(\frac{2\pi n}{L}\right)}\right) = l(L-l). \tag{B.63}$$

Applying these relations in Eq. (B.61) drastically simplifies it and the resulting equation is given by

$$\sum_q \left(\frac{f_q}{\lambda_q}\right) = L\Gamma_0 - 2\chi(\rho,\gamma). \tag{B.64}$$

Using the above equation in Eq. (B.59), we finally obtain the expression of $\mathcal{C}_0^{QQ}(t,t)$ used in the main text in Eq. (3.75), which is given by

$$\mathcal{C}_0^{QQ}(t,t) = \frac{2\chi(\rho,\gamma)}{L}t + \frac{1}{D(\rho,\gamma)L}\sum_q \frac{f_q}{\lambda_q^2}\left(1-e^{-\lambda_q D(\rho,\gamma)t}\right). \tag{B.65}$$

B.8 Limiting cases of $\mathcal{C}_0^{QQ}(t,t)$

In this section, we are going to calculate $\mathcal{C}_0^{QQ}(t,t)$ in three distinct time regimes, which is shown in Eq. (3.78) in the main text.

Case I: Small time $t \ll 1/D$

It is easy to check that in this particular time regime, the second and the third terms in Eq. (B.59) identically cancel each other, which ultimately results in the following:

$$\mathcal{C}_0^{QQ}(t,t) = \Gamma_0 t. \tag{B.66}$$

Case II: Intermediate time $1/D \ll t \ll L^2/D$

To calculate $\mathcal{C}_0^{QQ}(t,t)$ in the intermediate regime, we use the expression derived in Eq. (B.67) and follow the footsteps of the analysis in Appendix F. As before, for infinitely large system size, i.e. $L \to \infty$, one can convert the summation into the following integral form:

$$\mathcal{C}_0^{QQ}(t,t) = \frac{2\chi(\rho,\gamma)}{L}t + \frac{2}{D(\rho,\gamma)}\int_0^{1/2} \frac{f(x)dx}{\lambda^2(x)}\left(1-e^{-\lambda(x)D(\rho,\gamma)t}\right), \tag{B.67}$$

where we have used the transformations, $q = 2\pi n/L \equiv 2\pi x$, $\lambda_q \to \lambda(x)$ and $f_q \to f(x)$. Note that, the integrand in the above equation primarily contributes in the limit $x \to 0$ in which case, following Eqs. (3.25) and (3.30) in the main text, we can write $\lambda(x) \simeq 4\pi^2 x^2$ and $f(x) \simeq 8\pi^2 x^2 \chi$. Finally, using the aforementioned transformations the above equation in terms of a new variable $z = 4\pi^2 x^2 Dt$ can be written as,

$$\mathcal{C}_0^{QQ}(t,t) = \frac{2\chi(\rho,\gamma)}{L}t + \frac{\chi(\rho,\gamma)}{\pi\sqrt{D(\rho,\gamma)}}\int_0^\infty z^{-3/2}\left(1-e^{-z}\right)dz. \tag{B.68}$$

Finally using the relation $\int_0^\infty z^{-3/2}\left(1-e^{-z}\right)dz = 2\sqrt{\pi}$ and neglecting the first term which is a subleading contributor, the leading order contribution to $\mathcal{C}_0^{QQ}(t,t)$ can be written as,

$$\mathcal{C}_0^{QQ}(t,t) \simeq \frac{2\chi(\rho,\gamma)}{\sqrt{\pi D(\rho,\gamma)}}\sqrt{t} + \mathcal{O}(t), \tag{B.69}$$

which is presented in the main text in Eq. (3.78).

Case III: Long-time $t \gg L^2/D$

From Eq. (B.67), it is straightforward to see that, in the limit of large t such that $t \gg L^2/D$, the exponential term contributes nothing, whereas the second term gives a constant value and the leading order contribution comes directly from the first term, which shows linear growth of $\mathcal{C}_0^{QQ}(t,t)$ with t, and the resulting equation becomes

$$\mathcal{C}_0^{QQ}(t,t) = \frac{2\chi(\rho,\gamma)}{L}t. \tag{B.70}$$

B.9 Scaling relation of the effective mobility $\chi(\rho,\gamma)$

In this section, we will obtain the scaling relation for $\chi(\rho,\gamma)$ in the limit $\rho \to 0$, $\gamma \to 0$, such that the ratio $\psi = \rho/\gamma$ is finite, and calculate the corresponding scaling function $\mathcal{H}(\psi)$ shown in the main text in Eqs. (3.70) and (3.72). We begin our analysis with the expression $\chi(\rho,\gamma)$ shown in Eq. (3.41) in the main text, i.e.,

$$\chi(\rho,\gamma) = \frac{\rho}{2}\sum_{l=1}^{\infty}\phi(l)\left[\sum_{g=1}^{l-1}g^2P(g) + l^2\sum_{g=l}^{\infty}P(g)\right]. \tag{B.71}$$

Note that, the hop-length distribution $\phi(l)$ is given in Eq. (2.4) in the main text as,

$$\phi(l) = Ae^{-\gamma l}, \tag{B.72}$$

where the normalization constant $A = (1 - e^{-1/l_p})$. Moreover, the steady-state gap distribution function $P(g)$, which is assumed to be exponentially distrubuted for $g > 0$, has the following form:

$$P(g) \simeq N_* \exp(-g/g_*), \tag{B.73}$$

where the prefactor N_*, as shown in the main text in Eq. (3.47), is given by,

$$N_* = \left(\frac{1}{\rho} - 1\right) \frac{(e^{1/g_*} - 1)^2}{e^{1/g_*}}. \tag{B.74}$$

Now using the above expression of $P(g)$ in Eq. (B.71) and performing some algebraic manipulations, we obtain

$$\chi(\rho, \gamma) = \frac{(1-\rho)}{2} \frac{(e^{1/g_*} - 1)(e^{\gamma + 1/g_*} + 1)}{(e^{\gamma + 1/g_*} - 1)^2}. \tag{B.75}$$

Note that, the above expression of $\chi(\rho, \gamma)$ is valid for any arbitrary ρ and γ. However, in the following analysis, we look at two specific cases:

- Case I, $\rho \to 0$ and $\gamma \to \infty$: In this case, the typical gap-size g_* is given by,

$$g_* = \frac{1}{\rho}. \tag{B.76}$$

  Now, to calculate $\chi(\rho, \gamma)$, we use Eq. (B.76) in Eq. (B.75), and with the limit $\rho \to 0$ such that $\gamma + 1/g_* \simeq \gamma \gg 1$ in consideration, we obtain

$$\chi(\rho, \gamma) = \frac{(e^{\rho} - 1)(1-\rho)}{2} e^{-\gamma} \tag{B.77}$$

$$\simeq \frac{\rho(1-\rho)}{2} e^{-\gamma} = \frac{\chi^{(0)} e^{-\gamma}}{2}, \tag{B.78}$$

  where $\chi^{(0)} = \rho(1-\rho)$ is the particle mobility in SSEP.

- Case II, $\rho \to 0$ and $\gamma \to 0$: In the limit of $\rho \to 0$, $\gamma \to 0$, such that the ratio $\psi = \rho/\gamma$ is finite, we make the following transformations in Eq. (B.75):

  – the typical gap-size g_* obeys the following scaling relation:

$$g_* \simeq \frac{1}{\rho} \mathcal{G}(\psi), \tag{B.79}$$

    where $\mathcal{G}(\psi)$ is the scaling function corresponding to g_*, which upon consideration

of the two limiting cases is assumed to be $\mathcal{G}(\psi) = \sqrt{1+\psi}$ (see the paragraph before Eq. (3.70) in the main text),

– all the exponential terms are approximated up to the leading order contributions, i.e.,

$$e^{\gamma+1/g_*} - 1 \simeq \gamma + 1/g_* = \gamma + \rho/\mathcal{G}(\psi) = \gamma(1 + \psi/\mathcal{G}(\psi)), \tag{B.80}$$

$$e^{1/g_*} - 1 \simeq 1/g_* = \gamma\psi/\mathcal{G}(\psi), \tag{B.81}$$

$$e^{\gamma+1/g_*} + 1 \simeq 2. \tag{B.82}$$

Finally, by substituting the above transformation in Eq. (B.75), we get the leading order contribution to $\chi(\rho, \gamma)$ in the limit $\rho \to 0$ and $\gamma \to 0$, as shown below,

$$\chi(\rho, \gamma) \simeq \frac{\rho(1-\rho)}{\gamma^2} \frac{\mathcal{G}(\psi)}{(\psi + \mathcal{G}(\psi))^2}. \tag{B.83}$$

Note that, by replacing $\chi^{(0)} = \rho(1-\rho)$ in the above equation, we immediately obtain the scaling relation shown in Eq. (3.70) in the main text and the corresponding scaling function is given by,

$$\mathcal{H}(\psi) = \frac{\mathcal{G}(\psi)}{(\psi + \mathcal{G}(\psi))^2}. \tag{B.84}$$

C

Appendix for Chapter 4

Here we provide calculation details of deriving the loss and gain rates at a particular site for short and long-range hopping.

C.1 gLLG with hop-length distribution $\phi(g) = \delta_{g,l}$ having finite hopping range l

C.1.1 Hydrodynamics

To calculate mobility in the hydrodynamic time-evolution equation of the density field, we bias the system by applying a small force of magnitude F, say, in the anti-clockwise direction. Due to the presence of a small biasing force F, hopping rates are modified. We denote the modified long-hop rates as $\beta_R^F(l)$ and $\beta_L^F(l)$ and the modified short-hop rates as α_R^F and α_L^F, where the subscripts "R" and "g' denote anti-clockwise (in the direction of the biasing force) and clock-wise (opposite to biasing force) directions, respectively. We explicitly write the lattice spacing a in the equations below.

C.1.2 Gap size $g < l$

When gap size $g < l$, where l is the maximum possible hop length, the mass loss and gain in this case (including the short hop), are shown below through all possible hopping events and the corresponding gain and loss rates.

The rate of loss of mass from the site i due to hopping of length g and a short hop to the right

$$\begin{aligned} J^{-}_{R,<}(i \to i+g) &= \frac{\beta^F_R(g)}{2}\langle \eta_i \overline{\eta}_{i+1} \ldots \overline{\eta}_{i+g}\eta_{i+g+1}\rangle + \frac{\alpha^F_R}{2}\langle \eta_i \overline{\eta}_{i+1}\rangle \\ &\simeq \frac{\beta^F_R(g)}{2}\mathcal{V}^{(g+2)}_{i+g+1} + \frac{\alpha^F_R}{2}\langle \eta_i(1-\eta_{i+1})\rangle, \end{aligned}$$

where we denote the correlation $\langle \eta_{i-1}\overline{\eta}_i\overline{\eta}_{i+1}\ldots\overline{\eta}_{i+g-1}\eta_{i+g}\rangle \equiv \mathcal{V}^{(g+2)}_{i+g}$. For this particular hopping event to be possible, the following conditions to be satisfied: (i) Site i must be occupied, (ii) the sites from $(i+1)$ up to $(i+g)$ must be vacant (so that the particle can jump a distance g) and (iii) then the site $(i+g+1)$ must be occupied [so that the particle does not jump beyond site $(i+g)$]. Similarly, other possible gain and loss terms can be constructed as given below.

The rate of gain of mass from the site $i+g$ due to hopping of length g and a short hop to the left,

$$\begin{aligned} J^{+}_{L,<}(i+g \to i) &= \frac{\beta^F_L(g)}{2}\langle \eta_{i-1}\overline{\eta}_i \ldots \overline{\eta}_{i+g-1}\eta_{i+g}\rangle + \frac{\alpha^F_L}{2}\langle \overline{\eta}_i\eta_{i+1}\rangle \\ &\simeq \frac{1}{2}\beta^F_L(g)\mathcal{V}^{(g+2)}_{i+g} + \frac{1}{2}\alpha^F_L\langle(1-\eta_i)\eta_{i+1}\rangle \end{aligned}$$

The rate of loss of mass from site i due to hopping of length g plus short hop to the left,

$$\begin{aligned} J^{-}_{L,<}(i \to i-g) &= \frac{\beta^F_L(g)}{2}\langle \eta_{i-g-1}\overline{\eta}_{i-g} \ldots \overline{\eta}_{i-1}\eta_i\rangle + \frac{\alpha^F_L}{2}\langle \overline{\eta}_{i-1}\eta_i\rangle \\ &= \frac{1}{2}\beta^F_L(g)\mathcal{V}^{(g+2)}_{i} + \frac{1}{2}\alpha^F_L\langle(1-\eta_{i-1})\eta_i\rangle \end{aligned}$$

The rate of gain of mass at site i due to hopping of length g and short hop to the right,

$$\begin{aligned} J^{+}_{R,<}(i-g \to i) &= \frac{\beta^F_R(g)}{2}\langle \eta_{i-g}\overline{\eta}_{i-g+1} \ldots \overline{\eta}_i\eta_{i+1}\rangle + \frac{\alpha^F_R}{2}\langle \eta_{i-1}\overline{\eta}_i\rangle \\ &= \frac{1}{2}\beta^F_R(g))\mathcal{V}^{(g+2)}_{i+1} + \frac{1}{2}\alpha^F_R\langle\eta_{i-1}(1-\eta_i)\rangle \end{aligned}$$

Therefore, the net rate of change of mass at site i due to the above hopping processes can be written as

$$\begin{aligned}
J^{+}_{L,<}(l) - J^{-}_{R,<}(l) + J^{+}_{R,<}(l) - J^{-}_{L,<}(l) &= \sum_{g=1}^{l-1}\Bigg[J^{+}_{L,<}(i+g\to i) - J^{-}_{R,<}(i\to i+g) + J^{+}_{R,<}(i-g\to i) \\
&\qquad -J^{-}_{L,<}(i\to i-g)\Bigg] \\
&= -\frac{\beta}{2}\sum_{g=1}^{l-1}\left[\left\{(1+\frac{Fga}{2})\mathcal{V}^{(g+2)}_{i+g+1} - (1-\frac{Fga}{2})\mathcal{V}^{(g+2)}_{i+g}\right\} - \left\{(1+\frac{Fga}{2})\mathcal{V}^{(g+2)}_{i+1} - (1-\frac{Fga}{2})\mathcal{V}^{(g+2)}_{i}\right\}\right] \\
&\quad -\frac{\alpha}{2}\Big[(1+\frac{Fa}{2})\langle\eta_i(1-\eta_{i+1})\rangle + (1-\frac{Fa}{2})\langle(1-\eta_{i-1})\eta_i\rangle - (1-\frac{Fa}{2})\langle(1-\eta_i)\eta_{i+1}\rangle - (1+\frac{Fa}{2}) \\
&\qquad \times\langle\eta_{i-1}(1-\eta_i)\rangle\Big] \\
&= -\frac{\beta}{2}\sum_{g=1}^{l-1}[\ldots] + \frac{\alpha}{2}[\langle\eta_{i+1}\rangle - 2\langle\eta_i\rangle + \langle\eta_{i-1}\rangle] + \frac{\alpha}{2}\frac{Fa}{2}\left[-(\langle\eta_{i+1}\rangle - \langle\eta_{i-1}\rangle) + 2(\langle\eta_i\eta_{i+1}\rangle - \langle\eta_{i-1}\eta_i\rangle)\right].
\end{aligned} \tag{C.1}$$

By denoting $\langle\eta_i\rangle = \rho_i$ and $\langle\eta_{i-1}\eta_i\rangle = \mathcal{V}^{(2)}_i$, we obtain the net flux corresponding to the events when $g < l$ as given below,

$$\begin{aligned}
&J^{+}_{L,<}(l) - J^{-}_{R,<}(l) + J^{+}_{R,<}(l) - J^{-}_{L,<}(l) = \frac{\alpha}{2}[\rho_{i+1} - 2\rho_i + \rho_{i-1}] - \frac{\alpha}{2}\frac{Fa}{2}\left[(\rho_{i+1} - \rho_{i-1}) - 2\left\{\mathcal{V}^{(2)}_{i+1} - \mathcal{V}^{(2)}_{i}\right\}\right] \\
&-\frac{\beta}{2}\sum_{g=1}^{l-1}\left[\left\{(1+\frac{Fga}{2})\mathcal{V}^{(g+2)}_{i+g+1} - (1-\frac{Fga}{2})\mathcal{V}^{(g+2)}_{i+g}\right\} - \left\{(1+\frac{Fga}{2})\mathcal{V}^{(g+2)}_{i+1} - (1-\frac{Fga}{2})\mathcal{V}^{(g+2)}_{i}\right\}\right].
\end{aligned} \tag{C.2}$$

We now perform a small-gradient $\mathcal{O}(1/L)$ Taylor series expansion as given below,

$$\begin{aligned}
\mathcal{V}^{(k)}_{i+1} &\equiv \mathcal{V}^{(k)}(x+1/L) \\
&\simeq \mathcal{V}^{(k)}(\rho(x)) + \frac{1}{L}\partial_x\mathcal{V}^{(k)}(\rho(x)) + \frac{1}{2L^2}\partial^2_x\mathcal{V}^{(k)}(\rho(x)), \\
\mathcal{V}^{(k)}_{i+g+1} &\equiv \mathcal{V}^{(k)}(x+(g+1)/L) \\
&\simeq \mathcal{V}^{(k)}(\rho(x)) + \frac{(g+1)}{L}\partial_x\mathcal{V}^{(k)}(\rho(x)) \\
&\quad + \frac{(g+1)^2}{2L^2}\partial^2_x\mathcal{V}^{(k),}(\rho(x)), \\
\mathcal{V}^{(k)}_{i+g} &\equiv \mathcal{V}^{(k)}(x+g/L) \\
&\simeq \mathcal{V}^{(k)}(\rho(x)) + \frac{g}{L}\partial_x\mathcal{V}^{(k)}(\rho(x)) + \frac{g^2}{2L^2}\partial^2_x\mathcal{V}^{(k)}(\rho(x)).
\end{aligned}$$

In the diffusive scaling limit $i \to x = i/L$, $t \to t/L^2$ and $a \to 1/L$, we can recast the net rate of change of mass in the form of the divergence of a current upto $\mathcal{O}\left(1/L^2\right)$,

$$J^+_{L,<} - J^-_{R,<} + J^+_{R,<} - J^-_{L,<} = \frac{\partial}{\partial x}\left[D_<(\rho)\frac{\partial \rho}{\partial x} - \chi_<(\rho)F\right] \tag{C.3}$$

where we denote

$$\begin{aligned} D_<(\rho) &= -\frac{\beta}{2}\frac{\partial}{\partial \rho}\left[\sum_{g=1}^{l-1} g\mathcal{V}^{(g+2)}(\rho)\right] + \frac{\alpha}{2} \\ &= -\frac{\beta}{2}\frac{\partial}{\partial \rho}\left[\rho\sum_{g=1}^{l-1} gP(g|\tilde{\rho})\right] + \frac{\alpha}{2}, \end{aligned} \tag{C.4}$$

$$\begin{aligned} \chi_<(\rho) &= \frac{\beta}{2}\sum_{g=1}^{l-1} g^2\mathcal{V}^{(g+2)}(\rho) + \frac{\alpha}{2}\mathcal{V}^{(2)}(\rho) \\ &= \frac{\beta}{2}\rho\sum_{g=1}^{l-1} g^2P(g|\tilde{\rho}) + \frac{\alpha}{2}\mathcal{V}^{(2)}(\rho), \end{aligned} \tag{C.5}$$

by noting that the correlation $\mathcal{V}^{(g+2)}(\rho)$ in gLLG with density ρ is related to the single-site mass distribution $P(g|\tilde{\rho})$ in UgLLG with density $\tilde{\rho} = 1/\rho - 1$.

C.1.3 Gap size $g \geq l$

Let us first consider the case for which the gap in front of i th site is larger than or equal to l. In that case, the maximum hop length is l. If a particle hops from ith site to $(i+l)$th site, the corresponding mass-loss rate is given by

$$\begin{aligned} J^-_{R,\geq}(i \to i+l) &= \frac{\beta}{2}(1+\frac{Fla}{2})\langle \eta_i\overline{\eta}_{i+1}\overline{\eta}_{i+2}\ldots\overline{\eta}_{i+l}\rangle \\ &= \frac{\beta}{2}(1+\frac{Fla}{2})\langle (1-\overline{\eta}_i)\overline{\eta}_{i+1}\overline{\eta}_{i+2}\ldots\overline{\eta}_{i+l}\rangle, \end{aligned} \tag{C.6}$$

where we denote $\overline{\eta}_i = (1-\eta_i)$.

Similarly if a particle hops from $(i+l)$th to ith site site, the corresponding mass-gain rate is given by

$$\begin{aligned} J^+_{L,\geq}(i+l_p \to i) &= \frac{\beta}{2}(1-\frac{Fla}{2})\langle \eta_{i+l}\overline{\eta}_{i+l-1}\overline{\eta}_{i+l-2}\ldots\overline{\eta}_{i}\rangle \\ &= \frac{\beta}{2}(1-\frac{Fla}{2})\langle (1-\overline{\eta}_{i+l})\overline{\eta}_{i+l-1}\overline{\eta}_{i+l-2}\ldots\overline{\eta}_{i}\rangle. \end{aligned} \tag{C.7}$$

The net gain rate from the right side of the ith site is written as, by adding the above two terms,

$$\begin{aligned} J^{+}_{L,\geq}(i+l_p \to i) - J^{-}_{R,\geq}(i \to i+l) &= \frac{\beta}{2}\{\langle \overline{\eta}_{i+l-1}\overline{\eta}_{i+l-2}\dots\overline{\eta}_i\rangle - \langle \overline{\eta}_{i+1}\overline{\eta}_{i+2}\dots\overline{\eta}_{i+l}\rangle\} - \frac{\beta Fla}{4}\{\langle \overline{\eta}_{i+l-1}\overline{\eta}_{i+l-2} \\ &\quad \dots\overline{\eta}_i\rangle + \langle \overline{\eta}_{i+1}\overline{\eta}_{i+2}\dots\overline{\eta}_{i+l}\rangle - 2\langle \overline{\eta}_i\overline{\eta}_{i+1}\overline{\eta}_{i+2}\dots\overline{\eta}_{i+l}\rangle\} \\ &= \frac{\beta}{2}[\mathcal{U}^{(l)}_{i+l-1} - \mathcal{U}^{(l)}_{i+l}] - \frac{\beta Fla}{4}[\mathcal{U}^{(l)}_{i+l-1} + \mathcal{U}^{(l)}_{i+l} - 2\mathcal{U}^{(l+1)}_{i+l}], \end{aligned} \tag{C.8}$$

Similarly, the net gain rate from the left side of site i can be written as

$$J^{+}_{R,\geq}(i-l_p \to i) - J^{-}_{L,\geq}(i \to i-l) = \frac{\beta}{2}[\mathcal{U}^{(l)}_{i} - \mathcal{U}^{(l)}_{i-1}] + \frac{\beta Fla}{4}[\mathcal{U}^{(l)}_{i} + \mathcal{U}^{(l)}_{i-1} - 2\mathcal{U}^{(l+1)}_{i}]. \tag{C.9}$$

Therefore the net rate of change of mass at site i due to the above processes can be written by adding the above four terms, which, in the diffusive scaling limit $i \to x = i/L$, $t \to t/L^2$ and lattice spacing $a \to 1/L$, reduces to the divergence of a hydrodynamic current upto $\mathcal{O}\left(1/L^2\right)$,

$$\Rightarrow J^{+}_{L,\geq} - J^{-}_{R,\geq} + J^{+}_{R,\geq} - J^{-}_{L,\geq} = \frac{\partial}{\partial x}\left[D_{\geq}(\rho)\frac{\partial \rho}{\partial x} - \chi_{\geq}(\rho)F\right], \tag{C.10}$$

where we denote

$$\begin{aligned} D_{\geq}(\rho) &= -\frac{\beta l}{2}\frac{\partial \mathcal{U}^{(l)}(\rho)}{\partial \rho}, \\ \chi_{\geq}(\rho) &= \frac{\beta l^2}{2}\left[\mathcal{U}^{(l)}(\rho) - \mathcal{U}^{(l+1)}(\rho)\right], \end{aligned}$$

and use Taylor series expansion,

$$\begin{aligned} \mathcal{U}^{(l)}_{i+l} &\equiv \mathcal{U}^{(l)}(x+l/L) \\ &\simeq \mathcal{U}^{(l)}(\rho(x)) + \frac{l}{L}\frac{\partial \mathcal{U}^{(l)}(\rho(x))}{\partial x} + \frac{l^2}{2L^2}\frac{\partial^2 \mathcal{U}^{(l)}(\rho(x))}{\partial x^2} + \dots, \end{aligned}$$

and

$$\begin{aligned} \mathcal{U}^{(l+1)}_{i+l} &\equiv \mathcal{U}^{(l+1)}(x+l/L) \\ &\simeq \mathcal{U}^{(l+1)}(\rho(x)) + \frac{l}{L}\frac{\partial \mathcal{U}^{(l+1)}(\rho(x))}{\partial x} + \frac{l^2}{2L^2}\frac{\partial^2 \mathcal{U}^{(l+1)}(\rho(x))}{\partial x^2} + \dots, \end{aligned}$$

and similarly for the other terms.

C.1.4 Continuity equation for local density

Considering all possible hopping events and summing over the corresponding gap sizes, we obtain the hydrodynamic time-evolution for the density field $\rho(x,t)$,

$$\begin{aligned}
\frac{\partial\rho(x,t)}{\partial t} &= (J^+_{L,<} - J^-_{R,<} + J^+_{R,<} - J^-_{L,<}) + (J^+_{L,\geq} - J^-_{R,\geq} + J^+_{R,\geq} - J^-_{L,\geq}) = J^+_R + J^+_L - J^-_R - J^-_L \\
&= \frac{\beta}{2}\left[\{\mathcal{U}^{(l)}_{i+l-1} - \mathcal{U}^{(l)}_{i+l}\} - \{\mathcal{U}^{(l)}_{i-1} - \mathcal{U}^{(l)}_{i}\}\right] - \frac{\beta F l}{4}\left[\{\mathcal{U}^{(l)}_{i+l-1} + \mathcal{U}^{(l)}_{i+l}\} - \{\mathcal{U}^{(l)}_{i-1} + \mathcal{U}^{(l)}_{i}\} - 2\{\mathcal{U}^{(l+1)}_{i+l} - \mathcal{U}^{(l+1)}_{i}\}\right] \\
&+ \sum_{g=1}^{l-1}\frac{\beta}{2}\left[\{\mathcal{V}^{(g+2)}_{i+1} - \mathcal{V}^{(g+2)}_{i}\} - \{\mathcal{V}^{(g+2)}_{i+g+1} - \mathcal{V}^{(g+2)}_{i+g}\}\right] - \sum_{g=1}^{l-1}\frac{\beta F g}{4}\left[\{\mathcal{V}^{(l+2)}_{i+g+1} + \mathcal{V}^{g+2}_{i+g}\} - \{\mathcal{V}^{(g+2)}_{i+1} + \mathcal{V}^{(g+2)}_{i}\}\right] \\
&+ \frac{\alpha}{2}\left[\rho_{i+1} - 2\rho_i + \rho_{i-1}\right] + \frac{pF}{4}\left[\{\rho_{i-1} - \rho_{i+1}\} + 2\{\mathcal{V}^{(2)}_{i+1} - \mathcal{V}^{(2)}_{i}\}\right] \equiv -\frac{\partial}{\partial x}\left[-D_{l_p}(\rho)\frac{\partial\rho}{\partial x} + \chi_{l_p}(\rho)F\right],
\end{aligned} \tag{C.11}$$

where we denote $J^+_R = J^+_{R,<} + J^+_{R,\geq}$, $J^+_L = J^+_{L,<} + J^+_{L,\geq}$, $J^-_R = J^-_{R,<} + J^-_{R,\geq}$ and $J^-_L = J^-_{L,<} + J^-_{L,\geq}$ and the transport coefficients - the bulk-diffusion coefficient $D_{l_p}(\rho)$ and the mobility $\chi_{l_p}(\rho)$, are given by

$$\begin{aligned}
D_{l_p}(\rho) &= D_<(\rho) + D_\geq(\rho) \\
&= \frac{\alpha}{2} - \frac{\beta}{2}\frac{\partial}{\partial\rho}\left[\sum_{g=1}^{l-1} g\mathcal{V}^{(g+2)}(\rho)\right] - \frac{\beta l}{2}\frac{\partial\mathcal{U}^{(l)}(\rho)}{\partial\rho}, \\
\chi_{l_p}(\rho) &= \chi_<(\rho) + \chi_\geq(\rho) \\
&= \frac{\beta l^2}{2}\left[\mathcal{U}^{(l)}(\rho) - \mathcal{U}^{(l+1)}(\rho)\right] + \frac{\beta}{2}\sum_{g=1}^{l-1} g^2\mathcal{V}^{(g+2)}(\rho) + \frac{\alpha}{2}\mathcal{V}^{(2)}(\rho),
\end{aligned}$$

constituting the first main results of the main text.

C.2 Infinite-ranged gLLG with hop-length distribution $\phi(g) = \delta_{g,l}$ where $l_p \to \infty$

In gLLG (exclusion version), a particle at a site i hops to right or left (each direction chosen randomly with probability 1/2) with slightly biased rates $\beta^F_R/2$ ($\alpha^F_R/2$, depending on long or short hop) or $\beta^F_L/2$ ($\alpha^F_L/2$), respectively, in the presence of a small biasing force F according to the following rules.

(A) Long hop: With rate β^F_R (β^F_L), a particle hops, without crossing any particle, symmetrically to right or left (with equal probability 1/2) to the site adjacent to its *nearest*

occupied site, i.e., it hops g lattice spacing, provided its neighboring *empty* stretch has length g.

(B) Short hop: With rate α_R^F (α_L^F), a particle hops to its right (left) nearest neighbor, provided the destination site is unoccupied.

Below we consider all possible loss and gain terms and the corresponding rates with which a particle leaves or enters a site i. The rate of loss of mass or particle from site i due to hopping of length g and short hop to the right,

$$\begin{aligned} J_R^-(i \to i+g) &= \frac{1}{2}\beta_R^F(l)\langle \eta_i \overline{\eta}_{i+1} \ldots \overline{\eta}_{i+g}\eta_{i+g+1}\rangle + \frac{1}{2}\alpha_R^F\langle \eta_i\overline{\eta}_{i+1}\rangle \\ &\simeq \frac{1}{2}\beta_R^F(l)\mathcal{V}_{i+g+1}^{(g+2)} + \frac{1}{2}\alpha_R^F\langle \eta_i(1-\eta_{i+1})\rangle, \end{aligned}$$

The rate of gain of mass from the site $i+g$ due to hopping of length g and short hop to the left,

$$\begin{aligned} J_L^+(i+g \to i) &= \frac{1}{2}\beta_L^F(g)\langle \eta_{i-1}\overline{\eta}_i \ldots \overline{\eta}_{i+g-1}\eta_{i+g}\rangle + \frac{1}{2}\alpha_L^F\langle \overline{\eta}_i\eta_{i+1}\rangle, \\ &\simeq \frac{1}{2}\beta_L^F(g)\mathcal{V}_{i+g}^{(g+2)} + \frac{1}{2}\alpha_L^F\langle (1-\eta_i)\eta_{i+1}\rangle. \end{aligned}$$

The rate of loss of mass from site i due to hopping of length g plus short hop to the left,

$$\begin{aligned} J_L^-(i \to i-g) &= \frac{1}{2}\beta_L^F(g)\langle \eta_{i-g-1}\overline{\eta}_{i-g} \ldots \overline{\eta}_{i-1}\eta_i\rangle + \frac{1}{2}\alpha_L^F\langle \overline{\eta}_{i-1}\eta_i\rangle \\ &= \frac{1}{2}\beta_L^F(g)\mathcal{V}_i^{(g+2)} + \frac{1}{2}\alpha_L^F\langle (1-\eta_{i-1})\eta_i\rangle \end{aligned}$$

The rate of gain of mass at site i due to hopping of length g and short hop to the right,

$$\begin{aligned} J_R^+(i-g \to i) &= \frac{1}{2}\beta_R^F(g)\langle \eta_{i-g}\overline{\eta}_{i-g+1} \ldots \overline{\eta}_i\eta_{i+1}\rangle + \frac{1}{2}\alpha_R^F\langle \eta_{i-1}\overline{\eta}_i\rangle \\ &= \frac{1}{2}\beta_R^F(g)\mathcal{V}_{i+1}^{(g+2)} + \frac{1}{2}\alpha_R^F\langle \eta_{i-1}(1-\eta_i)\rangle \end{aligned}$$

Therefore, the net rate of change of mass at site i can be written as

$$\begin{aligned}
\frac{\partial \rho_i}{\partial t} &= \sum_{g=1}^{\infty}\left[J_L^+(i+g\to i) - J_R^-(i\to i+g) + J_R^+(i-g\to i) - J_L^-(i\to i-g)\right] \\
&= -\frac{\beta}{2}\sum_{g=1}^{\infty}\left[\left\{(1+\frac{Fga}{2})\mathcal{V}_{i+g+1}^{(g+2)} - (1-\frac{Fga}{2})\mathcal{V}_{i+g}^{(g+2)}\right\} - \left\{(1+\frac{Fga}{2})\mathcal{V}_{i+1}^{(g+2)} - (1-\frac{Fga}{2})\mathcal{V}_{i}^{(g+2)}\right\}\right] \\
&-\frac{\alpha}{2}\left[(1+\frac{Fa}{2})\langle\eta_i(1-\eta_{i+1})\rangle + (1-\frac{Fa}{2})\langle(1-\eta_{i-1})\eta_i\rangle - (1-\frac{Fa}{2})\langle(1-\eta_i)\eta_{i+1}\rangle - (1+\frac{Fa}{2})\langle\eta_{i-1}(1-\eta_i)\rangle\right] \\
&= -\frac{\beta}{2}\sum_{g=1}^{\infty}\left[\left\{(1+\frac{Fga}{2})\mathcal{V}_{i+g+1}^{(g+2)} - (1-\frac{Fga}{2})\mathcal{V}_{i+g}^{(g+2)}\right\} - \left\{(1+\frac{Fga}{2})\mathcal{V}_{i+1}^{(g+2)} - (1-\frac{Fga}{2})\mathcal{V}_{i}^{(g+2)}\right\}\right] \\
&+\frac{\alpha}{2}[\rho_{i+1} - 2\rho_i + \rho_{i-1}] - \frac{\alpha}{2}\frac{Fa}{2}\left[(\rho_{i+1}-\rho_{i-1}) - 2\left\{\rho_{i+1}(1-\tilde{c}(\rho_{i+1})) - \rho_i(1-\tilde{c}(\rho_i))\right\}\right], \qquad \text{(C.12)}
\end{aligned}$$

where we simply denote $c(\rho)$ as the occupation probability in UgLLG corresponding to the density ρ in gLLG. We now perform a small-gradient $\mathcal{O}(1/L)$ Taylor series expansion as done in the previous sections (also see main text) and in the diffusive scaling limit $i \to x = i/L$ and $t \to t/L^2$, we finally obtain the hydrodynamic time-evolution of the density field $\rho(x,t)$,

$$\frac{\partial \rho(x,t)}{\partial t} = \frac{\partial}{\partial x}\left[D(\rho)\frac{\partial \rho}{\partial x}\right] - \frac{\partial[\chi(\rho)F]}{\partial x} \qquad \text{(C.13)}$$

where the transport coefficients, the bulk-diffusion coefficient, and the mobility, are given by

$$\begin{aligned}
D(\rho) &= -\frac{\beta}{2}\frac{d}{d\rho}\left[\sum_{g=1}^{\infty} g\mathcal{V}^{(g+2)}\right] + \frac{\alpha}{2} \\
&= -\frac{\beta}{2}\frac{d}{d\rho}\left[\rho\sum_{g=1}^{\infty} gP(g|\tilde{\rho})\right] + \frac{\alpha}{2} \\
&= -\frac{\beta}{2}\frac{d}{d\rho}\left(\rho\tilde{\rho}(\rho)\right) + \frac{\alpha}{2} = \frac{\alpha+\beta}{2}, \qquad \text{(C.14)}
\end{aligned}$$

$$\begin{aligned}
\chi(\rho) &= \frac{\beta}{2}\sum_{g=1}^{\infty} g^2\mathcal{V}^{(g+2)} + \frac{\alpha}{2}\rho\tilde{c}(\tilde{\rho}(\rho)) \\
&= \frac{\beta}{2}\rho\sum_{g=1}^{\infty} g^2P(g|\tilde{\rho}) + \frac{\alpha}{2}\rho\tilde{c}(\tilde{\rho}(\rho)) \\
&= \frac{\beta}{2}\rho\theta_2(\tilde{\rho}(\rho)) + \frac{\alpha}{2}\rho\tilde{c}(\tilde{\rho}(\rho)). \qquad \text{(C.15)}
\end{aligned}$$

Here we have used the relation $\mathcal{V}^{(2)}(\rho) = \rho P(g = 0|\tilde{\rho}) = \rho[1 - \tilde{c}(\tilde{\rho}(\rho))]$ where

$$\tilde{c}(\tilde{\rho}(\rho)) = \frac{\tilde{\rho}(1-\tilde{\rho})}{(1+\tilde{\rho})}$$

is the probability that a site in UgLLG is occupied at a given density

$$\tilde{\rho}(\rho) = \sum_g g P(g|\tilde{\rho}) = \frac{1}{\rho} - 1,$$

ρ being the corresponding density in gLLG. For the derivation of occupation probability $\tilde{c}(\tilde{\rho})$ and second moment of mass $\theta_2(\tilde{\rho}(\rho))$ as a function of density $\tilde{\rho}$ in UgLLG, see the next section. Finally, using relation between c, θ_2 and $\tilde{\rho}$ as a function of ρ, we obtain the expressions for the two transport coefficients as a function of density ρ,

$$D(\rho) = \frac{\alpha+\beta}{2} \; ; \; \chi(\rho) = \frac{\rho(1-\rho)[(\alpha+\beta)\rho^2 - 2\beta\rho + \beta]}{2[\rho^2 - \beta/(\alpha+\beta)]},$$

which constitutes the second main result of Chapter 4.

C.3 Calculation of second moment $\langle g_i^2 \rangle$ of local mass g_i in UgLLG with $\phi(g) = \delta_{gl}$ and $l_p \to \infty$

We consider UgLLG with $\phi(g) = \delta_{gl}$ and $l_p \to \infty$. We denote a configuration of UgLLG as a set of mass variables $\{g_i\}$. The dynamics in this special case of UgLLG consist of two processes chipping of a single unit of mass and diffusion of the entire stack of mass from any site i.

Chipping: With rate p, single unit mass at site i is chipped off and transferred symmetrically to one of its nearest neighbor sites with equal probability 1/2:

$$g_i \to g_i - 1 \; ; \; g_{i\pm1} \to g_{i\pm1} + 1.$$

Diffusion: With rate q, an entire stack of mass at site i diffuses symmetrically to one of its nearest neighbor sites with equal probability 1/2:

$$g_i \to 0 \; ; \; g_{i\pm1} \to g_{i\pm1} + g_i.$$

The occupancy of ith site is given by an indicator variable $\tilde{c}_i$ at site i,

$$\tilde{c}_i = (1 - \delta_{g_i,0}).$$

The local mass variable $m_i(t)$ at site i and at time t evolves in an infinitesimal time-interval dt according to the following stochastic dynamics:

$$g_i(t+dt) = \begin{cases} g_i(t) + m_{i-1}(t) & \text{prob. } \tilde{c}_{i-1}\frac{\beta}{2}dt, \\ g_i(t) + m_{i+1}(t) & \text{prob. } \tilde{c}_{i+1}\frac{\beta}{2}dt, \\ g_i(t) - 1 & \text{prob. } \tilde{c}_i p dt, \\ g_i(t) + 1 & \text{prob. } \tilde{c}_{i+1}\frac{\alpha}{2}dt, \\ g_i(t) + 1 & \text{prob. } \tilde{c}_{i-1}\frac{\alpha}{2}dt, \\ 0 & \text{prob. } \tilde{c}_i q dt, \\ g_i(t) & \text{prob. } 1 - \Sigma dt, \end{cases} \tag{C.16}$$

with

$$\Sigma = \left[\frac{\beta}{2}\tilde{c}_{i-1} + \frac{\beta}{2}\tilde{c}_{i+1} + p\tilde{c}_i + q\tilde{c}_i + \frac{\alpha}{2}\tilde{c}_{i+1} + \frac{\alpha}{2}\tilde{c}_{i-1}\right].$$

Various moments $\langle g_i^n \rangle$ of local mass g_i can be straightforwardly calculated; see, e.g., Ref. [129]. Using the above time-evolution dynamics, the second moment of local mass $m_i(t)$ can be written as,

$$\begin{aligned} \frac{d\langle g_i^2(t)\rangle}{dt} &= \langle g_i^2(t)(-\tilde{c}_i q)\rangle + \langle g_{i+1}^2(t)\frac{\tilde{c}_{i+1}}{2}q\rangle + \langle g_{i-1}^2(t)\frac{\tilde{c}_{i-1}}{2}q\rangle \\ &+2\langle [g_i(t)g_{i+1}(t)\tilde{c}_{i+1}q + g_i(t)g_{i-1}(t)\tilde{c}_{i-1}q - g_i(t)\tilde{c}_i p]\rangle \\ &+\frac{\alpha}{2}\langle g_i(t)(\tilde{c}_{i+1} + \tilde{c}_{i-1})\rangle + p\langle [\tilde{c}_i + \frac{\tilde{c}_{i+1}}{2} + \frac{\tilde{c}_{i-1}}{2}]\rangle, \end{aligned}$$

which, in the steady state, leads to

$$\begin{aligned} 0 = -q\langle g_i^2\rangle + \frac{\beta}{2}\langle g_{i+1}^2\rangle + \frac{\beta}{2}\langle g_{i-1}^2 + q\rho^2 - 2p\rho\rangle \\ +q\rho^2 + 2p\tilde{\rho}\tilde{c}(\tilde{\rho}) + 2p\tilde{c}(\tilde{\rho}), \end{aligned}$$

where $\langle g_i \rangle = \tilde{\rho}$ is the density in UgLLG, $\langle \tilde{c}_i \rangle = \tilde{c}(\tilde{\rho})$ is the occupation probability of a site in UgLLG. Note that, in the above equation, we have used the following mean-field assumptions (which, as our finite-size scaling analysis indicates, could actually be exact): For $k \neq 0$, $\langle g_i g_{i+k}\rangle = \tilde{\rho}^2; \langle g_i \tilde{c}_{i+k}\rangle = \tilde{\rho}\tilde{c}(\tilde{\rho})$. This particular mean-field assumption is called "independent interval approximation", which indeed works very well in various other mass transport processes as well. Upon further algebraic manipulations, we obtain occupation probability in UgLLG as a function of density $\tilde{\rho}$,

$$\tilde{c}(\tilde{\rho}) = \frac{\tilde{\rho}(p - q\tilde{\rho})}{p(1+\tilde{\rho})}. \tag{C.17}$$

Then using the time-evolution of the third moment $\langle g_i^3 \rangle$ and the mean-field approximation as mentioned above, we get the expression of the second moment $\langle g_i^2 \rangle$ as a function of density $\tilde{\rho}$,

$$\langle g_i^2 \rangle \equiv \theta_2(\tilde{\rho}) = \frac{p[1+\tilde{c}(\tilde{\rho})]\tilde{\rho}}{p[1-\tilde{c}(\tilde{\rho})]-2q\tilde{\rho}}. \tag{C.18}$$

C.4 Calculation of single-site mass distribution $P(g)$ in UgLLG (equivalently, gap distribution in gLLG) in the limit $l_p \to \infty$

Assuming the approximation of independent intervals (or independent gaps), we write the joint probability distribution of masses, or gaps, in a product form,

$$\text{Prob.}[\{g_k\}] = \frac{1}{Z_U} \prod_k w(g_k) \delta \left(\sum_k g_k - M \right), \tag{C.19}$$

where masses or gaps $\{g_k\}$ are statistically independent of each other (except for the conservation constraint) and, consequently, the weight factor $w(g_k)$ for mass or gap g_k at site k is assumed to depend on only the gap size g_k (not the neighboring gaps), M is the total mass or total gap size in UgLLG and the normalization constant or the partition sum can be written as

$$Z_U = \sum_{\{g_k\}} \prod_k w(g_k) \delta(\sum_k g_k - M). \tag{C.20}$$

Then the probability distribution $P(g_k = g)$ of gap size g can be calculated as

$$P(g_k = g) = \frac{w(g)}{Z_U} \sum_{\{g'_k\}; k' \neq k} \prod_{k'} w(g_{k'}) \delta \left(\sum_{k'} g_{k'} - M + g \right)$$

Provided the product form of Eq. C.19 and the knowledge of the functional dependence of variance $\sigma^2(\tilde{\rho}) = \langle g_k^2 \rangle - \tilde{\rho}^2 = \theta_2(\tilde{\rho}) - \tilde{\rho}^2 = \tilde{\rho}(1+\tilde{\rho})(1+\tilde{\rho}^2)/(1-2\tilde{\rho}-\tilde{\rho}^2)$ on density $\tilde{\rho}$ where critical $\tilde{\rho}_c = \sqrt{2}-1$ beyond which the variance is diverging, one can analytically calculate. Indeed, by following Ref. [129], one can show that Laplace transform $\tilde{w}(s) = \int w(g) \exp(-sg) dg$ of weight factor $w(g)$ is related to Legendre transform of free energy density function $f_U(\tilde{\rho})$ in

UgLLG (unbounded version of the model) as given below

$$\lambda(s) = \inf_{\tilde{\rho}}\{f_U(\tilde{\rho}) + s\tilde{\rho}\},$$

where $\lambda(s) = -\ln \tilde{w}(s)$ and free energy density function $F_U(\tilde{\rho})$ is calculated by integrating a fluctuation response relation $d^2 f_U/d\tilde{\rho}^2 = 1/\sigma^2(\tilde{\rho})$. The weight factor $w(g)$ can then be calculated from the inverse (discrete) Laplace transform. As a consequence of the mobility $\chi \sim \theta_2 = \sum g^2 P(g)$ is proportional to the second moment of gap (in gLLG as shown in the main text and also in UgLLG [139]) and the Einstein relation $\sigma^2 = \chi/D$ (which holds also in UgLLG [139]), one can see that the same pole-type singular structure (a simple pole) as in the mobility appears also in the variance $\sigma^2(\tilde{\rho})$ of gap size, i.e., $\sigma^2(\tilde{\rho}) \sim (\rho_c - \tilde{\rho})^{-1}$. This particular simple-pole singularity in the variance $\sigma^2(\tilde{\rho})$ of gap implies that the weight factor $w(g)$, for large gap sizes $g \gg 1$, must have a form of a power law [129],

$$w(g) \simeq C g^{-5/2}, \tag{C.21}$$

where C is an arbitrary constant factor. Consequently, the probability distribution $P(g)$ of gap size can be written as

$$P(g) \equiv \text{Prob.}(g_k = g) \sim g^{-5/2} e^{\mu(\tilde{\rho})g}, \tag{C.22}$$

where $-\mu(\tilde{\rho})$ is a density-dependent cut-off; here μ can be thought of as a nonequilibrium chemical potential (see the discussions in the next section). As $\tilde{\rho} \to \tilde{\rho}_c^-$ (near criticality), the chemical potential $\mu(\tilde{\rho}) \to 0$ and, at $\tilde{\rho} = \tilde{\rho}_c$ (criticality), the mass (or gap) distribution $P(g) \sim g^{-5/2}$ becomes a pure power law. Above the critical density $\tilde{\rho} > \tilde{\rho}_c$, the excess mass (or gap) of amount $L(\tilde{\rho} - \tilde{\rho}_c)$ forms a condensate of gap (equivalently, a condensate of holes forms in the exclusion version of gLLG).

C.5 Calculation of two-point correlation $c(r)$ in gLLG in the limit $l_p \to \infty$

In this section, we calculate two-point density correlation function using the mapping between gLLG and UgLLG (see main text for the mapping) and the configuration probability weight Eq. (C.19) in UgLLG. Let us denote the weight factor $W(C)$ for a microscopic configuration C in gLLG. Then the probability of a microscopic configuration C can be written as

$$P(C) = \frac{W(C)}{Z(N, L)}, \tag{C.23}$$

where N and L are the total number of particles and lattice sites, respectively and $Z(N,L)$ is the corresponding partition sum

$$Z(N,L) = \sum_C W(C). \tag{C.24}$$

It is not difficult to see that the partition sums Z_U in UgLLG [as in Eq. (C.19)] and Z in gLLG are related to each other by a simple prefactor [167],

$$Z(N,L) = \frac{L}{N} Z_U(N', g), \tag{C.25}$$

where $N' = L - N$ is the total mass or gap size and $g = N$ is the number of lattice sites in UgLLG (through the mapping between gLLG and UgLLG, $N' = L - N$ and $g = N$). The generating function (discrete Laplace transform or the "grand-canonicag' partition sum) for the partition sum $Z_U(N', g)$ is given by

$$\widetilde{Z}_U(z,g) = \sum_{N'=0}^{\infty} Z_U(N', g) z^{N'} = [\tilde{w}(z)]^g \tag{C.26}$$

where $z = e^{\mu}$ is the fugacity and $\tilde{w}(z)$ is the generating function (discrete Laplace transform) of the weight factor $w(g)$,

$$\tilde{w}(z) = \sum_{g=0}^{\infty} z^g w(g).$$

Let us now define two-point correlation function in gLLG (the exclusion version) as $c(r) = \langle n_i n_{i+r} \rangle - \rho^2$, which we calculate here by following Ref. [167]. The first term $\langle n_i n_{i+r} \rangle$ in the correlation function $c(r)$ gives nonzero value when both ith and $(i+r)$th sites are occupied. Now consider a set of configurations in which there are k holes present in between ith and $(i+r-1)$th site. Using the mapping between gLLG and UgLLG and summing over all such allowed configurations, we get for large L and N [167],

$$\begin{aligned} \langle n_i n_{i+r} \rangle &= \sum_{k=0}^{r-1} \frac{Z_U(k, r-k) Z_U(L-N-k, N-r+k)}{Z(N,L)} \\ &= \rho \sum_{k=0}^{r-1} \frac{Z_U(k, r-k) Z_U(L-N-k, N-r+k)}{Z_U(L-N, N)}. \end{aligned} \tag{C.27}$$

Using Taylor series expansion,

$$\ln\left[\frac{Z_U(L-N-k,N-r+k)}{Z_U(L-N,N)}\right] = (k-r)\frac{\partial[\ln Z_U(N',g)]}{\partial g} - k\frac{\partial[\ln Z_U(N',g)]}{\partial N'} = k\mu-(r-k)P$$

where $\mu = \partial F(N',g)/\partial N'$ and $P = -\partial F(N',g)/\partial g$ are chemical potential and pressure function, respectively, and $F(N',g) = -\ln Z_U(N',g)]$ is a free energy function in UgLLG, one obtains the following identity [167],

$$\langle n_i n_{i+r}\rangle = \rho e^{r\mu}\sum_{k=0}^{r} Z_U(r-k,k)e^{-k(\mu+P)}. \tag{C.28}$$

The above identity Eq. (C.28) can be used to obtain the generating function $G(y) = \sum_{r=0}^{\infty} y^r c(r)$,

$$G(y) = \left[\frac{\rho}{1-ye^{-P}\tilde{w}(yz)} - \frac{\rho^2}{1-y}\right] = \left[\frac{\rho\tilde{w}(z)}{\tilde{w}(z)-y\tilde{w}(yz)} - \frac{\rho^2}{1-y}\right], \tag{C.29}$$

which is expressed here in terms of (discrete) Laplace transform $\tilde{w}(z)$ of the weight factor $w(g)$ and where fugacity $z = e^{\mu}$ and $e^{-P} = 1/\tilde{w}(z)$. Note that $\tilde{w}(z)$ is calculated from the explicit form of the weight factor as already obtained in Eq. (C.21). We now perform asymptotic analysis around the critical point $z = 1$ (i.e., $\mu = 0$). By replacing the variable $y = \exp(-s)$ and then obtaining the leading order singularity in small $s = (1-y)$ expansion of Eq. (C.29), one can immediately determine the large r behaviour of the correlation function $c(r)$. In the limit of small $s \to 0$, we get, from Eq. (C.21), $\tilde{w}(yz)|_{z=1,y=1-s} \sim s^{3/2}$ and, consequently from Eq. (C.29), $G(y = 1-s) \sim s^{-1/2}$. The asymptotic form of the correlation function $c(r)$ is obtained by doing inverse Laplace transform,

$$c(r) \simeq \frac{1}{2\pi i}\int_{-i\infty}^{i\infty} ds e^{sr}G(s) \sim r^{-1/2}, \tag{C.30}$$

which is precisely the functional behavior of the correlation function at criticality as mentioned in the main text. Note that, although there are no spatial correlations in UgLLG (unbounded version), the spatial correlations in gLLG (exclusion version) are indeed long-ranged.

Bibliography

[1] James Clerk Maxwell. Illustrations of the dynamical theory of gases. part i. on the motions and collisions of perfectly elastic spheres. *The London, Edinburgh, and Dublin Philosophical Magazine and Journal of Science*, 19:19, 1860.

[2] James Clerk Maxwell. Illustrations of the dynamical theory of gases. part ii. on the process of diffusion of two or more kinds of moving particles among one another. *The London, Edinburgh, and Dublin Philosophical Magazine and Journal of Science*, 20:21, 1860.

[3] Ludwig Boltzmann and Friedrich Hasenöhrl. Studien über das gleichgewicht der lebendigen kraft zwischen bewegten materiellen punkten. 2012.

[4] Lev Davidovich Landau and Evgenii Mikhailovich Lifshitz. *Statistical Physics: Volume 5*, volume 5. Elsevier, 2013.

[5] Pavel L. Krapivsky, Sidney Redner, and Eli Ben-Naim. *A Kinetic View of Statistical Physics*. Cambridge University Press, 2010.

[6] Thomas Milton Liggett and Thomas M Liggett. *Interacting particle systems*, volume 2. Springer, 1985.

[7] Thomas M Liggett. *Stochastic interacting systems: contact, voter and exclusion processes*, volume 324. springer science & Business Media, 2013.

[8] Toni Feder. Statistical physics is for the birds. *Physics Today*, 60(10):28–30, 10 2007.

[9] Erik M Rauch, Mark M Millonas, and Dante R Chialvo. Pattern formation and functionality in swarm models. *Physics Letters A*, 207(3-4):185–193, 1995.

[10] Simon Hubbard, Petro Babak, Sven Th. Sigurdsson, and Kjartan G. Magnússon. A model of the formation of fish schools and migrations of fish. *Ecological Modelling*, 174(4):359–374, 2004.

[11] Christopher Dombrowski, Luis Cisneros, Sunita Chatkaew, Raymond E. Goldstein, and John O. Kessler. Self-concentration and large-scale coherence in bacterial dynamics. *Phys. Rev. Lett.*, 93:098103, Aug 2004.

[12] Gil Ariel, Amit Rabani, Sivan Benisty, Jonathan D. Partridge, Rasika M. Harshey, and Avraham Be'er. Swarming bacteria migrate by lévy walk. *Nature Communications*, 6(1):8396, Sep 2015.

[13] Liang Li, Simon F. Nørrelykke, and Edward C. Cox. Persistent cell motion in the absence of external signals: A search strategy for eukaryotic cells. *PLOS ONE*, 3(5):1–11, 05 2008.

[14] Franziska Matthäus, Marko Jagodič, and Jure Dobnikar. E. coli superdiffusion and chemotaxis—search strategy, precision, and motility. *Biophysical journal*, 97(4):946–957, 2009.

[15] Yuhai Tu and G. Grinstein. How white noise generates power-law switching in bacterial flagellar motors. *Phys. Rev. Lett.*, 94:208101, May 2005.

[16] Jeremie Palacci, Stefano Sacanna, Asher Preska Steinberg, David J. Pine, and Paul M. Chaikin. Living crystals of light-activated colloidal surfers. *Science*, 339(6122):936–940, 2013.

[17] Tamás Vicsek, András Czirók, Eshel Ben-Jacob, Inon Cohen, and Ofer Shochet. Novel type of phase transition in a system of self-driven particles. *Phys. Rev. Lett.*, 75:1226–1229, Aug 1995.

[18] András Czirók and Tamás Vicsek. Collective behavior of interacting self-propelled particles. *Physica A: Statistical Mechanics and its Applications*, 281(1-4):17–29, 2000.

[19] Hugues Chaté, Francesco Ginelli, Guillaume Grégoire, Fernando Peruani, and Franck Raynaud. Modeling collective motion: variations on the vicsek model. *The European Physical Journal B*, 64:451–456, 2008.

[20] J. Tailleur and M. E. Cates. Statistical mechanics of interacting run-and-tumble bacteria. *Phys. Rev. Lett.*, 100:218103, May 2008.

[21] Yaouen Fily and M. Cristina Marchetti. Athermal phase separation of self-propelled particles with no alignment. *Phys. Rev. Lett.*, 108:235702, Jun 2012.

[22] Michael E. Cates and Julien Tailleur. Motility-induced phase separation. *Annual Review of Condensed Matter Physics*, 6(1):219–244, 2015.

[23] Fernando Peruani, Andreas Deutsch, and Markus Bär. Nonequilibrium clustering of self-propelled rods. *Phys. Rev. E*, 74:030904, Sep 2006.

[24] Fernando Peruani. Active brownian rods. *The European Physical Journal Special Topics*, 225(11):2301–2317, Nov 2016.

[25] Fernando Peruani, Jörn Starruß, Vladimir Jakovljevic, Lotte Søgaard-Andersen, Andreas Deutsch, and Markus Bär. Collective motion and nonequilibrium cluster formation in colonies of gliding bacteria. *Phys. Rev. Lett.*, 108:098102, Feb 2012.

[26] Vijay Narayan, Sriram Ramaswamy, and Narayanan Menon. Long-lived giant number fluctuations in a swarming granular nematic. *Science*, 317(5834):105–108, 2007.

[27] H. P. Zhang, Avraham Be'er, E.-L. Florin, and Harry L. Swinney. Collective motion and density fluctuations in bacterial colonies. *Proceedings of the National Academy of Sciences*, 107(31):13626–13630, 2010.

[28] Julian Bialké, Hartmut Löwen, and Thomas Speck. Microscopic theory for the phase separation of self-propelled repulsive disks. *Europhysics Letters*, 103(3):30008, aug 2013.

[29] Subhadip Chakraborti, Shradha Mishra, and Punyabrata Pradhan. Additivity, density fluctuations, and nonequilibrium thermodynamics for active brownian particles. *Phys. Rev. E*, 93:052606, May 2016.

[30] Mingji Huang, Wensi Hu, Siyuan Yang, Quan-Xing Liu, and H. P. Zhang. Circular swimming motility and disordered hyperuniform state in an algae system. *Proceedings of the National Academy of Sciences*, 118(18):e2100493118, 2021.

[31] Salvatore Torquato. Swimming in circles can lead to exotic hyperuniform states of active living matter. *Proceedings of the National Academy of Sciences*, 118(24):e2107276118, 2021.

[32] Qun-Li Lei, Massimo Pica Ciamarra, and Ran Ni. Nonequilibrium strongly hyperuniform fluids of circle active particles with large local density fluctuations. *Science Advances*, 5(1):eaau7423, 2019.

[33] HOWARD C. BERG and DOUGLAS A. BROWN. Chemotaxis in escherichia coli analysed by three-dimensional tracking. *Nature*, 239(5374):500–504, Oct 1972.

[34] HOWARD C. BERG and ROBERT A. ANDERSON. Bacteria swim by rotating their flagellar filaments. *Nature*, 245(5425):380–382, Oct 1973.

[35] Mark J. Schnitzer. Theory of continuum random walks and application to chemotaxis. *Phys. Rev. E*, 48:2553–2568, Oct 1993.

[36] Rodrigo Soto and Ramin Golestanian. Run-and-tumble dynamics in a crowded environment: Persistent exclusion process for swimmers. *Phys. Rev. E*, 89:012706, Jan 2014.

[37] A. B. Slowman, M. R. Evans, and R. A. Blythe. Jamming and attraction of interacting run-and-tumble random walkers. *Phys. Rev. Lett.*, 116:218101, May 2016.

[38] Stefanie Put, Jonas Berx, and Carlo Vanderzande. Non-gaussian anomalous dynamics in systems of interacting run-and-tumble particles. *Journal of Statistical Mechanics: Theory and Experiment*, 2019(12):123205, dec 2019.

[39] Arghya Das, Abhishek Dhar, and Anupam Kundu. Gap statistics of two interacting run and tumble particles in one dimension. *Journal of Physics A: Mathematical and Theoretical*, 53(34):345003, aug 2020.

[40] Prashant Singh and Anupam Kundu. Crossover behaviours exhibited by fluctuations and correlations in a chain of active particles. *Journal of Physics A: Mathematical and Theoretical*, 54(30):305001, jul 2021.

[41] Subhajit Paul, Abhishek Dhar, and Debasish Chaudhuri. Dynamical crossovers and correlations in a harmonic chain of active particles. *arXiv preprint arXiv:2402.11358*, 2024.

[42] Thibault Bertrand, Yongfeng Zhao, Olivier Bénichou, Julien Tailleur, and Raphaël Voituriez. Optimized diffusion of run-and-tumble particles in crowded environments. *Phys. Rev. Lett.*, 120:198103, May 2018.

[43] Pierre Rizkallah, Alessandro Sarracino, Olivier Bénichou, and Pierre Illien. Microscopic theory for the diffusion of an active particle in a crowded environment. *Phys. Rev. Lett.*, 128:038001, Jan 2022.

[44] Aurélien Grabsch, Théotim Berlioz, Pierre Rizkallah, Pierre Illien, and Olivier Bénichou. From particle currents to tracer diffusion: Universal correlation profiles in single-file dynamics. *Phys. Rev. Lett.*, 132:037102, Jan 2024.

[45] Antoine Bricard, Jean-Baptiste Caussin, Nicolas Desreumaux, Olivier Dauchot, and Denis Bartolo. Emergence of macroscopic directed motion in populations of motile colloids. *Nature*, 503(7474):95–98, Nov 2013.

[46] Julien Deseigne, Olivier Dauchot, and Hugues Chaté. Collective motion of vibrated polar disks. *Phys. Rev. Lett.*, 105:098001, Aug 2010.

[47] Gabriel S. Redner, Michael F. Hagan, and Aparna Baskaran. Structure and dynamics of a phase-separating active colloidal fluid. *Phys. Rev. Lett.*, 110:055701, Jan 2013.

[48] John D. Weeks, David Chandler, and Hans C. Andersen. Role of Repulsive Forces in Determining the Equilibrium Structure of Simple Liquids. *The Journal of Chemical Physics*, 54(12):5237–5247, 06 1971.

[49] Julian Bialké, Thomas Speck, and Hartmut Löwen. Crystallization in a dense suspension of self-propelled particles. *Phys. Rev. Lett.*, 108:168301, Apr 2012.

[50] Claudio B. Caporusso, Leticia F. Cugliandolo, Pasquale Digregorio, Giuseppe Gonnella, Demian Levis, and Antonio Suma. Dynamics of motility-induced clusters: Coarsening beyond ostwald ripening. *Phys. Rev. Lett.*, 131:068201, Aug 2023.

[51] Néstor Sepúlveda, Laurence Petitjean, Olivier Cochet, Erwan Grasland-Mongrain, Pascal Silberzan, and Vincent Hakim. Collective cell motion in an epithelial sheet can be quantitatively described by a stochastic interacting particle model. *PLOS Computational Biology*, 9(3):1–12, 03 2013.

[52] Grzegorz Szamel. Self-propelled particle in an external potential: Existence of an effective temperature. *Phys. Rev. E*, 90:012111, Jul 2014.

[53] David Martin, Jérémy O'Byrne, Michael E. Cates, Étienne Fodor, Cesare Nardini, Julien Tailleur, and Frédéric van Wijland. Statistical mechanics of active ornstein-uhlenbeck particles. *Phys. Rev. E*, 103:032607, Mar 2021.

[54] Pritha Dolai, Arghya Das, Anupam Kundu, Chandan Dasgupta, Abhishek Dhar, and K. Vijay Kumar. Universal scaling in active single-file dynamics. *Soft Matter*, 16:7077–7087, 2020.

[55] M. E. Cates and J. Tailleur. When are active brownian particles and run-and-tumble particles equivalent? consequences for motility-induced phase separation. *Europhysics Letters*, 101(2):20010, feb 2013.

[56] A. P. Solon, M. E. Cates, and J. Tailleur. Active brownian particles and run-and-tumble particles: A comparative study. *The European Physical Journal Special Topics*, 224(7):1231–1262, Jul 2015.

[57] Mourtaza Kourbane-Houssene, Clément Erignoux, Thierry Bodineau, and Julien Tailleur. Exact hydrodynamic description of active lattice gases. *Phys. Rev. Lett.*, 120:268003, Jun 2018.

[58] Demian Levis and Ludovic Berthier. Clustering and heterogeneous dynamics in a kinetic monte carlo model of self-propelled hard disks. *Phys. Rev. E*, 89:062301, Jun 2014.

[59] Indranil Mukherjee, Adarsh Raghu, and Pradeep Kumar Mohanty. Nonexistence of motility induced phase separation transition in one dimension. *SciPost Phys.*, 14:165, 2023.

[60] Chandraniva Guha Ray, Indranil Mukherjee, and Pradeep Kumar Mohanty. Increased motility impedes clustering. *arXiv preprint arXiv:2307.03216*, 2023.

[61] Thibaut Arnoulx de Pirey, Gustavo Lozano, and Frédéric van Wijland. Active hard spheres in infinitely many dimensions. *Phys. Rev. Lett.*, 123:260602, Dec 2019.

[62] Robert Brown. Xxvii. a brief account of microscopical observations made in the months of june, july and august 1827, on the particles contained in the pollen of plants; and on the general existence of active molecules in organic and inorganic bodies. *The philosophical magazine*, 4(21):161–173, 1828.

[63] Albert Einstein. Über die von der molekularkinetischen theorie der wärme geforderte bewegung von in ruhenden flüssigkeiten suspendierten teilchen. *Annalen der physik*, 4, 1905.

[64] William Sutherland. Lxxv. a dynamical theory of diffusion for non-electrolytes and the molecular mass of albumin. *The London, Edinburgh, and Dublin Philosophical Magazine and Journal of Science*, 9(54):781–785, 1905.

[65] M. von Smoluchowski. Zur kinetischen theorie der brownschen molekularbewegung und der suspensionen. *Annalen der Physik*, 326(14):756–780, 1906.

[66] Paul Langevin. Sur la théorie de movement brownien. *Compt. Rend. Acad. Sci*, 1908.

[67] Carlos Mejía-Monasterio, Ralf Metzler, and Jürgen Vollmer. Anomalous transport: Applications, mathematical perspectives, and big data. *Frontiers in Physics*, page 550, 2020.

[68] Pinaki Chaudhuri, Ludovic Berthier, and Walter Kob. Universal nature of particle displacements close to glass and jamming transitions. *Phys. Rev. Lett.*, 99:060604, Aug 2007.

[69] Bo Wang, Stephen M. Anthony, Sung Chul Bae, and Steve Granick. Anomalous yet brownian. *Proceedings of the National Academy of Sciences*, 106(36):15160–15164, 2009.

[70] Kyriacos C. Leptos, Jeffrey S. Guasto, J. P. Gollub, Adriana I. Pesci, and Raymond E. Goldstein. Dynamics of enhanced tracer diffusion in suspensions of swimming eukaryotic microorganisms. *Phys. Rev. Lett.*, 103:198103, Nov 2009.

[71] Simona Hapca, John W Crawford, and Iain M Young. Anomalous diffusion of heterogeneous populations characterized by normal diffusion at the individual level. *Journal of the Royal Society Interface*, 6(30):111–122, 2009.

[72] Bo Wang, James Kuo, Sung Chul Bae, and Steve Granick. When brownian diffusion is not gaussian. *Nature Materials*, 11(6):481–485, Jun 2012.

[73] Juan Guan, Bo Wang, and Steve Granick. Even hard-sphere colloidal suspensions display fickian yet non-gaussian diffusion. *ACS Nano*, 8(4):3331–3336, 2014. PMID: 24646449.

[74] W. He, H. Song, Y. Su, L. Geng, B. J. Ackerson, H. B. Peng, and P. Tong. Dynamic heterogeneity and non-gaussian statistics for acetylcholine receptors on live cell membrane. *Nature Communications*, 7(1):11701, May 2016.

[75] Mykyta V Chubynsky and Gary W Slater. Diffusing diffusivity: a model for anomalous, yet brownian, diffusion. *Physical review letters*, 113(9):098302, 2014.

[76] Tomoshige Miyaguchi, Takuma Akimoto, and Eiji Yamamoto. Langevin equation with fluctuating diffusivity: A two-state model. *Physical Review E*, 94(1):012109, 2016.

[77] Rohit Jain and Kizhakeyil L. Sebastian. Diffusing diffusivity: Survival in a crowded rearranging and bounded domain. *The Journal of Physical Chemistry B*, 120(34):9215–9222, 2016. PMID: 27478982.

[78] Rohit Jain and K. L. Sebastian. Lévy flight with absorption: A model for diffusing diffusivity with long tails. *Phys. Rev. E*, 95:032135, Mar 2017.

[79] Neha Tyagi and Binny J. Cherayil. Non-gaussian brownian diffusion in dynamically disordered thermal environments. *The Journal of Physical Chemistry B*, 121(29):7204–7209, 2017. PMID: 28718637.

[80] Aleksei V Chechkin, Flavio Seno, Ralf Metzler, and Igor M Sokolov. Brownian yet non-gaussian diffusion: from superstatistics to subordination of diffusing diffusivities. *Physical Review X*, 7(2):021002, 2017.

[81] Rohit Jain and K. L. Sebastian. Diffusing diffusivity: Fractional brownian oscillator model for subdiffusion and its solution. *Phys. Rev. E*, 98:052138, Nov 2018.

[82] M Hidalgo-Soria and E Barkai. Hitchhiker model for laplace diffusion processes. *Physical Review E*, 102(1):012109, 2020.

[83] Sho C Takatori, Raf De Dier, Jan Vermant, and John F Brady. Acoustic trapping of active matter. *Nature communications*, 7(1):1–7, 2016.

[84] Andrey G Cherstvy, Oliver Nagel, Carsten Beta, and Ralf Metzler. Non-gaussianity, population heterogeneity, and transient superdiffusion in the spreading dynamics of amoeboid cells. *Physical Chemistry Chemical Physics*, 20(35):23034–23054, 2018.

[85] Andrey Sokolov, Leonardo Dominguez Rubio, John F Brady, and Igor S Aranson. Instability of expanding bacterial droplets. *Nature communications*, 9(1):1–8, 2018.

[86] Sara Dal Cengio, Demian Levis, and Ignacio Pagonabarraga. Linear response theory and green-kubo relations for active matter. *Phys. Rev. Lett.*, 123:238003, Dec 2019.

[87] M J Metson, M R Evans, and R A Blythe. Jamming of multiple persistent random walkers in arbitrary spatial dimension. *Journal of Statistical Mechanics: Theory and Experiment*, 2020(10):103207, oct 2020.

[88] Xia-qing Shi, Giordano Fausti, Hugues Chaté, Cesare Nardini, and Alexandre Solon. Self-organized critical coexistence phase in repulsive active particles. *Phys. Rev. Lett.*, 125:168001, Oct 2020.

[89] Tal Agranov, Sunghan Ro, Yariv Kafri, and Vivien Lecomte. Exact fluctuating hydrodynamics of active lattice gases—typical fluctuations. *Journal of Statistical Mechanics: Theory and Experiment*, 2021(8):083208, 2021.

[90] Oleksandr Chepizhko and Fernando Peruani. Diffusion, subdiffusion, and trapping of active particles in heterogeneous media. *Phys. Rev. Lett.*, 111:160604, Oct 2013.

[91] Ludovic Berthier. Nonequilibrium glassy dynamics of self-propelled hard disks. *Phys. Rev. Lett.*, 112:220602, Jun 2014.

[92] Alexander Liluashvili, Jonathan Ónody, and Thomas Voigtmann. Mode-coupling theory for active brownian particles. *Phys. Rev. E*, 96:062608, Dec 2017.

[93] Vincent E. Debets, Xander M. de Wit, and Liesbeth M. C. Janssen. Cage length controls the nonmonotonic dynamics of active glassy matter. *Phys. Rev. Lett.*, 127:278002, Dec 2021.

[94] Pierre Rizkallah, Alessandro Sarracino, Olivier Bénichou, and Pierre Illien. Microscopic theory for the diffusion of an active particle in a crowded environment. *Phys. Rev. Lett.*, 128:038001, Jan 2022.

[95] Omer Granek, Yariv Kafri, and Julien Tailleur. Anomalous transport of tracers in active baths. *Physical Review Letters*, 129(3):038001, 2022.

[96] Christina Kurzthaler, Clémence Devailly, Jochen Arlt, Thomas Franosch, Wilson C. K. Poon, Vincent A. Martinez, and Aidan T. Brown. Probing the spatiotemporal dynamics of catalytic janus particles with single-particle tracking and differential dynamic microscopy. *Phys. Rev. Lett.*, 121:078001, Aug 2018.

[97] AR Dulaney and JF Brady. Waves in active matter: The transition from ballistic to diffusive behavior. *Physical Review E*, 101(5):052609, 2020.

[98] Ehsan Irani, Zahra Mokhtari, and Annette Zippelius. Dynamics of bacteria scanning a porous environment. *Phys. Rev. Lett.*, 128:144501, Apr 2022.

[99] Tirthankar Banerjee, Robert L Jack, and Michael E Cates. Tracer dynamics in one dimensional gases of active or passive particles. *Journal of Statistical Mechanics: Theory and Experiment*, 2022(1):013209, jan 2022.

[100] S. C. Takatori, W. Yan, and J. F. Brady. Swim pressure: Stress generation in active matter. *Phys. Rev. Lett.*, 113:028103, Jul 2014.

[101] Alexandre P. Solon, Joakim Stenhammar, Raphael Wittkowski, Mehran Kardar, Yariv Kafri, Michael E. Cates, and Julien Tailleur. Pressure and phase equilibria in interacting active brownian spheres. *Phys. Rev. Lett.*, 114:198301, May 2015.

[102] Ahmad K Omar, Hyeongjoo Row, Stewart A Mallory, and John F Brady. Mechanical theory of nonequilibrium coexistence and motility-induced phase separation. *Proceedings of the National Academy of Sciences*, 120(18):e2219900120, 2023.

[103] Thomas Speck. Coexistence of active brownian disks: Van der waals theory and analytical results. *Physical Review E*, 103(1):012607, 2021.

[104] Léon Van Hove. Correlations in space and time and born approximation scattering in systems of interacting particles. *Phys. Rev.*, 95:249–262, Jul 1954.

[105] Francisco J. Sevilla and Mario Sandoval. Smoluchowski diffusion equation for active brownian swimmers. *Phys. Rev. E*, 91:052150, May 2015.

[106] Christina Kurzthaler, Sebastian Leitmann, and Thomas Franosch. Intermediate scattering function of an anisotropic active brownian particle. *Scientific reports*, 6(1):1–11, 2016.

[107] Christina Kurzthaler and Thomas Franosch. Intermediate scattering function of an anisotropic brownian circle swimmer. *Soft Matter*, 13(37):6396–6406, 2017.

[108] Francisco J. Sevilla and Pavel Castro-Villarreal. Generalized persistence dynamics for active motion. *Phys. Rev. E*, 104:064601, Dec 2021.

[109] Matteo Paoluzzi, Demian Levis, and Ignacio Pagonabarraga. From motility-induced phase-separation to glassiness in dense active matter. *Communications Physics*, 5(1):1–10, 2022.

[110] S Hanna, W Hess, and R Klein. The velocity autocorrelation function of an overdamped brownian system with hard-core intraction. *Journal of Physics A: Mathematical and General*, 14(12):L493, dec 1981.

[111] A. De Masi and P. A. Ferrari. Flux fluctuations in the one dimensional nearest neighbors symmetric simple exclusion process. *Journal of Statistical Physics*, 107(3):677–683, May 2002.

[112] Tanmoy Chakraborty and Punyabrata Pradhan. Time-dependent properties of run-and-tumble particles: Density relaxation. *Phys. Rev. E*, 109:024124, Feb 2024.

[113] Chikashi Arita, P. L. Krapivsky, and Kirone Mallick. Generalized exclusion processes: Transport coefficients. *Phys. Rev. E*, 90:052108, Nov 2014.

[114] Anirban Mukherjee and Punyabrata Pradhan. Dynamic correlations in the conserved manna sandpile. *Phys. Rev. E*, 107:024109, Feb 2023.

[115] L. Bertini, A. De Sole, D. Gabrielli, G. Jona-Lasinio, and C. Landim. Fluctuations in stationary nonequilibrium states of irreversible processes. *Phys. Rev. Lett.*, 87:040601, Jul 2001.

[116] L Bertini, A De Sole, D Gabrielli, G Jona-Lasinio, and C Landim. Macroscopic fluctuation theory for stationary Non-Equilibrium states. *Journal of Statistical Physics*, 107(3):635–675, May 2002.

[117] T. Bodineau and B. Derrida. Current fluctuations in nonequilibrium diffusive systems: An additivity principle. *Phys. Rev. Lett.*, 92:180601, May 2004.

[118] Lorenzo Bertini, Alberto De Sole, Davide Gabrielli, Giovanni Jona-Lasinio, and Claudio Landim. Macroscopic fluctuation theory. *Rev. Mod. Phys.*, 87:593–636, Jun 2015.

[119] Herbert Spohn. *Large Scale Dynamics of Interacting Particles*. 1991.

[120] Hugo Touchette. The large deviation approach to statistical mechanics. *Physics Reports*, 478(1):1–69, 2009.

[121] Arghya Das, Anupam Kundu, and Punyabrata Pradhan. Einstein relation and hydrodynamics of nonequilibrium mass transport processes. *Phys. Rev. E*, 95:062128, Jun 2017.

[122] Anupam Kundu, Sanjib Sabhapandit, and Abhishek Dhar. Application of importance sampling to the computation of large deviations in nonequilibrium processes. *Phys. Rev. E*, 83:031119, Mar 2011.

[123] Cristian Giardinà, Jorge Kurchan, and Luca Peliti. Direct evaluation of large-deviation functions. *Phys. Rev. Lett.*, 96:120603, Mar 2006.

[124] Gregory L Eyink, Joel L Lebowitz, and Herbert Spohn. Hydrodynamics and fluctuations outside of local equilibrium: Driven diffusive systems. *Journal of Statistical Physics*, 83(3):385–472, May 1996.

[125] Eric Bertin, Olivier Dauchot, and Michel Droz. Definition and relevance of nonequilibrium intensive thermodynamic parameters. *Phys. Rev. Lett.*, 96:120601, Mar 2006.

[126] Eric Bertin, Kirsten Martens, Olivier Dauchot, and Michel Droz. Intensive thermodynamic parameters in nonequilibrium systems. *Phys. Rev. E*, 75:031120, Mar 2007.

[127] Punyabrata Pradhan, Christian P. Amann, and Udo Seifert. Nonequilibrium steady states in contact: Approximate thermodynamic structure and zeroth law for driven lattice gases. *Phys. Rev. Lett.*, 105:150601, Oct 2010.

[128] Sayani Chatterjee, Punyabrata Pradhan, and P. K. Mohanty. Gammalike mass distributions and mass fluctuations in conserved-mass transport processes. *Phys. Rev. Lett.*, 112:030601, Jan 2014.

[129] Arghya Das, Sayani Chatterjee, Punyabrata Pradhan, and P. K. Mohanty. Additivity property and emergence of power laws in nonequilibrium steady states. *Phys. Rev. E*, 92:052107, Nov 2015.

[130] Arghya Das, Sayani Chatterjee, and Punyabrata Pradhan. Spatial correlations, additivity, and fluctuations in conserved-mass transport processes. *Phys. Rev. E*, 93:062135, Jun 2016.

[131] Pablo I. Hurtado and Pedro L. Garrido. Test of the additivity principle for current fluctuations in a model of heat conduction. *Phys. Rev. Lett.*, 102:250601, Jun 2009.

[132] Pablo I. Hurtado and Pedro L. Garrido. Large fluctuations of the macroscopic current in diffusive systems: A numerical test of the additivity principle. *Phys. Rev. E*, 81:041102, Apr 2010.

[133] T. Bodineau and B. Derrida. Distribution of current in nonequilibrium diffusive systems and phase transitions. *Phys. Rev. E*, 72:066110, Dec 2005.

[134] Rahul Dandekar, Subhadip Chakraborti, and R. Rajesh. Hard core run and tumble particles on a one-dimensional lattice. *Phys. Rev. E*, 102:062111, Dec 2020.

[135] Sheldon Katz, Joel L. Lebowitz, and Herbert Spohn. Nonequilibrium steady states of stochastic lattice gas models of fast ionic conductors. *Journal of Statistical Physics*, 34(3):497–537, Feb 1984.

[136] Claude Kipnis and Claudio Landim. *Scaling limits of interacting particle systems*, volume 320. Springer Science & Business Media, 1998.

[137] George H Weiss. Some applications of persistent random walks and the telegrapher's equation. *Physica A: Statistical Mechanics and its Applications*, 311(3):381–410, 2002.

[138] Tanmoy Chakraborty, Subhadip Chakraborti, Arghya Das, and Punyabrata Pradhan. Hydrodynamics, superfluidity, and giant number fluctuations in a model of self-propelled particles. *Phys. Rev. E*, 101:052611, May 2020.

[139] Subhadip Chakraborti, Tanmoy Chakraborty, Arghya Das, Rahul Dandekar, and Punyabrata Pradhan. Transport and fluctuations in mass aggregation processes: Mobility-driven clustering. *Phys. Rev. E*, 103:042133, Apr 2021.

[140] Nisha Katyal, Supravat Dey, Dibyendu Das, and Sanjay Puri. Coarsening dynamics in the vicsek model of active matter. *The European Physical Journal E*, 43(2):10, Feb 2020.

[141] L. Caprini, U. Marini Bettolo Marconi, and A. Puglisi. Spontaneous velocity alignment in motility-induced phase separation. *Phys. Rev. Lett.*, 124:078001, Feb 2020.

[142] Lorenzo Caprini, Umberto Marini Bettolo Marconi, Claudio Maggi, Matteo Paoluzzi, and Andrea Puglisi. Hidden velocity ordering in dense suspensions of self-propelled disks. *Phys. Rev. Res.*, 2:023321, Jun 2020.

[143] Lorenzo Caprini and Umberto Marini Bettolo Marconi. Spatial velocity correlations in inertial systems of active brownian particles. *Soft Matter*, 17:4109–4121, 2021.

[144] Grzegorz Szamel and Elijah Flenner. Long-ranged velocity correlations in dense systems of self-propelled particles. *Europhysics Letters*, 133(6):60002, 2021.

[145] Simon Garcia, Edouard Hannezo, Jens Elgeti, Jean-François Joanny, Pascal Silberzan, and Nir S Gov. Physics of active jamming during collective cellular motion in a monolayer. *Proceedings of the National Academy of Sciences*, 112(50):15314–15319, 2015.

[146] Andrea Cavagna, Daniele Conti, Chiara Creato, Lorenzo Del Castello, Irene Giardina, Tomas S Grigera, Stefania Melillo, Leonardo Parisi, and Massimiliano Viale. Dynamic scaling in natural swarms. *Nature Physics*, 13(9):914–918, 2017.

[147] Silke Henkes, Kaja Kostanjevec, J Martin Collinson, Rastko Sknepnek, and Eric Bertin. Dense active matter model of motion patterns in confluent cell monolayers. *Nature communications*, 11(1):1405, 2020.

[148] Yann-Edwin Keta, Robert L. Jack, and Ludovic Berthier. Disordered collective motion in dense assemblies of persistent particles. *Phys. Rev. Lett.*, 129:048002, Jul 2022.

[149] Bernard Derrida and Joel L. Lebowitz. Exact large deviation function in the asymmetric exclusion process. *Phys. Rev. Lett.*, 80:209–213, Jan 1998.

[150] RJ Harris, A Rákos, and Gunter M Schütz. Current fluctuations in the zero-range process with open boundaries. *Journal of Statistical Mechanics: Theory and Experiment*, 2005(08):P08003, 2005.

[151] C. Appert-Rolland, B. Derrida, V. Lecomte, and F. van Wijland. Universal cumulants of the current in diffusive systems on a ring. *Phys. Rev. E*, 78:021122, Aug 2008.

[152] Bernard Derrida and Antoine Gerschenfeld. Current fluctuations of the one dimensional symmetric simple exclusion process with step initial condition. *Journal of Statistical Physics*, 136(1):1–15, Jul 2009.

[153] Tridib Sadhu and Bernard Derrida. Correlations of the density and of the current in non-equilibrium diffusive systems. *Journal of Statistical Mechanics: Theory and Experiment*, 2016(11):113202, 2016.

[154] L. Bertini, A. De Sole, D. Gabrielli, G. Jona-Lasinio, and C. Landim. Current fluctuations in stochastic lattice gases. *Phys. Rev. Lett.*, 94:030601, Jan 2005.

[155] Bernard Derrida and Antoine Gerschenfeld. Current fluctuations in one dimensional diffusive systems with a step initial density profile. *Journal of Statistical Physics*, 137(5):978–1000, Dec 2009.

[156] F. Cagnetta, F. Corberi, G. Gonnella, and A. Suma. Large fluctuations and dynamic phase transition in a system of self-propelled particles. *Phys. Rev. Lett.*, 119:158002, Oct 2017.

[157] Tirthankar Banerjee, Satya N. Majumdar, Alberto Rosso, and Grégory Schehr. Current fluctuations in noninteracting run-and-tumble particles in one dimension. *Phys. Rev. E*, 101:052101, May 2020.

[158] Trevor GrandPre and David T Limmer. Current fluctuations of interacting active brownian particles. *Physical Review E*, 98(6):060601, 2018.

[159] Tal Agranov, Sunghan Ro, Yariv Kafri, and Vivien Lecomte. Macroscopic fluctuation theory and current fluctuations in active lattice gases. *SciPost Physics*, 14(3):045, 2023.

[160] Animesh Hazra, Anirban Mukherjee, and Punyabrata Pradhan. Dynamic fluctuations of current and mass in nonequilibrium mass transport processes. *arXiv preprint*, 2309.14705 (2023).

[161] Frank Spitzer. Interaction of markov processes. *Advances in Mathematics*, 5(2):246–290, 1970.

[162] Tanmoy Chakraborty and Punyabrata Pradhan. Time-dependent properties of run-and-tumble particles. ii. current fluctuations. *Phys. Rev. E*, 109:044135, Apr 2024.

[163] M R Evans and T Hanney. Nonequilibrium statistical mechanics of the zero-range process and related models. *Journal of Physics A: Mathematical and General*, 38(19):R195, apr 2005.

[164] Matthias Beck and Ross Geoghegan. *The art of proof: basic training for deeper mathematics*. Springer, 2010.

[165] Subhadip Chakraborti. *Studies of fluctuations in systems of selfpropelled particles*. PhD thesis, Ph. D. thesis, University of Calcutta, 2018.

[166] Satya N. Majumdar, Supriya Krishnamurthy, and Mustansir Barma. Nonequilibrium phase transitions in models of aggregation, adsorption, and dissociation. *Phys. Rev. Lett.*, 81:3691–3694, Oct 1998.

[167] Priyanka, Arvind Ayyer, and Kavita Jain. Two-point correlation function of an exclusion process with hole-dependent rates. *Phys. Rev. E*, 90:062104, Dec 2014.

[168] Satya N. Majumdar, M. R. Evans, and R. K. P. Zia. Nature of the condensate in mass transport models. *Phys. Rev. Lett.*, 94:180601, May 2005.

[169] Léon Van Hove. Time-dependent correlations between spins and neutron scattering in ferromagnetic crystals. *Phys. Rev.*, 95:1374–1384, Sep 1954.

[170] P. C. Hohenberg and B. I. Halperin. Theory of dynamic critical phenomena. *Rev. Mod. Phys.*, 49:435–479, Jul 1977.

[171] Héctor Matías López, Jérémie Gachelin, Carine Douarche, Harold Auradou, and Eric Clément. Turning bacteria suspensions into superfluids. *Phys. Rev. Lett.*, 115:028301, Jul 2015.

[172] Yashodhan Hatwalne, Sriram Ramaswamy, Madan Rao, and R. Aditi Simha. Rheology of active-particle suspensions. *Phys. Rev. Lett.*, 92:118101, Mar 2004.